Ceramic Membranes for Fouling and Organic Micropollutant Control
Integration of Catalytic Modification and Advanced Oxidation Processes

Zhang, S.

DOI
10.4233/uuid:b1253104-23ae-4d0d-8a09-d6187251b620

Publication date
2026

Document Version
Final published version

Citation (APA)
Zhang, S. (2026). *Ceramic Membranes for Fouling and Organic Micropollutant Control: Integration of Catalytic Modification and Advanced Oxidation Processes*. [Dissertation (TU Delft), Delft University of Technology]. https://doi.org/10.4233/uuid:b1253104-23ae-4d0d-8a09-d6187251b620

Ceramic Membranes for Fouling and Organic Micropollutant Control

Integration of Catalytic Modification and Advanced Oxidation Processes

Shuo ZHANG

Proposition

Accompanying the dissertation

Ceramic Membranes for Fouling and Organic Micropollutant Control

Integration of Catalytic Modification and Advanced Oxidation Processes

by

Shuo ZHANG

1. Permeability decline during the filtration of nano-sized particles can be largely affected by concentration polarization (this thesis).
2. Cleaning of fouled ceramic membranes can be enhanced by Fenton-like backwash (this thesis).
3. Ceramic membranes with low catalysts loadings and oxidant dosing are effective in fouling mitigation and micropollutant degradation (this thesis).
4. Fouling has a minimal effect on the degradation of micropollutants in the coupled system with catalytic membranes and oxidant dosing (this thesis).
5. Low-loaded catalyst approaches, offering a high treatment efficacy with reduced costs, hold potential for broader application.
6. The contributions of coexisting reactive species—beyond the dominant one—to pollutant degradation should be carefully considered, particularly when treating complex water matrices.
7. The development of ceramic membranes with smaller pore sizes is essential for achieving precise separation of target molecules or ions, particularly in applications that demand high selectivity under chemically harsh conditions.
8. Two-dimensional materials can be integrated as the selective layer in ceramic membranes to improve permeability, due to their ultrathin thickness and minimal transport resistance.
9. Whatever unfolds today, the sun will rise again tomorrow — unshaken and sure.
10. ‘‘Empty talk harms the nation, practical action helps it thrive.’’ — (Xiaoping Deng, 1992)

These propositions are regarded as opposable and defendable, and have been approved as such by the promoters Prof.dr.ir. L.C. Rietveld and Dr.ir. S.G.J. Heijman

Invitation

You are cordially invited to the public defense of the PhD thesis:

Ceramic Membranes for Fouling and Organic Micropollutant Control

Integration of Catalytic Modification and Advanced Oxidation Processes

by

Shuo ZHANG

Tuesday 6th January 2026

At 10:00

Laymen's talk & Defense

Aula, TU Delft

You are also invited to the reception at 11:30, Aula;

Paranymph

Qin Ou

Yanghui Xu

Ceramic Membranes for Fouling and Organic Micropollutant Control

Integration of Catalytic Modification and Advanced Oxidation Processes

Dissertation

for the purpose of obtaining the degree of doctor
at Delft University of Technology
by the authority of the Rector Magnificus prof.dr.ir. T.H.J.J. van der Hagen
chair of the Board for Doctorates
to be defended publicly on
Tuesday 6 January 2026 at 10:00 o'clock

by

Shuo ZHANG

Master of Science in Chemical Engineering,
Technion – Israel Institute of Technology, Israel,
born in Jiangsu, China

This dissertation has been approved by the promotors.

Composition of the doctoral committee:

Rector Magnificus	Chairperson
Dr.ir. S.G.J. Heijman	Delft University of Technology, promotor
Prof.dr.ir. L.C. Rietveld	Delft University of Technology, promotor

Independent members:

Prof.dr. M.D. Kennedy	Delft University of Technology
Prof.dr.ir. E.R. Cornelissen	Ghent University / KWR, Belgium / NL
Prof.dr. B. Liu	Sichuan University, China
Dr. M.B. Tanis	Delft University of Technology
Prof.dr. Ing. T. Wintgens	RWTH Aachen University, Germany
Prof.dr.ir. J.B. van Lier	Delft University of Technology, reserve member

Partially supported by Lamminga Fund

Keywords: Ceramic membrane, Fouling, Micropollutants, Advanced oxidation processes, Low catalyst loading

Pribt by: https://proefschrift-aio.nl/

Cover by: Shuo ZHANG and Wenxuan HUANG

Design inspired by: A stubborn donkey boring a hole in the wall to borrow light, Nüwa mending the heavens, and Xu Zhimo's poem Saying Goodbye to Cambridge Again.

ISBN: 978-94-6518-212-4

An electronic version of this dissertation is available at

https://repository.tudelft.nl/

To my family

Contents

清平乐

银钩流火，叶叶株湿透。蜷卧层衾灯尚弱，梦里方程无数。

之乎者也诗词，碳氢氧氮习题。欲语休文隋柳，悲鸿奔马风流。

2010

Chapter 1

Introduction

1.1. Ceramic membranes in water treatment

The rapid growth of industrialization, urbanization, and global population over recent decades has intensified the pressure on water resources, making water scarcity a critical challenge to sustainable development (Dong et al., 2022). More advanced technologies are thus required for clean water production and wastewater reclamation. Membranes have been regarded as a promising alternative in water and wastewater treatment. Although polymeric membranes currently dominate the market, they suffer from poor resistance to chemicals, and high fouling propensity, due to their hydrophobic nature. In contrast, ceramic membranes, known for their robustness, chemical stability, and long lifespan, offer a good alternative to conventional polymeric membranes in various water treatment applications, including wastewater reuse, and removal of specific contaminants (Asif and Zhang, 2021).

Ceramic membranes are typically fabricated from inorganic materials such as alumina (Al_2O_3), zirconia (ZrO_2), titania (TiO_2), or silicon carbide (SiC), having a high mechanical strength and thermal stability, which make them withstand harsh operating conditions, including high temperature, extreme pH, and exposure to aggressive chemicals. Based on the pore sizes, ceramic membranes can be classified into microfiltration (MF) ultrafiltration (UF), and nanofiltration (NF) with pore sizes ranging from > 100 nm, 1–100 nm, and < 1 nm, respectively. The large range of pore sizes of ceramic membranes makes them suitable for both industrial and drinking water treatment. As a highly effective and promising separation technology, ceramic membranes have therefore a growing research interest in water treatment, as evidenced by the exponential increase in related publications over the past decades (Fig. 1.1a). As reviewed by Dong et al. (2022), ceramic membranes for water treatment have mainly been employed for applications such as the treatment of oily water and organic wastewater.

MF, UF, and NF, used for water treatment, account for 40%, 42%, and 18% of the applications, respectively, as shown in Fig. 1.1b. Ceramic MF/UF membranes, with relatively large sizes, are effective in the removal of suspended solids, bacteria, and organic macromolecules, common contaminants in water and wastewater streams. However, ceramic NF membranes are still emerging, with limited commercial suppliers and few standardized products on the market. Moreover, the small pore sizes of ceramic NF membranes require precise fabrication, often involving expensive materials

and precise process control. Its high production costs, therefore, limit its wide application.

Despite the broad application of ceramic membranes in water treatment, several challenges remain, including high production costs, limited rejection of small, organic micropollutants, membrane fouling, and the relatively low permeability caused by the dense selective layers.

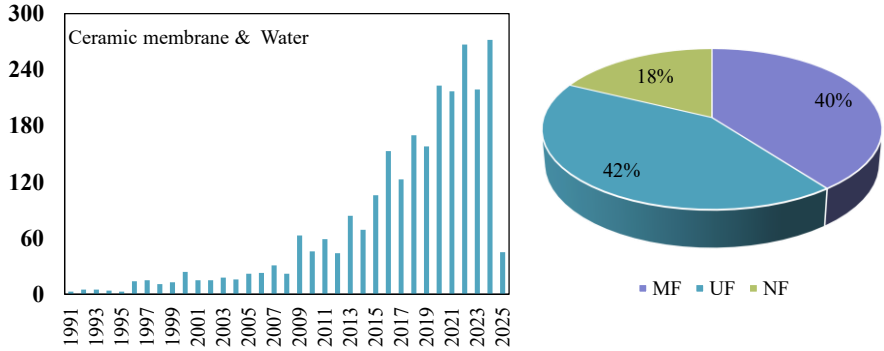

Figure 1.1. (a) Number of publications on ceramic membranes for water treatment from 1991 to 2025, based on a Web of Science search conducted in March 2025 using the keywords “ceramic membrane AND water treatment.” (b) Percentage of different types of ceramic membranes reported in water treatment studies, based on Web of Science search conducted in March 2025 using the keywords “ceramic microfiltration/ultrafiltration/nanofiltration membrane or ceramic MF/UF/NF membrane AND water treatment.”

1.2. Fouling in ceramic membrane filtration

Natural and industrial waters typically contain a wide variety of dissolved and suspended constituents, including organic matter, inorganic salts, colloids, microorganisms, and particulate matter. In industrial effluents, the compositions, mainly depending on the source and process, are even more complex. Membrane fouling occurs when these contaminants accumulate on the membrane surface or within its pores, leading to reduced permeability, resulting in increased energy consumption, and higher operational costs. In an earlier study Jafari et al. (2021) have quantified that the costs of membrane fouling in seven full-scale installations accounted for up to 24% of the total treatment cost. However, in the treatment of anoxic groundwater, the induced low fouling potential reduced the cost to 11%.

Fouling mechanisms are typically categorized into pore blocking and cake layer formation, where pore blocking contributes more to the flux decline, compared to cake formation (Lin et al., 2023). To reveal the fouling mechanism of pore blocking and cake fouling, varying models have been developed (Field et al., 1995; Herima, 1982). The fouling retained in the pores is much harder to remove, which will lead to irreversible fouling. The cleaning method, such as hydraulic backwash, is more effective in removing cake layer fouling, while it has limited efficacy against pore blocking. It often requires chemical or advanced oxidative cleaning to address irreversible fouling.

Ceramic membranes, despite their high mechanical strength and chemical resistance compared to polymeric membranes, still face fouling challenges during water treatment applications. In fact, fouling remains one of the primary limitations hindering the broader application of ceramic membranes in water and wastewater treatment (Asif and Zhang, 2021). Consequently, fouling has attracted increasing attention from researchers and engineers. As shown in Fig. 1.2a, the number of studies focusing on fouling in ceramic membranes has grown rapidly over the past few decades, reflecting the critical importance of fouling in both academic and practical domains. Among these studies, the majority have concentrated on ceramic UF membranes, which account for 44% of all ceramic membrane types (Fig. 1.2b). Among the typical organic foulants that cause membrane fouling, alginate, humic acids, and bovine serum albumin, which represent polysaccharide, humic substances, and protein fouling, respectively, have been widely studied due to their prevalence in natural and industrial wastewater systems. Taking alginate as an example, it originates mainly from algal and microbial activity in natural water, while in wastewater, they are abundant in biological effluents and sludge-derived substances. Their strong affinity for divalent cations like Ca^{2+} promotes alginate gel formation and the development of a dense, resistant fouling layer on membrane surfaces, leading to severe permeability decline. Traditional cleaning methods, such as hydraulic backwash and forward flush, can be ineffective in the detachment of such pertinacious fouling from ceramic membranes (Chen and Columbia, 2011; Lin et al., 2021). Therefore, there is a need to develop novel strategies to mitigate fouling on ceramic membranes, particularly the fouling retained within the membrane pores.

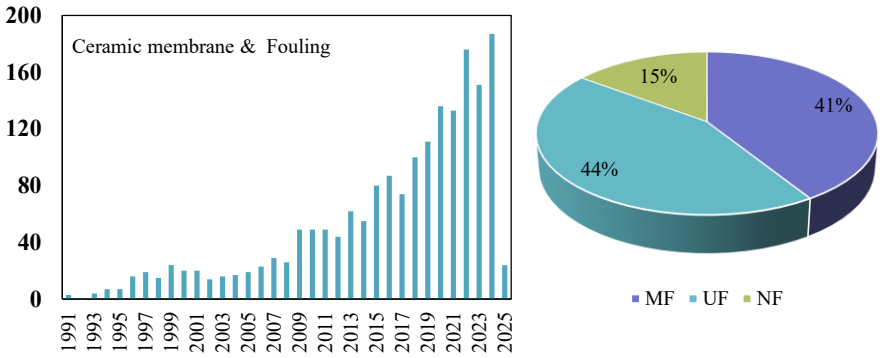

Figure1. 2. (a) Number of publications on fouling of ceramic membranes from 1991 to 2025, based on a Web of Science search conducted in March 2025 using the keywords "ceramic membrane AND fouling." (b) Percentage of different types of ceramic membranes reported in fouling studies.

1.3. Pollutant removal by ceramic membranes

The efficiency of contaminant removal by ceramic membranes largely depends on the membrane's pore size, which determines its separation mechanism (Fig. 1.3). MF membranes (>100 nm) are commonly used to remove the larger contaminants, such as colloids; UF membranes (10-100 nm) can also remove macromolecules, (pathogenic) micro-organisms, and proteins; NF membranes (0.7-1 nm) are designed to remove low-molecular-weight compounds and some dissolved solutes. In addition to size exclusion, other mechanisms such as charge repulsion (Donnan exclusion) and surface interactions (e.g., hydrophobicity) contribute to pollutant rejection, particularly in ceramic NF membranes (Árki et al., 2019; Asif and Zhang, 2021; Chen et al., 2022). These combined mechanisms enable commercial ceramic NF membranes to achieve a partial removal of (small) ions and organic contaminants.

However, due to the technical challenges associated with precise fabrication, the smallest pore sizes of currently available commercial ceramic NF membranes typically fall within the range of 200–400 Da (approximately 0.7–0.9 nm). Despite these nominal specifications, the actual pore sizes are often larger than those indicated by manufacturers. Previous work has revealed that 10 out of the 29 commercial ceramic NF membranes exhibited surface defects exceeding 5%, while similar problems have also been reported in commercial ceramic UF membranes (Kramer et al., 2019). These relatively large pore sizes and the presence of defects limit the applicability of ceramic NF membranes,

especially in comparison to the polymeric counterparts, for the removal of small-sized, dissolved contaminants such as heavy metals and emerging organic pollutants (Fujioka et al., 2014). These contaminants often have a size much smaller than the nominal pore sizes of ceramic membranes, resulting in insufficient rejection. This limitation is also evident in the existing literature: a screening of the Web of Science database using the keywords “ceramic membrane AND micropollutant OR emerging organic pollutant” yields only a limited number of studies, further highlighting the current gap in research and application in this field.

Various surface and structural modifications of ceramic membranes have been proposed to narrow their pore sizes and enhance separation performance, especially for NF. One of the approaches for surface modification is atomic layer deposition (ALD), which offers atom-level control over the deposition of inorganic and organic-inorganic hybrid layers, respectively. This technique enables the conformal coating of membrane pores with ultra-thin, uniform layers, effectively reducing the pore diameter while preserving membrane integrity. Ceramic membranes with a pore size of 0.7-2.9 nm have been narrowed to 0.5-1.1 nm by ALD (Nijboer et al., 2024; Shang et al., 2017). However, the ALD-modified NF membranes frequently suffer from a high permeability loss, e.g., dropping from 26 L/(m^2·h·bar) at 1 nm to 11 L/(m^2·h·bar) at 0.8 nm pore size (Shang et al., 2017). Also, metal-organic frameworks and zeolites, because of their tunable pore sizes and functional chemistry, have been grown onto ceramic membranes to enhance the rejection of small-sized contaminants. Despite their promising separation performance, these materials also tend to induce considerable permeability losses. This trade-off between selectivity and permeability thus presents a major challenge for practical applications of modified membranes, underscoring the need for continued optimization in layer thickness, porosity, and interfacial compatibility to minimize transport resistance while maintaining a high rejection efficacy.

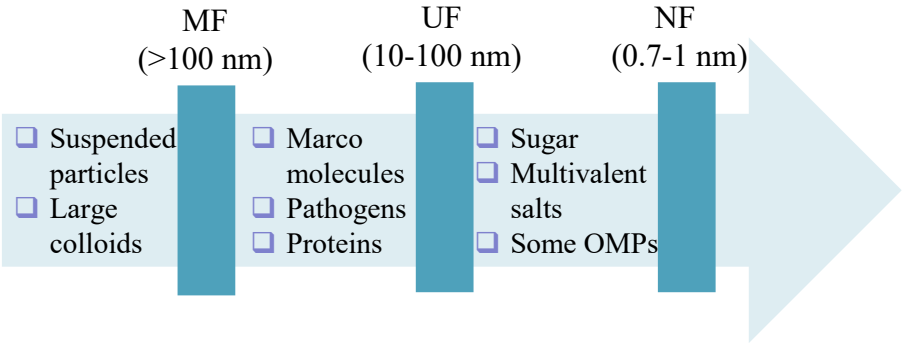

Figure 1.3. Pore sizes of commercial ceramic membranes, and their application in the removal of contaminants.

1.4. Permeability loss caused by concentration polarization and fouling

Membranes can experience a high permeability loss during filtration, especially when treating a complex feedwater. The permeability loss is typically attributed to fouling. However, osmotic pressure or concentration polarization (CP) can also lead to a high permeability loss, especially at the initial stage of filtration. The understanding of the contribution of fouling and CP to permeability decline is important for the optimization of membrane performance.

CP refers to the accumulation of retained dissolved compounds or colloids near the membrane surface, leading to the development of a concentration gradient between the membrane interface and the bulk solution. As water permeates through the membrane, the matters are rejected and become concentrated near the membrane surface. CP is defined by $(C_m - C_p)/(C_b - C_p)$, where C_m, C_p, and $C_b$is solute concentration at the membrane surface, in the permeate side, and in the bulk, respectively. The increasing solute concentration near the membrane surface can result in elevated osmotic pressure and reduced driving force across the membrane, thereby lowering the permeate flux, exacerbating membrane fouling, and potentially affecting the rejection of other contaminants, such as OMPs.

The CP is widely studied using the traditional film diffusion mode, due to its simplicity and its ability to provide relatively reliable estimations under conditions of low CP and minimal fouling. However, it does not account for the effects of fouling on the mass balance, which can lead to deviations (Liu et

al., 2018). The high salt rejection by reverse osmosis membranes can result in a relatively large CP, compared to NF and UF. The CP caused by ions in reverse osmosis systems is typically in the range of 1–2 (Qiu and Davies, 2015). In contrast, the CP of ions in NF, UF, and MF can generally be neglected due to their lower ion rejection.

When filtering feedwater containing nano-sized contaminations like colloids, the high rejection by NF, UF, or MF and the low diffusion of these colloids can lead to a high CP of these contaminants, potentially leading to a high permeability loss. However, limited studies have focused on colloidal CP in membrane filtration. Moreover, the traditional CP model does not allow for quantification of the contribution of CP to permeability decline, which may lead to a misunderstanding of the relative contribution of CP and membrane fouling to flux loss.

1.5. Modification of ceramic membrane for fouling and OMPs removal

To address the challenges associated with ceramic membranes, various modification strategies have been developed to enhance their selectivity and antifouling properties by altering the surface chemistry, pore structure, or functionality of ceramic membranes.

The use of metals in ceramic membranes has been a strategy to enhance their antifouling properties and OMP removal efficacy. Metals, including transition metals (e.g., iron, titanium, manganese) and noble metals (e.g., palladium, platinum), are typically introduced as nanoparticles, coatings, or dopants, either on the membrane surface or within its porous structure.

As discussed in Section 1.3, ALD has been used to modify the ceramic membranes. However, a few cycles of ALD growth can lead to a discontinuous layer on the membrane surface, thus influencing the membrane performance (Zhou et al., 2018), while the extension of ALD cycles for a continuous separative layer could lead to a low porosity, which will, in turn, result in a low permeability (Shang et al., 2017).

However, the metal-based materials such as TiO_2, $CuFe_2O_4$, and Pd have also been grown on the membrane surface or within the pores, to act as catalysts. The catalytic ceramic membrane can then be coupled with advanced oxidation processes (AOPs), such as Fenton-like reactions, photocatalysis, or peroxymonosulfate (PMS) activation, to enhance the removal of fouling and

OMPs (Dong et al., 2022). Despite their advantages, the long-term stability of catalytic ceramic membranes remains a concern. One of the major challenges is the leaching of catalytic coating during operation, especially when treating harsh feedwater. Metal leaching not only compromises the structural and chemical stability of the membrane but also reduces catalytic activity over time. Besides, excessive catalyst loading may introduce pore blocking, resulting in permeability loss. The large loading of catalysts can also increase the fabrication costs, and even deactivate the catalytic process. It has been reported that overloading can result in reduced catalyst use efficacy and quenching of the radicals induced by AOPs (Feng et al., 2017; Li et al., 2018).

1.6. Strategies to reduce the cost of ceramic membrane applications

As discussed above, the cost of materials and operation is still one of the major challenges limiting the wider application of ceramic membranes. To address this limitation, several strategies have been proposed.

Using low-cost materials. The cost of polymeric membrane is 20-200 \$ m^{-2}, comparing to 500-3000 \$ m^{-2} for Al_2O_3 and ZrO_2 based ceramic membranes, according to the review of Dong et al., (2022). Therefore, using lower-cost materials, such as mineral-based or waste-derived materials, represents a promising strategy to reduce the overall production cost of ceramic membranes.

Using low-cost manufacturing techniques. The formation of ceramic membranes normally requires high sintering temperatures (up to 1500–1700 °C) (Dong et al., 2022). Therefore, one of the promising methods is to use sintering additives in the sintering process to reduce final sintering temperature. In addition, the thick selective layers of ceramic membranes not only increase manufacturing costs but also reduce permeability, which in turn raises operational costs. Consequently, developing thinner selective layers is another effective strategy for cost reduction.

Optimization of filtration process. The total cost of membrane application also includes operational costs (Jafari et al., 2021). Optimizing the filtration process can therefore significantly reduce the overall costs. Filtration parameters such as flux, pressure, and cross-flow velocity can be adjusted to improve energy efficiency and reduce fouling formation. In addition, an appropriate cleaning strategy, such as the choice of cleaning agents, the cleaning interval, and the cleaning duration, can be further optimized to lower chemical use and

maintenance costs. Pretreatment of the feedwater can also contribute to removing large particles or NOM, which can reduce fouling formation and increase water production. Moreover, coupling ceramic membranes with AOPs can improve the removal of fouling or OMPs. Together, these optimization methods can significantly decrease the operational cost of membrane systems.

1.7. Overall objective and research questions

According to the discussion presented above, fouling and OMPs removal are still a challenge for ceramic membranes. Further modification of ceramic membranes may suffer from permeability decline after coating, which limits their application. Therefore, the presented study aims to develop novel ceramic membranes with a high permeability that are able to mitigate fouling and enhance OMPs removal.

The overall objective is further specified into the following research questions (RQ):

- ***RQ 1:*** *What is the contribution of CP and fouling to permeability decline?*
- ***RQ2:*** *How does Fenton-like cleaning influence backwash?*
- ***RQ3:*** *Can ceramic membranes with low-loading catalysts achieve effective degradation of OMPs?*
- ***RQ4:*** *What role does fouling play in the degradation of OMPs by catalytic ceramic membranes?*

1.8. Thesis outline

In **Chapter 2**, a new method is described to distinguish the effect of fouling and CP on permeability decline in the filtration of nano-sized contaminants. Therefore, the contribution of fouling and CP to permeability loss was determined. Besides, the traditional model was modified to better estimate the CP values.

In **Chapter 3**, the integration of Fenton-like backwash with a catalytic ceramic membrane was proposed. The backwash intensities, i.e., pressure and duration, and fouling structures are presented to reveal their effect on the cleaning.

In **Chapter 4**, catalytic ceramic membranes, fabricated by ALD, to achieve a low loading of catalysts, are discussed. The modified membranes were evaluated for OMPs' removal under varying conditions, including different catalytic loading, PMS concentrations, pH, ions, fluxes, and types of feedwaters (brine and river water). Besides, the mechanisms, such as the

dominant reactive species and the contribution of catalysts grown on the surface and in the pores, were determined.

In **Chapter 5**, the simultaneous degradation of fouling and OMPs during membrane filtration, with a special focus on the effect of fouling on OMPs degradation, is described. The PMS concentrations, foulant types, fluxes, and calcium were studied in this work. In addition, the effect of fouling on the contribution of reactive species to OMPs degradation was revealed.

The thesis ends with **Chapter 6** on conclusions and outlook.

Reference

Árki, P., Hecker, C., Tomandl, G., Joseph, Y., 2019. Streaming potential properties of ceramic nanofiltration membranes – Importance of surface charge on the ion rejection. Sep. Purif. Technol. 212, 660–669. https://doi.org/10.1016/j.seppur.2018.11.054

Asif, M.B., Zhang, Z., 2021. Ceramic membrane technology for water and wastewater treatment: A critical review of performance, full-scale applications, membrane fouling and prospects. Chem. Eng. J. 418, 129481. https://doi.org/10.1016/j.cej.2021.129481

Bahrouni, J., Aloulou, H., Attia, A., Dammak, L., Amar, R.B., 2024. Surface modification of a zeolite microfiltration membrane: characterization and application to the treatment of colored and oily wastewaters. Chem. Afr. 7, 4513–4527. https://doi.org/10.1007/s42250-024-01035-9

Chen, D., Columbia, M., 2011. Enzymatic control of alginate fouling of dead-end MF and UF ceramic membranes. J. Membr. Sci. 381, 118–125. https://doi.org/10.1016/j.memsci.2011.07.033

Chen, M., Heijman, S.G.J., Luiten-Olieman, M.W.J., Rietveld, L.C., 2022. Oil-in-water emulsion separation: fouling of alumina membranes with and without a silicon carbide deposition in constant flux filtration mode. Water Res. 216, 118267. https://doi.org/10.1016/j.watres.2022.118267

Dong, Y., Wu, H., Yang, F., Gray, S., 2022. Cost and efficiency perspectives of ceramic membranes for water treatment. Water Res. 220, 118629. https://doi.org/10.1016/j.watres.2022.118629

Feng, Y., Lee, P.-H., Wu, D., Shih, K., 2017. Surface-bound sulfate radical-dominated degradation of 1,4-dioxane by alumina-supported palladium (Pd/Al2O3) catalyzed peroxymonosulfate. Water Res. 120, 12–21. https://doi.org/10.1016/j.watres.2017.04.070

Field, R.W., Wu, D., Howell, J.A., Gupta, B.B., 1995. Critical flux concept for microfiltration fouling. J. Membr. Sci. 100, 259–272. https://doi.org/10.1016/0376-7388(94)00265-Z

Fujioka, T., Khan, S.J., McDonald, J.A., Nghiem, L.D., 2014. Nanofiltration of trace organic chemicals: A comparison between ceramic and polymeric membranes. Sep. Purif. Technol. 136, 258–264. https://doi.org/10.1016/j.seppur.2014.08.039

Herima, J., 1982. Constant pressure blocking filtration laws: application to power-law non-newtonian fluids. Trans. Inst. Chem. Eng. V 60, 183–187.

Jafari, M., Vanoppen, M., van Agtmaal, J.M.C., Cornelissen, E.R., Vrouwenvelder, J.S., Verliefde, A., van Loosdrecht, M.C.M., Picioreanu, C., 2021. Cost of fouling in full-scale reverse osmosis and nanofiltration installations in the Netherlands. Desalination 500, 114865. https://doi.org/10.1016/j.desal.2020.114865

Kramer, F.C., Shang, R., Scherrenberg, S.M., Rietveld, L.C., Heijman, S.J.G., 2019. Quantifying defects in ceramic tight ultra- and nanofiltration membranes and investigating their robustness. Sep. Purif. Technol. 219, 159–168. https://doi.org/10.1016/j.seppur.2019.03.019

Li, X., Huang, X., Xi, S., Miao, S., Ding, J., Cai, W., Liu, S., Yang, X., Yang, H., Gao, J., Wang, J., Huang, Y., Zhang, T., Liu, B., 2018. Single cobalt atoms anchored on porous N-doped graphene with dual reaction sites for efficient Fenton-like catalysis. J. Am. Chem. Soc. 140, 12469–12475. https://doi.org/10.1021/jacs.8b05992

Lin, B., Heijman, S.G.J., Shang, R., Rietveld, L.C., 2021. Integration of oxalic acid chelation and Fenton process for synergistic relaxation-oxidation of persistent gel-like fouling of ceramic nanofiltration membranes. J. Membr. Sci. 636, 119553. https://doi.org/10.1016/j.memsci.2021.119553

Lin, B., Rietveld, L.C., Yao, L., Heijman, S.G.J., 2023. Adsorption and cake layer fouling in relation to Fenton cleaning of ceramic nanofiltration membranes. J. Membr. Sci. 122097. https://doi.org/10.1016/j.memsci.2023.122097

Liu, J., Wang, Z., Tang, C.Y., Leckie, J.O., 2018. Modeling dynamics of colloidal fouling of RO/NF membranes with a novel collision-attachment approach. Environ. Sci. Technol. 52, 1471–1478. https://doi.org/10.1021/acs.est.7b05598

Nijboer, M., Jan, A., Chen, M., Batenburg, K., Peper, J., Aarnink, T., Roozeboom, F., Kovalgin, A., Nijmeijer, A., Luiten-Olieman, M., 2024. Tuning nanopores in tubular ceramic nanofiltration membranes with atmospheric-pressure atomic layer deposition: prospects for pressure-based in-line monitoring of pore narrowing. Separations 11, 24. https://doi.org/10.3390/separations11010024

Qiu, T.Y., Davies, P.A., 2015. Concentration polarization model of spiral-wound membrane modules with application to batch-mode RO desalination of brackish water. Desalination 368, 36–47. https://doi.org/10.1016/j.desal.2014.12.048

Shang, R., Goulas, A., Tang, C.Y., de Frias Serra, X., Rietveld, L.C., Heijman, S.G.J., 2017. Atmospheric pressure atomic layer deposition for tight ceramic nanofiltration membranes: synthesis and application in water purification. J. Membr. Sci. 528, 163–170. https://doi.org/10.1016/j.memsci.2017.01.023

Zhou, X., Zhao, Y.-Y., Kim, S.-R., Elimelech, M., Hu, S., Kim, J.-H., 2018. Controlled TiO2 growth on reverse osmosis and nanofiltration membranes by atomic layer deposition: mechanisms and potential applications. Environ. Sci. Technol. 52, 14311–14320. https://doi.org/10.1021/acs.est.8b03967

汉宫春

巷陌人稀，雨打马蹄过，门掩春帷。莺莺远伫，古调催唤谁归？西边燕子，怕呢喃、江左风回。无是处、徒增年岁，频说流水难追。

又把纸烟新卷，便长云细雾，弹指飞灰。从来世间扰扰，鸟雀皆卑。轻谈自己，到而今、也似尘微。些许事、何言其味，应知流水别追。

2021.02.19

Chapter 2

Concentration polarizations of PEG and silica colloids in ceramic nanofiltration

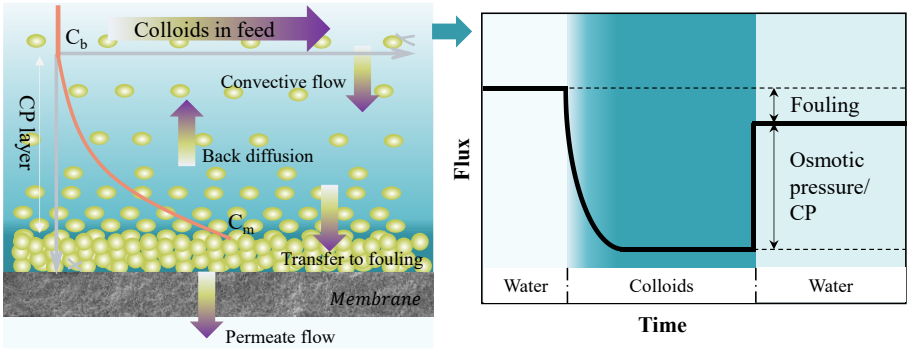

This chapter is based on

Zhang, S., Liang, Y., Yang, C., Venema, P., Rietveld, L. C., & Heijman, S. G. (2024). Concentration polarizations of PEG and silica colloids in ceramic nanofiltration. Desalination, 583, 117722.

Abstract

A large decrease in permeability is often observed during the filtration of nano-sized colloids, while fouling is widely regarded as the main explanation for this phenomenon. The osmotic pressure or concentration polarization (CP) of colloids can also contribute to the flux decline. However, the contribution of CP to flux loss cannot be determined by the traditional CP model. This work aims to evaluate colloid-induced CP by eliminating the effect of fouling, thereby revealing the impact of CP and fouling on flux decline. In this study, the effects of fouling and CP/osmotic pressure on flux were distinguished. The CP values of polyethylene glycol (PEG) and silica-colloids were determined by the osmotic pressures near the membrane surface and in the feed. The CP induced by colloids accounted for 43-95% of the flux loss in our experiments. Silica exhibited higher CP values (127-460), compared to 7-71 for PEG. This was attributed to the slower back diffusion caused by the larger colloids, as evidenced by the diffusion coefficients of 4.30×10^{-11} m^2/s for silica (10 nm) and 1.45×10^{-10} m^2/s for PEG (2.9 nm). Although the CP was mitigated by increasing the cross-flow velocity, CP values of 31 and 250 were observed for PEG and silica at high Reynolds number of 7317, respectively. The experimentally obtained CP values were also compared with those calculated by the film diffusion model.

2.1. Introduction

During the filtration by pressure-driven membranes, such as reverse osmosis (RO) and nanofiltration (NF), a transmembrane pressure as the driving force is applied onto the membrane, and particles and dissolved components will be retained on the feed side (Van Der Bruggen et al., 2003). However, concentration polarization (CP) inevitably occurs during this filtration process, leading to the accumulation of dissolved compounds and colloidal particles near the membrane surface. This will potentially result in a decrease in permeability of the membrane (Shirazi et al., 2010; Subramani et al., 2006). Therefore, understanding CP is important for the interpretation of permeability decrease when filtering dissolved compounds and colloids (Hejase and Tarabara, 2021; Hoek and Elimelech, 2003; Li et al., 2018).

Colloidal particles are prevailing in the aquatic environment and can have either an organic or an inorganic composition in a size range from 1 to 1000 nm (Tang et al., 2011). During filtration of feedwater containing colloids, the membrane is prone to a considerable flux decline. Although colloidal fouling would not result in a high resistance increase due to the relatively large size of colloids compared to the pore size of the NF membrane, the CP of colloids near the membrane surface can cause a sharp rise in the osmotic pressure potentially affecting the permeability of the membrane (Gowman and Ross Ethier, 1997; May et al., 2021; Quay et al., 2018; Rey et al., 2019). Elimelech and Bhattacharjee have demonstrated that the CP for 2 nm-size rigid hard spherical particles in crossflow filtration was around 300 at a feed pressure of 4 bar (Elimelech and Bhattacharjee, 1998). It has also been revealed that the CP of bovine serum albumin and lysozyme in RO membrane could reach up to a value of 4645 and 612, respectively (Quay et al., 2018). In addition, CP values of around 300 have been found for macromolecular polymers in polymeric NF (May et al., 2021), RO (Laghmari et al., 2021), and ultrafiltration membranes (Minnikanti et al., 1999). Although high CP values were revealed in filtration of macromolecule, flux decline was attributed more to fouling because the contribution of CP to flux decline cannot be quantified from the traditional model like the film diffusion model used for CP calculation. Moreover, for practical applications, mitigation of fouling and CP/osmotic pressure phenomenon can be completely different. Fouling is normally removed by the cleaning such as forward flush, backwash, and chemical cleaning, while CP mitigation can be achieved by: a) increase turbulence in order to decrease the CP-layer near the membrane surface, b) decrease permeate flux, and c)

decrease concentration of colloids in the feed. Hence, it is also important to understand the effect of fouling and CP/osmotic pressure on permeability decrease for practice.

The film diffusion model is widely used in the rejection of molecules (ions etc.) to estimate the CP (May et al., 2021; Sablani et al., 2001; Subramani et al., 2006; Zhou et al., 2021). In a membrane system, the convective flow drives solutes towards the membrane and at the same time the solutes are rejected by the membrane. These solutes (ions, molecules, or colloids) also move away from the membrane surface owing to back diffusion. The phenomenon is depicted in Fig. 2.1a. Hence, when reaching equilibrium, this solute transport can be described by the following solute mass balance equation (Eq. 2.1) (May et al., 2021):

$$J\,C = D\,\frac{dC}{dx} + J\,C_p \qquad 2.1$$

Where J is the flux (m/s), D is the solute diffusion coefficient in the solvent (m^2/s), x is the distance from the membrane surface (m), C and C_p are concentrations of solute near the membrane surface and permeate side (g/L), respectively. Integrating Eq. 2.1 towards a boundary layer condition gives Eq. 2.2 (Subramani et al., 2006):

$$\beta = \frac{C_m - C_p}{C_b - C_p} = \exp\left(\frac{J\,\delta}{D}\right) = exp\left(\frac{J}{K}\right) \qquad 2.2$$

Where δ is the thickness of the boundary layer near the membrane (m), K is the mass transfer coefficient (m/s) in the boundary layer, β is the CP factor, C_m and C_b are the solute concentrations near the membrane surface and in bulk (g/L), respectively. If the size of the solute is larger than the membrane pore size, the solute is completely rejected by the membrane, and as a result, C_p is equal to zero. In this case, the CP factor can be described by Eq. 2.3 (Zhou et al., 2021):

$$\beta = \frac{C_m}{C_b} = exp\left(\frac{J}{K}\right) \qquad 2.3$$

The mass transfer coefficient K in Eq. 2.3 is generally determined by the Sherwood equation (Eq. 2.4) (Sablani et al., 2001):

$$Sh = \frac{K\, d_h}{D} = a\, Re^b\, Sc^c = a\left(\frac{u\, d_h}{v}\right)^b \left(\frac{v}{D}\right)^c \quad 2.4$$

Where Sh is the Sherwood number, Re is the Reynolds number, Sc is the Schmidt number, a, b, c are empirical constants, u is the flow velocity (m/s), d_h is the (tubular) hydraulic diameter of the membrane channel (m), v is the kinematic viscosity of the fluid (m^2/s). However, when fouling deposits on the membrane surface (Fig. 2.1b), the solute mass balance described by Eq. 2.1 in the film diffusion model is not valid, because it does not involve the mass of fouling. Therefore, Eq. 2.1 should be re-formulated into Eq. 2.5 to include the fouling part (Liu et al., 2018). a represents the ratio of the total mass turning into fouling, but it could be affected by the complex hydraulic conditions and the thermodynamics of the solute. Given that this phenomenon is dynamic and complicated, a is difficult to be measured or presumed (Liu et al., 2018). In addition, the film diffusion model should also consider the effect of fouling on the CP and boundary layer thickness (δ) (Fig. 2.1a and 2.1b). The real δ^* (Fig. 2.1b) is probably only equal to δ' for a clean membrane. Also, for the solute concentrations near the membrane surface ($C_m{}'$ and $C_m{}^*$), they should only be the same when no fouling was formed on surface.

$$J\, C = D\, \frac{dC}{dx} + J\, C_p + a\, J\, C \quad 2.5$$

Most studies limit their focus on the influence of the caked-enhanced CP (CECP), caused by the enhanced osmotic pressure of the retained ions in the fouling layer (Chong et al., 2008; Hoek and Elimelech, 2003). So far, the effect of fouling itself on the CP has been neglected. However, a significant deviation in CP resulting from the film diffusion model has been found when employing a more accurate model like the finite element numerical model (Subramani et al., 2006). This deviation is particularly pronounced at low feed flow velocity and high flux (Subramani et al., 2006; Gowman and Ross Ethier, 1997; Aimar et al., 1994; Kim and Hoek, 2005; Song and Liu, 2012). In addition, a deviation between directly monitored values and modelling results has been observed with respect to the CP profiles and the thickness of the boundary layer (Chen et al., 2004; Gowman and Ross Ethier, 1997).

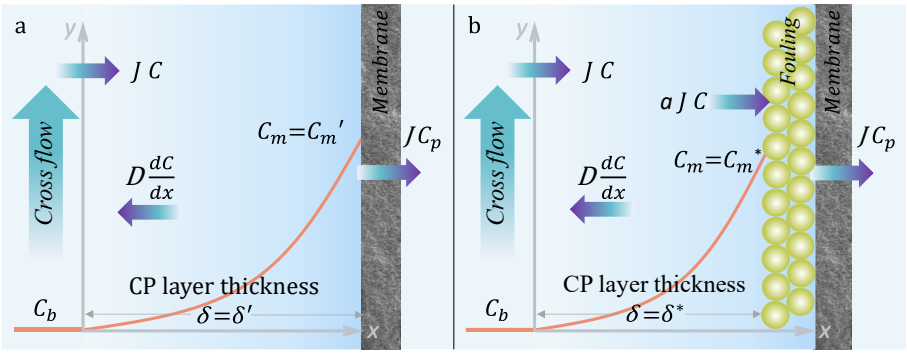

Figure 2.1. CP profiles without (a) and with (b) fouling formation.

Fouling will not contribute to the osmotic pressure, hence the CP value can be predicted from the osmotic pressures near the membrane surface and in the feed. According to Van't Hoff's theory, osmotic pressure has a linear relation with the concentration for an ideal solution (Budd, 1989; Nikolova and Islam, 1998). When all solutes are retained by the membrane, the permeate-side osmotic pressure is equal to zero. Therefore, CP can be expressed in Eq. 2.6:

$$\beta = \frac{C_m}{C_b} = \frac{\pi_m}{\pi_b} = \frac{\Delta\pi}{\pi_b} \qquad 2.6$$

Where $\Delta\pi$ (Pa) is the osmotic pressure difference across the membrane, $\pi_m$and π_b are the osmosis pressures (Pa) on the membrane surface and in the bulk solution, respectively.

For a nonideal solution, the relation between osmotic pressure and concentration is nonlinear. However this nonlinear relationship is easily overlooked when the osmotic pressure is used in the prediction of CP by the traditional model (Boussu et al., 2007; Cai et al., 2021; Chong et al., 2007; Mahlangu et al., 2014). To address this challenge, the above equation (Eq. 2.6) is rewritten as shown in Eq. 2.7.

$$\beta = \frac{C_m}{C_b} = \frac{f(\Delta\pi)}{f(\pi_b)} \qquad 2.7$$

Where $f(\Delta\pi)$ and $f(\pi_b)$ means that C_m and C_b are the functions of $\Delta\pi$ and π_b, respectively.

In order to contribute to the understanding of the role of CP enhanced osmotic pressure of colloids on the permeability of membranes, we developed a

strategy to evaluate the CP generated by colloids and the flux loss only caused by CP in ceramic NF, while the effect of fouling on CP prediction was eliminated. To distinguish between the flux declines caused by fouling and CP, pure water flux was measured before and after filtration of colloids. The osmotic pressure generated near the membrane was also obtained via the above-mentioned method. Afterwards, the CP of two model colloids, polyethylene glycol (PEG) with a molecular weight of 6000 Da, and silica with a diameter of 10 nm, were obtained. Although measuring flux before and after filtration has been used to evaluate fouling resistance, this method has not been applied to distinguish the contributions of fouling and CP to flux loss or to calculate CP. In this work, a short-cycle filtration of colloids was also conducted to understand the effect of CP and fouling on flux decline, compared with a long-cycle test. Given that the Sherwood equation is widely used in the film diffusion model for CP prediction, the theoretical results were compared with our experimental CP values. CP of colloids under various crossflows was also examined in this work.

2.2. Materials and methods

2.2.1. Filtration set-up and materials

Ceramic NF experiments were carried out in a crossflow setup, as shown in Fig. 2.2. Tanks 1 and 2 contained feed solutions of demineralized water and targeted solution, respectively, where a three-way valve was used to change the feed solutions. Two solutes of PEG (Sigma-Aldrich, Germany) with a molecular weight of 6000 Da, corresponding to 2.9 nm (Eq. S2.1), and silica (LUDOX® SM colloidal silica, Sigma-Aldrich, Germany) with an average particle diameter of 10 nm (Fan et al., 2007; Liu et al., 2017) were used. The commercial TiO_2 NF membrane (Inopor GmbH, Germany) had one channel of 7 mm internal diameter, 100 mm in length, and a porosity in the range of 30-40%. The effective filtration area of the membrane was 0.000163 m^2. The ceramic NF had a measured molecular weight cut-off (MWCO) of 1623 Da (Fig. S2.1), corresponding to a pore size of 1.66 nm (Text S2.1), suggesting that both PEG and silica will be completely rejected.

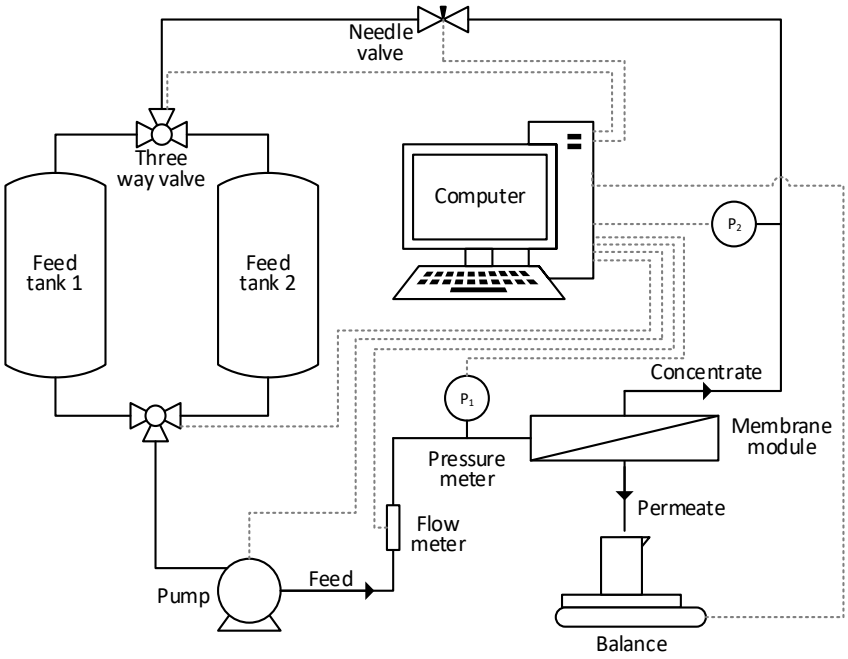

Figure 2.2. Cross-flow filtration setup

2.2.2. Permeability declines caused by CP and fouling

CP is regarded as reversible phenomenon by removing colloids from the feed, while fouling, in the absence of cleaning (either hydraulic or chemical), is not, which can be observed through the flux decline (Airey et al., 1998; Jönsson, 1995). Therefore, our experiments were divided into three parts (Fig. 2.3) to distinguish between the effect of fouling and CP on the permeability decrease of the membrane.

In the first step, demineralized water was filtrated over the pristine membrane. In this way, flux of the clean membrane can be expressed by Eq. 2.10:

$$J_w = \frac{\Delta P}{\mu_w R_m} \qquad 2.10$$

Where J_w is the permeate flux of demineralized water (m/s), μ_w is the dynamic viscosity of demineralized water (Pa s), R_m is the membrane resistance (1/m), and ΔP is the applied pressure (Pa). The permeability of the clean membrane during pure water filtration (L_w in m) is defined as the inverse of hydraulic membrane resistance, as shown in Eq. 2.11 (Verberk, 2005):

$$L_w = \frac{1}{R_m} = \frac{J_w\,\mu_w}{\Delta P} \qquad 2.11$$

In the second step, the solution, containing colloids, was filtrated at the same applied pressure, and therefore an extra osmotic pressure difference ($\Delta\pi$) occurred. Permeability (L in m) is the result of membrane resistance and fouling resistance (R_f in 1/m). In addition, the L can be described by flux (J in m/s), the dynamic viscosity of permeate-side solution (μ), and the effective transmembrane pressure ($\Delta P - \Delta\pi$). Hence, L is described by Eq. 2.12:

$$L = \frac{1}{R_m + R_f} = \frac{J\,\mu}{\Delta P - \Delta\pi} \qquad 2.12$$

In the final step, demineralized water was used again to measure the permeability of the fouled membrane (L_r in m) through the measured flux (J_r in m/s), as presented in Eq. 2.13. During this step, the concentration gradient on the membrane surface will be eliminated which means that the osmotic pressure disappeared, but membrane fouling still existed.

$$L_r = \frac{1}{R_m + R_f} = \frac{J_r\,\mu_w}{\Delta P} \qquad 2.13$$

During steps 2 and 3, the total resistances were caused by the membrane itself and fouling resistance, which means that L was equal to L_r (Verberk, 2005). Therefore, when Eq. 2.12 and 2.13 are combined, $\Delta\pi$ will be determined. Since the rejection by the NF membrane was complete, the values of $\Delta\pi$ and π_m were equal, and also the viscosities were equal: $\mu = \mu_w$ (Field and Wu, 2022). Hence $\Delta\pi$ can be obtained through Eq. 2.14:

$$\Delta\pi = \pi_m = \Delta P\left(1 - \frac{J}{J_r}\right) \qquad 2.14$$

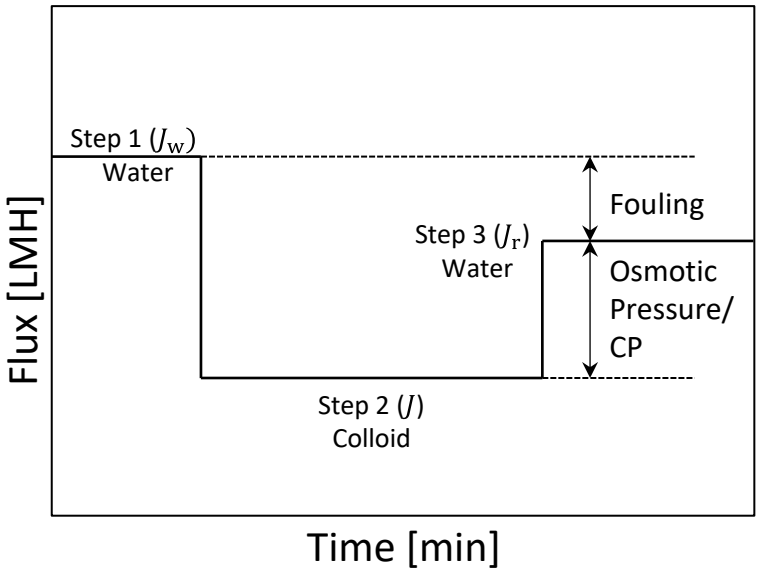

Figure 2.3. Schematic diagram to separate the effect of fouling and osmotic pressure $\Delta\pi$ on flux, where step 1, 2, and 3 means the consecutive filtration of demineralized water with virgin membrane, targeted colloidal solution, and demineralized water in sequence.

2.2.3. Osmotic pressure

The relations between osmotic pressure and concentration of PEG and silica were shown in Fig. S2.2. The osmotic pressure equation (Fig. S2.2a) for the PEG (Mw=6000) was obtained from literature (Alexandrowicz, 1959; Nichol et al., 1967). However, there is no proper relation between concentration and osmotic pressure of charged hard colloids like silica. This is because the counter ions in the diffuse double layer of the charged colloids also contribute to the osmotic pressure. The calculated osmotic pressure for uncharged hard spheres via Eq. S2.3, described in Text S2.2, therefore always underestimates the osmotic pressure of charged hard spheres (Fig. S2.2b). Hence osmotic pressure of silica in this study was based on the virial expansion equation (Eq. S2.2) fitted with osmotic pressures measured by Osmomat 090 osmometer (Gonotec, Berlin, German), as described in Text S2.2 and shown in Fig. S2.2b.

2.3. Results and discussions

2.3.1. Effect of CP and fouling on flux decline

To distinguish between CP and fouling caused by colloidal particles, experiments were conducted with PEG and silica colloids, as described in the section of Materials and Methods. Detailed results of the conducted filtration experiments are given in Table 2.1. Prediction of CP via the film diffusion model (Eq. 2.3) is normally based on the constant mass transfer coefficient of K calculated from Sherwood equation (Eq. 2.4) (Peeva et al., 2004). However, various K values were found in our runs. Sutzkover et al. developed a method to evaluate K via the permeate flux before and after adding the trace salt (Sutzkover et al., 2000). However, their results gave a scattered image of the K values (e.g., 102% error), even when the Re numbers and equipment geometries were similar. It was argued that K can be affected by the factors such as hydraulic conditions, viscosity, the concentration gradient, the suction effect, and solute-membrane interaction (Bader and Veenstra, 1996; Bhatia et al., 2007; Dražević et al., 2014; Field and Wu, 2022; Gekas and Ölund, 1988; Kim and Hoek, 2005; Sutzkover et al., 2000). Hence, employing a constant K in the film diffusion model may limit the acquirement of an accurate CP. In addition, our results indicate that the osmotic pressure difference ($\Delta\pi$) between membrane surface and permeate side cannot be ignored, e.g., in the case of 10 g/L PEG, the induced $\Delta\pi$ was 2.80 bar accounting for 56% of the applied pressure of 5.02 bar.

In addition, Fig. 2.4 shows the flux declined with time for (a) PEG, and (b) silica with different concentrations. The filtration was performed with pure water, colloidal solution, and pure water in sequence. Fig. 2.4a and b indicate that the initial flux declined with an increase in PEG or silica concentration, afterwards the flux tended to reach a plateau in all runs. The flux recovered rapidly when the feed was switched from a colloidal solution to pure water at the last step. The rapid, initial flux declines were probably attributed to the immediately generated osmotic pressure and adsorption of pollutants (Akamatsu et al., 2020; Bacchin et al., 2002; Chen et al., 1997; Koyuncu et al., 2004; Lin et al., 2021; Matthiasson, 1983; Nghiem and Schäfer, 2002). Wang and Song found that an equilibrium exists in membrane separation to reach a steady-state flux, and such flux will attain a lower plateau for the concentrated solution, which is in agreement with our finding (Wang and Song, 1999). The flux loss during moderate fouling would mainly be related to the gradual build-

up and compression of the cake layer. At the last step, where water was filtered over the fouled membrane, colloids that raised the transmembrane osmotic pressure were flushed away with clean water, and therefore, the permeability was restored rapidly. However, the retained foulants on the membrane inhibited the flux from regaining its initial performance.

Based on the effect of fouling and osmotic pressure on flux, the recovered part of the flux can be considered as the attribution of osmotic pressure, and the irreversible flux decline is the result of fouling, as explained in Fig. 2.3. In all series of operations, it is observed that the CP had a prominent impact on the flux loss, as shown in Fig. 2.4. The contribution of CP to the flux decline can be described by $(J_r - J)/(J_w - J)$×100%. 95% of flux loss due to CP was found in filtering 5 g/L PEG at 3 bar. Due to the high back diffusion of ions, CP of ions typically ranges from 1 to 2 in spiral-wound RO or NF treatment (Qiu and Davies, 2015; Yang et al., 2003). Consequently, these low CP values of ions have a limited effect on flux decline. However, as shown in Table 2.1, CP of 7-71 and 127-460 was found in the filtration of PEG and silica, respectively. The relatively high CP of colloids compared to ions thus exerted a more pronounced effect on flux decline. This finding suggests that in the NF of colloids, more attention should be paid to the CP and its potential effect on water production and fouling.

To further explore the impact of fouling and CP on flux decline, an additional short fouling cycle was employed before the long fouling cycle (Fig. 2.5a and 2.5b). During this experiment, demineralized water was filtered over a clean membrane for a few minutes, then the feed was adjusted to the colloidal solution for a short time (short fouling cycle), demineralized water, the colloidal solution for a longer time (long fouling cycle), and demineralized water, respectively. Here it is observed (Fig. 2.5) that the flux recovery of both PEG and silica during the first, short fouling cycle, was similar to that after the second, much longer, fouling cycle. This illustrates that colloidal fouling mainly formed at the beginning of the filtration. Moreover, a sharp flux loss also existed in this short-time fouling cycle, indicating that the effect of CP and fouling on flux behaviour occurred rapidly and simultaneously at the initial stage, with less dependence on filtration duration. The rapid formation of the CP layer in the initial phase of filtration has been directly monitored (Luo et al., 2010; Fernández-Sempere et al., 2009; Salcedo-Díaz et al., 2014). In addition, Hoek et al. (Hoek et al., 2002) reported that in RO and NF, the increased osmotic pressure (i.e., enhanced by CP) was more significant

compared to the negligible drop of hydraulic pressure across the fouling layer, thus dramatically reducing the driving force for flux.

Table 2.1. Experimental conditions and results of filtering PEG and silica in ceramic NF.

Feed	C_b, g/L	ΔP, bar	Flux, L/(m^2·h)			π_b, bar	$\Delta\pi$, bar	C_m, g/L	K, ×10^{-6}	CP
			Pure water (J_w)	Silica/PEG (J)	Pure water (J_r)					
PEG	1	1.58	36.5	33.7	35.2	4.2 ×10^{-3}	0.065	13.1	3.64	13.1
		3.05	68.1	61.2	65.7		0.211	32.8	4.87	32.8
		4.10	91.2	80.6	88.2		0.352	46.6	5.83	46.6
		5.40	125.3	97.9	112.1		0.684	70.5	6.39	70.5
	5	1.67	43.1	34.7	42.6	2.3 ×10^{-2}	0.311	42.9	4.48	8.6
		3.00	73.2	49.5	71.9		0.936	84.5	4.86	16.9
		4.00	94.1	53.5	82.5		1.404	105.5	4.88	21.1
		4.94	112.6	65.0	107.2		1.946	125.1	5.60	25.0
	10	1.65	42.2	24.6	39.1	5.0 ×10^{-2}	0.613	66.0	3.62	6.6
		3.00	72.8	36.7	69.2		1.410	105.7	4.32	10.6
		3.96	97.2	45.6	83.8		1.806	120.4	5.09	12.0
		5.02	120.6	45.8	103.7		2.804	150.2	4.69	15.0
Silica	3	1.52	45.0	35.3	40.2	4.5 ×10^{-5}	0.187	563.8	1.87	187.9
		2.27	65.2	47.4	55.1		0.316	736.8	2.39	245.6
		3.00	84.0	55.5	69.2		0.595	1015.7	2.65	338.6
		4.00	109.2	66.0	90.8		1.093	1380.0	2.99	460.0
	6	1.61	55.4	34.9	44.3	1.0 ×10^{-4}	0.340	764.2	2.00	127.4
		2.15	69.2	44.4	55.9		0.442	874.0	2.48	145.7
		3.17	99.9	47.6	80.0		1.286	1498.3	2.39	249.7
		4.10	125.1	50.4	102.5		2.083	1909.9	2.43	318.3

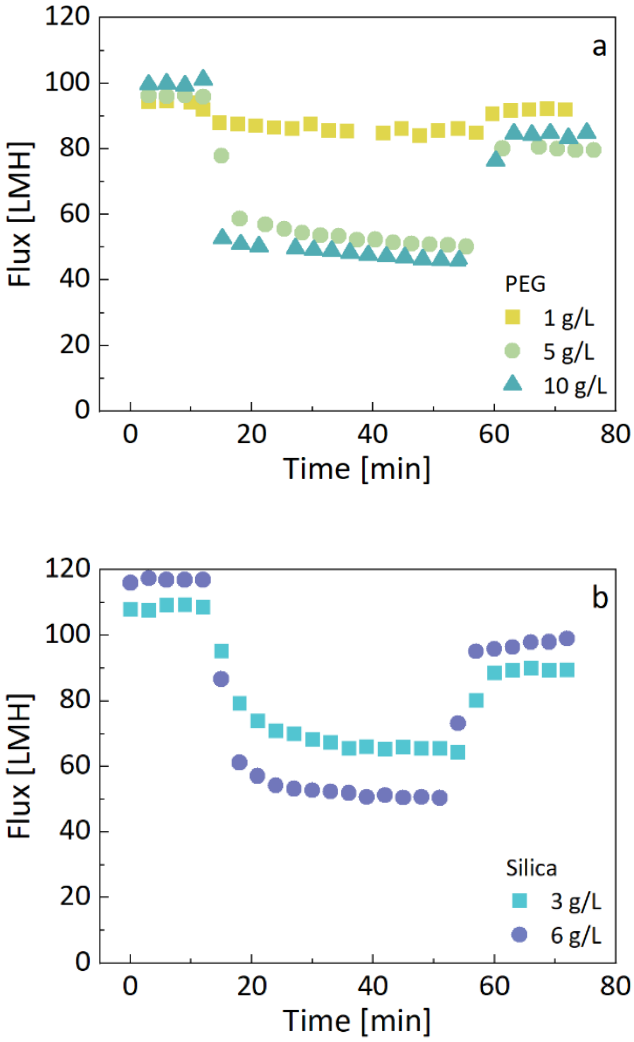

Figure 2.4. Flux decline with the time of (a) PEG, and (b) silica-colloids with different concentrations for the distinction of the impact of fouling and osmotic pressure/CP on flux. The ceramic NF membrane was performed with water, colloidal solution, and water in sequence. All of the continuous operations were at a constant pressure of 4 bar, and a crossflow velocity of 0.5 m/s.

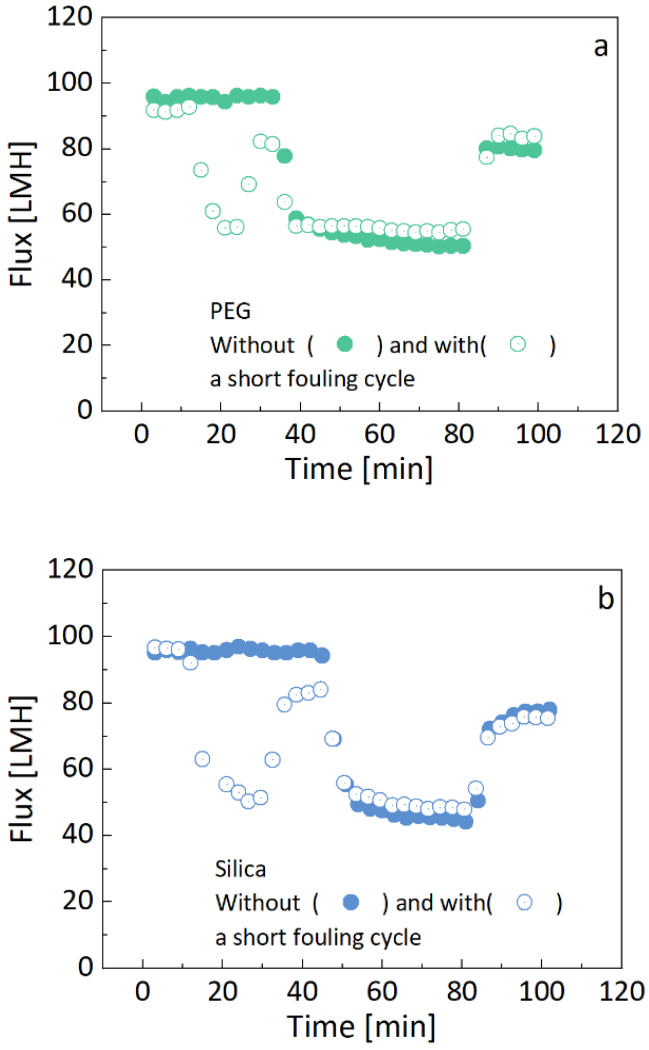

Figure 2.5. Flux decline with (open symbols) and without (closed symbols) additional short-time fouling cycle for (a) 5 g/L PEG, and (b) 6 g/L silica.

2.3.2. Effect of applied pressure on CP

CP values of PEG (Mw=6000) and silica were depicted in Fig. 2.6 and 2.7. Based on Eq. 2.14, the $\Delta\pi$ was obtained, and afterwards the solute concentration near the membrane surface was determined by the relationship between osmotic pressure and concentration (Fig. S2.2a and S2.2b). Then, the

CP values were calculated by the colloid concentrations near the membrane interface and in the feed.

It can be observed from Fig. 2.6a that CP increased with pressure for both PEG and silica. The driving force ($\Delta P - \Delta\pi$), increasing with the applied pressure, resulted in a higher flux. This will, in turn, lead to a higher CP, according to Eq. 2.2. Fig. 2.6a also shows that at a lower PEG concentration, pressure played a more important role in the CP increase, compared to the higher PEG concentration, e.g., the CP of 1 g/L PEG grew to 65.5 at 5.4 bar, 5.3 times higher than CP (i.e., 12.3) at 1.58 bar, while for 10 g/L PEG, the CP only increased 2.5 times when the applied pressures raised from 1.65 to 5.02 bar. In addition, Fig. 2.6a and 2.6b show that the CP of silica (in the range of 127-460) was larger than when filtering PEG (in the CP range of 7-71). Based on the Stokes-Einstein equation, larger particles have a smaller diffusion coefficient (Bowen and Jenner, 1995). Compared with the high diffusion coefficient of ions (in the order of magnitude of 10^{-9} m^2/s), the diffusion coefficients of PEG and silica were calculated at 1.45×10^{-10} and 4.30×10^{-11} m^2/s, respectively. As a result, larger-size silica (10 nm, diameter) was prone to accumulation at the membrane surface on account of its low back diffusion, thus generating a higher CP than small-size PEG (2.9 nm, diameter). Similarly, such high CP indexes generated by macromolecules have also been discovered by groups of Elimelech (Elimelech and Bhattacharjee, 1998; Quay et al., 2018), Ulbricht (Laghmari et al., 2021; May et al., 2021), and Tang (Liu et al., 2020).

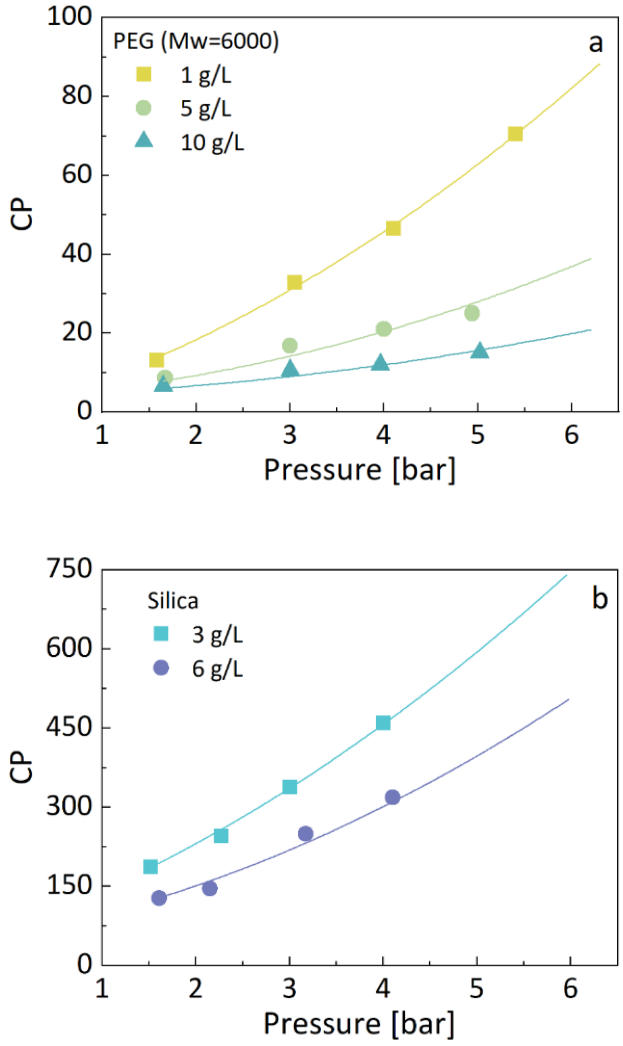

Figure 2.6. CP was calculated from measurements at different transmembrane pressures for (a) PEG, and (b) silica with various concentrations at a constant cross-flow velocity of 0.5 m/s.

2.3.3. Experimental and theoretical CP

Fig. 2.7 shows how flux correlated with the CP during membrane filtration. It indicates that for both PEG and silica, at a given flux, CP values were similar, e.g., the CP of 246 for 3 g/L silica at the flux of 1.13×10^{-5} m/s was comparable

to 250 for 6 g/L silica at the flux of 1.13×10^{-5} m/s. This implies that CP was more affiliated with flux than bulk concentration, which has also been confirmed by literature (Jang et al., 2019). Moreover, an increase in CP with flux was observed. For instance, CP increased 5 times, rising from 13 at 9.37×10^{-5} m/s to 71 at 2.72×10^{-5} m/s, in the case of 1 g/L PEG. This was because that the larger driving force due to the higher flux can lead to more accumulation of colloids near the membrane surface.

Evaluation of CP by the film diffusion model is also depicted in Fig. 2.7. The assessment was realized by employing various Sherwood equations from literature in the film diffusion model (dash lines in Fig. 2.7) (Chang et al., 2012; Gekas and Hallström, 1987; Imbrogno and Schäfer, 2019; Sutzkover et al., 2000; van den Berg et al., 1989). The solid lines for both PEG and silica in Fig. 2.7 were based on our calibrated Sherwood equation ($Sh = 0.027\, Re^{0.868}\, Sc^{0.25}$). The calibration was achieved by employing our experimental CP values in Eq. 2.3 to get the values of K (Table 2.1), then various values of K were used in Eq. 2.4 to calibrate the Sherwood equation. The calibrated Sherwood equation ($Sh = 0.027\, Re^{0.868}\, Sc^{0.25}$) was comparable to the ones used in literature (Chang et al., 2012; Gekas and Hallström, 1987; Imbrogno and Schäfer, 2019; Sutzkover et al., 2000; van den Berg et al., 1989). However, the deviation between experimental and theoretical CP values was observed. The CP deviation caused by the film model was also found when comparing to CP values which was obtained from the finite element numerical model (Subramani et al., 2006). As discussed in the Introduction, the effect of fouling has not been considered in the film model, which can lead to the CP deviation. Besides, the constant K employed in the film diffusion model will also impact the acquirement of an accurate CP. As shown in Table 2.1, the K varied under different filtration conditions, which is consistent with the previous finding (Sutzkover et al., 2000).

CP_{max} values in Fig. 2.7 referred to the theory of close-packing density (Bacchin et al., 2002). Taking silica as an example, the maximal possible silica concentration should be 1961 g/L, when the close-packed volume fraction (74%) was taken into account with an assumed silica density equal to 2650 g/L (Bacchin et al., 2002; Persoff et al., 1999). Therefore, the CP_{max} of 654 and 327 was obtained for 3 and 6 g/L silica, respectively. When the steady-state flux is reached, the CP layer will become constant. Once the colloidal concentration is higher than the CP_{max} (Bacchin et al., 2006, 2002; Wang and Song, 1999), the extra colloids will be flushed away from the CP boundary layer or

converted to fouling which can increase the thickness of cake layer (Chen et al., 1997; Luo et al., 2012, 2010; Yang et al., 2003). However, CP_{max} is not taken into consideration in the film diffusion model, thus leading to the high CP, e.g., 1694 for 3 g/L silica at the flux of 1.8×10^{-5} m/s, which was 3.7 times higher than the experimental CP (i.e., 460), and beyond CP_{max} (i.e., 654).

Our findings demonstrated that a high osmotic pressure near the membrane wall can be caused by colloids due to the high CP. The CP values given here were based on the fitted virial expansion equations used for the relation between osmotic pressure and concentration of the colloids (Text S2.2, Fig. S2.2a and S2.2b). However, for silica, when the osmotic pressure equation (Eq. S2.3) based on Carnahan-Stirling theory for hard-sphere particles was employed (Pasquier et al., 2016), completely different silica CP values were given (Fig. S2.3a and S2.3b). As shown in Fig. S2.2, the calculated osmotic pressures of silica via Eq. S2.3 were underestimated, because the contribution of counter ions to osmotic pressures was not considered in the Carnahan-Stirling theory (Jönsson et al., 2011). Consequently, the concentration of silica near the membrane wall will be overestimated when using Eq. S2.3. As a result, it led to an overestimation of silica CP values, as shown in Fig. S2.3. However, for PEG, this problem does not arise because PEG is uncharged and does not have counterions that contribute to osmotic pressure. This suggests that more attention should be paid to the relation between colloidal concentration and osmotic pressure, especially when colloids are with charges.

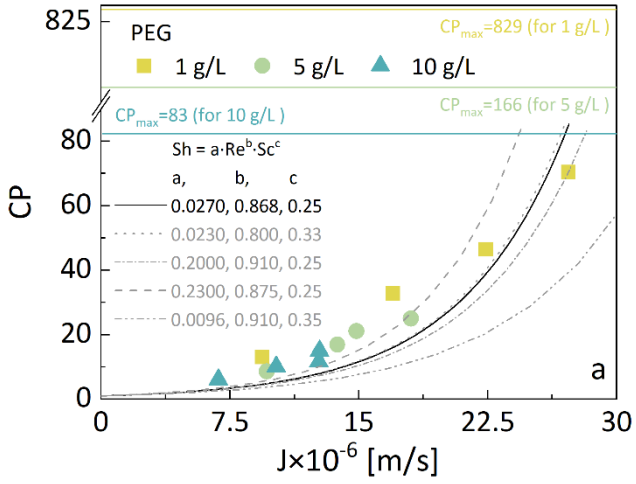

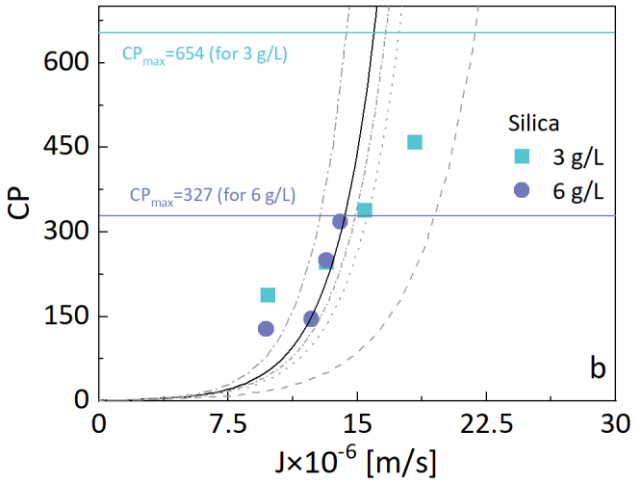

Figure 2.7. Theoretical and experimental CP vs. flux for (a) 1, 5, and 10 g/L PEG, and (b) 3 and 6 g/L silica at a cross-flow velocity of 0.5 m/s. The solid curves in both (a) and (b) on behalf of the predicted CP profile were obtained through the film diffusion model by using the same calibrated Sherwood equation with calibrated constants of a=0.027, b=0.868, and c=0.25, while dashed lines represented the theoretical CP with flux via the film diffusion model through employing different Sherwood equations from literature (Chang et al., 2012; Gekas and Hallström, 1987; Imbrogno and Schäfer, 2019; Sutzkover et al., 2000; van den Berg et al., 1989).

2.3.4. Effect of cross-flow velocity on CP mitigation

CP of both colloids were also evaluated via our method under various cross-flow velocities (i.e., Re numbers), as shown in Fig. 2.8. CP values of both PEG and silica decreased as Re numbers increased from 3532 to 7317 (Fig. 2.8a). It is reported that CP can be mitigated at a high cross flow due to the promoted back diffusion process of solutes and the elevated shear forces (Hoek et al., 2002; Qiu and Davies, 2015; Yang et al., 2003). However, compared to the Re, it was found that colloidal size played a more crucial role in CP. The CP value of silica, for example, was still as high as 250 under a high cross flow with Re number of 7317, which was higher than CP (48) of PEG at a small Re of 3532. Fig. 2.8 b and c show that as Re increased from 3532 to 7317, the contribution of CP to flux decline was reduced from 71% to 50% for PEG and from 48% to 35% for silica, suggesting that increasing the cross-flow velocity can

effectively mitigate the CP effect on flux. Although CP values (Fig. 2.8a) and CP contributions to flux decline (Fig. 2.8b and 2.8c), for the smaller-size colloids of PEG, were much smaller than that of silica, the normalized flux (Fig. S2.4) shows that the higher CP found in silica led to a more significant flux drop during the filtration of colloids. The prominent flux drop was probably attributed to the synergetic effect of CP and fouling because high CP caused by the larger-size colloids can facilitate fouling formation.

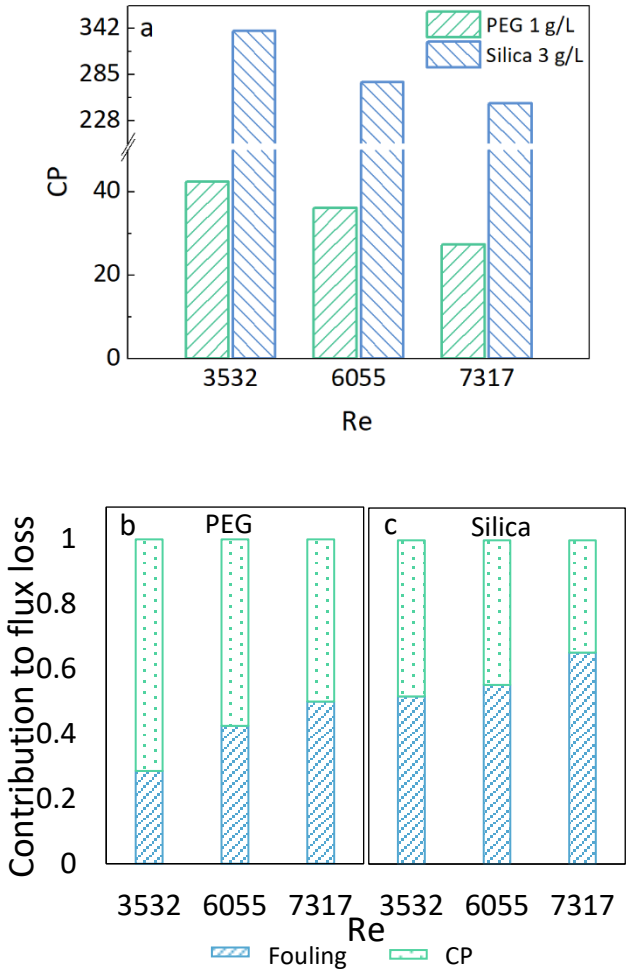

Figure 2.8. (a) Experimental CP values with various *Re* numbers for 1 g/L PEG and 3 g/L silica, and contributions of CP and fouling to flux loss for (b) PEG and (c) silica.

2.4. Conclusion

In this study, we proposed a new strategy to determine the contribution of fouling and CP to flux decline by comparing the pure water flux before and after filtering colloidal solutions with a ceramic NF membrane. Besides, CP values of PEG and silica colloids were evaluated via the osmotic pressures in the feed and near the membrane surface by this method. The main conclusions were:

1) Flux loss of 43-95% during filtration of colloids was caused by CP-enhanced osmotic pressure near the membrane wall.
2) Silica colloids with a diameter of 10 nm, 3 times larger than PEG (2.9 nm), resulted in the largest CP due to the slow back diffusion from the membrane surface towards the bulk.
3) CP values evaluated from the film diffusion model gave a deviation because the inaccurate K values calculated from the Sherwood equation were used in the model. In addition, CP values beyond the CP_{max} were calculated from the film diffusion model.
4) CP of uncharged colloids like PEG was evaluated through the established relation between its high concentrations and osmotic pressures. However, CP prediction of hard spherical charged colloids like silica can be subject to the potential contribution of counter ions to osmotic pressure.
5) As Re number increased at higher cross-flow velocities, the CP of the two colloids (PEG and silica) was decreased but remained at a high level, especially for the larger colloidal particles of silica.
6) Contribution of CP to flux loss for silica can be reduced at a higher Re number. However, the effect of the higher CP resulting from larger-size colloids on fouling formation should be taken into account.

References

Aimar, P., Meireles, M., Bacchin, P., Sanchez, V., 1994. Fouling and Concentration Polarisation in Ultrafiltration and Microfiltration, in: Crespo, J.G., Böddeker, K.W. (Eds.), Membrane Processes in Separation and Purification, NATO ASI Series. Springer Netherlands, Dordrecht, pp. 27–57. https://doi.org/10.1007/978-94-015-8340-4_3

Airey, D., Yao, S., Wu, J., Chen, V., Fane, A.G., Pope, J.M., 1998. An investigation of concentration polarization phenomena in membrane filtration of colloidal silica suspensions by NMR micro-imaging. J. Membr. Sci. 145, 145–158. https://doi.org/10.1016/S0376-7388(98)00051-9

Akamatsu, K., Kagami, Y., Nakao, S., 2020. Effect of BSA and sodium alginate adsorption on decline of filtrate flux through polyethylene microfiltration membranes. J. Membr. Sci. 594, 117469. https://doi.org/10.1016/j.memsci.2019.117469

Alexandrowicz, Z., 1959. Light-scattering measurement of the osmotic activity of a polyethylene glycol solution. J. Polym. Sci. 40, 107–112. https://doi.org/10.1002/pol.1959.1204013607

Bacchin, P., Aimar, P., Field, R.W., 2006. Critical and sustainable fluxes: Theory, experiments and applications. J. Membr. Sci. 281, 42–69. https://doi.org/10.1016/j.memsci.2006.04.014

Bacchin, P., Meireles, M., Aimar, P., 2002. Modelling of filtration: From the polarised layer to deposit formation and compaction. Desalination 145, 139–146. https://doi.org/10.1016/S0011-9164(02)00399-5

Bader, M.S.H., Veenstra, J.N., 1996. Analysis of concentration polarization phenomenon in ultrafiltration under turbulent flow conditions. J. Membr. Sci. 114, 139–148. https://doi.org/10.1016/0376-7388(95)00136-0

Bhatia, S., DasGupta, S., De, S., 2007. Performance prediction of membrane modules incorporating the effects of suction in the mass transfer coefficient under turbulent flow conditions. Sep. Purif. Technol. 55, 182–190. https://doi.org/10.1016/j.seppur.2006.11.020

Boussu, K., Belpaire, A., Volodin, A., Van Haesendonck, C., Van der Meeren, P., Vandecasteele, C., Van der Bruggen, B., 2007. Influence of membrane and colloid characteristics on fouling of nanofiltration membranes. J. Membr. Sci. 289, 220–230. https://doi.org/10.1016/j.memsci.2006.12.001

Bowen, W.R., Jenner, F., 1995. Theoretical descriptions of membrane filtration of colloids and fine particles: An assessment and review. Adv. Colloid Interface Sci. 56, 141–200. https://doi.org/10.1016/0001-8686(94)00232-2

Budd, P.M., 1989. 11 - Polyelectrolytes, in: Allen, G., Bevington, J.C. (Eds.), Comprehensive Polymer Science and Supplements. Pergamon, Amsterdam, pp. 215–230. https://doi.org/10.1016/B978-0-08-096701-1.00011-2

Cai, Y.H., Galili, N., Gelman, Y., Herzberg, M., Gilron, J., 2021. Evaluating the impact of pretreatment processes on fouling of reverse osmosis membrane by secondary wastewater. J. Membr. Sci. 623, 119054. https://doi.org/10.1016/j.memsci.2021.119054

Chang, E.E., Liang, C.H., Huang, C.P., Chiang, P.C., 2012. A simplified method for elucidating the effect of size exclusion on nanofiltration membranes. Sep. Purif. Technol. 85, 1–7. https://doi.org/10.1016/j.seppur.2011.05.002

Chen, J.C., Li, Q., Elimelech, M., 2004. In situ monitoring techniques for concentration polarization and fouling phenomena in membrane filtration. Adv. Colloid Interface Sci. 107, 83–108. https://doi.org/10.1016/j.cis.2003.10.018

Chen, V., Fane, A.G., Madaeni, S., Wenten, I.G., 1997. Particle deposition during membrane filtration of colloids: Transition between concentration polarization and cake formation. J. Membr. Sci. 125, 109–122. https://doi.org/10.1016/S0376-7388(96)00187-1

Chong, T.H., Wong, F.S., Fane, A.G., 2008. Implications of critical flux and cake enhanced osmotic pressure (CEOP) on colloidal fouling in reverse osmosis: Experimental observations. J. Membr. Sci. 314, 101–111. https://doi.org/10.1016/j.memsci.2008.01.030

Chong, T.H., Wong, F.S., Fane, A.G., 2007. Enhanced concentration polarization by unstirred fouling layers in reverse osmosis: Detection by sodium chloride tracer response technique. J. Membr. Sci. 287, 198–210. https://doi.org/10.1016/j.memsci.2006.10.035

Dražević, E., Košutić, K., Dananić, V., 2014. Mass transfer of differently sized organic solutes at spacer covered and permeable nanofiltration wall. Chem. Eng. J. 244, 152–159. https://doi.org/10.1016/j.cej.2014.01.043

Elimelech, M., Bhattacharjee, S., 1998. A novel approach for modeling concentration polarization in crossflow membrane filtration based on the equivalence of osmotic pressure model and filtration theory. J. Membr. Sci. 145, 223–241. https://doi.org/10.1016/S0376-7388(98)00078-7

Fan, W., Meneau, F., Bras, W., Ogura, M., Sankar, G., Okubo, T., 2007. Effects of silicon sources on the formation of nanosized LTA: An in situ small angle X-ray scattering and wide angle X-ray scattering study. Microporous Mesoporous Mater. 101, 134–141. https://doi.org/10.1016/j.micromeso.2006.10.007

Fernández-Sempere, J., Ruiz-Beviá, F., García-Algado, P., Salcedo-Díaz, R., 2009. Visualization and modelling of the polarization layer and a reversible adsorption process in PEG-10000 dead-end ultrafiltration. J. Membr. Sci. 342, 279–290. https://doi.org/10.1016/j.memsci.2009.06.046

Field, R.W., Wu, J.J., 2022. Permeate flux in ultrafiltration processes—understandings and misunderstandings. Membranes 12, 187. https://doi.org/10.3390/membranes12020187

Gekas, V., Hallström, B., 1987. Mass transfer in the membrane concentration polarization layer under turbulent cross flow: I. Critical literature review and adaptation of existing sherwood correlations to membrane operations. J. Membr. Sci. 30, 153–170. https://doi.org/10.1016/S0376-7388(00)81349-6

Gekas, V., Ölund, K., 1988. Mass transfer in the membrane concentration polarization layer under turbulent cross flow: II. Application to the characterization of ultrafiltration membranes. J. Membr. Sci. 37, 145–163. https://doi.org/10.1016/S0376-7388(00)83069-0

Gowman, L.M., Ross Ethier, C., 1997. Concentration and concentration gradient measurements in an ultrafiltration concentration polarization layer Part II: Application to hyaluronan. J. Membr. Sci. 131, 107–123. https://doi.org/10.1016/S0376-7388(97)00033-1

Hejase, C.A., Tarabara, V.V., 2021. Nanofiltration of saline oil-water emulsions: Combined and individual effects of salt concentration polarization and fouling by oil. J. Membr. Sci. 617, 118607. https://doi.org/10.1016/j.memsci.2020.118607

Hoek, E.M.V., Elimelech, M., 2003. Cake-enhanced concentration polarization: a new fouling mechanism for salt-rejecting membranes. Environ. Sci. Technol. 37, 5581–5588. https://doi.org/10.1021/es0262636

Hoek, E.M.V., Kim, A.S., Elimelech, M., 2002. Influence of Crossflow Membrane Filter Geometry and Shear Rate on Colloidal Fouling in Reverse Osmosis and Nanofiltration Separations. Environ. Eng. Sci. 19, 357–372. https://doi.org/10.1089/109287502320963364

Imbrogno, A., Schäfer, A.I., 2019. Comparative study of nanofiltration membrane characterization devices of different dimension and configuration (cross flow and dead end). J. Membr. Sci. 585, 67–80. https://doi.org/10.1016/j.memsci.2019.04.035

Jang, E.S., Mickols, W., Sujanani, R., Helenic, A., Dilenschneider, T.J., Kamcev, J., Paul, D.R., Freeman, B.D., 2019. Influence of concentration polarization and thermodynamic non-ideality on salt transport in reverse osmosis membranes. J. Membr. Sci. 572, 668–675. https://doi.org/10.1016/j.memsci.2018.11.006

Jönsson, A., 1995. Concentration polarization and fouling during ultrafiltration of colloidal suspensions and hydrophobic solutes. Sep. Sci. Technol. 30, 301–312. https://doi.org/10.1080/01496399508015840

Jönsson, B., Persello, J., Li, J., Cabane, B., 2011. Equation of State of Colloidal Dispersions. Langmuir 27, 6606–6614. https://doi.org/10.1021/la2001392

Kim, S., Hoek, E.M.V., 2005. Modeling concentration polarization in reverse osmosis processes. Desalination 186, 111–128. https://doi.org/10.1016/j.desal.2005.05.017

Koyuncu, I., Topacik, D., Wiesner, M.R., 2004. Factors influencing flux decline during nanofiltration of solutions containing dyes and salts. Water Res. 38, 432–440. https://doi.org/10.1016/j.watres.2003.10.001

Laghmari, S., May, P., Ulbricht, M., 2021. Polyzwitterionic hydrogel coating for reverse osmosis membranes by concentration polarization-enhanced in situ “click” reaction that is applicable in modules. J. Membr. Sci. 629, 119274. https://doi.org/10.1016/j.memsci.2021.119274

Li, X., Hasson, D., Shemer, H., 2018. Flow conditions affecting the induction period of CaSO4 scaling on RO membranes. Desalination, “Desalination, energy and the environment” in honor of Professor Raphael Semiat 431, 119–125. https://doi.org/10.1016/j.desal.2017.08.014

Lin, B., Heijman, S.G.J., Shang, R., Rietveld, L.C., 2021. Integration of oxalic acid chelation and Fenton process for synergistic relaxation-oxidation of persistent gel-like fouling of ceramic nanofiltration membranes. J. Membr. Sci. 636, 119553. https://doi.org/10.1016/j.memsci.2021.119553

Liu, H., Peng, Y., Yang, C., Wang, M., 2017. Silica nanoparticles as adhesives for biological tissues? Re-examining the effect of particles size, particle shape, and the unexpected role of base. Part. Part. Syst. Charact. 34, 1700286. https://doi.org/10.1002/ppsc.201700286

Liu, J., Huang, T., Ji, R., Wang, Z., Tang, C.Y., Leckie, J.O., 2020. Stochastic Collision–Attachment-Based Monte Carlo Simulation of Colloidal Fouling: Transition from Foulant–Clean-Membrane Interaction to Foulant–Fouled-Membrane Interaction. Environ. Sci. Technol. 54, 12703–12712. https://doi.org/10.1021/acs.est.0c04165

Liu, J., Wang, Z., Tang, C.Y., Leckie, J.O., 2018. Modeling dynamics of colloidal fouling of RO/NF membranes with a novel collision-attachment approach. Environ. Sci. Technol. 52, 1471–1478. https://doi.org/10.1021/acs.est.7b05598

Luo, J., Ding, L., Su, Y., Wei, S., Wan, Y., 2010. Concentration polarization in concentrated saline solution during desalination of iron dextran by nanofiltration. J. Membr. Sci. 363, 170–179. https://doi.org/10.1016/j.memsci.2010.07.033

Luo, J., Ding, L., Wan, Y., Paullier, P., Jaffrin, M.Y., 2012. Fouling behavior of dairy wastewater treatment by nanofiltration under shear-enhanced extreme hydraulic conditions. Sep. Purif. Technol. 88, 79–86. https://doi.org/10.1016/j.seppur.2011.12.008

Mahlangu, T.O., Hoek, E.M.V., Mamba, B.B., Verliefde, A.R.D., 2014. Influence of organic, colloidal and combined fouling on NF rejection of NaCl and carbamazepine: Role of solute–foulant–membrane interactions and cake-enhanced concentration polarisation. J. Membr. Sci. 471, 35–46. https://doi.org/10.1016/j.memsci.2014.07.065

Matthiasson, E., 1983. The role of macromolecular adsorption in fouling of ultrafiltration membranes. J. Membr. Sci. 16, 23–36. https://doi.org/10.1016/S0376-7388(00)81297-1

May, P., Laghmari, S., Ulbricht, M., 2021. Concentration Polarization Enabled Reactive Coating of Nanofiltration Membranes with Zwitterionic Hydrogel. Membranes 11, 187. https://doi.org/10.3390/membranes11030187

Minnikanti, V.S., DasGupta, S., De, S., 1999. Prediction of mass transfer coefficient with suction for turbulent flow in cross flow ultrafiltration. J. Membr. Sci. 157, 227–239. https://doi.org/10.1016/S0376-7388(98)00371-8

Nghiem, L.D., Schäfer, A.I., 2002. Adsorption and Transport of Trace Contaminant Estrone in NF/RO Membranes. Environ. Eng. Sci. 19, 441–451. https://doi.org/10.1089/109287502320963427

Nichol, L.W., Ogston, A.G., Preston, B.N., 1967. The equilibrium sedimentation of hyaluronic acid and of two synthetic polymers. Biochem. J. 102, 407–416.

Nikolova, J.D., Islam, M.A., 1998. Contribution of adsorbed layer resistance to the flux-decline in an ultrafiltration process. J. Membr. Sci. 146, 105–111. https://doi.org/10.1016/S0376-7388(98)00086-6

Pasquier, C., Beaufils, S., Bouchoux, A., Rigault, S., Cabane, B., Lund, M., Lechevalier, V., Floch-Fouéré, C.L., Pasco, M., Pabœuf, G., Pérez, J., Pezennec, S., 2016. Osmotic pressures of lysozyme solutions from gas-like

to crystal states. Phys. Chem. Chem. Phys. 18, 28458–28465. https://doi.org/10.1039/C6CP03867K

Peeva, L.G., Gibbins, E., Luthra, S.S., White, L.S., Stateva, R.P., Livingston, A.G., 2004. Effect of concentration polarisation and osmotic pressure on flux in organic solvent nanofiltration. J. Membr. Sci. 236, 121–136. https://doi.org/10.1016/j.memsci.2004.03.004

Persoff, P., Apps, J., Moridis, G., Whang, J.M., 1999. Effect of dilution and contaminants on sand grouted with colloidal silica. J. Geotech. Geoenvironmental Eng. 125, 461–469. https://doi.org/10.1061/(ASCE)1090-0241(1999)125:6(461)

Qiu, T.Y., Davies, P.A., 2015. Concentration polarization model of spiral-wound membrane modules with application to batch-mode RO desalination of brackish water. Desalination, Reverse Osmosis 368, 36–47. https://doi.org/10.1016/j.desal.2014.12.048

Quay, A.N., Tong, T.Z., Hashmi, S.M., Zhou, Y., Zhao, S., Elimelech, M., 2018. Combined organic fouling and inorganic scaling in reverse osmosis: Role of protein–silica interactions. Environ. Sci. Technol. 52, 9145–9153. https://doi.org/10.1021/acs.est.8b02194

Rey, C., Hengl, N., Baup, S., Karrouch, M., Dufresne, A., Djeridi, H., Dattani, R., Pignon, F., 2019. Velocity, stress and concentration fields revealed by micro-PIV and SAXS within concentration polarization layers during cross-flow ultrafiltration of colloidal Laponite clay suspensions. J. Membr. Sci. 578, 69–84. https://doi.org/10.1016/j.memsci.2019.02.019

Sablani, S., Goosen, M., Al-Belushi, R., Wilf, M., 2001. Concentration polarization in ultrafiltration and reverse osmosis: a critical review.

Salcedo-Díaz, R., García-Algado, P., García-Rodríguez, M., Fernández-Sempere, J., Ruiz-Beviá, F., 2014. Visualization and modeling of the polarization layer in crossflow reverse osmosis in a slit-type channel. J. Membr. Sci. 456, 21–30. https://doi.org/10.1016/j.memsci.2014.01.019

Shirazi, S., Lin, C.J., Chen, D., 2010. Inorganic fouling of pressure-driven membrane processes — A critical review. Desalination 250, 236–248. https://doi.org/10.1016/j.desal.2009.02.056

Song, L., Liu, C., 2012. A total salt balance model for concentration polarization in crossflow reverse osmosis channels with shear flow. J. Membr. Sci. 401–402, 313–322. https://doi.org/10.1016/j.memsci.2012.02.023

Subramani, A., Kim, S., Hoek, E.M.V., 2006. Pressure, flow, and concentration profiles in open and spacer-filled membrane channels. J. Membr. Sci. 277, 7–17. https://doi.org/10.1016/j.memsci.2005.10.021

Sutzkover, I., Hasson, D., Semiat, R., 2000. Simple technique for measuring the concentration polarization level in a reverse osmosis system. Desalination 131, 117–127. https://doi.org/10.1016/S0011-9164(00)90012-2

Tang, C.Y., Chong, T.H., Fane, A.G., 2011. Colloidal interactions and fouling of NF and RO membranes: A review. Adv. Colloid Interface Sci., Membrane Separation and Colloid Science 164, 126–143. https://doi.org/10.1016/j.cis.2010.10.007

van den Berg, G.B., Rácz, I.G., Smolders, C.A., 1989. Mass transfer coefficients in cross-flow ultrafiltration. J. Membr. Sci. 47, 25–51. https://doi.org/10.1016/S0376-7388(00)80858-3

Van Der Bruggen, B., Vandecasteele, C., Van Gestel, T., Doyen, W., Leysen, R., 2003. A review of pressure-driven membrane processes in wastewater treatment and drinking water production. Environ. Prog. 22, 46–56. https://doi.org/10.1002/ep.670220116

Verberk, J.Q.J.C., 2005. Application of air in membrane filtration (PhD thesis). Delft University of Technology, Netherlands.

Wang, L., Song, L., 1999. Flux decline in crossflow microfiltration and ultrafiltration: Experimental verification of fouling dynamics. J. Membr. Sci. 160, 41–50. https://doi.org/10.1016/S0376-7388(99)00075-7

Yang, G., Xing, W., Xu, N., 2003. Concentration polarization in spiral-wound nanofiltration membrane elements. Desalination 154, 89–99. https://doi.org/10.1016/S0011-9164(03)00210-8

Zhou, Z., Ling, B., Battiato, I., Husson, S.M., Ladner, D.A., 2021. Concentration polarization over reverse osmosis membranes with engineered surface features. J. Membr. Sci. 617, 118199. https://doi.org/10.1016/j.memsci.2020.118199

Supporting Information

Text S2.1. Relation between molecular size and molecular weight of PEG

The correlation between the molecular size of PEG (d_s in nm) and their molecular weight (M_w in Da) is given in previous work (Shang et al., 2017), as shown in Eq. S2.1. The MWCO of ceramic NF was 1623 Da (Fig. S2.1), corresponding to a pore size of 1.66 nm, where the MWCO measurement can be found in previous studies (Kramer et al., 2019; Shang et al., 2017).

$$d_s = 0.065(M_w)^{0.438} \quad \text{S2.1}$$

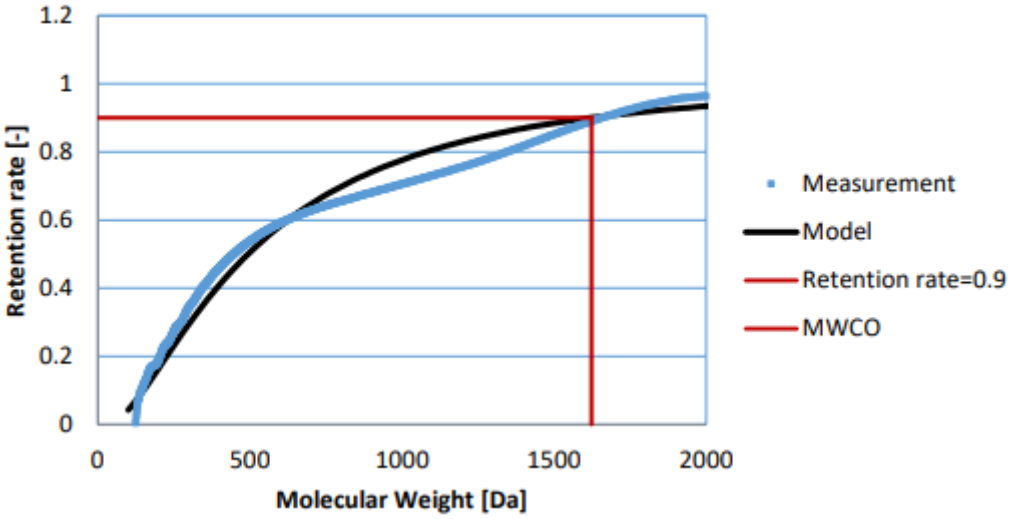

Figure S2.1. Molecular weight cut-off of the ceramic NF membrane.

Text S2.2. Calculation of osmotic pressure of colloids

For a nonideal solution, previous studies found that osmotic pressure would deviate from van't Hoff's law. Therefore, the virial expansion has been used to express the osmotic pressure (Eq. S2.2) (Bonnet-Gonnet et al., 1994; McClendon, 1981, p. 6; Michel and Kaufmann, 1973, p. 600; Vilker et al., 1984):

$$\frac{\pi}{RTc} = \left(\frac{1}{M} + A_2 c + A_3 c^2 + \cdots\right) \quad \text{S2.2}$$

Where R is the ideal gas constant (0.083 L bar/(K mol), T is the temperature (K), c is the concentration (g/L), M is the molar mass (g/mol), and A_2(mol L/g^2) and A_3(mol L^2/g^3) are the second and third virial coefficients account for the deviations from ideal condition.

As for the colloidal particle silica with a diameter of 10 nm, the osmotic pressure is the consequence of its particle, not the molecule of silica (Bonnet-Gonnet et al., 1994). As a result, M in Eq. S2.2 is associated with the silica particle instead of the single-molecule silica (60.08 g/mol). If we assume that both the silica particle and silica molecule (Si–O bond length is 0.16 nm) are hard spheres, one colloidal silica particle contains 30517.6 molecules of silica, contributing to 1833496 g/mol of molar mass. As given in Fig. S2.2, the osmotic pressures of both PEG and silica rapidly increased with the concentration, and at the same concentration, silica showed a lower osmotic pressure due to its larger size and higher density.

Eq. S2.3 is the osmotic pressure equation for silica based on the Carnahan-Stirling theory for hard-sphere particles (Pasquier et al., 2016), where φ is the volume fraction defined by $\varphi = C_m/\rho$ (ρ is the density of silica, 2650 g/L).

$$\frac{\Pi}{RTC_m} = \frac{1 + \varphi + \varphi^2 - \varphi^3}{(1-\varphi)^3} \quad \text{S2.3}$$

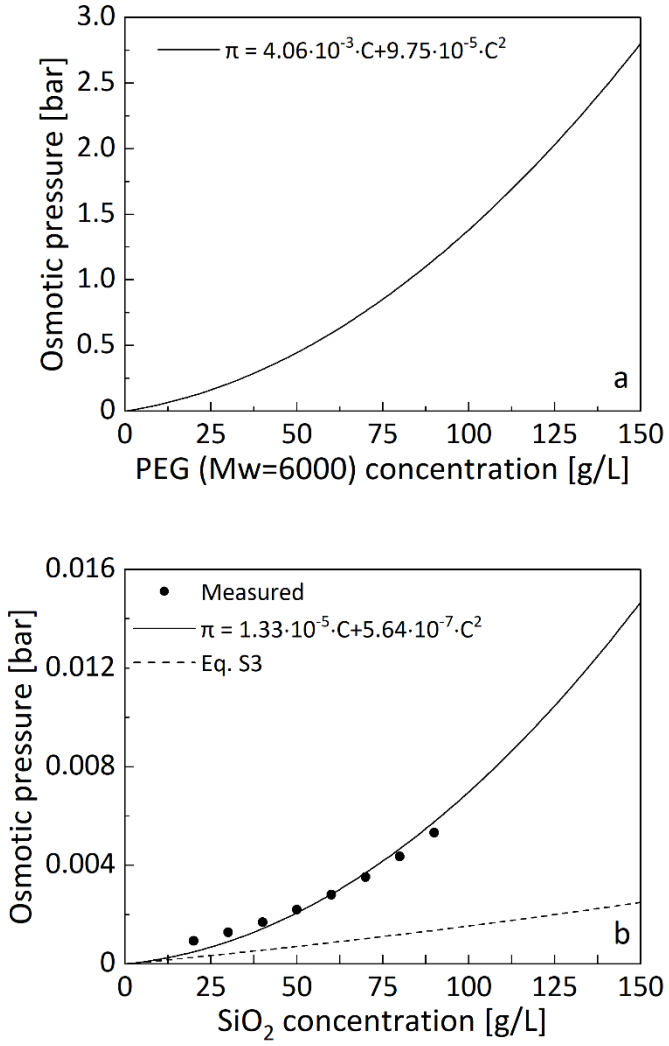

Figure S2.2. The osmotic pressure equations of (a) PEG (Mw = 6000) from literature (Alexandrowicz, 1959; Nichol et al., 1967) by the regression analysis, and (b) silica based on measurement and fitting. The solid lines in (a) and (b) were based on the virial expansion of Eq. S2.2, while the dash line in (b) was based on the Eq. S2.3.

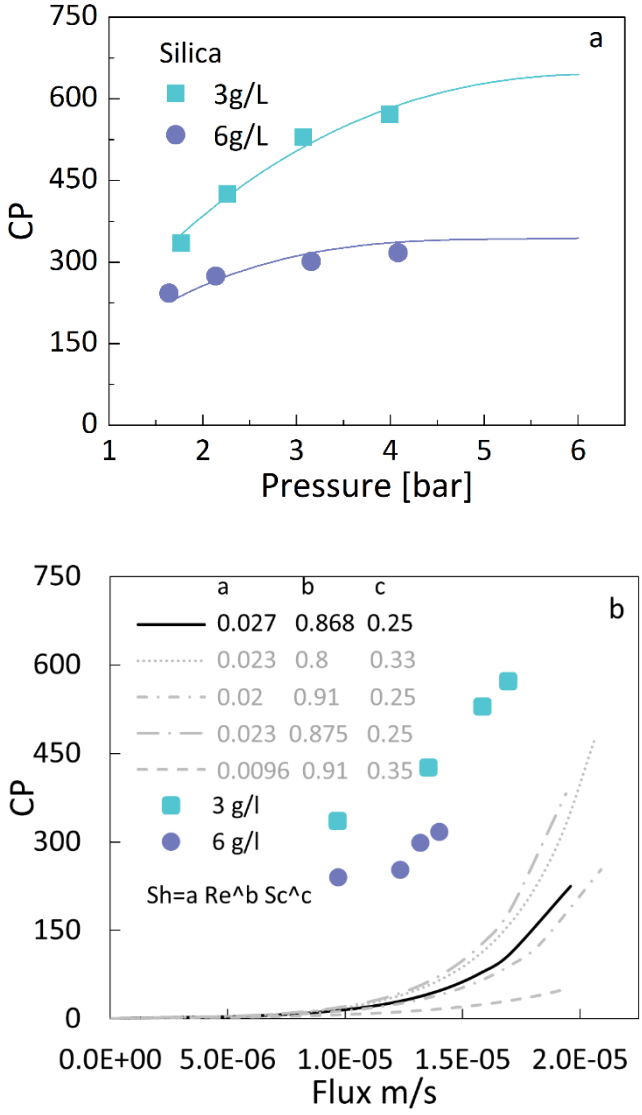

Figure S2.3. CP values with the applied pressure (a) and flux (b). The experimental CP values were based on osmotic pressures predicted from the Carnahan-Stirling theory (Eq. S2.3).

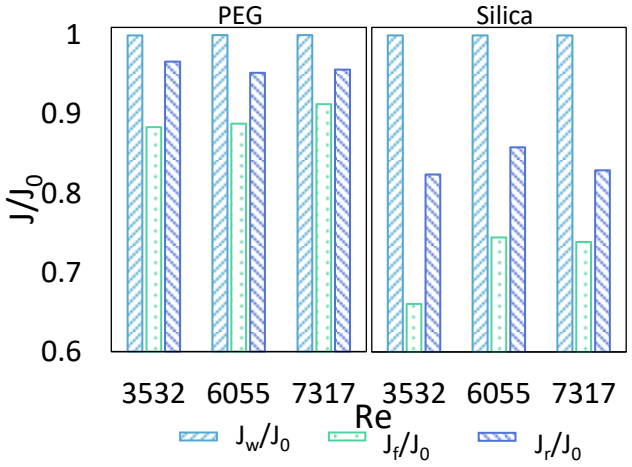

Figure S2.4. Normalized flux of PEG and silica under various Re numbers.

References

Alexandrowicz, Z., 1959. Light-scattering measurement of the osmotic activity of a polyethylene glycol solution. J. Polym. Sci. 40, 107–112. https://doi.org/10.1002/pol.1959.1204013607

Bonnet-Gonnet, C., Belloni, L., Cabane, B., 1994. Osmotic pressure of latex dispersions. Langmuir 10, 4012–4021. https://doi.org/10.1021/la00023a019

Kramer, F.C., Shang, R., Scherrenberg, S.M., Rietveld, L.C., Heijman, S.J.G., 2019. Quantifying defects in ceramic tight ultra- and nanofiltration membranes and investigating their robustness. Sep. Purif. Technol. 219, 159–168. https://doi.org/10.1016/j.seppur.2019.03.019

McClendon, J.H., 1981. The osmotic pressure of concentrated solutions of polyethylene glycol 6000, and its variation with temperature. J. Exp. Bot. 32, 861–866. https://doi.org/10.1093/jxb/32.4.861

Michel, B.E., Kaufmann, M.R., 1973. The osmotic potential of polyethylene glycol 6000. Plant Physiol. 51, 914–916. https://doi.org/10.1104/pp.51.5.914

Nichol, L.W., Ogston, A.G., Preston, B.N., 1967. The equilibrium sedimentation of hyaluronic acid and of two synthetic polymers. Biochem. J. 102, 407–416.

Pasquier, C., Beaufils, S., Bouchoux, A., Rigault, S., Cabane, B., Lund, M., Lechevalier, V., Floch-Fouéré, C.L., Pasco, M., Pabœuf, G., Pérez, J., Pezennec, S., 2016. Osmotic pressures of lysozyme solutions from gas-like to crystal states. Phys. Chem. Chem. Phys. 18, 28458–28465. https://doi.org/10.1039/C6CP03867K

Shang, R., Goulas, A., Tang, C.Y., de Frias Serra, X., Rietveld, L.C., Heijman, S.G.J., 2017. Atmospheric pressure atomic layer deposition for tight ceramic nanofiltration membranes: synthesis and application in water purification. J. Membr. Sci. 528, 163–170. https://doi.org/10.1016/j.memsci.2017.01.023

Vilker, V.L., Colton, C.K., Smith, K.A., Green, D.L., 1984. The osmotic pressure of concentrated protein and lipoprotein solutions and its significance to ultrafiltration. J. Membr. Sci. 20, 63–77. https://doi.org/10.1016/S0376-7388(00)80723-1

满江红

回望来时，满暮雨，心志未息。风且住，破空出剑，血马卢的。欲把强奴皆斩首，试将蝼蚁俱焚泥。待天宫，赏赐我王侯，归旧籍。

金杯酒，罗锦衣。夜行者，可知其？已负东流水，往事别提。而立三十翻旧历，笑说都是少年愚。对青灯，看壁影重重，华发稀。

2021.02.18

Chapter 3

Fouling removal in ceramic ultrafiltration membrane via catalyst modification with Fenton-like backwash

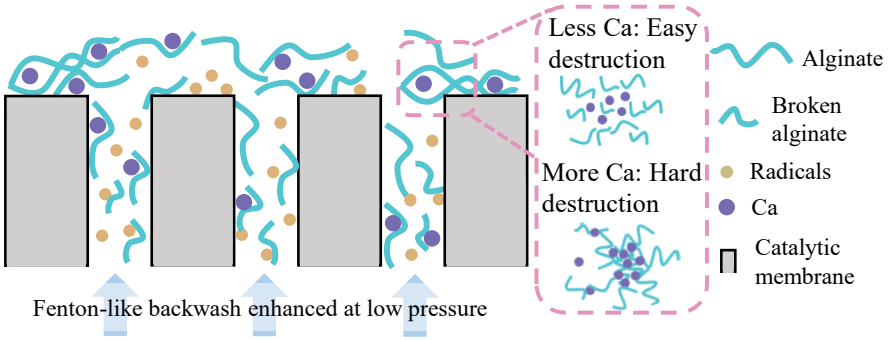

This chapter is based on

Zhang, S., Wang, K., Rietveld, L. C., & Heijman, S. G. (2025). Fouling removal in ceramic ultrafiltration membrane via catalyst modification with Fenton-like backwash. Journal of Membrane Science, 734, 124411.

Abstract

Fouling remains a critical challenge for ceramic ultrafiltration membranes, limiting their long-term performance for water treatment. Fenton-like reactions have been widely used for fouling removal due to the formation of strong radicals. Integrating these reactions into backwash offers a promising strategy for fouling control. However, it has been unclear how Fenton-like backwash is influenced by operational parameters and fouling structures. Here we reveal the key factors influencing Fenton-like backwash by systematically studying its performance under varying conditions, such as backwash pressure (0.3–1 bar), duration (18–36 min), fouling structure (caused by 1–5 mM Ca), and the long-term operation, to provide an effective and practical cleaning. $CuFe_2O_4$ was grown on ceramic ultrafiltration membranes due to its stability and high catalytic efficiency in activating Fenton-like reactions. We found that Fenton-like backwash achieved the highest cleaning efficacy of approximately 70% over three cycles at a low backwash pressure of 0.3 bar, while hydraulic backwash remained ineffective under all conditions. Backwash pressure, rather than duration, was identified as the dominant factor governing the Fenton-like cleaning, due to its impact on the residence time of Fenton-like agents (H_2O_2). The presence of a high Ca concentration (3 and 5 mM) altered the fouling behaviour, and reduced the cleaning efficacy of Fenton-like backwash. This reduction was attributed to the formation of rigid alginate clusters that were resistant to Fenton-like reactions. The contribution of •OH to the enhanced Fenton-like backwash was confirmed by the quenching experiments. Furthermore, the $CuFe_2O_4$-coated membranes exhibited stable flux recovery (83%–94%) in the long-term treatment of a concentrated alginate (800 mg/L), showed low or negligible leaching in harsh environments (30 mM H_2O_2, 0.1% NaClO or 10 mM NaOH), and maintained comparable performance after 96 h aging by 30 mM H_2O_2. This study clarifies the factors governing Fenton-like backwash and demonstrates that a robust and effective strategy for fouling removal can be achieved by coupling this cleaning method with catalytic ceramic membranes.

3.1. Introduction

Ceramic ultrafiltration (UF) membranes have been regarded as a promising technology in the treatment of various complex polluted waters, due to their high thermal stability, low carbon footprint, and resistance to chemicals (Chen et al., 2022). However, membrane fouling can account for 11%–24% of the operational expenses in treatment plants (Jafari et al., 2021). In addition, more than 60% of flux decline is caused by the fouling formed on the ceramic membrane, as reported by Zhang et al. (2024). Among the different natural organic matter (NOM) fractions, polysaccharides—particularly alginate—have been identified as major contributors to irreversible membrane fouling. Compared to other organic foulants such as humic acids and proteins, alginate forms a dense and sticky gel layer that is more resistant to conventional cleaning techniques (Alresheedi et al., 2019a). The NOM fouling can be influenced by the water matrix and operational parameters (Alresheedi et al., 2019a). For example, alginate fouling is further deteriorated by the presence of divalent cations such as calcium (Ca), which can interact with alginate to alter its physicochemical properties. These interactions lead to aggregation, crosslinking, and compaction of the fouling layer, thereby reducing membrane permeability and increasing cleaning difficulty (Alresheedi et al., 2019b; Zhang et al., 2017). As such, effective removal of alginate-Ca-induced fouling remains a bottleneck in the operation of ceramic UF membranes.

Hydraulic backwash is commonly employed to remove loose foulants from the membrane surface, but its efficacy against compacted alginate-Ca fouling is limited. Reported cleaning recoveries range from as low as 23% for ceramic membranes to below 1% for polymeric ones (Angelis and Cortalezzi, 2016; Resosudarmo et al., 2013). This low efficacy results from the hydraulically irreversible nature of alginate fouling layer, which adheres strongly to the membrane surface and resists physical cleaning. To address this, various fouling mitigation techniques have been explored, including enhancing membrane hydrophilicity, chemical cleaning with sodium hydroxide (NaOH), hydrochloric acid (HCl), or sodium hypochlorite (NaClO), and integration with advanced oxidation processes (AOPs) (Xu et al., 2022; Zhao et al., 2022; Alresheedi et al., 2019b). However, hydrophilic modifications can deteriorate fouling when adhesive forces dominate over surface properties (Xu et al., 2022). Chemical cleaning with NaOH and HCl yields modest efficacies of 31% and 45%, respectively (Ding et al., 2023). NaClO can achieve 60% alginate removal contributing to its oxidative potential (Alresheedi et al., 2019a).

However, NaClO, as harsh chemical, can pose environmental challenges due to its harsh nature and the need for post-treatment of cleaning wastewater (Ding et al., 2023). AOPs, which generate reactive radicals for foulant degradation, offer a promising alternative. For instance, ozone-based cleaning in place outperforms NaClO and NaOH due to the radical-induced degradation, but its practical application is limited by low efficacy and high energy demands (Alresheedi et al., 2019b). These limitations underscore the need for alternative, sustainable, and cost-effective cleaning strategies.

Fenton-like reaction, one type of AOPs, has been regarded as a potential solution for the removal of persistent fouling. In these reactions, hydroxyl radicals (•OH) can be induced from hydrogen peroxide (H_2O_2) in the presence of catalysts such as $CuFe_2O_4$, which exhibits a higher activity and stability over other spinel ferrites in radical generation (Feng and Zhang, 2023). Importantly, H_2O_2 decomposes into water and oxygen, making it an environmentally-friendly oxidant. Previous studies have integrated Fenton-like reactions into forward flush using catalytic ceramic membranes, and demonstrated enhanced fouling removal (Lin et al., 2021). However, these methods require continuous dosing of H_2O_2 during a long-time flush process, leading to increased costs and concerns over oxidant consumption and residuals. An alternative and less-explored approach is to couple Fenton-like reactions with backwash. In hydraulic backwash, operational parameters such as backwash pressure and duration have been widely studied to physically loosen the cake layer (Katsoufidou et al., 2007). When coupled with Fenton-like reactions backwash, the performance can be influenced by both hydraulic force and the oxidation process. A higher backwash pressure can enhance drag force and promote partial fouling detachment, creating pathways for radicals' transport, which may improve radical-based cleaning. However, it can also increase flux, reducing H_2O_2 residence time and limiting radical formation, thus hindering fouling degradation. Similarly, while extended backwash duration may increase the total contact time of H_2O_2, its actual influence on the efficacy of Fenton-like backwash remains unclear. At present, it is not well understood how backwash pressure or duration interacts with the Fenton-like reaction to influence the overall cleaning performance, and which mechanism plays the dominant role under different conditions. Furthermore, the effect of Ca ions on Fenton-like backwash remains unstudied, although Ca is known to alter fouling structure (Zhang et al., 2017), increase flux decline (van den Brink et al., 2009), and reduce the efficacy of hydraulic backwash and Fenton-like forward flush (Katsoufidou et al., 2007; Lin et al., 2021). The presence of Ca can form cake

layer, which can limit the transport of H_2O_2. Notably, the interaction between Ca and alginate can result in distinct structures, such as the egg-box structures or rigid, cross-linking alginate-Ca clusters. These distinct structures may influence how the fouling attaches to the membrane and how •OH radicals diffuse into the fouling layer, thereby affecting the overall efficacy of Fenton-like backwash. These knowledge gaps highlight the need for a systematic investigation of how operational parameters and Ca-induced fouling structures affect Fenton-like backwash. A better understanding, therefore, is crucial to improve its cleaning performance and practical applicability

This work aims to gain a comprehensive understanding of the effect of backwash duration, backwash pressure and the presence of Ca on the performance of Fenton-like backwash for catalytic UF membranes fouled by alginate, thereby providing a practical and cost-effective cleaning strategy. $CuFe_2O_4$ was deposited as a stable and efficient catalyst to generate radicals from H_2O_2. The operational parameters of backwash pressure and duration were studied to reveal their roles in Fenton-like backwash. Additionally, we explored the effect of Ca on fouling structures, and its subsequent effect on cleaning performance. Finally, this study evaluated the cleaning performance for fouling caused by high-concentration alginate and the leaching of the catalytic UF membrane when exposed to H_2O_2, NaClO, and NaOH.

3.2. Materials and methods

3.2.1. Ceramic (un)coated UF Membranes

Ceramic UF membranes with a selective layer of Al_2O_3, and a nominal pore size of 100 nm, were obtained from CoorsTek (the Netherlands). The tubular membranes had a single channel, an internal diameter of 7 mm, an outer diameter of 10 mm, and a length of 100 mm. The edges of the membranes (10 mm for each side) were sealed by two-component epoxy adhesives (Araldite AW 5047-1 and Hardener HW 5067-1, from VIBA, the Netherlands) to avoid potential leaking from the two edges of the membrane during filtration.

The precursor solution of the catalyst $CuFe_2O_4$ was prepared by dissolving copper nitrate trihydrate ($Cu(NO_3)_2 \cdot 3H_2O$, from Merck, Germany), ferric nitrate nonahydrate ($Fe(NO_3)_3 \cdot 9H_2O$, from Sigma-Aldrich), and citric acid (from Sigma-Aldrich) with a molar ratio of 1:2:3.6, respectively. The mixed solution was stirred at 80 ℃ for 1 h. Then, 50 mL of precursor solution was filtered through the pristine UF membrane via a dead-end setup under a pressure of 0.1 bar to ensure that the membrane surface and body had sufficient

contact time with the precursor solution. Afterward, the wet membrane was dried at 100 ℃ for 10 min. The coating and drying processes were repeated three times. Afterward, the membranes, covered with catalyst precursors, were calcined at 400 ℃ for 2 h, and then washed with demineralized water. This water was produced at WaterLab, TU Delft (conductivity < 0.1 μs cm^{-1}, water filtered by a reverse osmosis filter, a candle filter, and a resin vessel).

3.2.2. Crossflow setup

A constant pressure crossflow setup (Fig. 3.1) was designed and constructed for the fouling and cleaning experiments. A balance (KERN, Germany) was used to measure the permeate flux with a time interval of 30 s. To capture the initial sharp drop in flux, which typically occurs within the first few min of filtration, the balance and pressure sensors (ESI, UK) were initiated before activating the pump (AxFlow, the Netherlands). For the backwash process, tubes were first connected to a pure water container, and the system was flushed with clean water. Subsequently, the orientation of the membrane module was reversed for backwash.

3.2.3. Performance tests

3.2.3.1. Effect of backwash intensities and Ca concentration over three cycles

Before fouling tests, the pure water flux was tested to ensure that the membranes were clean. An extended description of the preparation of the alginate solution is given in Text S1. 50 mg/L alginate solution, containing $CaCl_2$ (1, 3, and 5 mM), was filtered over the membranes at 0.3 bar and a crossflow velocity of 0.65 m/s (Re = 4531) for 45 min to reach the steady flux. The membranes were cleaned via backwashing with demineralized water or 30 mM H_2O_2 (pH 2.5) using varying times (6, 18, 36 min) and pressures (0.3, 0.5, 1 bar). A 1-min forward flush at a crossflow velocity of 1.1 m/s (Re = 7552) was followed to remove loose foulants. During the forward flush process, the tube connected to the permeate side of the membrane module was closed to prevent permeate flow. Temperature was monitored for permeability adjustments (Eq. S3.1). The (un)coated membranes cleaned with demineralized water served as blank experiments. The fouling and cleaning processes were conducted during three cycles.

3.2.3.2. Radical quenching experiments

Tert-butyl alcohol (TBA) was used to quench •OH radicals during Fenton-like backwash, in order to assess the role of •OH in fouling removal. The fouling

process was conducted at 0.3 bar for 75 min by using a solution containing 50 mg/L alginate and 3 mM Ca. Then the fouled $CuFe_2O_4$ membranes were backwashed with demineralized water, 30 mM H_2O_2 and 300 mM TBA (at pH=2.5), or 30 mM H_2O_2 (at pH=2.5), at 0.5 bar for 36 min. Afterwards, 1-min forward flush by demineralized water was applied. The pure water flux was measured before and after cleaning to determine flux recovery to assess the effect of radicals on fouling removal.

In addition to flux recovery tests, methylene blue degradation experiments were conducted to verify the oxidative activity of the coated membranes in a simplified system and to further confirm the involvement of •OH radicals. In these tests, the coated membranes were immersed in the prepared 50 mL solution containing 10 mg/L methylene blue and 30 mM H_2O_2 (pH 2.5), or 30 mM H_2O_2 with 300 mM TBA (pH 2.5).

3.2.3.3. Effect of the concentrated alginate

Single-cycle fouling and cleaning of the (un)coated membranes. In this experiment, the demineralized water flux of the clean (un)coated membrane was measured at 0.3 bar. Subsequently, a concentrated alginate solution (800 mg/L) containing $CaCl_2$ (3 mM), NaCl (1 mM), and $NaHCO_3$ (1 mM), was filtered through the pristine or coated membrane at 0.3 bar and a crossflow velocity of 0.65 m/s to simulate a municipal sewage filtration experiment of approximately 1.7 days (Kramer et al., 2020). Then the demineralized water flux was re-measured at 0.3 bar. The cleaning process involved a backwash using either demineralized water or the H_2O_2 solution (30 mM, pH 2.5) at 0.5 bar for 18 min, followed by a 1-min forward flush with demineralized water at a crossflow velocity of 1.1 m/s. After cleaning, the demineralized water flux was measured again at 0.3 bar. The pristine membranes, backwashed with demineralized water and the H_2O_2 solution, were used as blank experiments.

Long-term (seven-cycle) fouling and cleaning of the coated membrane. In the seven-cycle fouling and cleaning experiment, the $CuFe_2O_4$-coated membrane was fouled by 800 mg/L alginate with 3 mM $CaCl_2$, 1 mM NaCl, and 1 mM $NaHCO_3$ at 0.3 bar, 0.65 m/s crossflow velocity. The membrane was then cleaned by a 6-min backwash with a H_2O_2 solution (30 mM, pH=2.5) at 0.5 bar, followed by a 1-min forward flush with demineralized water. This test aimed to examine the performance of the developed Fenton-like backwash under severe fouling conditions using a shorter 6-min backwash, thereby evaluating its practical feasibility for maintaining the cleaning efficacy during long-term application.

3.2.3.4. Stability of the $CuFe_2O_4$ membrane

The H_2O_2 solution (30 mM, pH = 2.5) and two other common cleaning agents (0.1% NaClO, and 10 mM NaOH) were chosen for leaching tests of Cu and Fe. The leaching test was carried out by immersing the used $CuFe_2O_4$ membrane in a 500 mL H_2O_2 solution (pH=2.5), 0.1% NaClO, and 10 mM NaOH, respectively, for 8 h. Then the Cu and Fe leaching were measured by inductively coupled plasma-mass-spectrometry (ICP-MS, Plasma Quant MS, Analytik Jena AG, Germany). Additionally, we compared the cleaning performances of the aged catalytic membrane (after immersion in H_2O_2 for 96 h) with that of the newly coated membrane. The structures of the new and aged catalytic membranes were also analyzed by X-ray diffraction (XRD).

3.2.4. Characterization

The top and cross-sections of the (un)coated membranes were examined by scanning electron microscopy (SEM, Hitachi S-3400 II, Japan) equipped with energy dispersive spectroscopy (EDS). The D8 discover diffractometer (Bruker, USA) with Cu Kα radiation at 50 kV and 1000 μA was employed for the X-ray diffraction (XRD) pattern of the membranes under a scan step size of 0.04° and a step time of 2 s. We measured the alginate's size distribution using a particle size analyzer (Bluewave, Microtrac, USA).

3.2.5. Performance analysis

Multi-cycle fouling and cleaning. Flux was determined through the filtration of the alginate solution. Calculations of cleaning efficacy and resistance were based on the work of Lee et al. (2021) and Zsirai et al. (2012).

$$Cleaning\ efficacy = \frac{J_c - J_f}{J_0 - J_f} \quad 3.1$$

$$R = R_m + R_t = R_m + R_r + R_{ir} = \frac{\Delta P}{\mu J_f} \quad 3.2$$

$$R_m = \frac{\Delta P}{\mu J_0} \quad 3.3$$

$$R_{ir} = \frac{\Delta P}{\mu J_c} - \frac{\Delta P}{\mu J_0} \quad 3.4$$

$$R_r = \frac{\Delta P}{\mu J_f} - \frac{\Delta P}{\mu J_c} \quad 3.5$$

where J_0 (in m/s) is the initial flux in the first fouling cycle, J_f (in m/s) is the final, steady flux at the end of the fouling (e.g., Cycle N), J_c (in m/s) is the initial flux in the subsequent fouling cycle (e.g., Cycle N+1), R (in m^{-1}) is the total resistance, R_t (in m^{-1}) is the total fouling resistance, R_m (in m^{-1}) is the membrane resistance, R_r (in m^{-1}) is the reversible resistance, R_{ir} (in m^{-1}) is the irreversible resistance, ΔP (in Pa) is the transmembrane pressure, and μ (in Pa s) is the dynamic viscosity of the permeate-side solution, depending on temperature.

To evaluate the fouling potential of the feed water, we used the unified membrane fouling index ($UMFI$), because it is independent from traditional fouling models (e.g., pore blocking and cake filtration) (Huang et al., 2009; Nguyen et al., 2011; Shang et al., 2015) in the multicycle test. The $UMFI$ (in $m^2\ L^{-1}$) is defined as the slope of the linear equation of Eq. 3.6, where J_s' is the normalized specific permeate flux (J/J_0) and V_s (in L m^{-2}) is the unit permeate volume. $UMFI$ can be expressed as $UMFI_t$ for each fouling curve, representing the total fouling index, while $UMFI_c$, being the chemically irreversible fouling index, can be obtained by using a two-point method based on the $1/J_s'$ values of the first and the last cycle.

$$\frac{1}{J_s'} = 1 + (UMFI) \times V_s \quad 3.6$$

Single-cycle fouling and cleaning. Backwash performance was evaluated by flux recovery (Eq. 3.7), based on the water flux measured before fouling (J_{w0}, in m/s) and after cleaning (J_{wc}, in m/s).

$$Flux\ recovery = \frac{J_{wc}}{J_{wo}} \quad 3.7$$

The residence time of the H_2O_2 solution. As given in Eq. 3.8, the residence time (in s) of the H_2O_2 solution passing the membrane was calculated by the flux (J, in m/s), porosity (ϕ), and the thickness of the selective layer of the membrane (L, in m).

$$Residence\ time = \frac{L\,\phi}{J} \qquad 3.8$$

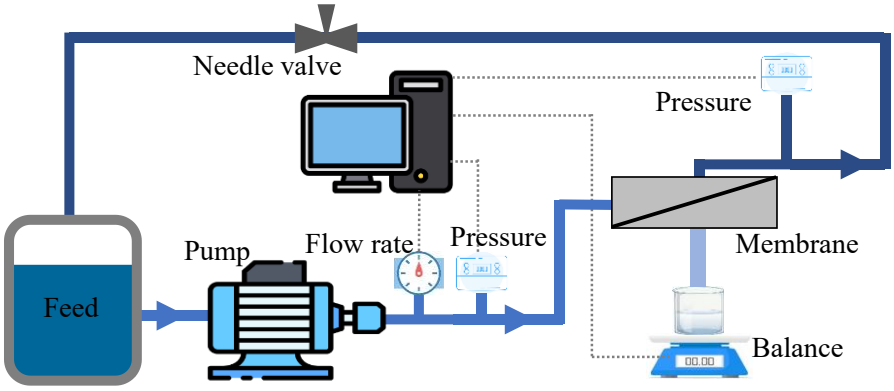

Figure 3.1. The constant pressure setup for fouling and backwash operation.

3.3. Results and discussions

3.3.1. Membrane characterization before and after modification

Fig. 3.2a and 3.2b show that the $CuFe_2O_4$ coating had a minimal influence on the overall morphology of the membrane, since no considerable structural difference was observed before and after the coating. This negligible effect of $CuFe_2O_4$ on the ceramic membrane has also been found in a previous study (Zhao et al., 2020). Additionally, a uniform distribution of $CuFe_2O_4$ on the surface of the membrane was observed from the SEM-EDS elemental mapping analysis of the top-view $CuFe_2O_4$ coated membrane (Fig. 3.2c). SEM-EDS line scanning verified that $CuFe_2O_4$ was grown on the entire selective layer of the membrane (Fig. 3.2d). The XRD of the coated membrane (Fig. S3.1) shows that the characteristic peaks at 2θ of 18.4, 30.2, 35.6, 37.2, 43.0, 57.1, and 62.7, corresponded to the (111), (220), (311), (222), (400), (511), and (440) lattice planes of $CuFe_2O_4$, respectively (Jiang et al., 2021; Xu et al., 2023; Zhao et al., 2020). Besides, Fig. S3.2 shows that the permeability of the ceramic UF membrane only declined from 362 to 346 L m^{-2} h^{-1} after coating, while a larger permeability drop (from 470 to 196 L m^{-2} h^{-1}) was observed in polymeric UF membranes after $CuFe_2O_4$ coating (Wang et al., 2019).

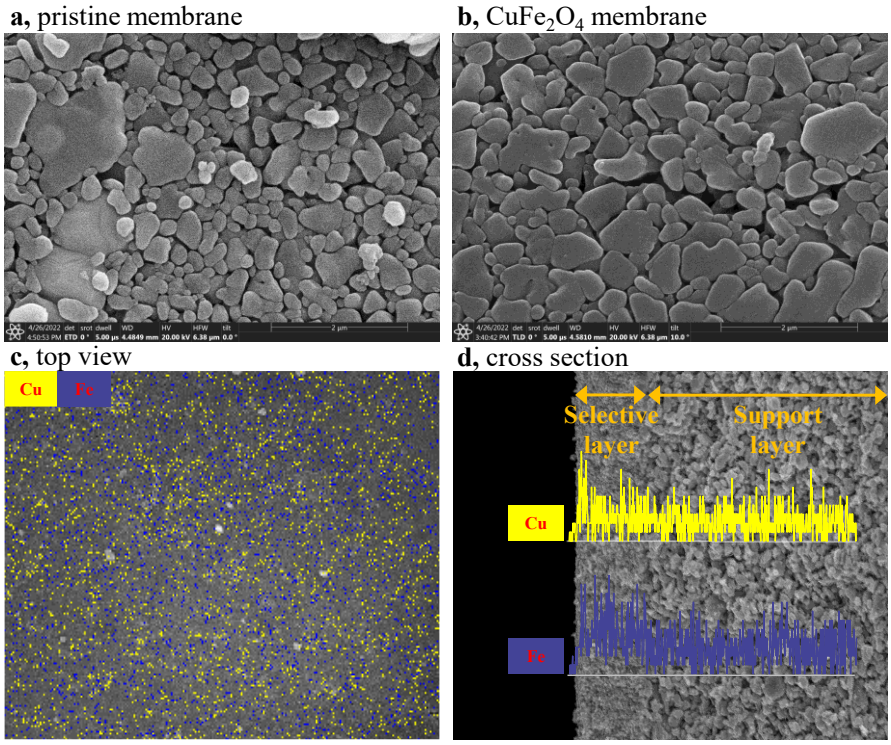

Figure 3.2. Top SEM view of (a) the pristine and (b) the $CuFe_2O_4$ membranes. SEM-EDS images of (c) top-view mapping and (d) cross-section line scanning of the $CuFe_2O_4$ membranes.

3.3.2. Effect of backwash duration

In the experiments where the fouled coated membranes were backwashed with demineralized water for 6, 18, and 36 min over three cycles, their R_{ir} (1.1×10^{10}–1.9×10^{10} m^{-1}) and R_{ir} ratio (85%–96%) remained at a high level (Fig. 3.3a–3.3d). An extended duration of the hydraulic backwash did not exhibit a positive effect on the cleaning. For example, in the third cycle, cleaning efficacies of only 1.6% and 1.0% were found for a backwash duration of 6 min and 36 min, respectively. Moreover, in the single fouling and cleaning test (Fig. S3.3), the flux recovery was only 45% after a 36-min hydraulic backwash. The extension of cleaning duration cannot improve the cleaning performance in the absence of chemical reactions, as reported by Ang et al. (2006). This is likely due to the inherent limitations of physical cleaning methods in removing strongly adhered alginate foulants.

With 6–36 min Fenton-like backwash, the R_{ir} of the $CuFe_2O_4$ membranes consistently remained at a low level, ranging from 1.7×10^9 to 7.6×10^9 m^{-1}, one order of magnitude lower than that of the hydraulic backwash counterpart (Fig. 3.3a). In addition, the R_{ir} values in the Fenton-like backwash test were maintained at a low level over three cycles. The marginally higher R_{ir}, found in 36-min case compared to 18-min case, can be caused by the experimental variations. To eliminate this effect and allow for more consistent comparison, the normalized R_{ir}/R_t was used to evaluate the contribution of irreversible fouling. It is observed that the R_{ir}/R_t of $CuFe_2O_4$ membranes decreased with increasing Fenton-like backwash duration, indicating that a longer backwash can effectively reduce the relative contribution of irreversible fouling. Moreover, when the duration of the H_2O_2 backwash was extended from 6 to 36 min, the cleaning efficacy improved from 32% to 62%, much higher than the efficacy (1%–7%) achieved in hydraulic backwash (Fig. 3.3b-3.3d). The prolonged H_2O_2 backwash increased contact time between H_2O_2 and catalytic sites, which, accordingly, generated more •OH radicals to degrade alginate fouling for the improved cleaning (Lin et al., 2021).

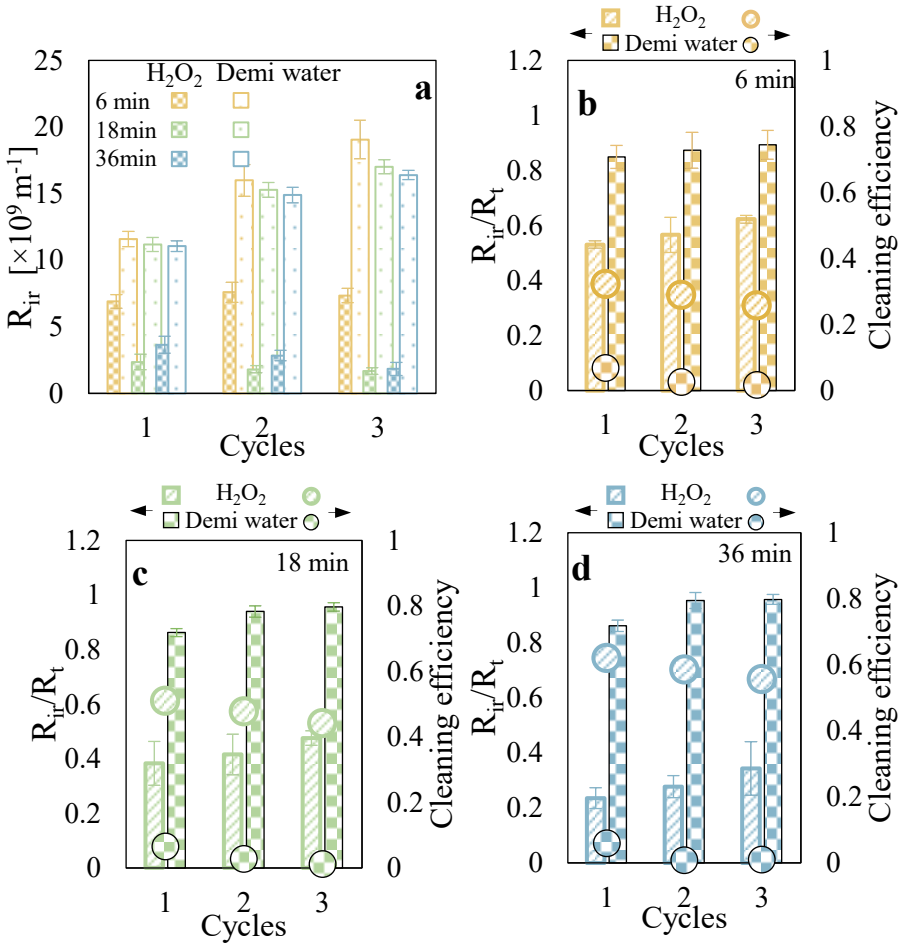

Figure 3.3. (a) R_{ir}, (b–c) R_{ir} ratio and cleaning efficacy of the coated membrane with H_2O_2 backwash or the pristine membrane with hydraulic backwash, conducted at 0.3 bar with 50 mg/L alginate solution for 45 min each fouling cycle, then backwashed at 0.5 bar with demineralized water or 30 mM H_2O_2 (pH = 2.5) for 6, 18 and 36 min, respectively, and rinsed by 1-min forward flush with demineralized water.

3.3.3. Effect of backwash pressure

Fig. 3.4 shows the effect of backwash pressure on cleaning efficacy over three cycles. The selected backwash pressures of 0.3, 0.5, and 1 bar were based on the correlation between applied filtration pressures and backwash pressures

(Fig. 3.4a), where most employed backwash pressures are higher than the applied filtration pressures.

The low cleaning efficacy (1%–14%) and high R_{ir} ratio (81%–96%) were found at 1 bar hydraulic backwash over three cycles (Fig. S3.4). These suggest that most alginate fouling, formed on the membrane surface or in the pores, could not be flushed off by hydraulic backwash, even at a high backwash pressure. In addition, the demineralized water flux measured after hydraulic backwash, was even lower than the final flux measured at the end of the fouling cycle, as found in the single-cycle fouling and cleaning test (Fig. S3.5).

Fig. 3.4b shows that the highest cleaning efficacy (68%–71%) was achieved at 0.3 bar with Fenton-like backwash over three cycles. Usually, backwash at a higher pressure is assumed to enhance the cleaning by providing an intensified drag force to loosen and remove the cake fouling (Resosudarmo et al., 2013; Katsoufidou et al., 2008). Therefore, a higher backwash pressure was widely used in previous studies, as shown in Fig. 3.4a. However, in the H_2O_2 backwash of the fouled $CuFe_2O_4$ membrane, higher backwash pressures resulted in a lower cleaning efficacy, along with a higher R_{ir} ratio and a higher R_{ir} (Fig. 3.4b and S3.6). As the backwash pressure increased from 0.3 to 1 bar, the residence time—calculated based on Eq. 3.8, and Fig. S3.7—decreased considerably from 0.15 to 0.06 s (Fig. 3.4c), due to the increased backwash flux. The reduced residence times, therefore, limited the transport of H_2O_2 towards the catalytic sites to form the $^{\bullet}OH$ radicals, and constrained the diffusion distance of the radicals. The linear relation (Fig. 3.4d) indicates that residence time, rather than the total backwash time (Fig. S3.8), dominated the backwash performance. The prominent effect of residence time on cleaning was further confirmed by experiments conducted at a constant backwash flux of 90 and 140 L m^{-2} h^{-1}, corresponding to residence times of 0.14 and 0.09 s, respectively (Fig. 3.4d).

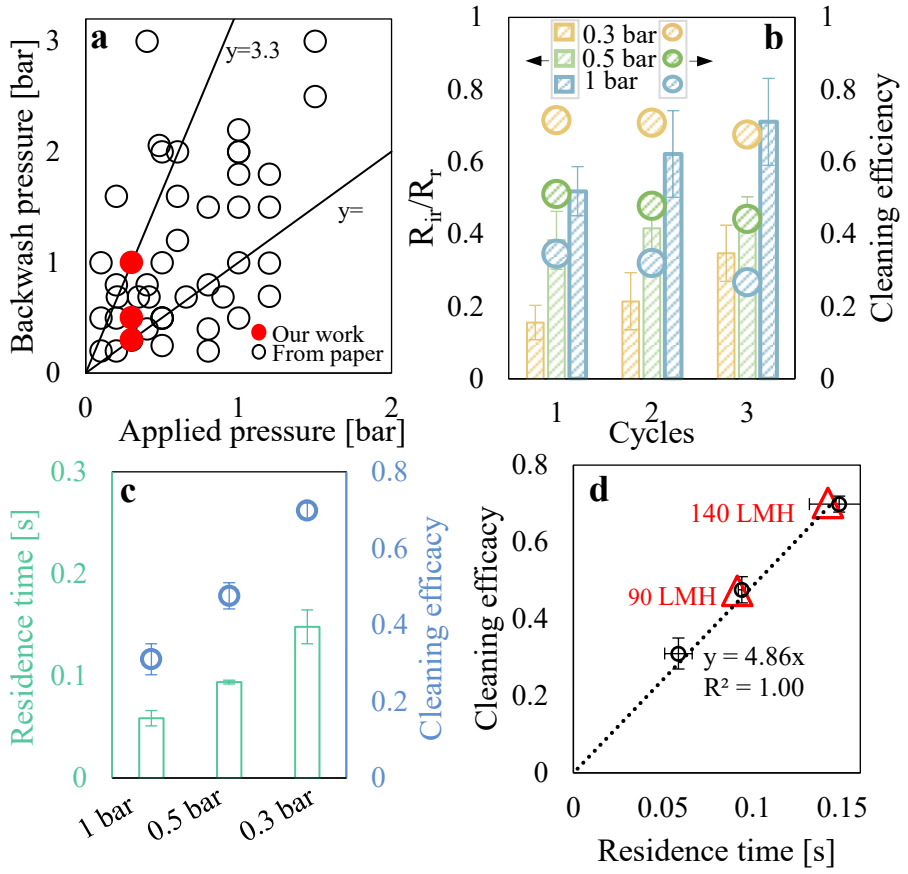

Figure 3.4. (a) Applied (filtration) and backwash pressures used in previous studies and in this work (red dots) (Al-Hammadi and Al-Bastaki, 2007; Chang et al., 2017b; Ferrer et al., 2016; Hong et al., 2005; Huang et al., 2020, 2014; Jermann et al., 2007; Katsoufidou et al., 2007; Kennedy et al., 1998; Nakatsuka et al., 1996; Pervov et al., 2003, 2003; Qu et al., 2014; Remize et al., 2010; Vroman et al., 2021; Xia et al., 2008; Zsirai et al., 2016), (b) fouling resistance ratios and cleaning efficacies of the coated membranes over three cycles, and (c, d) the residence time and cleaning efficacies. The coated membranes fouled by 50 mg/L alginate were backwashed for 18 min with 30 mM H_2O_2, under various backwash pressures, followed by 1 min forward flush, while the constant flux backwash was carried out at a flux of 90 and 140 L m^{-2} h^{-1}. The residence time in constant pressure backwash was calculated by using the average flux during the backwash.

3.3.4. Effect of calcium on cleaning performance

The presence of Ca will influence the fouling behaviour, which perhaps, in turn, will affect the Fenton-like backwash. Therefore, various Ca concentrations (1, 3, and 5 mM) were employed to evaluate the backwash performance with demineralized water or H_2O_2.

Fig. 3.5a shows that the total resistance caused by 1 mM Ca (3.1×10^9–3.3×10^{10} m^{-1}) was an order of magnitude higher than the range observed for both 3 and 5 mM Ca (3.5×10^9–7.2×10^9 m^{-1}). The higher fouling resistance, found in 1 mM Ca case, probably resulted from pore clogging. As reported in previous studies, a small dosage of Ca results in the formation of small alginate colloids (Katsoufidou et al., 2008, 2007). These small-sized alginate particles contribute to pore blocking, which leads to a low flux and a high fouling resistance (Katsoufidou et al., 2007; You et al., 2020). However, higher Ca concentrations promote alginate aggregation into more rigid clusters, resulting in the generation of a cake layer fouling with a relatively high porosity (You et al., 2020; Zhang et al., 2017). Fig. S3.9 shows that the size of the alginate indeed increased with an increased concentration of Ca. The highest cleaning efficacy (of 63%) was achieved in 1 mM Ca case (Fig. 3.5b). Although fouling resistance was similar for 3 mM and 5 mM Ca, the Fenton-like backwash achieved a higher cleaning efficacy at 3 mM (51%) than at 5 mM (36%). Similarly, 9 mM Ca exhibited comparable resistance but a further decreased cleaning efficacy (Fig. S3.10). However, for the fouled catalytic membranes, the hydraulic backwash resulted in low cleaning efficacies (1%–11%, Fig. S3.11a), and high R_{ir} values (5.1×10^9–3.0×10^{10} m^{-1}, Fig. S3.11b), under all Ca conditions.

Fig. 3.6 shows the proposed mechanisms for cleaning the $CuFe_2O_4$ membranes fouled with a calcium-rich alginate solution. Demineralized water backwash promotes the reorganization of the alginate-Ca structures and flushes away only part of the Ca ions. However, the alginate can still interact with the residual Ca ions, which can then bind to the membrane surface again. In addition, under low Ca concentrations, Fenton-like degradation leads to the formation of smaller alginate particles, which is more prone to pore blocking in the subsequent filtration cycle. This explains why hydraulic backwash gave a low cleaning efficacy in our experiments.

In contrast, during Fenton-like backwash, the stretchy egg-box alginate-Ca fouling (in less Ca case) is reorganized by the physical flush. This reorganization creates more space for H_2O_2 to transfer to $CuFe_2O_4$ areas,

facilitating the formation of the strongly oxidizing •OH radicals (Wu et al., 2014). Ca then can be released due to the partial degradation of the alginate structures, which further loosens the fouling and facilitates the transfer of H_2O_2 to break down the fouling. However, as reported by Zhang et al. (2017), at higher Ca concentrations, fouling is prone to cake formation by the cross-linking alginate-Ca clusters, where the ions are trapped in the inner structure of alginate clusters. These clusters are rigid and compact because they strongly interact with Ca ions. This makes it more difficult for the physical flush to disperse the rigid structures of alginate-Ca during the backwash, thereby limiting the diffusion of H_2O_2 to the catalytic sites (Alresheedi et al., 2019b; Xin et al., 2016). Besides, even if such complex rigid clusters are partially destroyed by the radials, the alginate fragments would be captured by and again bound to the Ca ions that are released from the inner fouling structure. These fragments would then reattach to the cleaning membrane surface or the residual fouling. Effective cleaning has been found to depend on the enhanced mass transfer of cleaning agents (towards fouling) and the fouling (towards the bulk), as well as the destruction of the intermolecular fouling interaction (Ang et al., 2006).

In this work, we have proposed a mechanism describing how different fouling structures would influence the performance of Fenton-like backwash. However, further studies are needed to verify this mechanism. Future work should directly characterize the alginate–Ca structures before and after Fenton-like reactions, assess the structural changes under different Ca levels, and measure how these changes affect mass transfer of radicals and cleaning efficiency. Such studies would provide stronger evidence for the proposed mechanism and the development of more effective cleaning strategies.

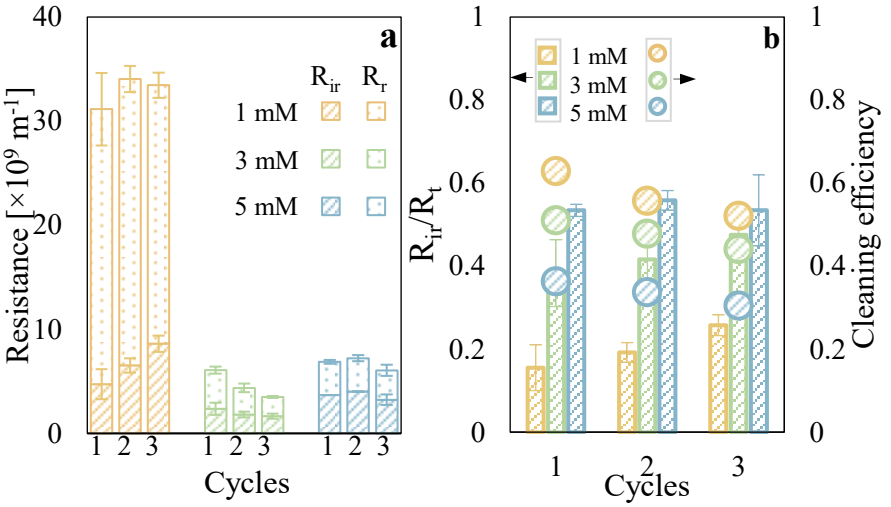

Figure 3.5. (a) Fouling resistance, (b) R_{ir} ratio and cleaning efficacy of the coated membranes. The fouling was conducted at a constant pressure of 0.3 bar with 50 mg/L alginate solution and with varying concentrations of Ca. The fouled membrane was cleaned by backwashing at 0.5 bar with 30 mM H_2O_2 (pH = 2.5) for 18 min, followed by 1 min forward flush.

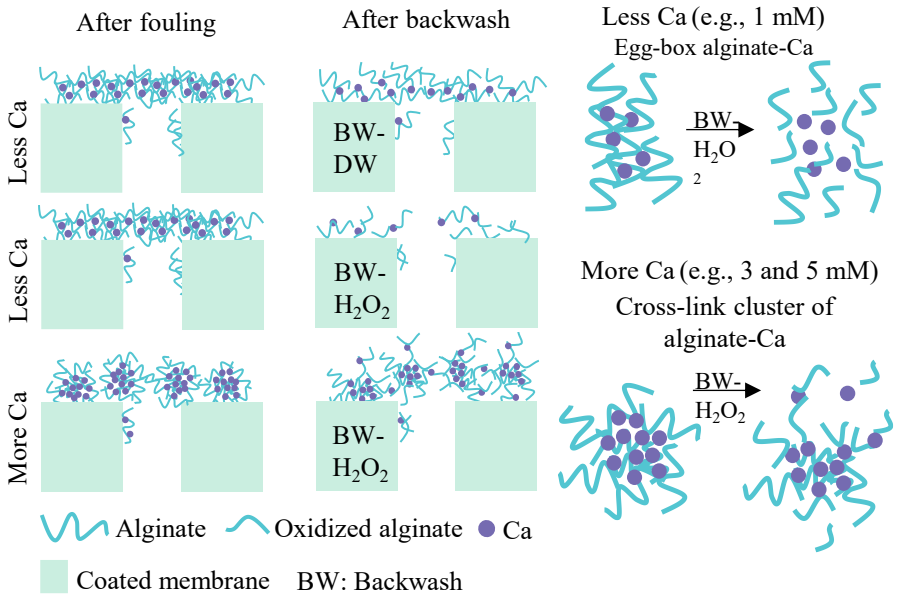

Figure 3.6. Schematic illustration of the structure of alginate with Ca and the proposed mechanism of backwash with demineralized water (DW) and the H_2O_2 solution for the cleaning of the fouled $CuFe_2O_4$ membranes.

3.3.5. Performance of (un)coated membranes fouled by concentrated alginate

The pristine and coated membranes were backwashed with either demineralized water or an H_2O_2 solution after fouling with 800 mg/L alginate with 3 mM Ca, followed by a 1-min forward flush. In addition, the demineralized water flux was determined before and after the fouling process as well as after the cleaning, as shown in Fig. 3.7a. Flux recoveries and (ir)reversible resistances are given in Fig. 3.7b, where the permeability recovery was determined by the flux of demineralized water before fouling and after cleaning (Eq. 3.7).

Flux curves show that both the pristine and coated membranes experienced a rapid flux decline during the initial phase of fouling. This phenomenon can be attributed to the rapid adsorption of alginate, leading to pore blocking and thus to a permeance decrease (Akamatsu et al., 2020). Subsequently, the flux exhibited a gradual decline, probably due to the formation of alginate-Ca gel layer and cake compression (Katsoufidou et al., 2007).

In all experiments, the demineralized water flux measured after fouling was comparable to the final, steady flux in the fouling test, suggesting that fouling could not be removed without cleaning. When an 18-min backwash with demineralized water was employed on the fouled pristine membrane, a flux recovery of 43% was found. An 18-min H_2O_2 backwash achieved a slightly higher flux recovery of 53%. An additional 18-min H_2O_2 backwash only increased the recovery from 53% to 58%. The modest improvement of backwash with H_2O_2 compared to the backwash with demineralized water likely resulted from the limited oxidation potential ($E°H_2O_2/H_2O$ = 1.763 V), due to the self-decomposition of H_2O_2 (Lin et al., 2021). An earlier study has also reported that the limited reaction between the cleaning agent and alginate-Ca leads to ineffective cleaning (Ang et al., 2006).

The highest flux recovery (80%) was achieved in the combination of the $CuFe_2O_4$ membranes and an 18-min H_2O_2 backwash, which is probably due to the highly reactive radicals of $^{\bullet}OH$ (E^0 = 2.73V) activated by $CuFe_2O_4$. This performance surpasses most existing cleaning strategies in alginate removal (Fig. 3.7c). It highlights the prominent influence of the Fenton-like backwash

on the destruction of persistent alginate-Ca fouling, compared to the cleaning methods such as forward flush, hydraulic backwash, and chemical cleaning.

The evolution of the fouling resistances is shown in Fig.3. 7b. The high resistances, caused by alginate fouling, have also been revealed in previous studies (Ye et al., 2005; van den Brink et al., 2009). The total fouling resistances were in the same order of magnitude (2.4×10^{10}–3.1×10^{10} m^{-1}) for the three experiments: the pristine membranes backwashed with either demineralized water, the pristine membranes backwashed with an H_2O_2 solution, and the coated membrane backwashed with an H_2O_2 solution. However, their irreversible resistances differed. Because of Fenton-like reactions the R_{ir} of the $CuFe_2O_4$ membrane with H_2O_2 backwash was reduced to 2.6×10^{9} m^{-1}, five times lower than with the pristine membrane with hydraulic backwash (1.3×10^{10} m^{-1}).

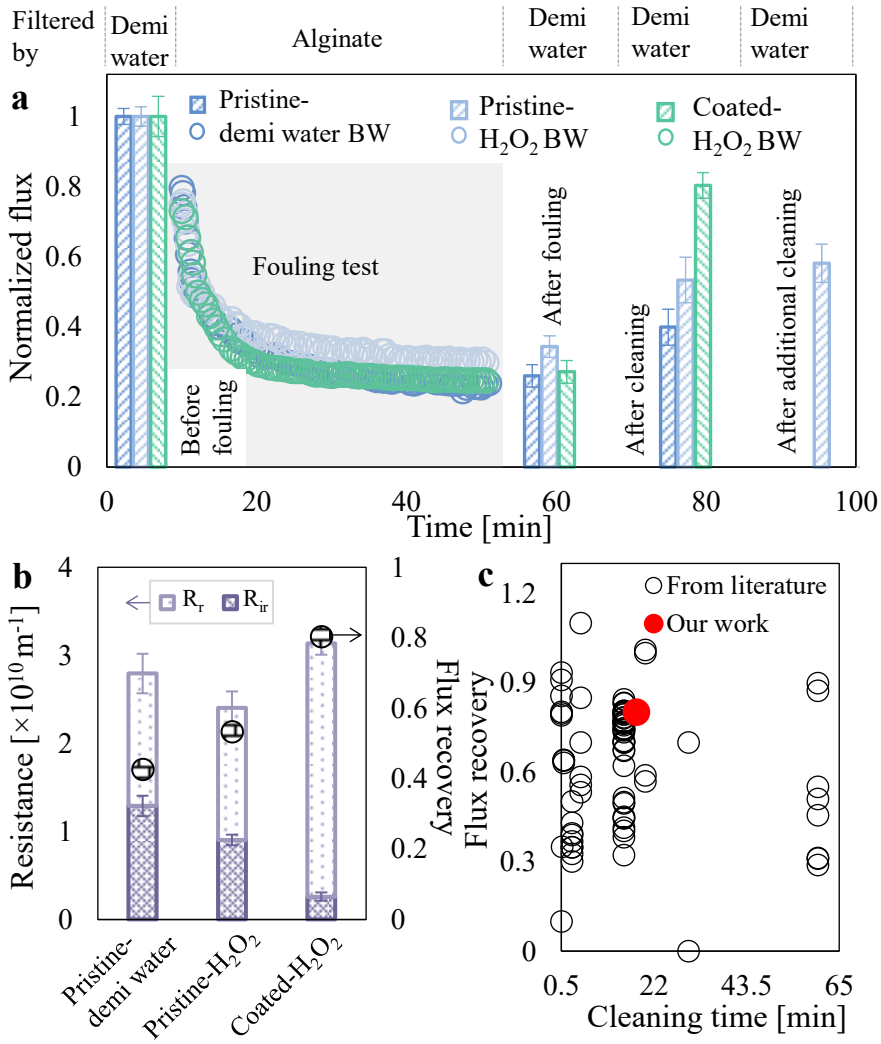

Figure 3.7. (a) Normalized flux declines during fouling, and normalized demineralized water flux measured before the alginate adding, at the end of fouling, after cleaning, and additional backwash procedure. (b) The resistances and flux recoveries for different systems. The fouling tests were conducted by 40 min filtration of 800 mg/L alginate solution with 3 mM Ca at 0.3 bar. Cleaning was done by backwashing with 30 mM H_2O_2 or demineralized water at 0.5 bar for 18 min, followed by a 1-min forward flush. The additional cleaning of the pristine membrane was performed by an H_2O_2 backwash for 18 min. (c) Performance comparison in removal of alginate fouling from the

fouled membranes (Ang et al., 2006; Chen and Columbia, 2011; Gray et al., 2011; Hashino et al., 2011; Huang et al., 2021; Kim et al., 2021; Kramer et al., 2020; Lee et al., 2021; Li and Elimelech, 2004; Lin et al., 2021; Meshram et al., 2016).

3.3.6. Long-term performance of the $CuFe_2O_4$ membrane fouled by concentrated alginate

To evaluate the long-term performance of Fenton-like backwash on the $CuFe_2O_4$ membrane, the fouling experiments were conducted using a concentrated alginate (800 mg/L) with 3 mM Ca over seven cycles. Fig. 3.8a shows that the normalized flux was restored to 89%–94% in the first three cycles, and then stabilized at 83%–87% over the rest of the four cycles. Since $UMFI$ is independent of the traditional fouling models, it can be used in the prediction of anti-fouling performance, regardless of whether pore blocking or cake filtration occurs (Shang et al., 2015). As depicted in Fig. 3.8b, $UMFI_t$ was 2.3×10^{-3} m^2 L^{-1}, higher than 1.13×10^{-3} m^2 L^{-1} in the ceramic UF membrane found by Alresheedi et al. (2019b). Their fouling experiments used an approximately 31 mg/L alginate with 0.75 mM Ca, which was much lower than our test using 800 mg/L alginate with 3 mM Ca. This possibly led to the higher $UMFI_t$ found in our experiment. However, our observed $UMFI_c$ only accounted for 2.2% of $UMFI_t$, much lower than 20% and 30% found in 10 mM NaOH and 14 mM NaClO backwash, respectively, found in the study by Alresheedi et al. (2019b). The low $UMFI_c$ observed in our seven-cycle experiment indicates that the Fenton-like backwash effectively removed alginate fouling that was resistant to hydraulic, NaOH, and NaClO cleaning, even when treating such a concentrated alginate feedwater.

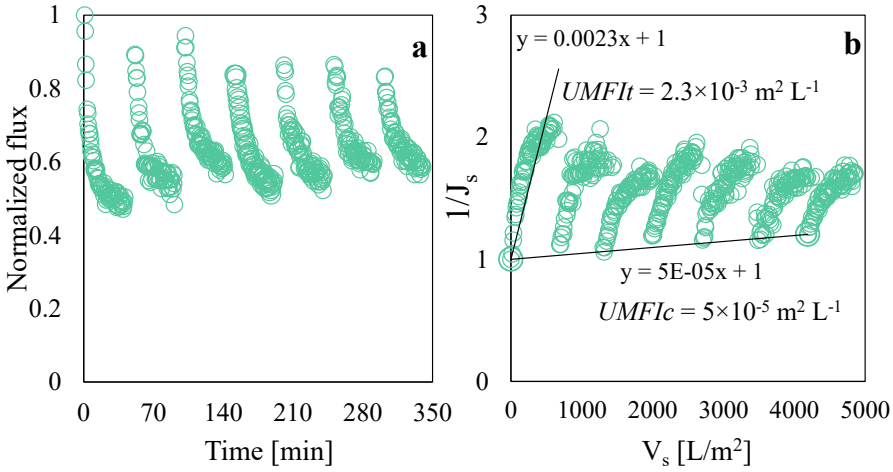

Figure 3.8. (a) Long-term fouling and cleaning experiment conducted by filtration of 800 mg/L alginate with 3 mM Ca and backwash with 30 mM H_2O_2 under 0.5 bar for seven cycles. (b) Assessment of total fouling index ($UMFI_t$) and chemically irreversible fouling index ($UMFI_c$) in the long-term running.

3.3.7. Radical quenching

The •OH radical scavenger of TBA was used to assess the role of •OH in the $CuFe_2O_4$-coated membranes with H_2O_2. TBA was first introduced in the H_2O_2 backwash solution to inhibit •OH activity and assess its impact on fouling removal by the $CuFe_2O_4$ membrane (Fig. 3.9a). Cleaning performance was evaluated through flux recovery, based on the pure water fluxes before and after fouling. It shows that the presence of TBA in H_2O_2 backwash reduced the flux recovery from 80% to 54%, which was only slightly higher than the pristine membrane with demineralized water backwash (45%). This suggests that •OH radicals play a key role in fouling removal during Fenton-like backwash by the $CuFe_2O_4$ membranes with H_2O_2.

The generation of •OH radicals was further confirmed using methylene blue as a model pollutant. As shown in Fig. 3.9b, 55% of methylene blue was degraded by the $CuFe_2O_4$ membrane with H_2O_2. In contrast, the degradation was considerably inhibited due to the presence TBA, confirming that •OH radicals were primarily responsible for the degradation process.

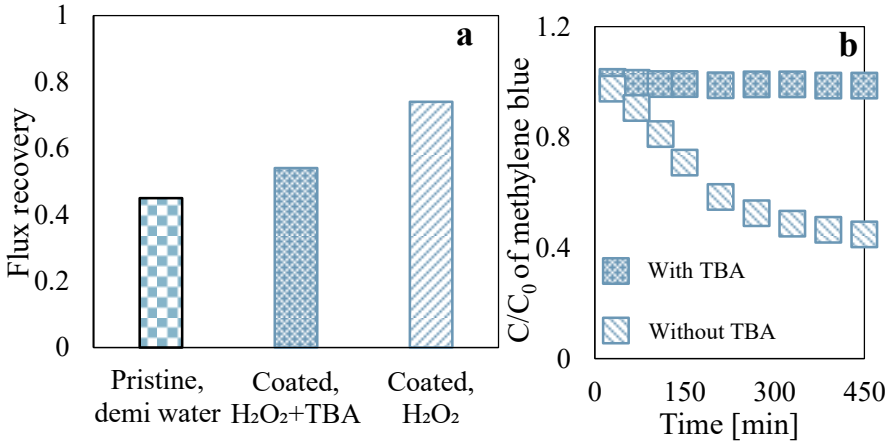

Figure 3.9. Radical quenching experiments. Flux recovery of (a) the pristine membrane backwashed with demineralized water, (b) the coated membrane backwashed with H_2O_2 and TBA, and (c) the coated membrane backwashed with H_2O_2 in treating alginate water. (c) C/C_0 of methylene blue conducted by the coated membranes with H_2O_2 or H_2O_2 and TBA.

3.3.8. Leaching of the catalytic membrane

NaClO and NaOH are widely used in the cleaning of the fouled membranes to restore flux (Alresheedi et al., 2019b). Hence, H_2O_2, NaClO, and NaOH were employed to examine the leaching of Cu and Fe. Besides, the performance of the newly coated membrane in alginate removal was compared to that of the aged catalytic membranes.

The $CuFe_2O_4$ membranes were examined by a prolonged leaching test, where the used membranes were immersed in 500 mL 30 mM H_2O_2 at a pH of 2.5, 0.1% NaClO, or 10 mM NaOH, for 8 h. The leaching rate of Cu eventually stabilized, reaching a final value of 0.08 mg/L per hour in the H_2O_2 test during the last hour (Fig. 3.10a and S3.12a). Previous studies show H_2O_2 alone has negligible effects on Cu and Fe leaching, but higher Cu leaching occurs with acids such as HCl (Boyanov et al., 2015; Fontecha-Cámara et al., 2016). Hence, the leaching of Cu in H_2O_2 was probably caused by HCl addition for pH adjustment. Negligible Cu and Fe leaching was found in NaClO and NaOH (Fig. 3.10a, Fig. S3.12b and S3.12c). The XRD test (Fig. S3.13) confirmed the coated membrane retained its spinel structure after aging in H_2O_2 for 96 h. A study has reported that a 2-h treatment with oxidizing agents can remove unstable catalysts from the modified ceramic UF membranes, resulting in low

leaching but maintaining high catalytic capacity (Xu et al., 2022). After 96-h aging, the catalytic membrane was tested in a single-cycle fouling and cleaning experiment. As shown in Fig. 3.10b, the aged membrane experienced a slightly higher flux drop but acquired a similar flux recovery (around 78%) compared to the newly coated membrane.

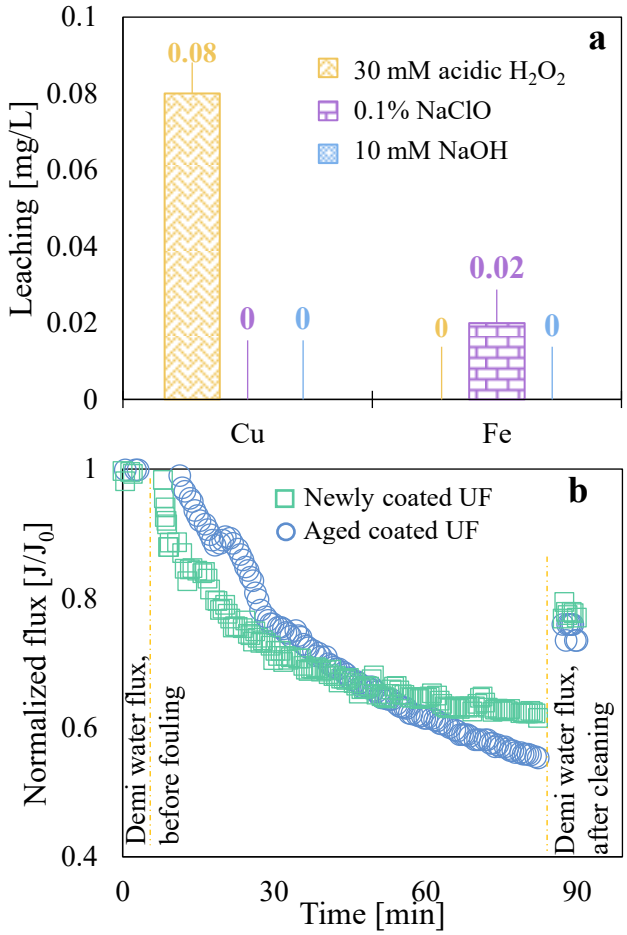

Figure 3.10. (a) Leaching of Cu and Fe ions per hour during last-hour leaching test. (b) Performance comparison of newly and aged (after immersion in 30 mM H_2O_2 solution at pH of 2.5 for 96 h) the catalytic membranes.

3.3.9. Comparison of Fenton-like cleaning during filtration and backwash

Direct injection of oxidant agents in feedwater is a broadly used method to mitigate the formation of fouling upon membranes (Zhao et al., 2020). Hence, 30 mM H_2O_2 was added to the alginate solution with an adjusted pH of 2.5 for the continuous oxidation of alginate during filtration process. The fouled catalytic membranes were then backwashed with demineralized water at 0.5 bar for 18 min, followed by a forward flush to remove the loosened alginate. We compared the cleaning performance and H_2O_2 consumption between two application methods: the H_2O_2-in-feed method and the H_2O_2 backwash method.

Fig. S3.14a shows that the flux of the H_2O_2-in-feed method faced a sharper flux drop in the early phase, followed by an increase that can be attributed to the continuous Fenton-like oxidation of alginate fouling during the filtration. However, the H_2O_2-in-feed method exhibited a lower flux recovery (71%) than the H_2O_2-backwash method (81%). The total organic carbon (TOC) tests showed that the H_2O_2-in-feed method had a lower TOC rejection (50%) than the H_2O_2-backwash method (79%) (Fig. S3.14b). This is because the continuous Fenton-like reactions break alginate into small fragments during filtration, which are more likely to pass through the membrane. Furthermore, the H_2O_2-in-feed method consumed more H_2O_2 (7.35 kg) than the H_2O_2-backwash method (0.05 kg) during a 24-h running (Fig. S3.14c).

Although Fenton-like cleaning has been integrated into filtration or into forward flush to mitigate membrane fouling, these methods often suffer from high chemical consumption, which considerably raises environmental concerns related to residual oxidants, and increases operational costs (e.g., the high chemical consumption). Besides, the low TOC rejection may lead to secondary contamination. In contrast, the integration of H_2O_2 into the backwash phase provides a more efficient use of oxidants while maintaining high pollutant rejection and effective backwash performance. Therefore, the application of H_2O_2 in backwash represents a more practical and cost-effective strategy for the long-term operation of catalytic UF systems in treating alginate fouling. However, for full-scale applications, the proposed Fenton-like backwash process requires further optimization. For example, a low-pressure Fenton-like backwash can be combined with a high-pressure hydraulic backwash to first degrade the fouling and then flush away the detached fouling. This combined approach may achieve effective fouling removal while further reducing chemical consumption. Besides, to evaluate the feasibility of this

proposed cleaning method, future work should also examine its performance in different types of wastewaters, which usually contain complex foulants that may influence the effectiveness of the Fenton-like backwash. Nevertheless, the evaluation and validation of such a hybrid cleaning strategy fall beyond the scope of the present study and should be addressed in future research.

3.4. Conclusion

To tackle fouling in ceramic UF membrane applications, we proposed a practical and efficient cleaning strategy by coupling Fenton-like reactions with backwash. This study reveals how backwash pressure, duration, and calcium concentration influence the efficacy of Fenton-like backwash in the $CuFe_2O_4$-coated membranes fouled by alginate. The long-term performance of the coupled systems and leaching of the $CuFe_2O_4$ membranes were also examined in this work. The main conclusions can be described as follows:

(1) Backwash with demineralized water on both pristine and coated ceramic UF membranes was ineffective for removing alginate-Ca fouling, with cleaning efficacy remaining low (1%–14%), even when the duration (6–36 min) and pressure (0.3–1 bar) were increased.
(2) The backwash efficacy was considerably enhanced in the presence of Fenton-like reactions, achieving 71% cleaning efficacy at a backwash pressure of 0.3 bar.
(3) The improved Fenton-like cleaning was dominated by reducing backwash pressure, rather than extending backwash duration. This improvement was attributed to the increased residence time of H_2O_2, facilitating the radical formation.
(4) Ca ions altered the fouling structure and impacted cleaning performance. At high concentrations, the rigid, and compacted alginate-Ca clusters restricted the backwash to loosen the fouling, limiting H_2O_2 and radical transport. Moreover, the broken alginate chains were captured and bound with the excess Ca ions released from the internal clusters, hindering fouling detachment.
(5) Fenton-like backwash effectively cleaned the catalytic membranes which was fouled by a concentrated alginate solution (800 mg/L), restoring 83%–94% of the initial flux over seven cycles.
(6) Cu leaching in 30 mM H_2O_2 gradually ceased to 0.08 mg/L. Negligible leaching of Cu and Fe ions occurred in 0.1% NaClO and 10 mM NaOH. Flux recovery of the aged, coated membranes backwashed with H_2O_2 was comparable to that of the newly coated membranes.

Reference

Akamatsu, K., Kagami, Y., Nakao, S., 2020. Effect of BSA and sodium alginate adsorption on decline of filtrate flux through polyethylene microfiltration membranes. J. Membr. Sci. 594, 117469. https://doi.org/10.1016/j.memsci.2019.117469

Al-Hammadi, H., Al-Bastaki, N., 2007. Experimental study of the dead-end ultrafiltration process using silicone dioxide suspensions. Desalination 206, 513–523. https://doi.org/10.1016/j.desal.2006.05.019

Alresheedi, M.T., Barbeau, B., Basu, O.D., 2019a. Comparisons of NOM fouling and cleaning of ceramic and polymeric membranes during water treatment. Sep. Purif. Technol. 209, 452–460. https://doi.org/10.1016/j.seppur.2018.07.070

Alresheedi, M.T., Basu, O.D., Barbeau, B., 2019b. Chemical cleaning of ceramic ultrafiltration membranes – Ozone versus conventional cleaning chemicals. Chemosphere 226, 668–677. https://doi.org/10.1016/j.chemosphere.2019.03.188

Ang, W.S., Lee, S., Elimelech, M., 2006. Chemical and physical aspects of cleaning of organic-fouled reverse osmosis membranes. J. Membr. Sci. 272, 198–210. https://doi.org/10.1016/j.memsci.2005.07.035

Angelis, L.D., Cortalezzi, M.M.F.D., 2016. Improved membrane flux recovery by Fenton-type reactions. J. Membr. Sci. 500, 255–264. https://doi.org/10.1016/j.memsci.2015.11.042

Boyanov, B.S., Peltekov, A.B., Ivanov, K.I., 2015. Ferrites of the MeFe2O4 system (Me – Zn, Cu, Cd) and their two faces. Int. J. Chem. Mol. Eng. 9, 765–771. https://doi.org/10.5281/zenodo.1109521

Chang, H., Liu, B., Liang, H., Yu, H., Shao, S., Li, G., 2017. Effect of filtration mode and backwash water on hydraulically irreversible fouling of ultrafiltration membrane. Chemosphere 179, 254–264. https://doi.org/10.1016/j.chemosphere.2017.03.122

Chen, D., Columbia, M., 2011. Enzymatic control of alginate fouling of dead-end MF and UF ceramic membranes. J. Membr. Sci. 381, 118–125. https://doi.org/10.1016/j.memsci.2011.07.033

Chen, M., Heijman, S.G.J., Luiten-Olieman, M.W.J., Rietveld, L.C., 2022. Oil-in-water emulsion separation: fouling of alumina membranes with and without a silicon carbide deposition in constant flux filtration mode. Water Res. 216, 118267. https://doi.org/10.1016/j.watres.2022.118267

Ding, J., Xiao, H., Huang, X., Zou, Y., Ye, Z., Wang, S., Xie, P., Chen, Y., Ma, J., 2023. Application of heat-activated peroxydisulfate process for the chemical cleaning of fouled ultrafiltration membranes. Chin. Chem. Lett. 34, 108316. https://doi.org/10.1016/j.cclet.2023.108316

Feng, J., Zhang, Y., 2023. Ascorbic acid enhanced CuFe2O4-catalyzed heterogeneous photo-Fenton-like degradation of phenol. J. Environ. Chem. Eng. 11, 111009. https://doi.org/10.1016/j.jece.2023.111009

Ferrer, O., Lefèvre, B., Prats, G., Bernat, X., Gibert, O., Paraira, M., 2016. Reversibility of fouling on ultrafiltration membrane by backwashing and chemical cleaning: differences in organic fractions behaviour. Desalin. Water Treat. 57, 8593–8607. https://doi.org/10.1080/19443994.2015.1022807

Fontecha-Cámara, M.A., Moreno-Castilla, C., López-Ramón, M.V., Álvarez, M.A., 2016. Mixed iron oxides as Fenton catalysts for gallic acid removal from aqueous solutions. Appl. Catal. B Environ. 196, 207–215. https://doi.org/10.1016/j.apcatb.2016.05.032

Gray, S.R., Dow, N., Orbell, J.D., Tran, T., Bolto, B.A., 2011. The significance of interactions between organic compounds on low pressure membrane fouling. Water Sci. Technol. 64, 632–639. https://doi.org/10.2166/wst.2011.488

Hashino, M., Hirami, K., Katagiri, T., Kubota, N., Ohmukai, Y., Ishigami, T., Maruyama, T., Matsuyama, H., 2011. Effects of three natural organic matter types on cellulose acetate butyrate microfiltration membrane fouling. J. Membr. Sci. 379, 233–238. https://doi.org/10.1016/j.memsci.2011.05.068

Hong, S., Krishna, P., Hobbs, C., Kim, D., Cho, J., 2005. Variations in backwash efficiency during colloidal filtration of hollow-fiber microfiltration membranes. Desalination 173, 257–268. https://doi.org/10.1016/j.desal.2004.07.049

Huang, B., Gu, H., Xiao, K., Qu, F., Yu, H., Wei, C., 2020. Fouling mechanisms analysis via combined fouling models for surface water ultrafiltration process. Membranes 10, 149. https://doi.org/10.3390/membranes10070149

Huang, H., Young, T., Jacangelo, J.G., 2009. Novel approach for the analysis of bench-scale, low pressure membrane fouling in water treatment. J. Membr. Sci. 334, 1–8. https://doi.org/10.1016/j.memsci.2009.01.049

Huang, J., Liu, L., Zeng, G., Li, Xue, Peng, L., Li, F., Jiang, Y., Zhao, Y., Huang, X., 2014. Influence of feed concentration and transmembrane pressure on membrane fouling and effect of hydraulic flushing on the performance of ultrafiltration. Desalination 335, 1–8. https://doi.org/10.1016/j.desal.2013.11.038

Huang, J.J., Chen, S., Liao, Y., Chen, Y., You, X., Wang, R., 2021. Performance, fouling and cleaning of a thin film composite hollow fiber membrane during fertiliser-drawn forward osmosis process for micro-polluted water. Environ. Sci.: Water Res.Technol. 7, 1279–1291. https://doi.org/10.1039/D0EW00996B

Jafari, M., Vanoppen, M., van Agtmaal, J.M.C., Cornelissen, E.R., Vrouwenvelder, J.S., Verliefde, A., van Loosdrecht, M.C.M., Picioreanu, C., 2021. Cost of fouling in full-scale reverse osmosis and nanofiltration installations in the Netherlands. Desalination 500, 114865. https://doi.org/10.1016/j.desal.2020.114865

Jermann, D., Pronk, W., Meylan, S., Boller, M., 2007. Interplay of different NOM fouling mechanisms during ultrafiltration for drinking water production. Water Res. 41, 1713–1722. https://doi.org/10.1016/j.watres.2006.12.030

Jiang, S.-F., Wang, L., Hu, W.-F., Tian, K., Jiang, H., 2021. Preparation of flower-like CuFe2O4 by a self-templating method for high-efficient activation of peroxymonosulfate to degrade carbamazepine. Ind. Eng. Chem. Res. 60, 11045–11055. https://doi.org/10.1021/acs.iecr.1c02254

Katsoufidou, K., Yiantsios, S.G., Karabelas, A.J., 2008. An experimental study of UF membrane fouling by humic acid and sodium alginate solutions: the effect of backwashing on flux recovery. Desalination 220, 214–227. https://doi.org/10.1016/j.desal.2007.02.038

Katsoufidou, K., Yiantsios, S.G., Karabelas, A.J., 2007. Experimental study of ultrafiltration membrane fouling by sodium alginate and flux recovery by backwashing. J. Membr. Sci. 300, 137–146. https://doi.org/10.1016/j.memsci.2007.05.017

Kennedy, M., Kim, S.-M., Mutenyo, I., Broens, L., Schippers, J., 1998. Intermittent crossflushing of hollow fiber ultrafiltration systems. Desalination 118, 175–187. https://doi.org/10.1016/S0011-9164(98)00121-0

Kim, H., Shim, I., Zhan, M., 2021. Chemical enhanced backwashing for controlling organic fouling in drinking water treatment using a novel hollow-fiber polyacrylonitrile nanofiltration membrane. Appl. Sci. 11, 6764. https://doi.org/10.3390/app11156764

Kramer, F.C., Shang, R., Rietveld, L.C., Heijman, S.J.G., 2020. Fouling control in ceramic nanofiltration membranes during municipal sewage treatment. Sep. Purif. Technol. 237, 116373. https://doi.org/10.1016/j.seppur.2019.116373

Lee, Hyunsu, Im, S.-J., Lee, Hyeonho, Kim, C.-M., Jang, A., 2021. Comparative analysis of salt cleaning and osmotic backwash on calcium-bridged organic fouling in nanofiltration process. Desalination 507, 115022. https://doi.org/10.1016/j.desal.2021.115022

Li, Q., Elimelech, M., 2004. Organic fouling and chemical cleaning of nanofiltration membranes: measurements and mechanisms. Environ. Sci. Technol. 38, 4683–4693. https://doi.org/10.1021/es0354162

Lin, B., Heijman, S.G.J., Shang, R., Rietveld, L.C., 2021. Integration of oxalic acid chelation and Fenton process for synergistic relaxation-oxidation of persistent gel-like fouling of ceramic nanofiltration membranes. J. Membr. Sci. 636, 119553. https://doi.org/10.1016/j.memsci.2021.119553

Meshram, P., Dave, R., Joshi, H., Dharani, G., Kirubagaran, R., Venugopalan, V.P., 2016. A fence that eats the weed: alginate lyase immobilization on ultrafiltration membrane for fouling mitigation and flux recovery. Chemosphere 165, 144–151. https://doi.org/10.1016/j.chemosphere.2016.09.017

Nakatsuka, S., Nakate, I., Miyano, T., 1996. Drinking water treatment by using ultrafiltration hollow fiber membranes. Desalination 106, 55–61. https://doi.org/10.1016/S0011-9164(96)00092-6

Nguyen, A.H., Tobiason, J.E., Howe, K.J., 2011. Fouling indices for low pressure hollow fiber membrane performance assessment. Water Res. 45, 2627–2637. https://doi.org/10.1016/j.watres.2011.02.020

Pervov, A.G., Andrianov, A.P., Efremov, R.V., Desyatov, A.V., Baranov, A.E., 2003. A new solution for the Caspian Sea desalination: low-pressure membranes. Desalination 157, 377–384. https://doi.org/10.1016/S0011-9164(03)00420-X

Qu, F., Liang, H., Zhou, J., Nan, J., Shao, S., Zhang, J., Li, G., 2014. Ultrafiltration membrane fouling caused by extracellular organic matter (EOM) from *Microcystis aeruginosa*: Effects of membrane pore size and surface hydrophobicity. J. Membr. Sci. 449, 58–66. https://doi.org/10.1016/j.memsci.2013.07.070

Remize, P.J., Guigui, C., Cabassud, C., 2010. Evaluation of backwash efficiency, definition of remaining fouling and characterisation of its contribution in irreversible fouling: cyer deposition for tight ceramic nanofiltration

membranes: sdraulically irreversible fouling on ceramic MF/UF membranes: comparison of foynthesis and applicaase of drinking water production by air-assisted ultra-filtration. J. Membr. Sci. 355, 104–111. https://doi.org/10.1016/j.memsci.2010.03.005

Resosudarmo, A., Ye, Y., Le-Clech, P., Chen, V., 2013. Analysis of UF membrane fouling mechanisms caused by organic interactions in seawater. Water Res. 47, 911–921. https://doi.org/10.1016/j.watres.2012.11.024

Shang, R., Vuong, F., Hu, J., Li, S., Kemperman, A.J.B., Nijmeijer, K., Cornelissen, E.R., Heijman, S.G.J., Rietveld, L.C., 2015. Hydraulically irreversible fouling on ceramic MF/UF membranes: comparison of fouling indices, foulant composition and irreversible pore narrowing. Sep. Purif. Technol. 147, 303–310. https://doi.org/10.1016/j.seppur.2015.04.039

van den Brink, P., Zwijnenburg, A., Smith, G., Temmink, H., van Loosdrecht, M., 2009. Effect of free calcium concentration and ionic strength on alginate fouling in cross-flow membrane filtration. J. Membr. Sci. 345, 207–216. https://doi.org/10.1016/j.memsci.2009.08.046

Vroman, T., Beaume, F., Armanges, V., Gout, E., Remigy, J.-C., 2021. Critical backwash flux for high backwash efficiency: case of ultrafiltration of bentonite suspensions. J. Membr. Sci. 620, 118836. https://doi.org/10.1016/j.memsci.2020.118836

Wang, T., Wang, Z., Wang, P., Tang, Y., 2019. An integration of photo-Fenton and membrane process for water treatment by a PVDF@CuFe2O4 catalytic membrane. J. Membr. Sci. 572, 419–427. https://doi.org/10.1016/j.memsci.2018.11.031

Wu, J., Contreras, A.E., Li, Q., 2014. Studying the impact of RO membrane surface functional groups on alginate fouling in seawater desalination. J. Membr. Sci. 458, 120–127. https://doi.org/10.1016/j.memsci.2014.01.056

Xia, S., Li, X., Yao, Ji, Dong, B., Yao, Juanjuan, 2008. Application of membrane techniques to produce drinking water in China. Desalination 222, 497–501. https://doi.org/10.1016/j.desal.2007.01.142

Xin, Y., Bligh, M.W., Kinsela, A.S., Waite, T.D., 2016. Effect of iron on membrane fouling by alginate in the absence and presence of calcium. J. Membr. Sci. 497, 289–299. https://doi.org/10.1016/j.memsci.2015.09.023

Xu, D., Zheng, J., Zhang, X., Lin, D., Gao, Q., Luo, X., Zhu, X., Li, G., Liang, H., Van der Bruggen, B., 2022. Mechanistic insights of a thermoresponsive interface for fouling control of thin-Film composite nanofiltration membranes. Environ. Sci. Technol. 56, 1927–1937. https://doi.org/10.1021/acs.est.1c06156

Xu, H., Cheng, W., Chen, Z., Zhai, X., Ma, J., Zhang, T., 2022. Selective oxidation of water pollutants by surface-complexed peroxymonosulfate during filtration with highly dispersed Co(II)-doped ceramic membrane. Chem. Eng. J. 448, 137686. https://doi.org/10.1016/j.cej.2022.137686

Xu, P., Wei, R., Wang, P., Li, X., Yang, C., Shen, T., Zheng, T., Zhang, G., 2023. CuFe2O4/diatomite actuates peroxymonosulfate activation process: mechanism for active species transformation and pesticide degradation. Water Res. 235, 119843. https://doi.org/10.1016/j.watres.2023.119843

Ye, Y., Clech, P.L., Chen, V., Fane, A.G., 2005. Evolution of fouling during crossflow filtration of model EPS solutions. J. Membr. Sci. 264, 190–199. https://doi.org/10.1016/j.memsci.2005.04.040

You, X., Teng, J., Chen, Y., Long, Y., Yu, G., Shen, L., Lin, H., 2020. New insights into membrane fouling by alginate: impacts of ionic strength in presence of calcium ions. Chemosphere 246, 125801. https://doi.org/10.1016/j.chemosphere.2019.125801

Zhang, M., Lin, H., Shen, L., Liao, B.-Q., Wu, X., Li, R., 2017. Effect of calcium ions on fouling properties of alginate solution and its mechanisms. J. Membr. Sci. 525, 320–329. https://doi.org/10.1016/j.memsci.2016.12.006

Zhang, S., Liang, Y., Yang, C., Venema, P., Rietveld, L.C., Heijman, S.G.J., 2024. Concentration polarizations of PEG and silica colloids in ceramic nanofiltration. Desalination 583, 117722. https://doi.org/10.1016/j.desal.2024.117722

Zhao, Y., Lu, D., Xu, C., Zhong, J., Chen, M., Xu, S., Cao, Y., Zhao, Q., Yang, M., Ma, J., 2020. Synergistic oxidation - filtration process analysis of catalytic CuFe2O4 - tailored ceramic membrane filtration via peroxymonosulfate activation for humic acid treatment. Water Res. 171, 115387. https://doi.org/10.1016/j.watres.2019.115387

Zhao, Yumeng, Zhao, Yanxin, Yu, X., Kong, D., Fan, X., Wang, R., Luo, S., Lu, D., Nan, J., Ma, J., 2022. Peracetic acid integrated catalytic ceramic membrane filtration for enhanced membrane fouling control: performance evaluation and mechanism analysis. Water Res. 220, 118710. https://doi.org/10.1016/j.watres.2022.118710

Zsirai, T., Al-Jaml, A.K., Qiblawey, H., Al-Marri, M., Ahmed, A., Bach, S., Watson, S., Judd, S., 2016. Ceramic membrane filtration of produced water: impact of membrane module. Sep. Purif. Technol. 165, 214–221. https://doi.org/10.1016/j.seppur.2016.04.001

Zsirai, T., Buzatu, P., Aerts, P., Judd, S., 2012. Efficacy of relaxation, backflushing, chemical cleaning and clogging removal for an immersed hollow fibre membrane bioreactor. Water Res. 46, 4499–4507. https://doi.org/10.1016/j.watres.2012.05.004

Support information

Text S3.1. Preparation of sodium alginate solution

The feed solution for fouling was prepared by sodium alginate as a model polysaccharide pollutant. 50 ppm sodium alginate solution was continuously stirred for one night. The high concentration of sodium alginate was employed to generate pronounced fouling, thereby examining the cleaning efficacy of coated membranes in mitigating severe fouling (Kramer et al., 2020). Background salts of 1 mM sodium chloride (NaCl, from Sigma-Aldrich), and calcium chloride dihydrate ($CaCl_2 \cdot 2H_2O$, from Sigma-Aldrich) were injected into sodium alginate solution. Considering the alginate would generate a strong bridging between the carboxylic groups of the alginate and divalent ion of Ca^{2+}, this phenomenon was also studied by mixing the fouling solution with different calcium concentrations (1, 3, 5 mM) to have a better understanding of the cleaning efficacy by H_2O_2 backwash. 1 mM sodium bicarbonate ($NaHCO_3$) was added to the alginate solution as the buffer to maintain the pH at 7. The pH of targeted solutions was adjusted by 1 mM NaOH and HCl.

Text S3.2. Permeability adjustments based on an earlier study (Shang et al., 2017).

$$L_{20\,℃} = \frac{J\ 9\ e^{-0.0239\,(T-20)}}{\Delta P} \qquad \text{S3.1}$$

where $L_{20\,℃}$ is the permeability after temperature calibration at 20 ℃ ($L/(m^2 \cdot h \cdot bar)$), J is membrane flux ($L/(m^2 \cdot h)$), T is the temperature (℃), and ΔP is the transmembrane pressure (bar).

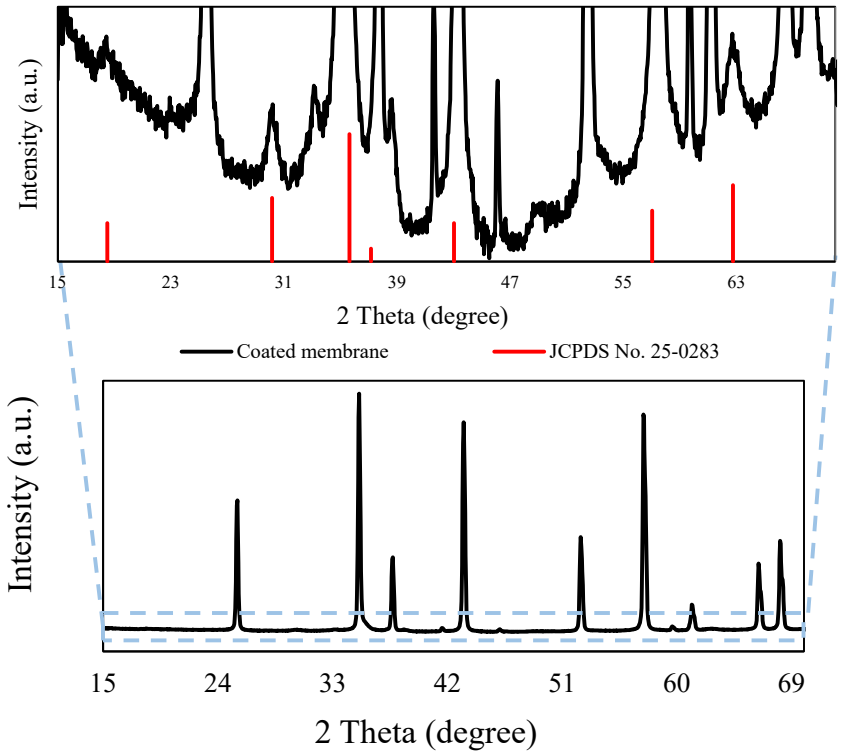

Figure S3.1. The XRD patterns of the coated membrane with its magnified insert and $CuFe_2O_4$ diffraction peaks (JCPDS, No. 25-0283).

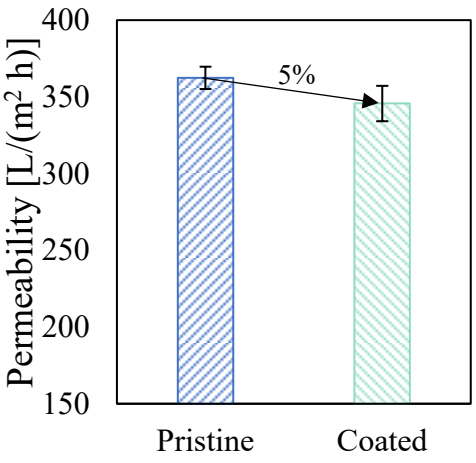

Figure S3.2. Permeability of the membrane before and after coating.

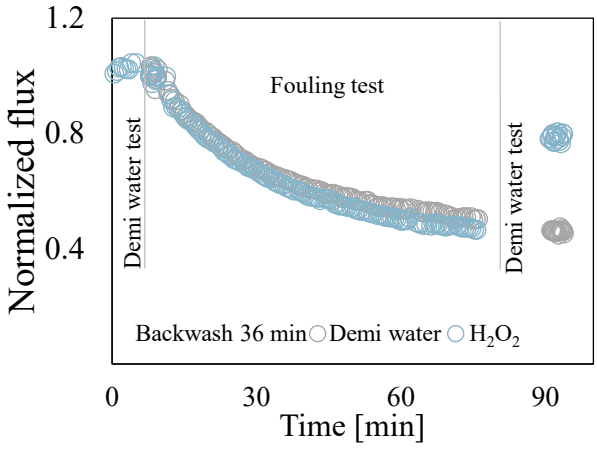

Figure S3.3. Demi water flux of coated membranes measured before fouling and after cleaning. 50 mg/L alginate was employed for 45 min fouling test, then the membrane was cleaned by backwash with demi water or H_2O_2 at 0.5 bar for 36 min, and 1 min forward flush.

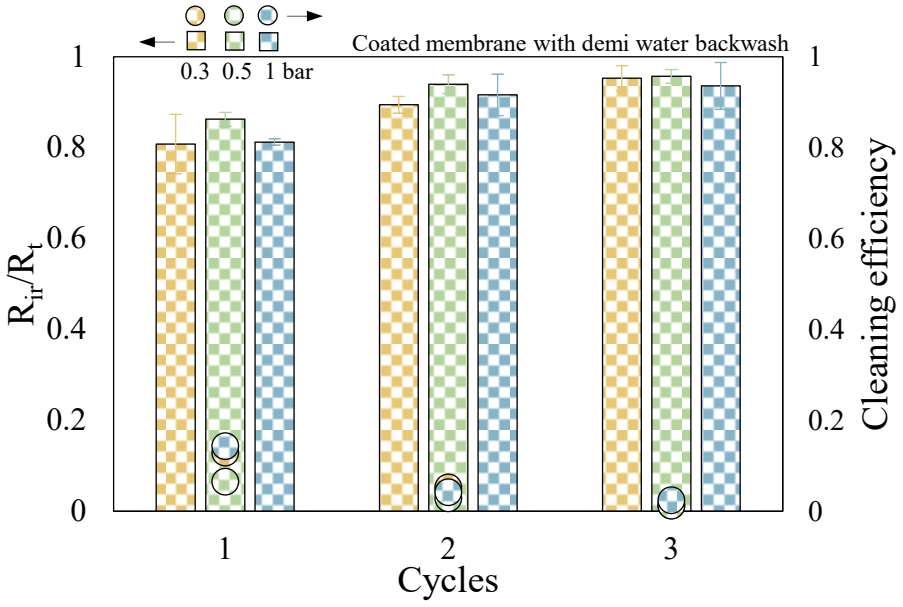

Figure S3.4. Irreversible resistance fouling ratio and cleaning efficacy of the coated membrane. 50 mg/L alginate was employed for 45 min fouling test, then the membrane was cleaned by backwash with demi water at 0.3, 0.5, 1 bar for 18 min, and 1 min forward flush.

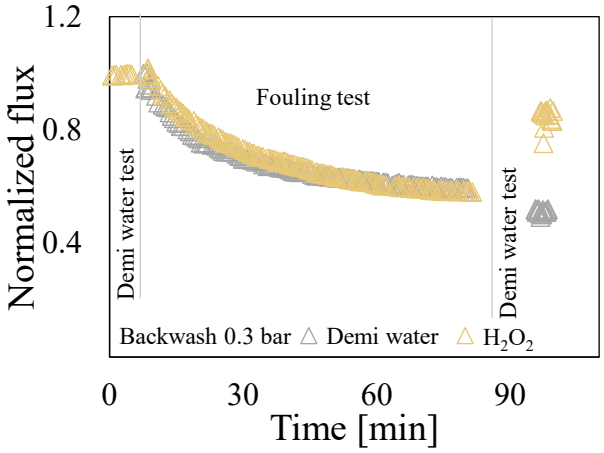

Figure S3.5. Demi water flux of coated membranes measured before fouling and after cleaning. 50 mg/L alginate was employed for 45 min fouling test, then the membrane was cleaned by the backwash with demi water or H_2O_2 at 0.3 bar for 18 min, and 1 min forward flush.

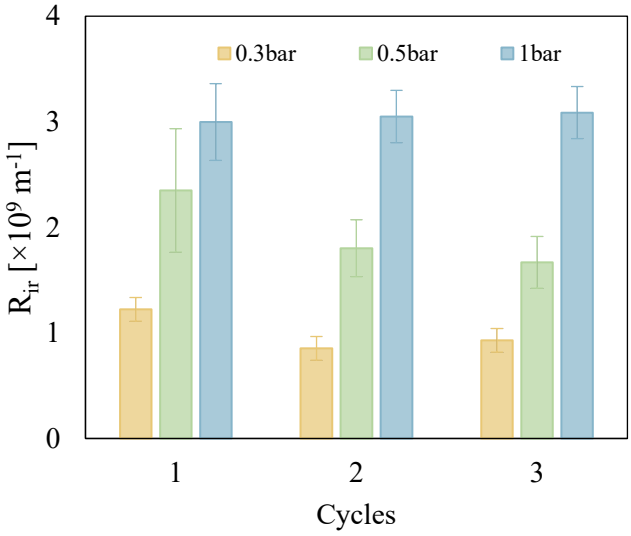

Figure S3.6. Irreversible fouling resistance of coated membrane performed with H_2O_2 backwash pressures of 0.3, 0.5, and 1 bar.

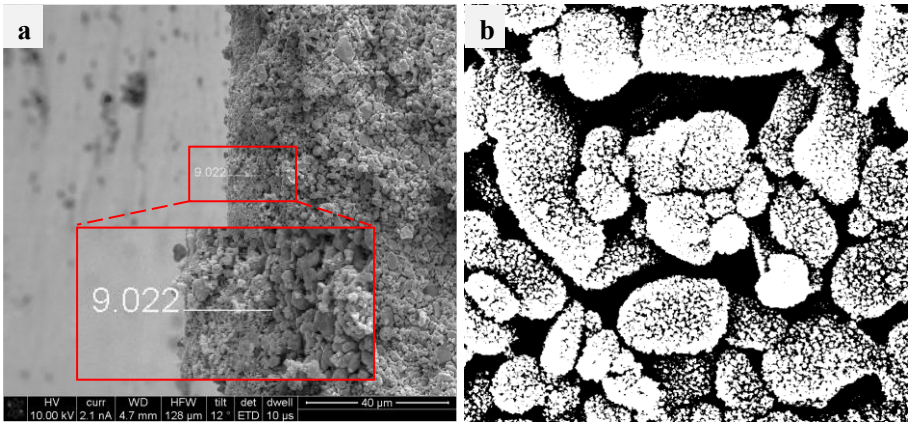

Figure S3.7. (a) Cross-section SEM view of the coated membrane with 9.022 µm measured thickness of the selective layer and (b) 39.5% porosity was determined by ImageJ analysis of top SEM view of the coated membrane.

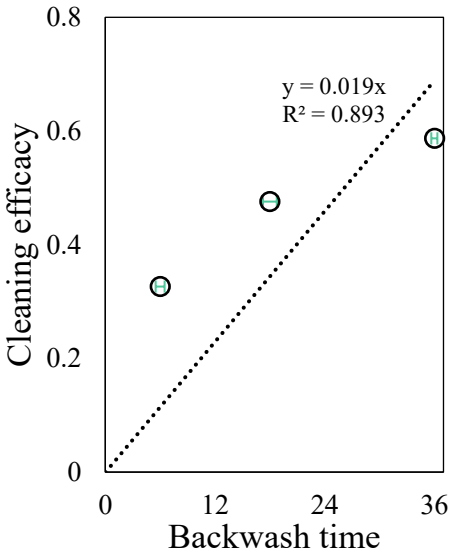

Figure S3.8. Relationship between total backwash time and cleaning efficacy based on the experiments of the coated membrane backwashed with 6, 18, and 36 minutes.

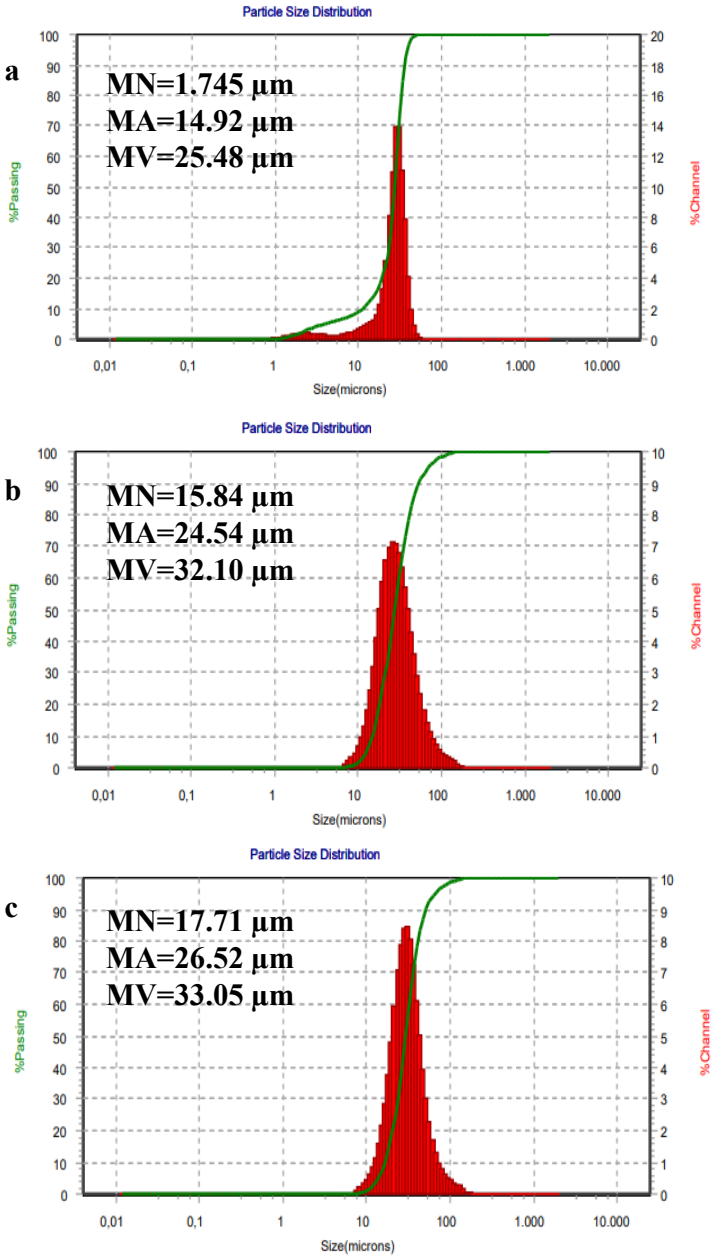

Figure S3.9. Size distributions of newly prepared alginate solutions with 1 (a), 3 (b), and 5 (c) mM calcium ions.

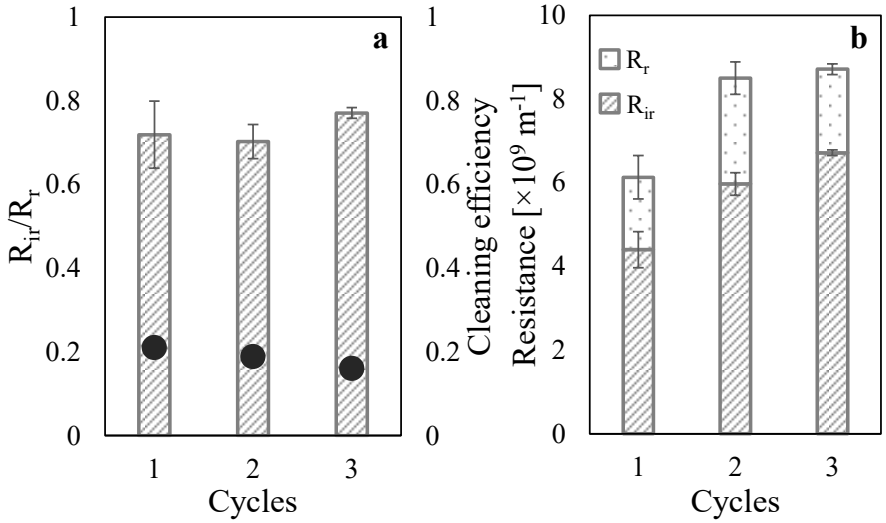

Figure S3.10. (a) The ratio of irreversible resistance, cleaning efficacy, and (b) fouling resistance of the coated membrane. The fouling was carried out by 50 mg/L alginate with 9 mM calcium, and the backwash was performed by 30 mM H_2O_2 at 0.3 bar for 18 min.

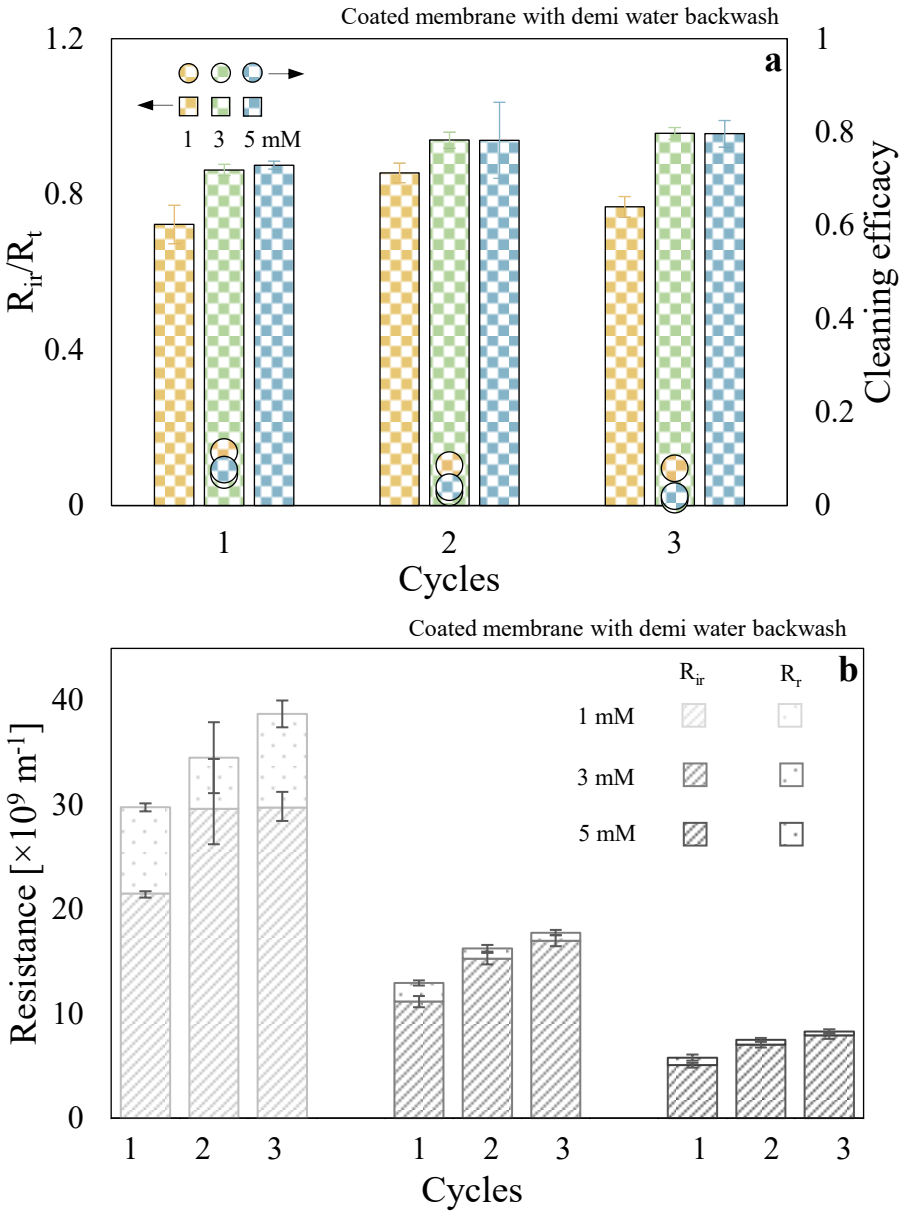

Figure S3.11. (a) R_{ir} ratio, (b) R_{ir}, and cleaning efficacy of the coated membrane fouled by 50 mg/L alginate with 1, 3, or 5 mM Ca when using demi water for the backwash under 0.3 bar for 18 min.

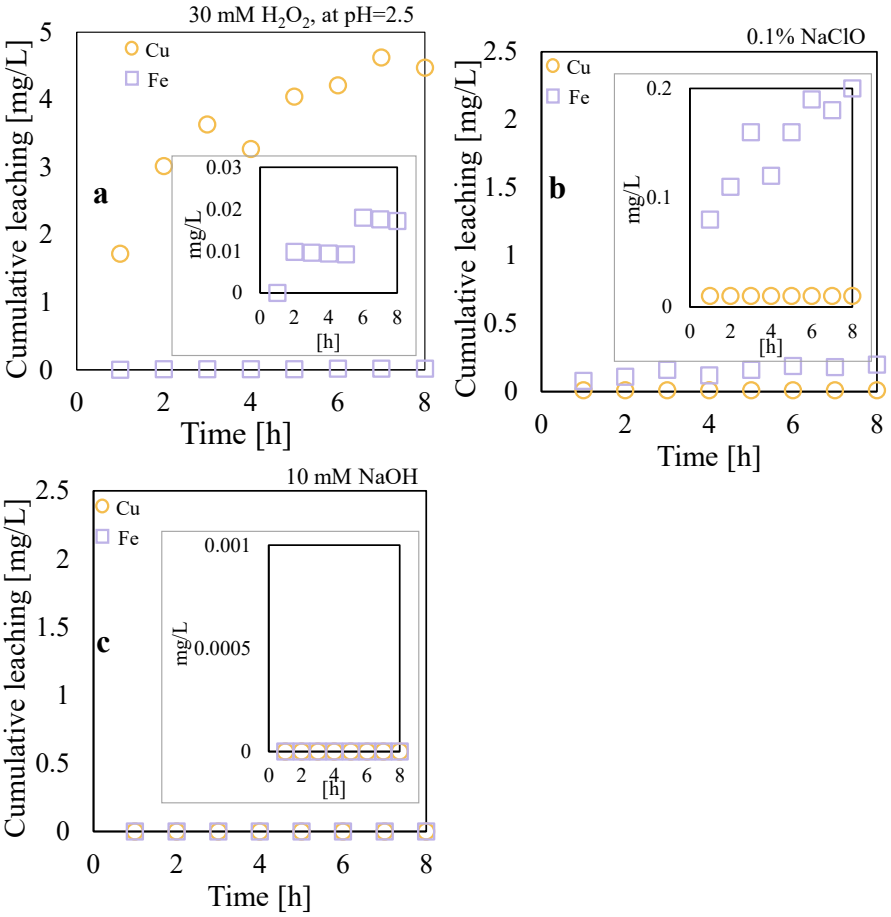

Figure S3.12. Leaching from the used $CuFe_2O_4$-membrane was tested by immersing such membrane in 500 mL cleaning agent solution of (a) 30 mM H_2O_2 at pH = 2.5 (adjusted by HCl), (b) 0.1% NaOCl, and (c) 10 mM NaOH for 8 hours. The insets in (a), (b), and (c) were the magnification of leaching results.

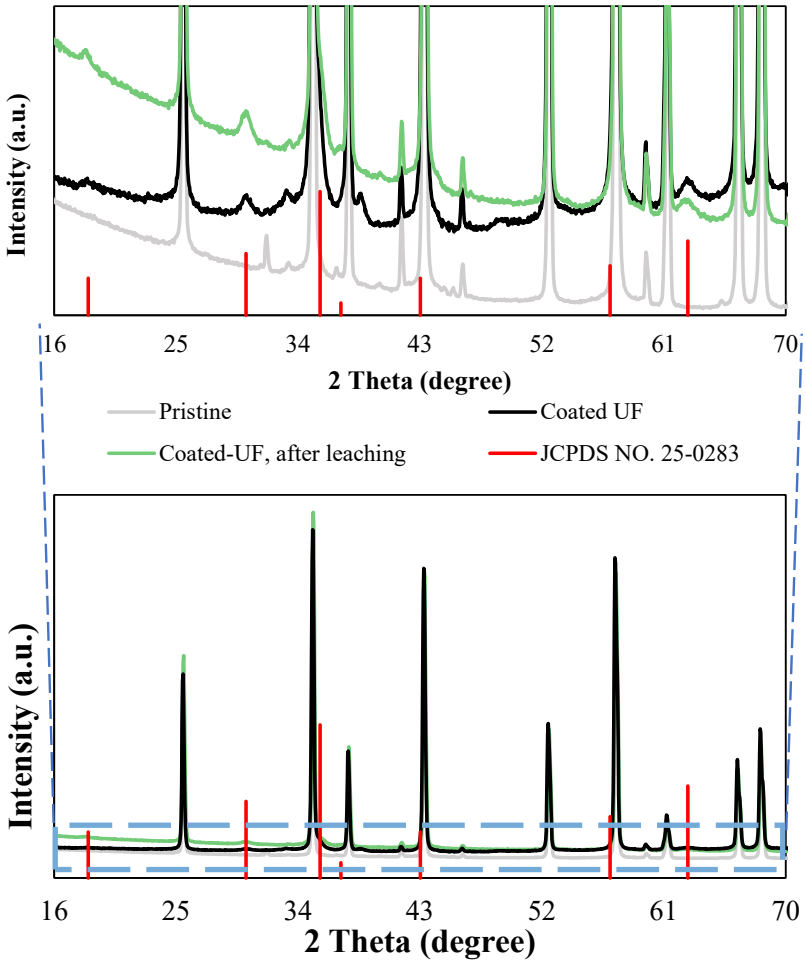

Figure S3.13. XRD patterns of the pristine membrane, and coating membranes (new and aged). The aged, coated membrane represents the newly coated CM after 96 h aging in H_2O_2. JCPDS, No. 25-0283, is the $CuFe_2O_4$ diffraction peaks.

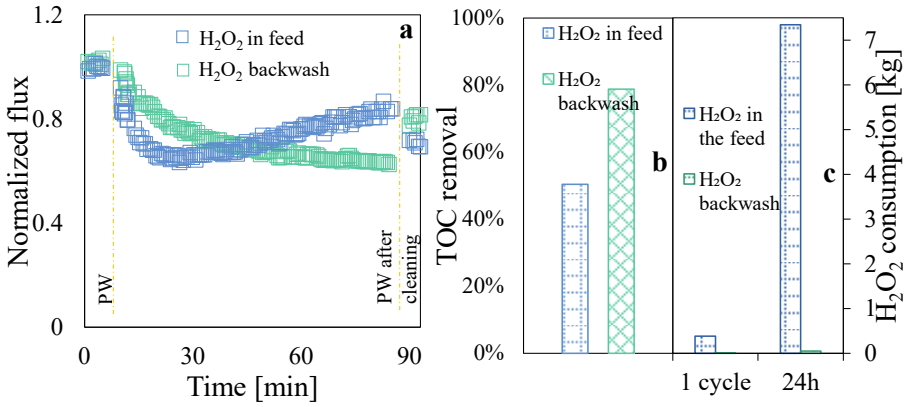

Figure S3.14. Comparison of alginate fouling removal by dosing 30 mM H_2O_2 at pH of 2.5 in the filtration and backwash. (a) Normalized flux, (b) TOC removal, and (c) H_2O_2 consumption. In the H_2O_2-in-feed method, 30 mM H_2O_2 was added to the prepared 50 mg/L alginate with 3 mM Ca. After filtration, 18 min water backwash at 0.5 bar was performed, followed by a water forward flush for 1 min. In H_2O_2 backwash method, alginate solution was filtered over catalytic membranes. Then, 18 min H_2O_2 (30 Mm, at pH=2.5) backwash at 0.5 bar was performed, followed by a water forward flush for 1 min. Before filtration and after cleaning, fluxes were measured by demineralized water to determine the flux recovery.

Reference

Aditya, T., Jana, J., Pal, A., Pal, T., 2018. One-pot fabrication of perforated graphitic carbon nitride nanosheets decorated with copper oxide by controlled ammonia and sulfur trioxide release for enhanced catalytic activity. ACS Omega 3, 9318–9332. https://doi.org/10.1021/acsomega.8b00968

Boyanov, B.S., Peltekov, A.B., Ivanov, K.I., 2015. Ferrites of the MeFe2O4 system (Me – Zn, Cu, Cd) and their two faces. Int. J. Chem. Mol. Eng. 9, 765–771. https://doi.org/10.5281/zenodo.1109521

Kramer, F.C., Shang, R., Rietveld, L.C., Heijman, S.J.G., 2020. Fouling control in ceramic nanofiltration membranes during municipal sewage treatment. Sep. Purif. Technol. 237, 116373. https://doi.org/10.1016/j.seppur.2019.116373

Shang, R., Goulas, A., Tang, C.Y., de Frias Serra, X., Rietveld, L.C., Heijman, S.G.J., 2017. Atmospheric pressure atomic layer deposition for tight ceramic nanofiltration membranes: synthesis and application in water purification. J. Membr. Sci. 528, 163–170. https://doi.org/10.1016/j.memsci.2017.01.023

贺新凉

向晚青石埠。怪长风、眉间吹冷，乱了欧鹭。醉里茶马轻又去，错把留园花误。一点雨、流红飞度。何处惹来尘与土，向人间种取菩提树。梦不复，酒还苦。

至今慢慢三年路。总虚空、皆因自我，也成街鼠。岁长方知柴米事，且任云烟轻吐。是有种、王侯将主。莫道牛犊不怕虎，狗若刀俎你则鸡兔。闲碎语，满天溯。

2021.02.22

Chapter 4

Ceramic ultrafiltration membrane with low palladium loading via atomic layer deposition for enhanced micropollutant degradation

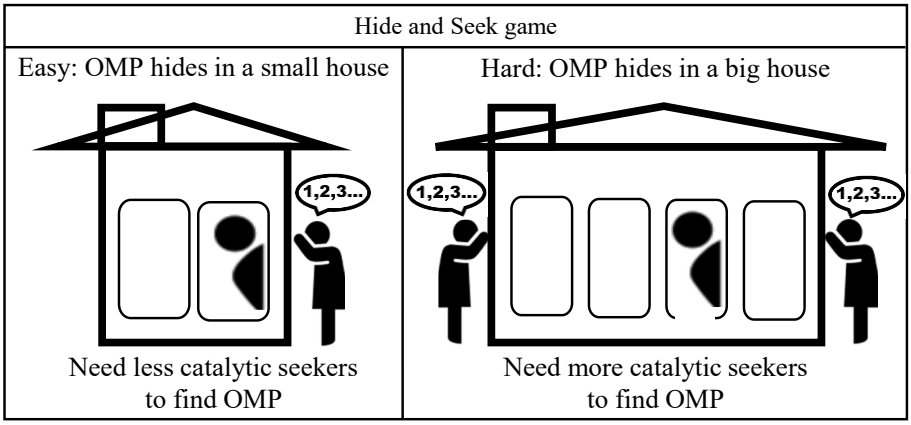

This chapter is based on

Zhang, S., Li, M., Tian, H., Van Ommen, J. R., Rietveld, L. C., & Heijman, S. G. (2025). Ceramic ultrafiltration membrane with low palladium loading via atomic layer deposition for enhanced micropollutant degradation. *To be submitted for publication*.

Abstract

Catalytic ceramic membranes are regarded as a promising technology for enhanced removal of organic micropollutants (OMPs). However, the excessive catalyst loading will increase the resistance of the membrane and the deposition costs, thus hindering their practical application. In this work, ceramic ultrafiltration membranes were modified by atomic layer deposition to achieve a low loading of palladium (Pd) for efficient OMP degradation. The Pd deposited on the membrane surface and within the pores activated peroxymonosulfate (PMS) to induce reactive species (RS) for the degradation of four OMPs (benzotriazole, diclofenac, sotalol, and trimethoprim). The Pd-modified membrane exhibited an almost complete degradation of the four OMPs at a flux below 100 L/(m^2·h). The presence of Pd deposition in the pores increased degradation kinetics by three orders of magnitude, which was attributed to the abundant catalytic sites and the improved mass transfer of RS and OMPs in the membrane pores. Varying RS can be generated from PMS activation by Pd-modified alumina membranes, but the dominant RS for degradation depended on the type of OMP. A high degradation efficacy was achieved at a pH of 7, while the PMS dosage (20-80 µM), anion (1 mM Cl^-, SO_4^{2-}, HCO_3^-, or ClO^-), and natural substances in river water had a minor impact on the OMPs' degradation. However, a high salinity, e.g., as present in brine water, exhibited a negative impact on the degradation of certain OMPs. This study demonstrates that a robust and effective strategy for OMPs' degradation can be achieved by ceramic membranes with a low loading of catalysts.

4.1. Introduction

Organic micropollutants (OMPs), present in drinking and source water, have a potentially adverse effect on human health and the environment. These OMPs, often originating from pharmaceuticals, personal care products, and industrial processes, can persist in water, and their removal by conventional wastewater treatment methods is challenging (Fu et al., 2021). Membrane-based processes have widely been used in water treatment due to its compact design, and small footprint, among other advantages (Chen et al., 2022; Zhang et al., 2024). In contrast to nanofiltration and reverse osmosis membranes, ultrafiltration (UF) membranes operate at low pressures, resulting in reduced energy consumption and operational expenses. Additionally, UF membranes can maintain a high flux under low pressures, and their ability to be backwashed simplifies the cleaning and maintenance. However, UF membranes usually do not remove OMPs, because of their large pore sizes (10-100 nm). The rejection of benzotriazole (BT) by UF, from surface water, e.g., has only been in the range of 29%-44% (Acero et al., 2015). The low rejection of OMPs by UF membranes underscores the need for additional treatment strategies to effectively remove these micropollutants.

To address the challenges of the low removal of OMPs, the integration of (catalytic) membranes with advanced oxidation processes (AOPs) has been explored to promote the degradation of OMPs. Unlike ozone and chlorine, which rely mainly on selective direct oxidation and often produce harmful by-products, AOPs utilize highly reactive species (RS) to non-selectively mineralize a broad range of OMPs with minimal toxic byproduct formation (Huang et al., 2022). Among various AOPs, peroxymonosulfate (PMS) is a promising oxidant with a high redox potential (1.82 V), e.g., compared to 1.76 V for H_2O_2 (Berruti et al., 2021). In the PMS activation, different RS can be induced, such as $^{\bullet}OH$, $SO_4^{\bullet-}$, $^1O_2$, and $O_2^{\bullet-}$ (Kong et al., 2021). Pd/Al_2O_3 has been reported to be an effective catalyst in PMS activation, which can achieve a higher degradation of OMPs compared to other catalysts (Ahn et al., 2019). However, in Pd/Al_2O_3-PMS system, the currently identified dominant RS remains controversial. A non-radical pathway was identified for 4-chlorophenol, whereas the surface-bound sulfate radical was found to dominate in the degradation of 1,4-dioxane (Ahn et al., 2016; Feng et al., 2017). Earlier studies have primarily focused on the degradation of individual OMP, which likely led to these inconsistent conclusions regarding the dominant RS in the same system.

Although catalytic membranes coupled with AOPs have garnered attention, the excessive loading of catalysts on the membrane can result in substantial flux loss and the inhibition of OMPs degradation. For instance, ceramic UF membranes experienced a flux loss of 20 % to 66 % after being coated with a TiO_2 photocatalyst (Berger et al., 2020), which is consistent with the finding of Ma et al. (2022). In addition, Feng et al. (2017) have found that the highest degradation kinetics of 1,4-dioxane were found at the lowest Pd/Al_2O_3 loading (0.02 g/L). The negative effects, caused by the high loading of catalysts, have been attributed to the quenching of catalytic surfaces on the formed RS. A decrease of OMP degradation with overloaded catalysts was also reported by Berger et al. (2020). Moreover, excessive catalyst loading will significantly increase the coating costs.

Atomic layer deposition (ALD) is a precise thin-film deposition technique that allows for the controlled modification of membranes at the atomic level (Berger et al., 2020). In addition, the conformal coating achieved by ALD can ensure uniform coverage of catalysts across the entire membrane structure, including the membrane surface and internal pores, thereby increasing the catalytic surface areas (Li et al., 2024; Lotfi et al., 2022). Currently, ALD has been employed to load catalysts onto membranes for the degradation of OMPs, although most studies report significant flux loss due to high catalyst loadings (Berger et al., 2020; Lotfi et al., 2022). Moreover, a high catalyst loading can also reduce catalytic efficiency and increase operational costs. To overcome these limitations, low catalyst loadings achieved via ALD have been explored in electrocatalytic applications, where they have demonstrated high efficacy (Pickrahn et al., 2015). Nevertheless, it remains unclear whether such low loadings can enhance the catalytic performance in PMS activation for OMPs' degradation.

Hence, this study aims to load a low amount of Pd on the surfaces and in the pores of a ceramic UF membrane by ALD to activate PMS for the enhanced degradation of four selected OMPs, being benzotriazole (BT), diclofenac (DIC), sotalol (SOT), and trimethoprim (TMP). Pd is used as a catalyst due to its ability to effectively activate PMS, and its low ALD growth rate that favors deposition of small amounts. To assess the influence of pore deposition of Pd, kinetic experiments were performed with only flow over the membrane surface and experiments with flow over the membrane surface and through the pores. The most important RS were determined by quenching experiments, where corresponding scavengers for different RS were added, and therefore the effect on the degradation of the four OMPs was measured. In addition, parameters

such as pH, PMS dosage, and ions, potentially affecting the performance, were studied. Finally, OMPs were spiked into reverse osmosis brine and river water to evaluate the degradation performance in complex water matrices.

4.2. Materials and Methods

4.2.1. Ceramic UF membranes

Single-channel tubular ceramic UF membranes (CoorsTek, the Netherlands), with a pore size of 20 nm (CoorsTek data), were used in this study. The membranes consist of top and support layers made of Al_2O_3, having an internal diameter of 7 mm, an outer diameter of 10 mm, and a length of 100 mm. To avoid membrane leaking during the filtration experiments, a two-component epoxy adhesive (Araldite AW 5047–1 and Hardener HW 5067–1, from VIBA, Netherlands) was used to seal the two edges of the membranes (10 mm for each side).

Pd-deposited ceramic UF membranes (Pd-UF) were prepared by ALD. $Pd(hfac)_2$ (Sigma-Aldrich), formalin (Sigma-Aldrich), and ultrahigh purity nitrogen (99.999%) were used as the precursor, co-reactant, and purging gas, respectively. Before initiating Pd deposition, the ALD reactor was stabilized at 200 °C. The time sequence of the one-cycle ALD used in this study was 30-30-40-30 s. A gas mixture of 0.5 L/min of $Pd(hfac)_2$and 0.5 L/min of N_2 was flowed over the membrane substrates for 30 s. 1 L/min N_2 was executed to purge the excessive $Pd(hfac)_2$. After purging, 0.7 L/min formalin with 0.3 L/min N_2 was introduced for 40 s, followed by a purging step of 1 L/min N_2 for 30s, completing one cycle of ALD. The ceramic UF membranes deposited with Pd by 3, 30, and 60 cycles of ALD are denoted as C3, C30, and C60, respectively, while the pristine membrane is referred to as C0.

The pristine and modified membranes were characterized by scanning electron microscopy (SEM, Hitachi S–3400 II, Japan) with energy dispersive spectroscopy (EDS). X-ray photoelectron spectroscopy (XPS) was carried out to examine the inner surface of the Pd-UF membrane by using a Kα system (ThermoFisher Scientific) with a photon energy of 1486.7 eV. To eliminate the charging effect on peak shift, the carbon 1s (C1s) spectrum peak at 284.8 eV was used as a reference to calibrate the XPS peak positions through CasaXPS software (Fang et al., 2020). The porosity of the membrane and the thickness of the selective layer were estimated by the SEM image through the ImageJ analysis (Chen et al., 2020; Lin et al., 2016).

4.2.2. OMPs degradation experiments

4.2.2.1. Constant-flux setup

The setup, shown in Fig. 4.1, was used for the filtration experiments. The dead-end setup consisted of a balance (KERN, Germany) to measure the permeate flux during a certain interval, a needle valve (connected in circulation feed flow) to control the pressure and flux, a peristaltic pump (Waston-Marlow, Netherlands) to pump the feed water, a ceramic membrane module, and a feed tank containing a mixed OMPs and PMS solution.

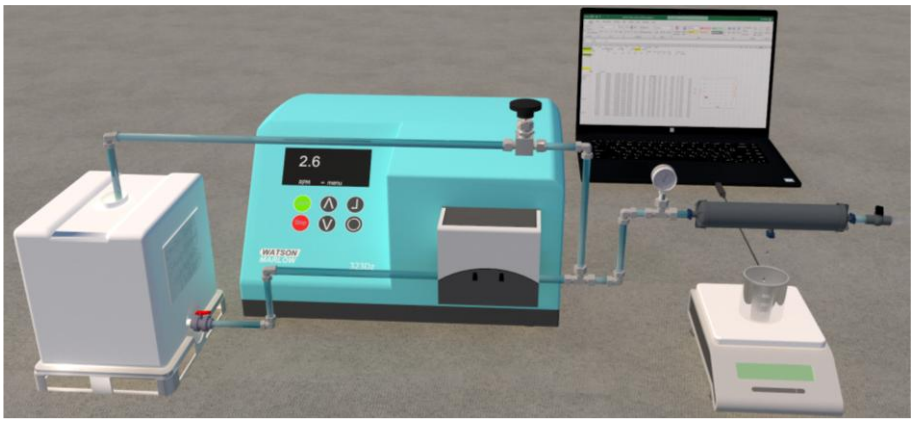

Figure 4.1. Constant flux setup for membrane filtration.

4.2.2.2. OMPs degradation during membrane filtration

Degradation of single OMPs over time. To have an insight into the removal of a single OMP over time, sotalol (SOT, from Sigma-Aldrich) was selected as the model OMP. After adding 40 µM potassium PMS (from Sigma-Aldrich) solution into 5 µg/L SOT solution, the pH was adjusted by HCl and NaOH. This solution was used as a feed for the subsequent experiment. Dead-end constant flux filtration started at a certain pressure for 5 min to achieve a stable fixed flux of 30 L/(m^2·h). Then the filtration experiment ran for 40 min. 5 mL permeate samples, taken at different time intervals to determine the SOT and PMS concentration, were immediately injected with 50 µL 40 mM $Na_2S_2O_3$ (from Sigma-Aldrich) to terminate any oxidation.

Degradation of multiple OMPs by Pd-UF with PMS. The four OMPs were purchased from Sigma-Aldrich, and their properties are listed in Table 4.1 (Fu et al., 2021). The stock solution, containing benzothiazole (BT), diclofenac (DIC), sotalol (SOT), and trimethoprim (TMP), with a concentration of 1 mg/L

was diluted with demineralized water to 5 μg/L each. 5 mL of the prepared OMPs' solution was taken to determine the initial concentrations. Then the OMPs' solution mixed with 20, 40, or 80 μM PMS at pH of 2.5, 7, or 11, respectively, was filtered over the Pd-UF membrane at a certain pressure for 5 min to achieve a stable fixed flux (i.e., 30, 100, 200, or 500 L/(m^2·h)). During the subsequent 40-min of filtration, 5 mL samples were taken from the permeate side and mixed with $Na_2S_2O_3$. Given that anions can quench RS, the presence of 1 mM Cl^-, SO_4^{2-}, HCO_3^-, or ClO^- was also studied.

Effect of Pd deposited on the surface and in the pores. The role of Pd deposited on the membrane surface in OMPs' degradation was conducted by closing the permeate side and opening the concentration side (Fig. S4.1b). As a result, the solution only flowed along the membrane surface. In this case, OMPs were only degraded by the Pd deposited on the surface without the contribution of Pd deposited in the pores. The residence time was calculated by the tubular membrane length and the flow velocity from feed side to the concentration side.

Scavenging experiments for RS identification. Based on earlier studies, different scavengers were dosed in the feed water to eliminate certain RS (Gao et al., 2022; Nandi and Chatterjee, 1987). Tert-butanol (TBA), and ethanol (EtOH) were used to quench RS of $^{\bullet}OH$, and both $^{\bullet}OH$ and $SO4^{\bullet-}$, respectively, while furfuryl alcohol (FFA), and L-ascorbic acid (LAA) were used to scavenge $^1O_2$ and $O_2^{\bullet-}$, respectively. In the quenching experiment, 0.4 mM scavenger was injected into the mixed OMPs and PMS solution, where the concentration of scavenger was 10 times higher than the concentration of PMS (40 μM).

Potential practical application. The applicability of the combined filtration-AOPs system was evaluated using real water types, including river water and two types of brines: brine A with low salinity and brine B with high salinity. The river water was collected from the canal Delftse Schie (Delft, the Netherlands) without pretreatment for the experiment, and brine water A and B were simulated based on the earlier studies (Ali, 2021; Martinetti et al., 2009; Yang et al., 2016). The total dissolved solids (TDS) were measured as 568 mg/L for river water, 4573 mg/L for brine A, and 22867 mg/L for brine B. Detailed water quality parameters are provided in Table S4.1.

Table 4.1. Structure and properties of the selected OMPs (Azzi et al., 2021; Fu et al., 2022; PubChem, n.d.).

Name	Molecular structure	Molecular weight (g/mol)	Log K_{ow}	Charge (at pH 7)	Min/Max projection radius (Å)
Benzothiazole (BT)		119	1.44	neutral	3.66/4.12
Diclofenac (DIC)	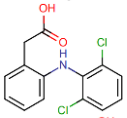	296	4.51	negative	4.62/6.34
Sotalol (SOT)	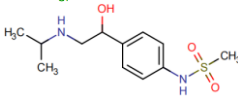	272	0.24	positive	4.21/7.94
Trimethoprim (TMP)	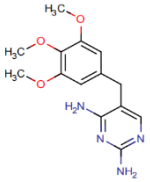	290	0.91	positive	4.97/6.95

4.2.2.3. Water sample analysis

The UPLC-MS/MS system (Waters, ACQUITY UPLC I-Class, Xevo TQ-S micro fitted with the ESI) equipped with a C18 column (ACQUITY UPLC™ BEH 2.1 × 50 mm, 1.7 µm particle size) was employed to measure the concentration of the OMPs (Fu et al., 2021). The PMS concentration was measured by adding 1.5 mL of a mixed solution containing 100 g/L KI and 5 g/L $NaHCO_3$ to 1.5 mL samples and then was tested by UV-Vis at 352 nm, as proposed by Liang et al. (2008). The calibrated curve of PMS concentration and corresponding UV spectra is shown in Fig. S4.2.

4.3. Results and discussion

4.3.1. Characterization of ceramic membranes

The top-view SEM image of the Pd-deposited membrane (C60) shows that, compared to the pristine membrane, hardly any morphological changes existed (Fig. 4.2a and 4.2b). This suggests that the Pd deposition process did not notably alter the membrane's surface structure, maintaining its original texture and integrity. Due to the low loading of Pd after 60-cycle ALD, no Pd was detected by SEM-EDX. As reported, the ALD growth rate of Pd on Al_2O_3 is 0.15-0.2 Å/cycle with a loading rate of 0.18 mg/m^2/cycle (Elam et al., 2006; Lu and Stair, 2010). This means that after 60 cycles ALD, the estimated Pd particle size was 0.9-1.2 nm, with a total Pd loading of 11.04 mg/m^2.

The full spectrum scan of XPS shows that Pd was successfully deposited on the membrane with Pd atomic ratios (ar.) of 1.36% (Pd/Al). The peak fit of the fine XPS spectra of Pd 3d was based on an earlier report by Datta et al. (2021), as shown in Fig. 4.2d. The binding energy of 335.3 and 340.6 eV were ascribed to Pd^0 which accounted for 83.8% (ar. of Pd^0/ Pd), while 337.3 and 342.6 eV represented Pd^{2+} with an ar. of 16.2% (Pd^{2+}/Pd) (Li et al., 2022; Militello and Simko, 1994a, 1994b). A 1.33% (ar.) of F was also found from the XPS full scan, which can be attributed to the formation Al–O–Pd(hfac)* or HhFac during the ALD reaction process (Elam et al., 2006).

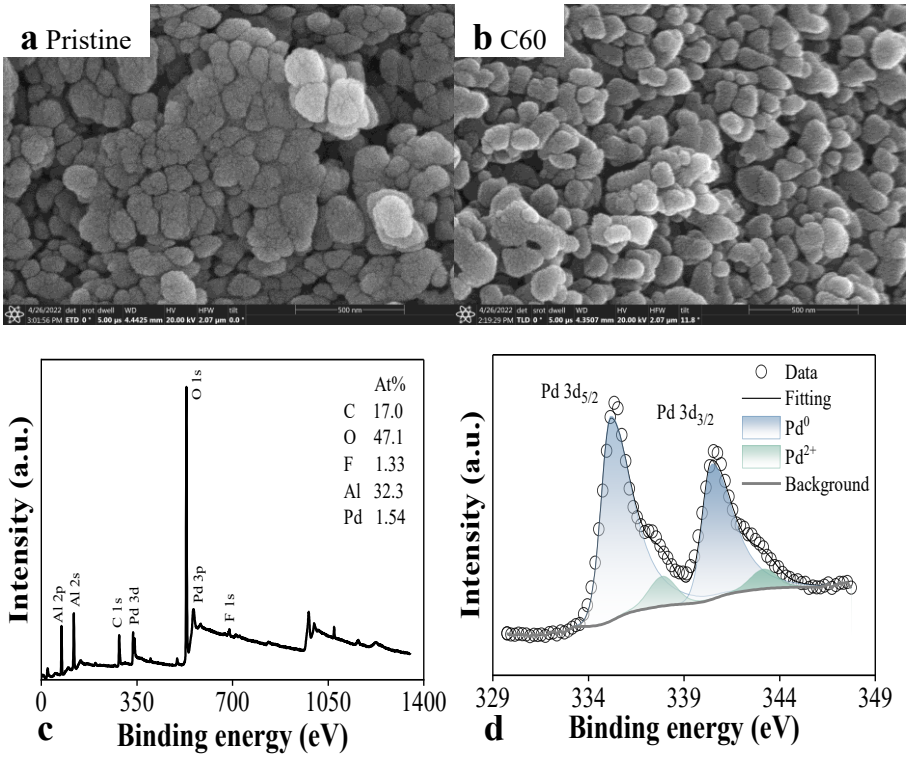

Figure 4.2. SEM image of the membrane surface of (a) pristine and (b) C60 membranes. XPS spectra of (c) full scan survey and (d) Pd fine spectra of C60.

4.3.2. PMS activated by Pd-UF

Different membrane systems were employed to evaluate their performance over filtration time during PMS activation for the removal of SOT.

The pristine Al_2O_3 UF membrane (C0) and C60 Pd-UF were first examined at a flux of 30 L/(m^2·h). The degradation efficacy was calculated by Eq. S4.4. As shown in Fig. 4.3a, both C0 and C60 exhibited low rejections of SOT (5%-14%), attributed to the large pore size of the UF membrane (17.7-20 nm) compared to the size of SOT (< 1 nm). These findings align with the study of Salehi et al. (2019), where it was reported that SOT rejection by UF membrane is in the range of 5%-32%, depending on the permeate flux. In addition, the addition of 40 μM H_2O_2 to the C60 Pd-UF resulted in only 3% SOT removal after 40 min of filtration at pH 2.5. However, the removal efficacy of SOT by the pristine membrane C0 with 40 μM PMS slightly increased to 20%, probably due to the direct oxidation by PMS. The highest SOT removal efficacy, around 98%, was achieved by the C60 Pd-UF membrane with 40 μM PMS. This enhanced removal was likely due to the high oxidation potential of RS, such as $SO4^{\bullet-}$, $^{\bullet}OH$, $^1O_2$, and $O_2^{\bullet-}$, induced by the catalyst-PMS system, with potentials ranging from 1.52 V to 3.1 V. To further evaluate the consumption of PMS in different systems, PMS concentration was measured during the filtration with the C0 and C60 membranes (Fig. 4.3b). The C0 membrane showed a gradual PMS decomposition from 27% at 3 min to 39% at 40 min, while the C60 membrane achieved a rapid PMS decomposition, ranging from 93% to 100% throughout the filtration process, also indicating the high efficacy of the C60 membrane in catalyzing PMS.

Fig. 4.3c shows the performance of the C3, C30, and C60 membranes in SOT degradation over time. All Pd-UF membrane systems exhibited a rapid degradation of SOT. After 40 min, the C3 membrane achieved 52% SOT degradation, while the C30 and C60 membranes achieved comparable results, with 99% and 98% SOT degradation, respectively. The relatively low SOT degradation by the C3 membrane with PMS can be caused by the much lower loading of Pd to catalyze PMS into RS. Based on Lu and Stair, (2010), the loading of Pd on the C3, C30, and C60 membranes was 0.55, 5.52, and 11.04 mg/m^2, respectively. Once the membrane surface is uniformly covered with a certain loading of catalysts, additional deposition will not further increase the available reactive area. Consequently, it will not enhance PMS activation for OMP degradation, as was evident after 30 ALD cycles. Feng et al. (2017) have reported that a high loading of Pd on the Al_2O_3 particles can even deteriorate the stoichiometric efficiency of PMS utilization due to the scavenging effect caused by the excess Pd.

Apart from the similar SOT degradation efficacies between the C30 and C60 membranes, the C30 membrane exhibited a smaller permeability decrease,

from 232 to 193 L/(m^2·h·bar), compared to the C60 membrane, from 235 to 184 L/(m^2·h·bar), respectively (Fig. 4.3d). This can be attributed to the low loading of Pd, which has a limited effect on the pore sizes (Fig. 4.3d). The representative pore sizes of the C30 and C60 membranes, for example, were estimated to be 18.2 nm and 17.7 nm, respectively, using the Carman-Kozeny equation (Eq. S4.1) developed for membrane (Levitsky et al., 2021). It should be noted that the pore sizes were estimated based on the assumption that the entire membrane structure was uniformly deposited by Pd, without altering membrane tortuosity or porosity due to the much lower loading. These calculated pore sizes were comparable to the values estimated based on the pore narrowing due to the deposited Pd particle size (Fig. S4.3). Given its higher permeability, efficient degradation, and lower chemical use for coating, the C30 membrane was selected for further experiments.

The capacities of C0 and C30 with and without PMS in the removal of the four selected OMPs are shown in Fig. 4.3e. Without PMS, the C0 membrane removed 3%–24% of the four OMPs. With PMS, the removal of BT, SOT, and TMP by the C0 membrane increased to 44%, 35%, and 28%, respectively, while DIC removal reached 90%, likely because PMS can directly oxidize DIC. However, the C30 membrane with PMS achieved an almost complete removal of all OMPs.

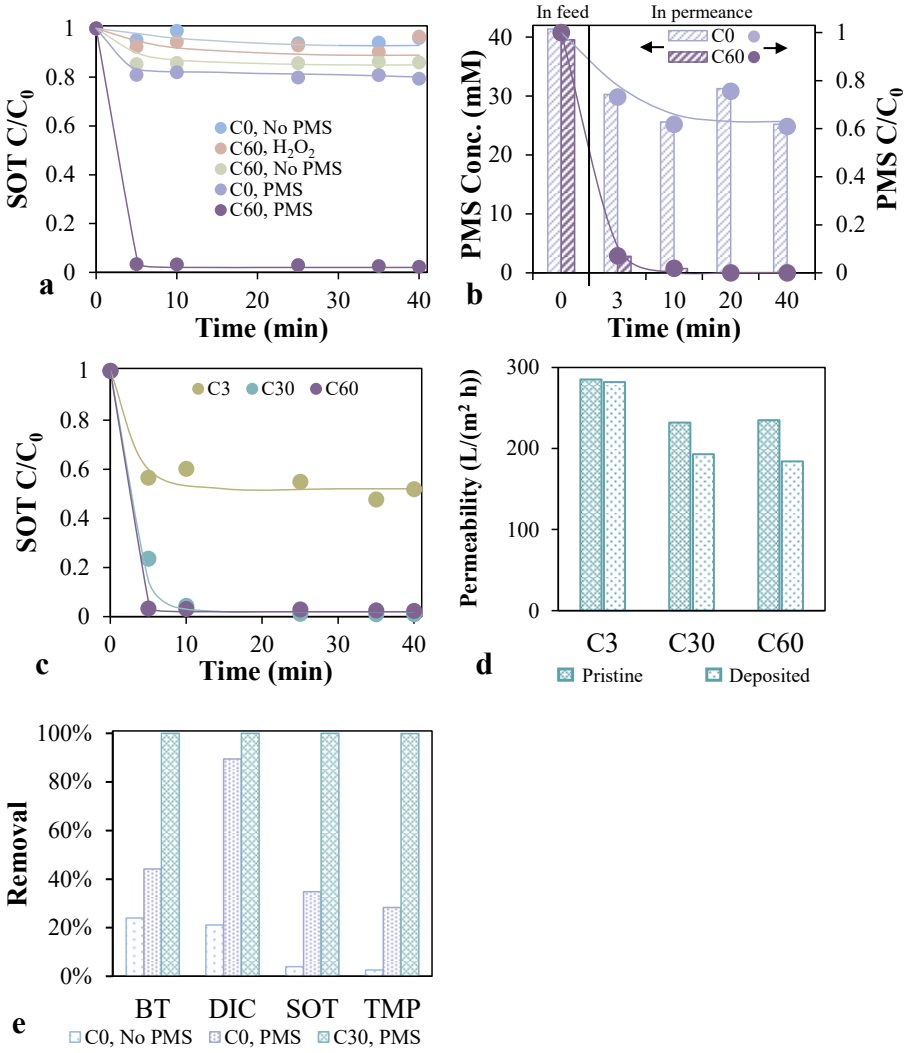

Figure 4.3. Performance examination of different membrane systems in (a) SOT removal over time, and (b) PMS consumption by C0 or C60. (c) SOT removal over time by the membranes (C3, C30, and C60) modified by 3, 30, and 60 ALD cycles, respectively. (d) Flux of pristine and deposited membranes. (e) Removal of four OMPs by different membrane systems. The experiments were conducted at 30 L/(m^2·h) with and without 40 μM PMS, at pH = 7, or (a) with 40 μM H_2O_2, at pH = 2.5.

4.3.3. Influence of pH, PMS concentration, and co-existed ions

The effects of pH, PMS concentration, and anion can play a role in the oxidation process (Ghanbari and Moradi, 2017). Hence, variations of pH (2.5, 7, and 11), PMS concentrations (20, 40, and 80 μM), and ions (Cl^-, SO_4^{2-}, HCO_3^-, and ClO^-) were examined, respectively, for their impact on OMP degradation and PMS activation, as shown in Fig. 4.4 and Fig. S4.4.

Although the degradation efficacy of BT and DIC exhibited a small decrease at a pH of 2.5, the degradation efficacies of the two other OMPs reduced considerably at a pH of 2.5, while the degradation of all four OMPs was reduced at a pH of 11, in comparison to the performance at a pH of 7 (Fig. 4.4a). Kang et al. (2021) have also found that in the α-Fe_2O_3-PMS system, the highest OMPs' degradation was achieved at a pH = 7, and the pH lower or higher than 7 has a negative influence on OMPs' degradation. Dong et al. (2021) also reported that in the $MoSe_2$-PMS system, the most effective pH for PMS was in the range of 4 to 9, while the OMPs' oxidation is reduced prominently when pH < 3 or > 11. The oxidation of OMPs at a pH of 2.5 and 11 can be ascribed to the inhibited consumption of PMS, since PMS decomposition was reduced from 100% at a pH of 7 to 44% and 48% at a pH of 2.5 and 11, respectively (Fig. 4.4b and Fig. S4.4a).

The degradation of TMP decreased considerably to 41% and 88% at PMS concentrations of 20 and 80 μM, respectively, while the degradation of the three other OMPs remained relatively high, ranging from 92% to 100% across PMS concentrations of 20, 40, and 80 μM (Fig. 4.4c), respectively. Although PMS was completely depleted at 20 and 40 μM, its consumption decreased to 90% at 80 μM (Fig. 4.4d and Fig. S4.4b). This decline is likely due to the limited catalytic surface area, which was insufficient to activate the excess PMS at higher concentrations.

It has been reported that anions can inhibit the degradation of OMPs due to the reaction between anions and radicals (Wang et al., 2020). However, when 1 mM anions of Cl^-, SO_4^{2-}, HCO_3^-, or ClO^- were present in the system, the degradation of most OMPs remained as high as 93%-100%, while only the degradation of BT was reduced to 81% in the presence of ClO^- (Fig. 4.4e). Fig. 4.4f and Fig. S4.4c show that none of these anions inhibited the PMS consumption. This can be attributed to the excess radicals formed in the membrane pores, which probably compensated for any potential interference caused by the anions (Zhang et al., 2020).

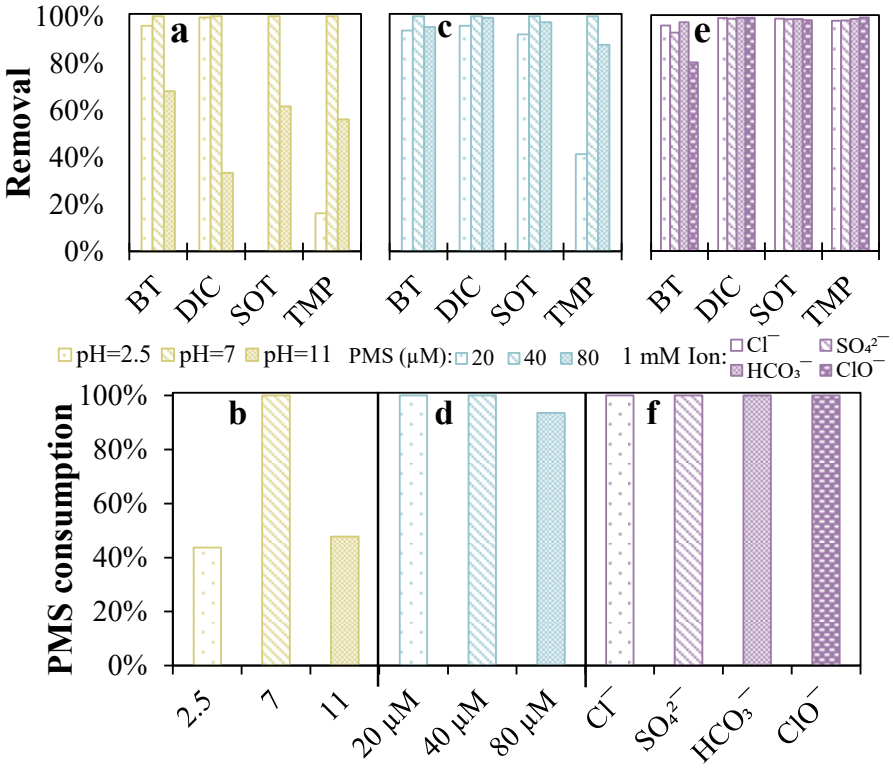

Figure 4.4. OMPs' removal and PMS consumption under different (a, and b) pH, (c, and d) PMS concentration, and (e, and f) anion (1 mM) presence. Unless otherwise specified, the filtration experiments were conducted by the C30 membrane at a permeate flux of 30 L/(m²·h), at pH 7, with 40 μM PMS, and an initial OMP concentration of 5 μg/L for each compound. For testing the effect of ions, different ions (1 mM) were individually added to assess their influence.

4.3.4. Effective degradation of OMPs at high flux

The flux, related to the residence time, can have an impact on the OMPs' degradation in the coupled system of the catalytic membrane with PMS (Meng et al., 2022). Therefore, fluxes of 30, 100, 200, and 500 L/(m^2·h) were employed over the C30 membrane for 40-min filtration. The residence time was calculated by the permeate flux, porosity of the membrane (Fig. S4.5), and thickness of the selective layer (Fig. S4.5) with Eq. S4.2.

Below 100 L/(m^2·h), almost complete degradation of the four OMPs was achieved. As the flux increased to 500 L/(m^2·h), the degradation efficacies of BT and TMP decreased considerably (Fig. 4.5a), e.g., at fluxes of 200 and 500 L/(m^2·h), BT was only degraded by 81% and 51%, respectively. This was likely due to the reduced residence time of the PMS and OMPs across the membrane at a higher flux. As a result, it led to a decrease in the contact opportunities between PMS and the Pd catalyst, as well as between the formed RS and OMPs. The removal of BT, DIC, SOT, and TMP by different membranes at varying fluxes, as obtained from literature, is summarized in Fig. 4.5b and Table S4.2. The high removal of the four selected OMPs is typically achieved by membranes with small pore sizes, such as nanofiltration and reverse osmosis membranes, at a low flux (4-55 L/(m^2·h)). In contrast, UF membranes, due to their larger pore sizes, generally exhibited low rejection of these small-sized OMPs. Ceramic UF membranes with low Pd loading, when coupled with PMS, achieved performance comparable to that of nanofiltration and reverse osmosis membranes. Besides, the high removal of OMPs was achieved by these membranes at a much higher flux while operating at a low transmembrane pressure.

PMS consumption measured in the permeate side was maintained at 98%-100% during 40-min filtration through the C30 membrane at a flux of 30 L/(m^2·h) (Fig. 4.5c). This suggests that the Pd deposited by ALD on the membrane was stable for continuous catalysis of PMS. However, it was found that PMS consumption decreased with an increased flux. At fluxes of 30, 100, 200, and 500 L/(m^2·h), PMS decomposition was 99%, 87%, 74%, and 43%, respectively (Fig. 4.5c and 4.5d). The decline of PMS decomposition, and thus OMP degradation, for fluxes above 100 L/(m^2·h) can be attributed to the decreased retention time (Fig. 4.5d). Moreover, increasing the flux could dilute the RS retained within the pores, thereby reducing the degradation efficacy of OMP.

The optimized flux needs to be further explored because the best balance between degradation efficacy and water production can change under different conditions. Real waters contain natural organic matter (NOM), ions, and particles that may influence fouling behaviour, residence time, and PMS activation. In addition, the optimal flux also depends on practical factors such as energy use, chemical cost, and the required level of OMP removal. Therefore, pilot-scale and long-term studies are necessary to determine the most suitable operating flux for real applications.

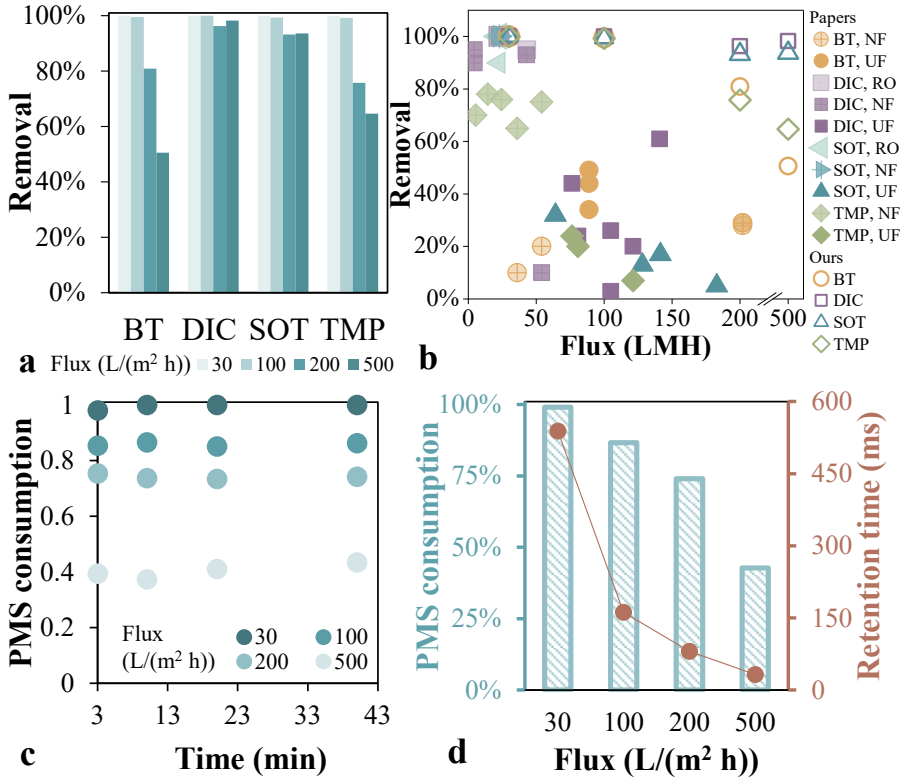

Figure 4.5. (a) Removal efficacy of four OMPs, (c and d) PMS consumption and retention time by the C30 membrane with PMS at the varying flux. (b) OMPs removal by membranes found in this study and reported in literature (as summarized in Table S4.2). A mixed OMPs solution (5 µg/L for each compound) with 40 µM PMS was adjusted at a pH of 7, and then the feed was filtered over the C30 membrane for 40-min at varying flux.

4.3.5. Important role of Pd deposited in the pores

It was expected that Pd deposited in the pores promotes the contact of reactants with the Pd catalyst and subsequently of the RS with the OMPs (Zhang et al., 2020). To gain insight into the contribution of Pd deposited on the membrane surface compared to the Pd in the pores, experiments were conducted to study this effect. The effect of Pd on the surface and within the pores was studied using the setup with and without permeate flow (Fig. 4.1 and S4.1), i.e., experiments involving flow exclusively over the membrane surface and flow both over the surface and through the pores.

When both the Pd on the surface and inside the pores were involved in the catalytic reactions (i.e., with permeate flow), almost 100% of the four OMPs were degraded within a retention time of 162 ms (at 100 L/(m^2·h)), as shown in Fig. 4.5a and 4.5d. However, when only Pd on the membrane surface was involved, the degradation efficacy of the four OMPs was less than 12%, even with an extended retention time (859-2412 ms) (Fig. 4.6a). This low removal can be attributed to the limited diffusion of RS from the active areas to the bulk water away from the membrane surface, as reported by Chang et al. (2025).

The degradation kinetics of the four OMPs by the sole Pd on the membrane surface, and Pd on the surface and in the pores are revealed in Fig. 4.6b and Fig. S4.6a and S4.6b, using Eq. S4.2 for the calculation. The kinetic constants of BT, DIC, SOT, and TMP were 4.2×10^{-5}, 3.6×10^{-5}, 6.0×10^{-2}, and 2.2×10^{-2} $(ms)^{-1}$, respectively, for Pd on the surface. However, the kinetic constants of OMPs degradation, achieved by Pd on the surfaces and in the pores, reached 0.028, 0.050, 0.034, and 0.030 $(ms)^{-1}$ for BT, DIC, SOT, and TMP, respectively. This suggests that the presence of Pd within the pores enhanced the kinetics by three orders of magnitude. This kinetic enhancement is consistent with an earlier study, where Fenton degradation kinetics of para-chlorobenzoic acid were increased by a factor of 107 when Fe_3O_4 was also deposited in 20 nm pores (Zhang et al., 2020). The high kinetic degradation, facilitated by Pd in the pores, can be attributed to the nanoconfinement effect. Studies have shown that the concentration of RS is highly dependent on the distance from the catalytic regions, with RS concentration increasing when RS is confined in nanopores, thereby promoting their mass transfer (Zhang et al., 2021, 2020). The membrane pores also provide abundant catalytic surface areas to trigger the formation of RS to degrade the nearby OMPs enriched within the pores.

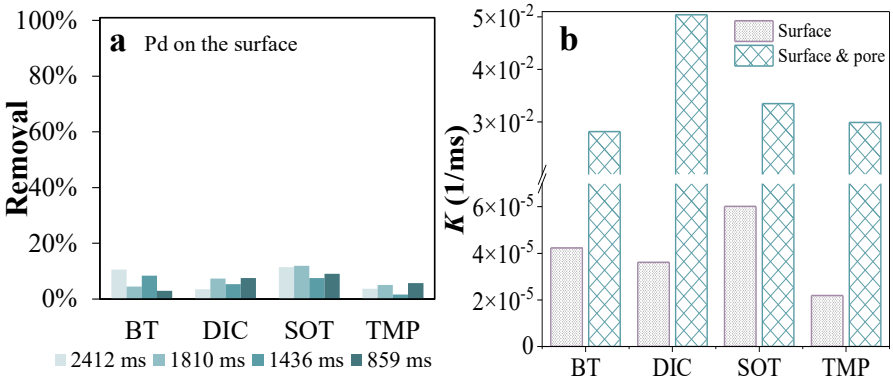

Figure 4.6. (a) Removal of OMPs by Pd deposited on the membrane surface at different residence times. (b) Kinetic constant comparison of OMPs' removal with and without the involvement of Pd deposited in the pores. The performance of Pd on the surface was evaluated by feeding OMPs (5 μg/L for each OMP) and 40 μM PMS over the C30 membrane surface by closing the permeate side.

4.3.6. Dependence of OMPs oxidation on the types of RS

Scavengers are typically used to identify the dominant RS in PMS activation. However, there are varying conclusions regarding the dominant RS generated by alumina-supported Pd catalysts. Feng et al. (2017) have reported that $SO_4^{\bullet-}$ and $^{\bullet}OH$ were the primary RS responsible for the degradation of 1,4-dioxane, whereas Ahn et al. (2019, 2016) have found that both $SO_4^{\bullet-}$ and non-radical pathways played dominant roles in the degradation of 4-chlorophenol. These studies, however, only focused on the degradation of individual OMPs, which likely overlooks the synergistic effects of different RS in the degradation of multiple OMPs, especially in real water containing complex mixtures of OMPs. Therefore, to study the influence of the RS, $SO_4^{\bullet-}$, $^{\bullet}OH$, $^1O_2$, and $O_2^{\bullet-}$ on the degradation of multiple OMPs by Pd/Al_2O_3-PMS system, TBA, MeOH, FFA, and LAA were used as their scavengers, respectively.

Fig. 4.7a-4.7d show the degradation efficacy of OMPs with the addition of the different scavengers. It can be concluded that none of the scavengers had an inhibiting effect on the degradation of BT. However, the scavenger LAA considerably inhibited the degradation of DIC and SOT, reducing their degradation efficacies from 100% to 9%-13%. In addition, all scavengers contributed to the reduction of TMP degradation. Apparently, the degradation of BT was subjected to other RS pathways than foreseen, while DIC and SOT degradation were probably governed by $O_2^{\bullet-}$ oxidation. All the considered RS had an impact on TMP degradation. This is in contrast with the findings of Feng et al. (2017) who have reported that $SO_4^{\bullet-}$ and $^{\bullet}OH$ should be considered as the dominant RS in PMS catalysis by alumina-supported Pd. These results indicate that varying RS can be induced in PMS activated by alumina-supported Pd, and the degradation of multiple OMPs is largely dependent on the combined effects of different RS rather than any single specific species.

However, it should be noted that OMPs and the quenchers of FAA and LAA can also react rapidly with $^{\bullet}OH$ or $SO_4^{\bullet-}$ (Table S4.3). This indicates that the relatively low reaction kinetics between MeOH or TBA and $^{\bullet}OH$ or $SO_4^{\bullet-}$

likely limit their capacity in scavenging such radicals. Probably, surface-bound $SO_4^{\bullet-}$ radicals in PMS with alumina-supported Pd systems, as proposed by Feng et al. (2017), also resulted in a failure of quenching. The resistance of $^{\bullet}OH$ radicals, accumulated surrounding the heterogeneous catalysts to the TBA scavenger, has also been found by Zhang et al. (2017). The surface-bound radicals can be ascribed to the short diffusion distance of the radicals, which, consequently, led to a gradient of radical concentration in the membrane pores (Zhang et al., 2020). The above discussion thus suggests that $^{\bullet}OH$ and $SO_4^{\bullet-}$ probably play important roles in the degradation of the four OMPs. However, the specific contribution of different RS is beyond the scope of this work. Further studies are recommended to quantitatively elucidate the roles of individual RS.

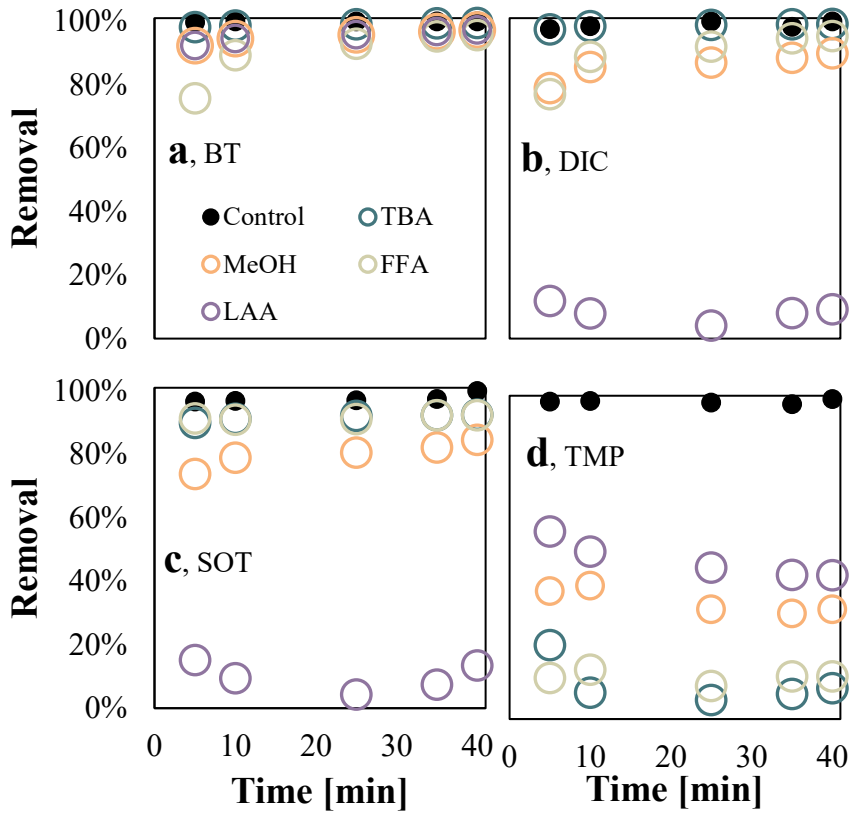

Fig. 4.7. Scavenger experiments by adding TBA, MeOH, FFA, and LAA (0.4 mM) to the mix of PMS (40 μM) and OMPs (5 μg/L for each compound)

solution at a pH of 7. The filtration was performed by the C30 membrane at a permeate flux of 30 L/(m^2·h).

4.3.7. Degradation of OMPs from brine and river water

The degradation of OMPs from brine water with a low (brine A) and high (brine B) salinity and from river water was performed to evaluate the potential application of the catalytic Pd-UF membrane. The water quality parameters of these water types are shown in Table S4.1, where the main anions in the brine A, brine B, and the river water were Cl^- (16.4, 81.8, and 1.4 mM for brine A, brine B and river water, respectively), and SO_4^{2-} (18.4, 91.9, and 0.7 mM for brine A, brine B and river water, respectively), with a TDS of 4573, 22867, and 538 mg/L, respectively. The OMPs' degradation and PMS consumption in brine and river water are shown in Fig. 4.8 and Fig. S4.7.

In brine A water, the degradation of DIC and SOT was retained at a high efficacy of around 97%, while the degradation of BT and TMP was reduced to 82% and 65%, respectively. In brine B, the degradation efficacies of BT, SOT, and TMP dropped to 78%, 57%, and 16%, respectively, whereas DIC maintained a high degradation efficacy of 97%. The negative impact of high ion concentrations on OMPs' degradation was consistent with the earlier study by Wang et al. (2020). This suggests that the efficacy of OMPs' degradation can be decreased due to the competitive reaction caused by the higher concentration of anions. Fig. 4.8d shows that PMS consumption in brine B was reduced to 79%, compared to 97% in brine A, thereby inhibiting the degradation of OMPs.

High OMPs' degradation efficacies, ranging from 89%-100 %, were kept during the duration of the experiment with river water, and all PMS was decomposed in this water type (Fig. 4.8c). These findings indicate that the main substance in the river water, i.e., the natural organic matter (characterized by a total organic carbon concentration of 24 mg/L), had a minor impact on the degradation of OMPs and on the high PMS decomposition to induce RS.

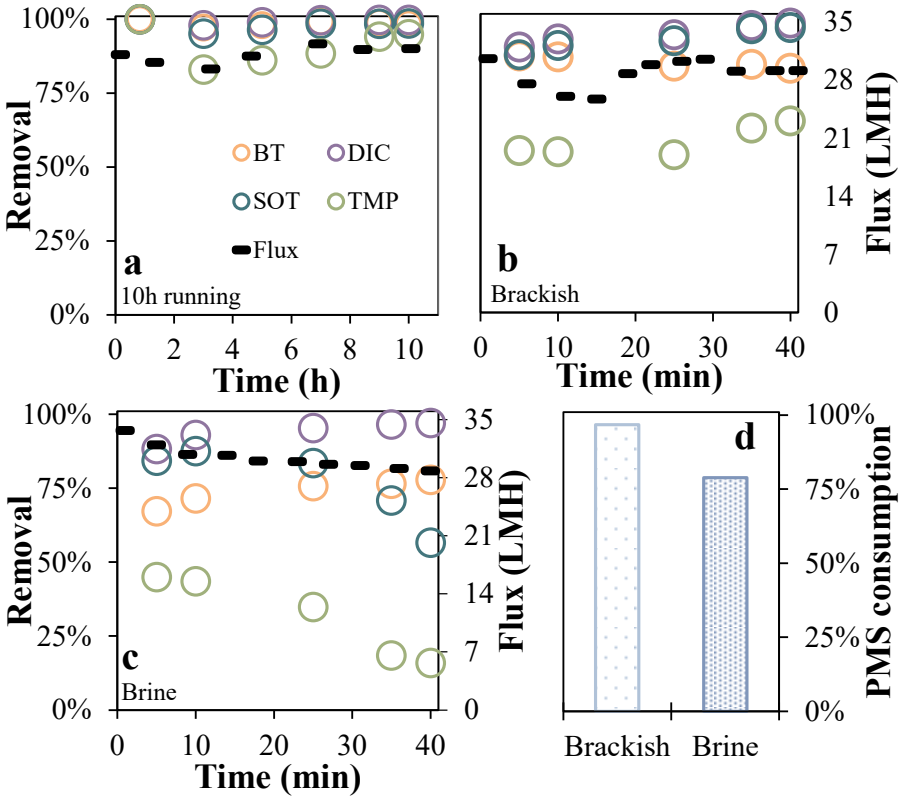

Figure 4.8. Degradation of OMPs from (a) brine A with a low concentration of ions, (b) brine B with a higher concentration of ions, and (c) river water. (d) PMS consumption in permeate water from the different water types after 40-min reaction. The mixed OMPs with 5 μg/L of each compound with 40 μM PMS were added to the brine A, brine B, and river water, and then the filtration was conducted by the C30 membrane at 30 L/(m^2·h).

4.4. Conclusion

To enhance the removal of OMPs, ceramic UF membranes, modified with low Pd loading through ALD were coupled with PMS. The Pd-UF membranes were studied for their performance in degrading four selected OMPs under varying conditions.

The membrane, deposited with a small amount of Pd by 30 ALD cycles, exhibited 100% degradation of the four selected OMPs by the activation of PMS at a flux of 30 L/(m^2·h). In contrast, the pristine UF membrane exhibited

only 3%-24% OMPs removal. At a high flux of 200 L/(m^2·h), the Pd-UF membrane still achieved a degradation efficacy of 76%-96%. Compared to nanofiltration and reverse osmosis membranes, these catalytic UF membranes not only provided a high flux at a low applied pressure, but also achieved an efficient removal of OMPs.

The degradation kinetics of the OMPs by Pd within the pores were found to be three orders of magnitude higher than that by Pd on the membrane surface. This enhanced performance was attributed to the abundant Pd-surface area and the enhanced mass transfer of RS and OMPs in the membrane pores.

Various RS can be induced in the system of Pd-UF membranes with PMS activation, but the primary RS responsible for the degradation was found to vary depending on the specific type of OMP.

The highest OMP degradation efficacy was achieved at a pH of 7, while at a pH of 2.5 and 11 OMP degradation was affected by the inhibition of PMS activation. Moreover, PMS concentrations (20-80 µM), ions (1 mM Cl^-, SO_4^-, and NO_3^-), and NOM (in river water) exhibited a mild effect on the degradation of OMPs in the Pd-UF systems activated by PMS. However, in the treatment of water with high salinity, the inhibited PMS activation and competing reaction led to a reduction in OMPs degradation.

References

Acero, J.L., Benitez, F.J., Real, F.J., Rodriguez, E., 2015. Elimination of selected emerging contaminants by the combination of membrane filtration and chemical oxidation processes. Water. Air. Soil Pollut. 226, 139. https://doi.org/10.1007/s11270-015-2404-8

Ahn, Y.-Y., Bae, H., Kim, H.-I., Kim, S.-H., Kim, J.-H., Lee, S.-G., Lee, J., 2019. Surface-loaded metal nanoparticles for peroxymonosulfate activation: efficiency and mechanism reconnaissance. Appl. Catal. B Environ. 241, 561–569. https://doi.org/10.1016/j.apcatb.2018.09.056

Ahn, Y.-Y., Yun, E.-T., Seo, J.-W., Lee, C., Kim, S.H., Kim, J.-H., Lee, J., 2016. Activation of peroxymonosulfate by surface-Loaded noble metal nanoparticles for oxidative degradation of organic compounds. Environ. Sci. Technol. 50, 10187–10197. https://doi.org/10.1021/acs.est.6b02841

Ali, M.E.A., 2021. Nanofiltration process for enhanced treatment of RO brine discharge. Membranes 11, 212. https://doi.org/10.3390/membranes11030212

Azzi, M., Ravier, S., Elkak, A., Coulomb, B., Boudenne, J.-L., 2021. Fast UHPLC-MS/MS for the Simultaneous Determination of Azithromycin, Erythromycin, Fluoxetine and Sotalol in Surface Water Samples. Appl. Sci. 11, 8316. https://doi.org/10.3390/app11188316

Berger, T.E., Regmi, C., Schäfer, A.I., Richards, B.S., 2020. Photocatalytic degradation of organic dye via atomic layer deposited TiO2 on ceramic membranes in single-pass flow-through operation. J. Membr. Sci. 604, 118015. https://doi.org/10.1016/j.memsci.2020.118015

Berruti, I., Oller, I., Polo-López, M.I., 2021. Direct oxidation of peroxymonosulfate under natural solar radiation: accelerating the simultaneous removal of organic contaminants and pathogens from water. Chemosphere 279, 130555. https://doi.org/10.1016/j.chemosphere.2021.130555

Chang, J., Yu, B., Peng, X., Zhang, P., Xu, X., 2025. Nanoconfined catalytic macrostructures for advanced water remediation: from basic understanding to future application strategies. Water Res. 272, 122960. https://doi.org/10.1016/j.watres.2024.122960

Chen, M., Heijman, S.G.J., Luiten-Olieman, M.W.J., Rietveld, L.C., 2022. Oil-in-water emulsion separation: fouling of alumina membranes with and without a silicon carbide deposition in constant flux filtration mode. Water Res. 216, 118267. https://doi.org/10.1016/j.watres.2022.118267

Chen, M., Zhu, L., Chen, J., Yang, F., Tang, C.Y., Guiver, M.D., Dong, Y., 2020. Spinel-based ceramic membranes coupling solid sludge recycling with oily wastewater treatment. Water Res. 169, 115180. https://doi.org/10.1016/j.watres.2019.115180

Datta, A., Deolka, S., Kumar, P., Ziadi, Z., Sasaki, T., Steinhauer, S., Singh, V., Jian, N., Danielson, E., Porkovich, A.J., 2021. In situ investigation of oxidation across a heterogeneous nanoparticle–support interface during metal support interactions. Phys. Chem. Chem. Phys. 23, 2063–2071. https://doi.org/10.1039/D0CP05697A

Dong, C., Wang, Z., Ye, Z., He, J., Zheng, Z., Gong, X., Zhang, J., Lo, I.M.C., 2021. Superoxide radicals dominated visible light driven peroxymonosulfate

activation using molybdenum selenide (MoSe2) for boosting catalytic degradation of pharmaceuticals and personal care products. Appl. Catal. B Environ. 296, 120223. https://doi.org/10.1016/j.apcatb.2021.120223

Elam, J.W., Zinovev, A., Han, C.Y., Wang, H.H., Welp, U., Hryn, J.N., Pellin, M.J., 2006. Atomic layer deposition of palladium films on Al2O3 surfaces. Thin Solid Films 515, 1664–1673. https://doi.org/10.1016/j.tsf.2006.05.049

Fang, D., He, F., Xie, J., Xue, L., 2020. Calibration of Binding Energy Positions with C1s for XPS Results. J. Wuhan Univ. Technol.-Mater Sci Ed 35, 711–718. https://doi.org/10.1007/s11595-020-2312-7

Feng, Y., Lee, P.-H., Wu, D., Shih, K., 2017. Surface-bound sulfate radical-dominated degradation of 1,4-dioxane by alumina-supported palladium (Pd/Al2O3) catalyzed peroxymonosulfate. Water Res. 120, 12–21. https://doi.org/10.1016/j.watres.2017.04.070

Fu, M., Heijman, B., van der Hoek, J.P., 2022. Removal of organic micropollutants from wastewater effluent: selective adsorption by a fixed-bed granular zeolite filter followed by in-situ ozone-based regeneration. Sep. Purif. Technol. 303, 122303. https://doi.org/10.1016/j.seppur.2022.122303

Fu, M., Wang, J., Heijman, B., van der Hoek, J.P., 2021. Removal of organic micropollutants by well-tailored granular zeolites and subsequent ozone-based regeneration. J. Water Process Eng. 44, 102403. https://doi.org/10.1016/j.jwpe.2021.102403

Gao, L., Guo, Y., Zhan, J., Yu, G., Wang, Y., 2022. Assessment of the validity of the quenching method for evaluating the role of reactive species in pollutant abatement during the persulfate-based process. Water Res. 221, 118730. https://doi.org/10.1016/j.watres.2022.118730

Ghanbari, F., Moradi, M., 2017. Application of peroxymonosulfate and its activation methods for degradation of environmental organic pollutants: review. Chem. Eng. J. 310, 41–62. https://doi.org/10.1016/j.cej.2016.10.064

Huang, W.-C., Liu, M., Zhang, F.-G., Li, D., Du, Y., Chen, Y., Wu, Q.-Y., 2022. Removal of disinfection byproducts and toxicity of chlorinated water by post-treatments of ultraviolet/hydrogen peroxide and ultraviolet /peroxymonosulfate. J. Clean. Prod. 352, 131563. https://doi.org/10.1016/j.jclepro.2022.131563

Kang, H., Lee, D., Lee, K.-M., Kim, H.-H., Lee, H., Sik Kim, M., Lee, C., 2021. Nonradical activation of peroxymonosulfate by hematite for oxidation of organic compounds: a novel mechanism involving high-valent iron species. Chem. Eng. J. 426, 130743. https://doi.org/10.1016/j.cej.2021.130743

Kong, L., Fang, G., Xi, X., Wen, Y., Chen, Y., Xie, M., Zhu, F., Zhou, D., Zhan, J., 2021. A novel peroxymonosulfate activation process by periclase for efficient singlet oxygen-mediated degradation of organic pollutants. Chem. Eng. J. 403, 126445. https://doi.org/10.1016/j.cej.2020.126445

Levitsky, I., Tavor, D., Gitis, V., 2021. Microbubbles and organic fouling in flat sheet ultrafiltration membranes. Sep. Purif. Technol. 268, 118710. https://doi.org/10.1016/j.seppur.2021.118710

Li, M., Fu, S., Saedy, S., Rajendrakumar, A., Tichelaar, F.D., Kortlever, R., van Ommen, J.R., 2022. Nanostructuring Pt-Pd bimetallic electrocatalysts for

CO2 reduction using atmospheric pressure atomic layer deposition. ChemCatChem 14, e202200949. https://doi.org/10.1002/cctc.202200949

Li, M., Saedy, S., Fu, S., Stellema, T., Kortlever, R., Ommen, J.R. van, 2024. Enhancing the durability of Pt nanoparticles for water electrolysis using ultrathin SiO2 layers. Catal. Sci. Technol. 14, 1328–1335. https://doi.org/10.1039/D3CY00996C

Liang, C., Huang, C.-F., Mohanty, N., Kurakalva, R.M., 2008. A rapid spectrophotometric determination of persulfate anion in ISCO. Chemosphere 73, 1540–1543. https://doi.org/10.1016/j.chemosphere.2008.08.043

Lin, L., Feng, C., Lopez, R., Coronell, O., 2016. Identifying facile and accurate methods to measure the thickness of the active layers of thin-film composite membranes – A comparison of seven characterization techniques. J. Membr. Sci. 498, 167–179. https://doi.org/10.1016/j.memsci.2015.09.059

Lotfi, S., Fischer, K., Schulze, A., Schäfer, A.I., 2022. Photocatalytic degradation of steroid hormone micropollutants by TiO2-coated polyethersulfone membranes in a continuous flow-through process. Nat. Nanotechnol. 17, 417–423. https://doi.org/10.1038/s41565-022-01074-8

Lu, J., Stair, P.C., 2010. Nano/subnanometer Pd nanoparticles on oxide supports synthesized by AB-type and low-temperature ABC-type atomic layer deposition: growth and morphology. Langmuir 26, 16486–16495. https://doi.org/10.1021/la101378s

Ma, W., Sun, M., Huang, D., Chu, C., Hedtke, T., Wang, X., Zhao, Y., Kim, J.-H., Elimelech, M., 2022. Catalytic membrane with copper single-atom catalysts for effective hydrogen peroxide activation and pollutant destruction. Environ. Sci. Technol. 56, 8733–8745. https://doi.org/10.1021/acs.est.1c08937

Martinetti, C.R., Childress, A.E., Cath, T.Y., 2009. High recovery of concentrated RO brines using forward osmosis and membrane distillation. J. Membr. Sci. 331, 31–39. https://doi.org/10.1016/j.memsci.2009.01.003

Meng, C., Ding, B., Zhang, S., Cui, L., Ostrikov, K.K., Huang, Z., Yang, B., Kim, J.-H., Zhang, Z., 2022. Angstrom-confined catalytic water purification within Co-TiOx laminar membrane nanochannels. Nat. Commun. 13, 4010. https://doi.org/10.1038/s41467-022-31807-1

Militello, M.C., Simko, S.J., 1994a. Elemental palladium by XPS. Surf. Sci. Spectra 3, 387–394. https://doi.org/10.1116/1.1247783

Militello, M.C., Simko, S.J., 1994b. Palladium oxide (PdO) by XPS. Surf. Sci. Spectra 3, 395–401. https://doi.org/10.1116/1.1247784

Nandi, A., Chatterjee, I.B., 1987. Scavenging of superoxide radical by ascorbic acid. J. Biosci. 11, 435–441. https://doi.org/10.1007/BF02704692

Pickrahn, K.L., Garg, A., Bent, S.F., 2015. ALD of Ultrathin Ternary Oxide Electrocatalysts for Water Splitting. ACS Catal. 5, 1609–1616. https://doi.org/10.1021/cs501532b

PubChem, n.d. PubChem [WWW Document]. URL https://pubchem.ncbi.nlm.nih.gov/ (accessed 4.8.25).

Salehi, R., Mousavi, S.M., Taherian, M., 2019. Assessment of micellar-enhanced ultrafiltration process performance for removal of pharmaceutical contaminant from wastewater using response surface methodology. Int. J.

Environ. Sci. Technol. 16, 6199–6206. https://doi.org/10.1007/s13762-018-2021-3

Wang, Y., Hui, S., Zhan, S., Djellabi, R., Li, J., Zhao, X., 2020. Activation of peroxymonosulfate by novel Pt/Al2O3 membranes via a nonradical mechanism for efficient degradation of electron-rich aromatic pollutants. Chem. Eng. J. 381, 122563. https://doi.org/10.1016/j.cej.2019.122563

Yang, Y., Pignatello, J.J., Ma, J., Mitch, W.A., 2016. Effect of matrix components on UV/H2O2 and UV/S2O82− advanced oxidation processes for trace organic degradation in reverse osmosis brines from municipal wastewater reuse facilities. Water Res. 89, 192–200. https://doi.org/10.1016/j.watres.2015.11.049

Zhang, S., Hedtke, T., Zhu, Q., Sun, M., Weon, S., Zhao, Y., Stavitski, E., Elimelech, M., Kim, J.-H., 2021. Membrane-confined iron oxychloride nanocatalysts for highly efficient heterogeneous fenton water treatment. Environ. Sci. Technol. 55, 9266–9275. https://doi.org/10.1021/acs.est.1c01391

Zhang, S., Liang, Y., Yang, C., Venema, P., Rietveld, L.C., Heijman, S.G.J., 2024. Concentration polarizations of PEG and silica colloids in ceramic nanofiltration. Desalination 583, 117722. https://doi.org/10.1016/j.desal.2024.117722

Zhang, S., Quan, X., Zheng, J.-F., Wang, D., 2017. Probing the interphase “HO zone” originated by carbon nanotube during catalytic ozonation. Water Res. 122, 86–95. https://doi.org/10.1016/j.watres.2017.05.063

Zhang, S., Sun, M., Hedtke, T., Deshmukh, A., Zhou, X., Weon, S., Elimelech, M., Kim, J.-H., 2020. Mechanism of heterogeneous fenton reaction kinetics enhancement under nanoscale spatial confinement. Environ. Sci. Technol. 54, 10868–10875. https://doi.org/10.1021/acs.est.0c02192

Supporting information

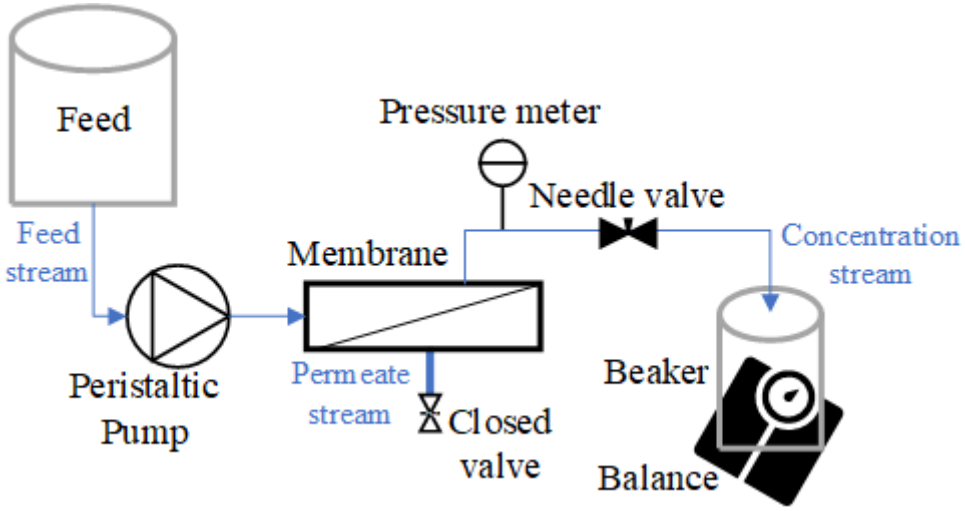

Figure S4.1. (a) The setup was designed for the examination of the performance of Pd coated on the membrane surface.

To examine the effect of Pd coating on the membrane surface, the setup (Fig. S4.1) was designed to ensure that the feed water only flowed over the membrane surface, where the permeate side of the membrane was closed by a valve.

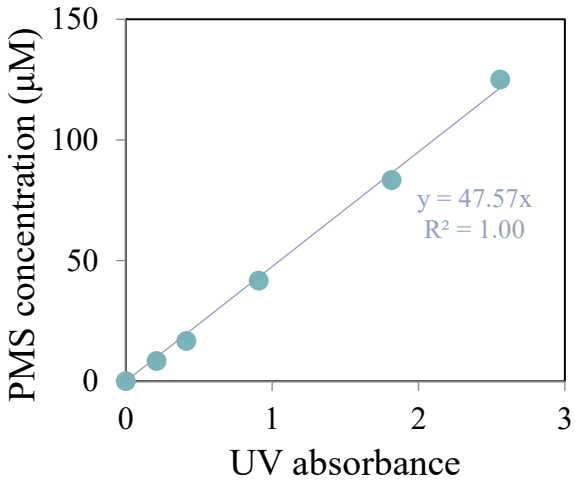

Figure S4.2. Calibrated curve of PMS concentration with UV absorbance at 352 nm.

The PMS concentration was measured by the UV method proposed by Liang et al., (2008), which relies on a reaction between PMS and iodide, resulting in the formation of iodine. In the calibration experiments, different volume of PMS stock solution (10 M) was added to the mixed solution containing 5 g/L $NaHCO_3$ and 100 g/L KI. Then the solution was shaken, and after 15 min, the sample was measured by UV (Genesys 10S UV-Vis, USA, λ = 352 nm). To determine the PMS concentration before, during, and after the OMPs degradation experiment, 1.5 mL sample was added to 1.5 mL stock solution containing $NaHCO_3$ and KI, and then it was measured by UV after 15 min.

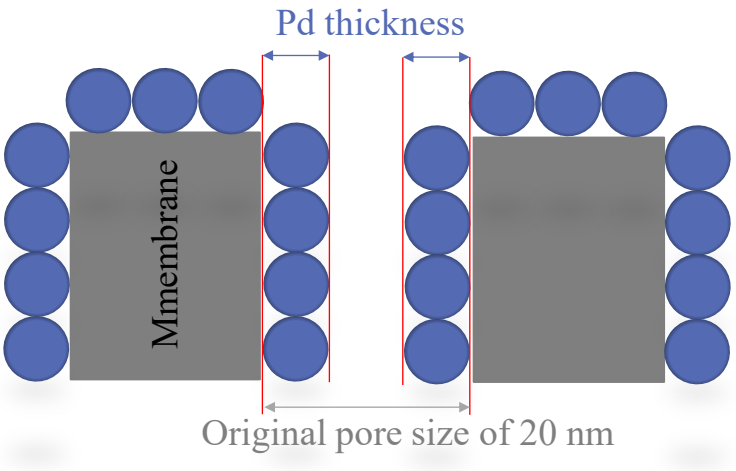

Figure S4.3. Pore sizes estimated based on the pore narrowing resulting from the grown Pd layer. The ALD growth rate of Pd on Al_2O_3 is 0.15-0.2 Å/cycle, which suggests that the Pd layer thickness after 30 and 60 ALD cycles will be 0.45-0.6 nm, and 0.9-1.2 nm, respectively. Assuming the original membrane pore (20 nm) walls on both sides are uniformly coated with Pd, the estimated pore sizes for the C30 and C60 membranes would be 18.8–19.1 nm, and 17.6–18.2 nm, respectively.

The pore size (r in nm) of membranes can also be calculated by comparing r before and after coating via the Carman-Kozeny equation (Eq. S4.1) (Levitsky et al., 2021). The pore size of 20 nm, specified by the manufacturer, was used for the pristine membranes.

$$r = \sqrt{\frac{J\ 8\ \mu\ H\ \tau}{\Delta P\ \phi\ \pi}} \qquad \text{(S4.1)}$$

where J is the flux (m/s), μ is the water dynamic viscosity (Pa s), H is the membrane thickness (m), τ is the pore tortuosity, ΔP is the applied pressure (Pa), ϕ is the porosity.

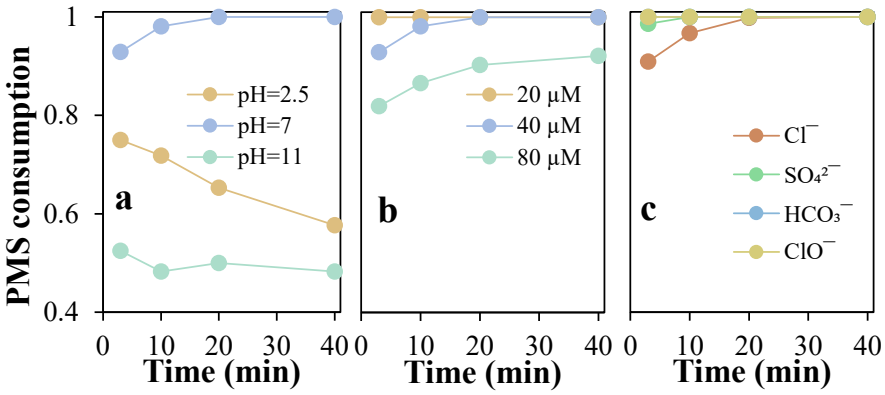

Figure S4.4. PMS consumption under different conditions (a) at pH of 2.5, 7, and 11, (b) with PMS concentration of 20, 40, and 80 μM, or with the addition of 1 mM anion of Cl^-, SO_4^{2-}, HCO_3^-, and ClO^-. Generally, the filtration experiment was conducted at a flux of 30 LMH, at a pH of 7, with 40 μM PMS, and without the injection of 1 mM anion.

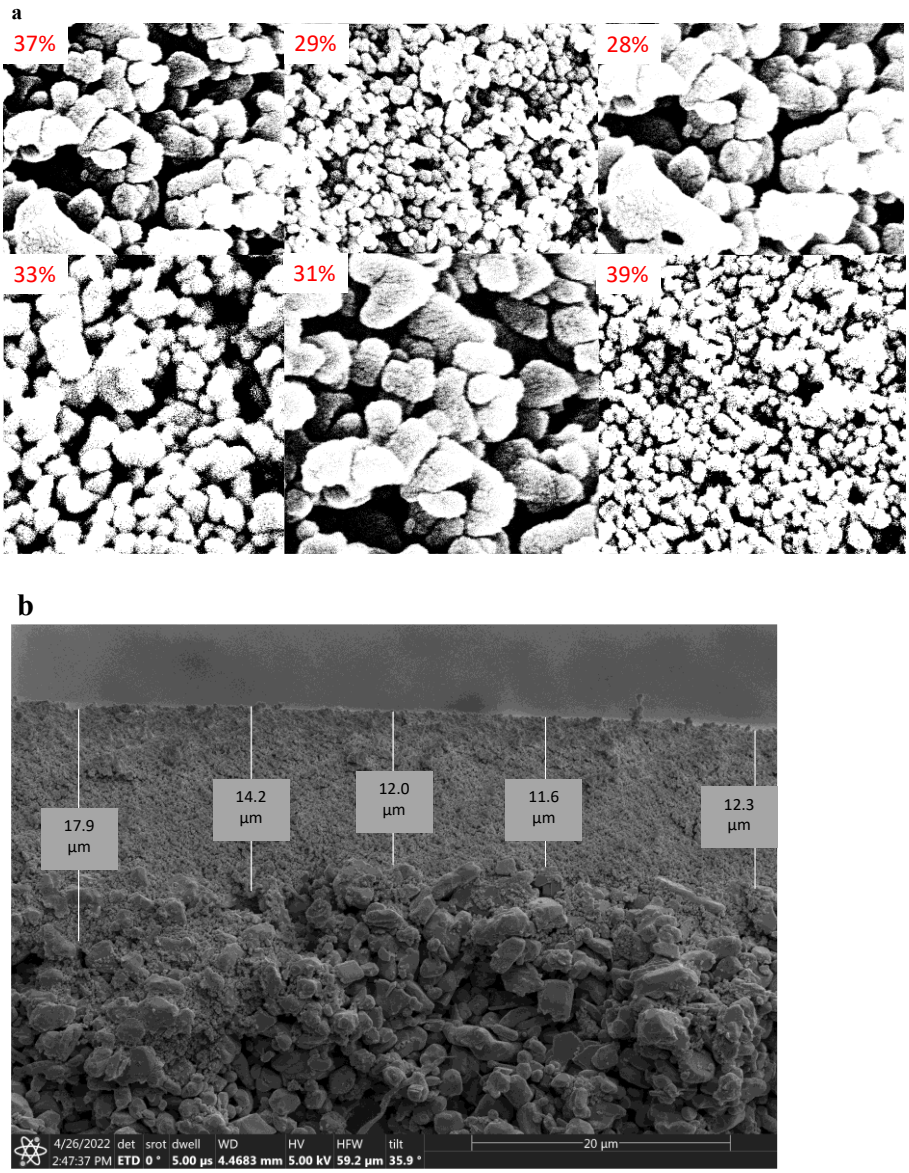

Figure S4.5. Porosity of different SEM top-view images of C30 (a), and the thickness of the selective layer of C30 (b), after examination by ImageJ.

Residence time calculation:

$$t = \phi \frac{J}{h} \tag{S4.2}$$

where t is the residence time (ms), ϕ is the porosity of the membrane (33%), J is the flux (m/ms), and h is the thickness of the selective layer (m). ϕ and h was determined by ImageJ (Fig. S4.5a and S4.5b) through the top-view and cross-section SEM image, respectively.

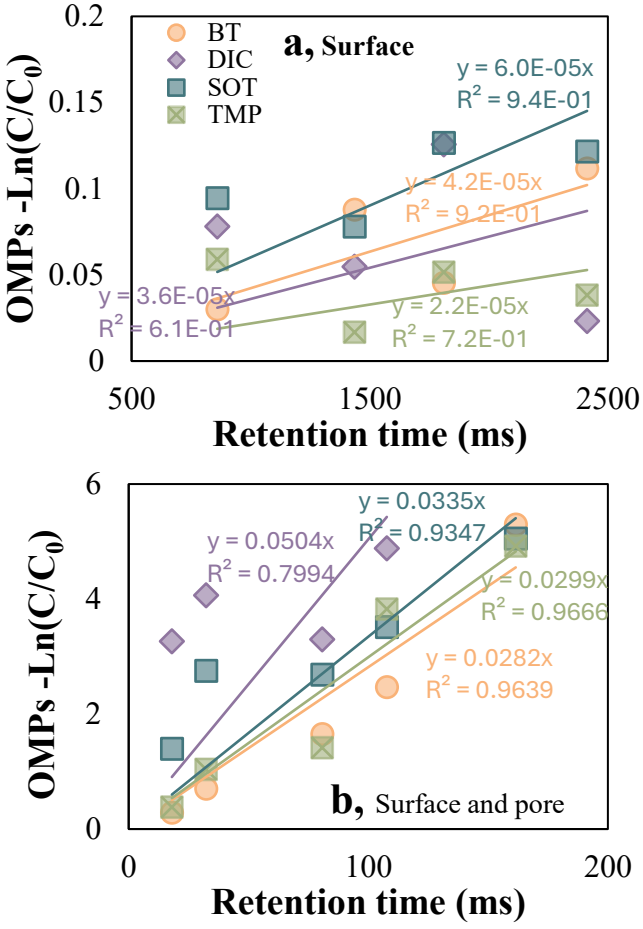

Figure S4.6. Degradation kinetics of OMPs with the presence of (a) Pd coated on the membrane surface and (b) Pd coated on the surface and in the pores.

The kinetics (K, in 1/ms) were calculated by Eq. S4.3, where C (in μg/L) is the concentration of OMP in the permeate side after oxidation, C_0 (in μg/L) is the initial concentration of OMP, and t (in ms) is the residence time computed by Eq. S4.2. Besides, the removal efficacy of OMPs was calculated by Eq. S4.4.

$$-ln\frac{C}{C_0} = K\,t \tag{S4.3}$$

$$\text{Removal efficacy } = 1 - \frac{C}{C_0} \tag{S4.4}$$

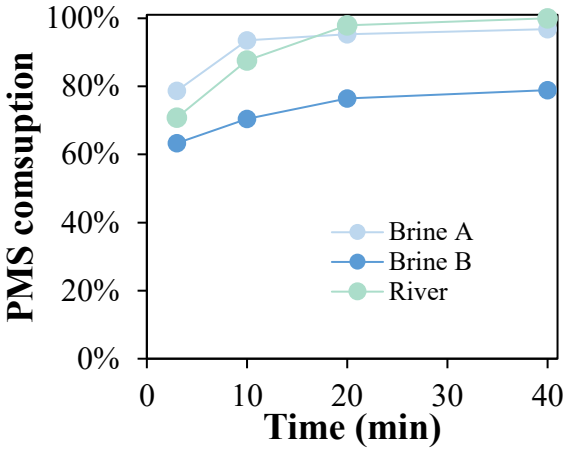

Figure S4.7. The consumption of PMS concentration in the oxidation of OMPs from brine A (with low anion concentration), brine B (with high anion concentration), and river water.

Table S4.1. Water quality parameters of brine and river water.

Water matrices	mg/L						
	Cl^-	Br^-	NH_4^+	NO_3^-	PO_4^{3-}	SO_4^{2-}	TDS
Brine water A	16.36	0.03	0.121	0.202	0.119	18.4	4573
Brine water B	81.81	0.14	0.606	1.011	0.595	91.9	22867
River water	1.44	0.02	/	0.073	0.014	0.7	568

The simulated brine A water was based on the previous work, while the brine B had the concentrated anions with a concentration five times higher than that of brine A (Yang et al., 2016). The river water was taken from collected from the Schie Canal (Delft, the Netherlands) with a chemical oxygen demand (COD) of 155 mg/L measured by the Hach spectrophotometer (DR 3900, US) with COD cuvettes (LCK 514 and LCK 314, Hach). The dissolved organic carbon (DOC, 23.7 mg/L), turbidity (0.354 NTU), and ion concentrations of river water were measured by the total organic carbon analyser (TOC-VCPH, Shimadzu, Japan), the turbidimeter (2100N, Hach, USA), and the ion chromatography (883 Basic IC plus, Metrohm Instrument, the Netherlands), respectively.

Table S4.2. The rejection of BT, DIC, SOT, and TMP by different kinds of membranes at different flux.

OMPs	Membrane	Flux (LMH)	Rejection	Reference
Benzotriazole (BT)	NF	36	10%	(Xu et al., 2020)
	NF	54	20%	
	NF	202	28%	(Acero et al., 2015)
	NF	202	29%	
	NF	202	29%	
	UF	89	44%	
	UF	89	34%	
	UF	89	49%	
Diclofenac (DIC)	NF	54	10%	(Maryam et al., 2020)
	NF	43	93%	(Kimura et al., 2003)
	RO	43	95%	
	UF	105	26%	(Plakas et al., 2019)
	UF	105	2.9%	
	NF	4.3	90%	(Alturki et al., 2010)
	NF	4.3	95%	
	UF	141	61%	(Vergili, 2013)
	NF	22.9	100%	(Radjenović et al., 2008)
	RO	22.5	100%	
	RO	22.5	100%	
	UF	76.4	44%	(Garcia-Ivars et al., 2017)
	UF	80.8	24%	
	UF	121.4	20%	
Sotalol (SOT)	NF	22.9	100%	(Radjenović et al., 2008)
	RO	22.5	90%	
	RO	22.5	100%	
	UF	64.15	32%	(Salehi et al., 2019)
	UF	141.51	17%	
	UF	128.3	13%	
	UF	183.01	5%	
Trimethoprim (TMP)	UF	76.4	24%	(Garcia-Ivars et al., 2017)

	UF	80.8	20%	
	UF	121.4	7%	
	NF	5.4	70%	
	NF	14.4	78%	
	NF	24.3	76%	
	NF	36	65%	(Xu et al., 2020)
	NF	54	75%	

Table S4.3. Scavengers used to eliminate the target reactive species, and the reaction kinetics between the radicals and scavengers or OMPs (Gao et al., 2022; Guo et al., 2022; Liu et al., 2019; Ma et al., 2019; Mahdi Ahmed et al., 2012; Mandal, 2018; Meng et al., 2022; Tay and Ismail, 2016; Wojnárovits and Takács, 2019; Xiao et al., 2022).

Scavenger /OMPs	Quench reactive species	$M^{-1} s^{-1}$			
		$K_{\bullet OH}$	$K_{SO4\bullet^-}$	$K_{O2\bullet^-}$	$K_{^1O2}$
MeOH	$^{\bullet}OH$, $SO4^{\bullet-}$	9.7×10^8	1.1×10^7	No reaction	3.89×10^3
TBA	$^{\bullet}OH$	4.8×10^9	8.3×10^5		1.8×10^3–3.0×10^3
FFA	$^1O_2$	1.5×10^{10}	1.3×10^{10}	3.5×10^3	1.2×10^8
LAA	$O_2^{\bullet-}$	4.5×10^9	1.0×10^8	5.4×10^6	
BT		7.6×10^9	1.1×10^9		
DIC		7.5×10^9	9.2×10^9		
SOT		7.9×10^9	3.0×10^{10}		
TMP		8.3×10^9	7.71×10^9	6.17×10^5	3.2×10^6

Reference

Acero, J.L., Benitez, F.J., Real, F.J., Rodriguez, E., 2015. Elimination of selected emerging contaminants by the combination of membrane filtration and chemical oxidation processes. Water. Air. Soil Pollut. 226, 139. https://doi.org/10.1007/s11270-015-2404-8

Alturki, A.A., Tadkaew, N., McDonald, J.A., Khan, S.J., Price, W.E., Nghiem, L.D., 2010. Combining MBR and NF/RO membrane filtration for the removal of trace organics in indirect potable water reuse applications. J. Membr. Sci. 365, 206–215. https://doi.org/10.1016/j.memsci.2010.09.008

Gao, L., Guo, Y., Zhan, J., Yu, G., Wang, Y., 2022. Assessment of the validity of the quenching method for evaluating the role of reactive species in pollutant abatement during the persulfate-based process. Water Res. 221, 118730. https://doi.org/10.1016/j.watres.2022.118730

Garcia-Ivars, J., Durá-María, J., Moscardó-Carreño, C., Carbonell-Alcaina, C., Alcaina-Miranda, M.-I., Iborra-Clar, M.-I., 2017. Rejection of trace pharmaceutically active compounds present in municipal wastewaters using ceramic fine ultrafiltration membranes: effect of feed solution pH and fouling phenomena. Sep. Purif. Technol. 175, 58–71. https://doi.org/10.1016/j.seppur.2016.11.027

Guo, Y., Long, J., Huang, J., Yu, G., Wang, Y., 2022. Can the commonly used quenching method really evaluate the role of reactive oxygen species in pollutant abatement during catalytic ozonation? Water Res. 215, 118275. https://doi.org/10.1016/j.watres.2022.118275

Kimura, K., Amy, G., Drewes, J.E., Heberer, T., Kim, T.-U., Watanabe, Y., 2003. Rejection of organic micropollutants (disinfection by-products, endocrine disrupting compounds, and pharmaceutically active compounds) by NF/RO membranes. J. Membr. Sci. 227, 113–121. https://doi.org/10.1016/j.memsci.2003.09.005

Levitsky, I., Tavor, D., Gitis, V., 2021. Microbubbles and organic fouling in flat sheet ultrafiltration membranes. Sep. Purif. Technol. 268, 118710. https://doi.org/10.1016/j.seppur.2021.118710

Liang, C., Huang, C.-F., Mohanty, N., Kurakalva, R.M., 2008. A rapid spectrophotometric determination of persulfate anion in ISCO. Chemosphere 73, 1540–1543. https://doi.org/10.1016/j.chemosphere.2008.08.043

Liu, W., Li, Y., Liu, F., Jiang, W., Zhang, D., Liang, J., 2019. Visible-light-driven photocatalytic degradation of diclofenac by carbon quantum dots modified porous g-C3N4: Mechanisms, degradation pathway and DFT calculation. Water Res. 151, 8–19. https://doi.org/10.1016/j.watres.2018.11.084

Ma, M., Chen, L., Zhao, J., Liu, W., Ji, H., 2019. Efficient activation of peroxymonosulfate by hollow cobalt hydroxide for degradation of ibuprofen and theoretical study. Chin. Chem. Lett. 30, 2191–2195. https://doi.org/10.1016/j.cclet.2019.09.031

Mahdi Ahmed, M., Barbati, S., Doumenq, P., Chiron, S., 2012. Sulfate radical anion oxidation of diclofenac and sulfamethoxazole for water decontamination. Chem. Eng. J. 197, 440–447. https://doi.org/10.1016/j.cej.2012.05.040

Mandal, S., 2018. Reaction rate constants of hydroxyl radicals with micropollutants and their significance in advanced oxidation processes. J. Adv. Oxid. Technol. 21. https://doi.org/10.26802/jaots.2017.0075

Maryam, B., Buscio, V., Odabasi, S.U., Buyukgungor, H., 2020. A study on behavior, interaction and rejection of paracetamol, diclofenac and ibuprofen (PhACs) from wastewater by nanofiltration membranes. Environ. Technol. Innov. 18, 100641. https://doi.org/10.1016/j.eti.2020.100641

Meng, S., Zhou, P., Sun, Y., Zhang, P., Zhou, C., Xiong, Z., Zhang, H., Liang, J., Lai, B., 2022. Reducing agents enhanced Fenton-like oxidation (Fe(III)/Peroxydisulfate): Substrate specific reactivity of reactive oxygen species. Water Res. 218, 118412. https://doi.org/10.1016/j.watres.2022.118412

Plakas, K.V., Mantza, A., Sklari, S.D., Zaspalis, V.T., Karabelas, A.J., 2019. Heterogeneous Fenton-like oxidation of pharmaceutical diclofenac by a catalytic iron-oxide ceramic microfiltration membrane. Chem. Eng. J. 373, 700–708. https://doi.org/10.1016/j.cej.2019.05.092

Radjenović, J., Petrović, M., Ventura, F., Barceló, D., 2008. Rejection of pharmaceuticals in nanofiltration and reverse osmosis membrane drinking water treatment. Water Res. 42, 3601–3610. https://doi.org/10.1016/j.watres.2008.05.020

Salehi, R., Mousavi, S.M., Taherian, M., 2019. Assessment of micellar-enhanced ultrafiltration process performance for removal of pharmaceutical contaminant from wastewater using response surface methodology. Int. J. Environ. Sci. Technol. 16, 6199–6206. https://doi.org/10.1007/s13762-018-2021-3

Tay, K.S., Ismail, N.S.B., 2016. Degradation of β-blockers in water by sulfate radical-based oxidation: kinetics, mechanism and ecotoxicity assessment. Int. J. Environ. Sci. Technol. 13, 2495–2504. https://doi.org/10.1007/s13762-016-1083-3

Vergili, I., 2013. Application of nanofiltration for the removal of carbamazepine, diclofenac and ibuprofen from drinking water sources. J. Environ. Manage. 127, 177–187. https://doi.org/10.1016/j.jenvman.2013.04.036

Warsinger, D.M., Tow, E.W., Maswadeh, L.A., Connors, G.B., Swaminathan, J., Lienhard V, J.H., 2018. Inorganic fouling mitigation by salinity cycling in batch reverse osmosis. Water Res. 137, 384–394. https://doi.org/10.1016/j.watres.2018.01.060

Wojnárovits, L., Takács, E., 2019. Rate constants of sulfate radical anion reactions with organic molecules: A review. Chemosphere 220, 1014–1032. https://doi.org/10.1016/j.chemosphere.2018.12.156

Xiao, R., Fu, Y., Bai, L., Chu, C., Ma, J., Wei, Z., Spinney, R., Dionysiou, D.D., Pu, J., 2022. Kinetics and mechanistic aspects of superoxide radical-mediated transformation of ascorbate. J. Environ. Chem. Eng. 10, 107736. https://doi.org/10.1016/j.jece.2022.107736

Xu, R., Zhou, M., Wang, H., Wang, X., Wen, X., 2020. Influences of temperature on the retention of PPCPs by nanofiltration membranes: Experiments and modeling assessment. J. Membr. Sci. 599, 117817. https://doi.org/10.1016/j.memsci.2020.117817

七律

指上残烟绕树深，西欧霜露自秋分。

平阳共照梁间鸟，大月独明塞外林。

只此孤鸦灯下影，之如野草宦游人。

荷兰再好非家院，信字连云作万金。

2021. 中秋

Chapter 5

Effect of fouling on the degradation of micropollutants by catalytic ceramic membranes activating peroxymonosulfate

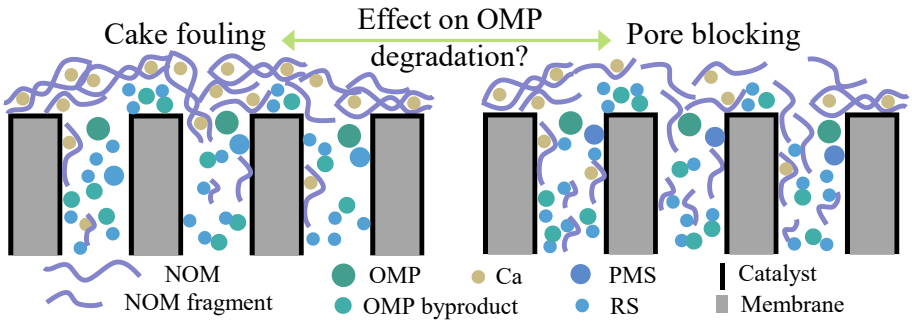

This chapter is based on

Zhang, S., Li, M., Ji, Y., Van Ommen, J. R., Rietveld, L. C., & Heijman, S. G. (2025). Effect of fouling on the degradation of micropollutants by catalytic ceramic membranes activating peroxymonosulfate. *To be submitted for publication*.

Abstract

Persistent fouling and the low rejection of organic micropollutants (OMPs) remain among the most significant challenges limiting the performance of ceramic ultrafiltration (UF) membranes. To address these, catalytic membranes have been coupled with peroxymonosulfate (PMS) to mitigate fouling and enhance OMP degradation simultaneously. However, it remains unclear how fouling influences the degradation of OMPs. In this study, palladium-modified ceramic UF membranes (Pd-UF) were employed to activate a low dosage of PMS for simultaneous fouling control and OMPs' degradation. The focus was on the effect of fouling on OMPs' degradation. We found that the Pd-UF membranes with PMS effectively mitigated fouling, and maintained a high degradation efficacy of OMPs, especially over multiple cycles. Although fouling severity and mechanism (pore blocking and cake fouling) were influenced by flux and feedwater chemistry (PMS concentration, foulant type, and calcium presence), fouling exhibited hardly any impact on PMS activation and OMPs' degradation. This was attributed to the size exclusion of the foulants, ensuring that the activity of the catalytic sites within the pores remained sufficient for PMS activation. Additionally, the nanoconfinement effect enriched PMS, reactive species (RS), and OMPs in the pores, thereby promoting their mass transfer. The dominant RS were almost consistent in fouling and non-fouling cases, but fouling influenced their relative contributions to OMPs' degradation and the oxidation pathway. The findings thus provided insights into the fouling control and its subsequent effect on OMPs' degradation, demonstrating the robustness of the coupled system of the Pd-UF membrane with PMS for water treatment, even under severe fouling.

5.1. Introduction

Ceramic ultrafiltration (UF) membranes have been increasingly applied in wastewater treatment due to their excellent chemical and thermal stability, high mechanical strength, and ease of cleaning via backwashing (Kramer et al., 2015). These properties make them particularly well-suited for long-term operation under harsh treatment conditions. Compared to polymeric membranes, ceramic membranes are more durable and allow for frequent cleaning without compromising integrity. Despite these advantages, their performance is still limited by two major challenges: persistent membrane fouling and the poor rejection of small organic micropollutants (OMPs). Fouling can cause considerable flux decline and increase cleaning frequency and operational costs, especially in the filtration of natural organic matter (NOM) such as alginate (Chen and Columbia, 2011). Simultaneously, the relatively large pore size of ceramic UF membranes (typically 10–100 nm) limits their ability to remove low-molecular-weight OMPs, resulting in the low rejection (Garcia-Ivars et al., 2017). These limitations restrict the broader application of ceramic UF membranes, particularly in treating complex water matrices that contain a mixture of NOM and trace contaminants.

To improve the removal of fouling and OMPs, a promising approach is to couple catalytic ceramic UF membranes with in-situ advanced oxidation processes (AOPs). Among the AOPs, peroxymonosulfate (PMS) has gained attention for degrading foulants and OMPs, due to its high redox potential (Dong et al., 2021; Zhao et al., 2020). In this hybrid system, catalytic membranes activate PMS to form reactive species (RS) during filtration, enabling simultaneous fouling mitigation and pollutant degradation. While size exclusion mechanisms help retain larger foulants and protect catalyst activity in membrane pores, the generated RS oxidizes foulants and OMPs, promoting a synergistic effect between physical separation and chemical oxidation. Nevertheless, most existing studies have focused either on fouling mitigation or on OMP degradation (Meng et al., 2022; Zhang et al., 2024, 2023; Zhao et al., 2020). This leaves a knowledge gap regarding the effect of fouling on the degradation of OMPs in this coupled system.

In the normal membrane filtration process, fouling can significantly alter membrane performance depending on its mechanism—whether through pore blocking, cake layer formation, or a combination of both. These mechanisms not only affect membrane permeability but can also influence the rejection of OMPs. For instance, pore blocking has been shown to enhance steric exclusion

and improve OMP rejection, while cake layer formation may reduce rejection efficacy (Zhu, 2015; Yangali-Quintanilla et al., 2009). Besides, the fouling behaviour is strongly influenced by operating conditions, such as flux, foulant type, and calcium concentration (Lin et al., 2024; Long et al., 2021). When AOPs are integrated with membrane filtration, RS may modify the fouling structure, leading to either fragmentation into smaller species or aggregation into larger clusters. This can result in a shift between fouling mechanisms from cake formation to pore blocking (Zhang et al., 2024), or the reverse (Zhao et al., 2020). Moreover, the presence of NOM in the feedwater can interfere with PMS activation by scavenging RS (Luo et al., 2024), competing with target pollutants (Dong et al., 2021), or deactivating catalytic sites (Awfa et al., 2020). These results provide insights into how fouling influences the normal or AOPs-based filtration processes. However, the effect of fouling on the degradation of OMPs in AOPs-based membrane systems remains poorly understood

This work explored the simultaneous fouling mitigation and OMP degradation by a catalytic ceramic UF membrane with low-dose PMS. The goal was to reveal the effect of fouling on the degradation of OMPs. A catalytic palladium (Pd) UF membrane (Pd-UF) was fabricated via atomic layer deposition (ALD), enabling uniform, low Pd loading throughout the membrane structure to facilitate PMS activation. A controlled dosage of PMS was introduced into the different feedwaters: (i) containing sodium alginate (SA) and benzothiazole (BT) as the model OMP due to its wide detection in wastewater and surface water. Traditional treatment, like adsorption, can remove 20-30% of BT (Kowalska et al., 2019); (ii) containing SA and multiple OMPs (BT, diclofenac (DIC), and sotalol (SOT)). The effects of process conditions on fouling and its subsequent influence on OMPs' degradation were examined, including PMS concentration, foulant type, flux, and calcium (Ca). Given that little is known about how fouling influences the dominant RS, scavenging experiments were conducted under both fouling and non-fouling conditions to determine the contribution of different RS to OMPs' degradation.

5.2. Materials and Methods

5.2.1. Ceramic UF membranes

Tubular ceramic UF membranes with a single channel and a nominal pore size of 20 nm were obtained from CoorsTek (the Netherlands). Composed of Al_2O_3 membrane layer and support layers, the membranes have a 7 mm internal diameter, a 10 mm external diameter, and a 100 mm length. The edges of the

membrane were sealed by a two-component epoxy adhesive (Hardener HW 5067–1 and Araldite AW 5047–1, VIBA, Netherlands) to prevent potential leaking during the filtration process.

The Pd-UF membranes were fabricated using ALD. $Pd(hfac)_2$ (Sigma-Aldrich) served as the precursor, formalin (Sigma-Aldrich) as the co-reactant, and ultrahigh purity nitrogen (99.999%) as the purging gas. To prevent the reabsorption of $Pd(hfac)_2$, the ALD reactor was preheated and maintained at 200 °C before initiating Pd deposition. The ALD cycle sequence was 30-30-40-30 s. During each cycle, $Pd(hfac)_2$ was introduced over the membrane substrate with a flow of 0.5 L/min, accompanied by 0.5 L/min N_2, for 30 s. Excess $Pd(hfac)_2$ was purged using 1 L/min N_2 for 30 s. Subsequently, a mixture of 0.7 L/min formalin and 0.3 L/min N_2 was introduced for 40 s, followed by another purging step with 1 L/min N_2 for 30 s. The process was repeated during 30 cycles.

5.2.2. Performance examination of the catalytic membrane

5.2.2.1. Filtration setup

The experimental setup (Fig. 5.1), designed for constant flux operation, consists of a syringe pump with a 300 mL stainless steel syringe (No. 1, Fusion 6000-X, Chemxy, USA), a pressure sensor (No. 2, GS4200-USB, ESI, UK) connected to a computer (No. 4), a module (No. 3) for tubular ceramic membranes, and a backwash vessel (No. 5) linked to a compressed air system (No. 6). During constant flux filtration, the valves No. 9 and 10 were opened, while valves of No. 7 and 8 remained closed. During backwash, the valves No. 9 and 10 were closed, while the valves of No. 7 and 8 were opened. For the backwash, demineralized water was pressurized from the backwash vessel under constant pressure, flowing from the permeate side to the concentration side.

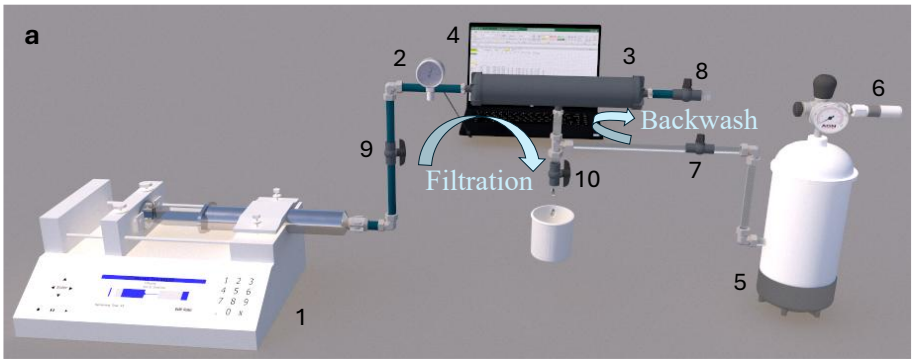

Figure 5.1. Constant flux setup for membrane filtration.

5.2.2.2. Fouling mitigation and OMPs' degradation

Performance comparison of the pristine and Pd-UF membranes. The performance of the pristine and Pd-UF membranes was evaluated, with and without PMS, to assess the cleaning efficacy of the fouled membranes. A fouling solution containing 10 mg/L SA (Sigma-Aldrich), 1 mM $CaCl_2$ (Sigma-Aldrich), 3.3 mM NaCl (Sigma-Aldrich), and with or without 40 μM PMS (Sigma-Aldrich), was filtered through the pristine and the Pd-UF membranes in a constant pressure setup (Fig. S5.1), starting filtration at 100 L/(m^2·h). After filtration, membrane cleaning was performed by backwashing with demineralized water for 1 min at 1 bar. The degradation of a single model compound, 5 μg/L BT (Sigma-Aldrich), was evaluated under SA fouling conditions using pristine and Pd-UF membranes in the presence of PMS. Samples were collected from the permeate side at specific time intervals, and then mixed with 40 mM $Na_2S_2O_3$ (Sigma-Aldrich) to stop the oxidation. The prepared solutions for the filtration experiments were adjusted to a pH of 7 by using HCl or NaOH.

Fouling mitigation and single OMP degradation in a single cycle under varying conditions. To better understand the fouling effect on OMP degradation by the Pd-UF membrane, the degradation of model OMP, BT, was examined across different experimental conditions at constant flux. The fouling solution was prepared by mixing 10 mg/L SA, bovine serum albumin (BSA, Sigma-Aldrich), or humic acid (HA, Sigma-Aldrich) with a background salt concentration of either 1 or 1.9 mM $CaCl_2$ and 3.3 mM NaCl. Then 5 μg/L BT together with 40, 100, or 400 μM PMS was injected into the fouling solution. The mixed solution was adjusted to a pH of 7. Before filtration, a sample was taken to check the initial BT and PMS concentration. Afterwards,

the mixed solution was filtered over the pristine and the Pd-UF membranes under a constant flux of 30, 100, or 150 L/(m^2·h), using the setup as shown in Fig. 5.1. After filtration, the backwash with demineralized water was performed at 1 bar for 1min Samples were taken from the permeate side, and mixed with 40 mM $Na_2S_2O_3$ (Sigma-Aldrich).

Fouling mitigation and multiple OMPs' degradation over multicycles. This experiment was designed to evaluate the long-term performance of the Pd-UF membrane in fouling removal and its effectiveness in degrading multiple OMPs. Therefore, a solution containing 10 mg/L SA, 1 mM $CaCl_2$, and 3.3 mM NaCl was mixed with BT, diclofenac (DIC, Sigma-Aldrich), and sotalol (SOT, Sigma-Aldrich) at 5 μg/L each, then adjusted to a pH of 7. Filtration (at 100 L/(m^2·h)) was applied to the pristine membrane without PMS and the Pd-UF membrane with 40 μM PMS for four cycles. 1 min backwash with demineralized water at 1 bar was used for the cleaning. Water samples were taken from the permeate side and then mixed with 40 mM $Na_2S_2O_3$.

Determination of the dominant RS. Considering the distinct reaction kinetics between scavengers and RS, different scavengers were employed to selectively target specific radicals (Gao et al., 2022; Nandi and Chatterjee, 1987). Tert-butanol (TBA, Sigma-Aldrich) was used to scavenge hydroxyl radicals (•OH), while ethanol (EtOH, Sigma-Aldrich) served to scavenge both •OH and sulfate radicals (SO_4•$^-$). Additionally, furfuryl alcohol (FFA, Sigma-Aldrich) was utilized to scavenge singlet oxygen ($^1O_2$), and L-ascorbic acid (LAA, Sigma-Aldrich) was applied to scavenge superoxide radicals (O_2•$^-$). In the scavenging experiment, each scavenger (1000 μM) was added into the mixed solution containing 10 mg/L SA with 1 mM $CaCl_2$ and 3.3 mM NaCl, the three OMPs (5 μg/L for each OMP), and 40 μM PMS. The solution was adjusted to a pH of 7. Then the prepared solution was filtered over the Pd-UF membrane at 100 L/(m^2·h). For comparison, a separate filtration experiment was conducted using the solution without SA, allowing the determination of RS under non-fouling conditions. The degradation of OMPs in the absence of both SA and scavengers served as a control. Water samples were collected from the permeate side and subsequently mixed with 40 mM $Na_2S_2O_3$.

5.2.3. OMPs and PMS concentration measurement

The UPLC-MS/MS (Waters ACQUITY UPLC I-Class, Xevo TQ-S micro with ESI) featuring a C18 column (ACQUITY UPLC™ BEH, 2.1 × 50 mm, 1.7 μm

particle size) and standard addition was used to determine the concentrations of the OMPs (Fu et al., 2021).

The PMS concentration was measured by adding 1.5 mL of a mixed solution containing 100 g/L KI (Sigma-Aldrich) and 5 g/L $NaHCO_3$ (Sigma-Aldrich) to 1.5 mL of the sample. The mixture was then analyzed by UV-Vis spectrophotometry at 352 nm, following the method proposed by Liang et al. (2008). The calibration curve and corresponding UV spectra for PMS concentration are shown in Fig. S5.2.

5.2.4. Data analysis

The resistance of the membrane was calculated by Eq. 5.1-5.3:

$$R_m = \frac{1}{\mu\, L_{pw}} \quad 5.1$$

$$R_t = \frac{1}{\mu\, L_p} \quad 5.2$$

$$R_{ir} = \frac{1}{\mu}\left(\frac{1}{L_{pn}} - \frac{1}{L_{p1}}\right) \quad 5.3$$

where R_m (in 1/m) is the resistance of the clean membrane, R_t (in 1/m) is the total resistance during filtration, R_{ir} (in 1/m) is the irreversible fouling resistance, μ (in Pa s) is the dynamic viscosity, L_{pw} (in m/(Pa s)) is the pure water permeability of the clean membrane, L_p is the permeability during fouling filtration, and L_{pn} is the initial permeability in the nth cycle fouling filtration.

The cake fouling mechanism was evaluated based on the work of Kirschner et al. (2019), as shown in Eq. 5.4:

$$TMP = TMP_0\,(1 + K_c\, J\, t) \quad 5.4$$

where TMP (in bar) is the transmembrane pressure measured during filtration, TMP_0 is the initial transmembrane pressure, K_c (in 1/m) is the cake filtration constant, J (in m/min) is the flux, and t (in min) is the filtration time.

The degradation efficacies of the OMPs and the consumption of PMS were calculated by the initial (C_0 in μg/L) and final (C in μg/L) concentrations, as shown in Eq. 5.5:

$$Removal\ efficacy\ or\ PMS\ consumption = 1 - \frac{C}{C_0} \quad 5.5$$

5.3. Results and discussion

5.3.1. Performance of the pristine and Pd-UF membranes

To examine the efficacy of the Pd-UF-PMS system, its performance was compared with that of the pristine membrane with and without PMS, as shown in Fig. 5.2. The filtration started with an initial flux of 100 L/(m^2·h) at each cycle by the constant pressure setup, followed by backwashing with demineralized water at 1 bar for 1 min to assess cleaning efficacy.

Similar permeability declines (Fig. 5.2a) were observed in the pristine membrane without PMS, the Pd-UF membrane without PMS, and the pristine membrane with PMS. This indicates that without PMS activation by the catalyst, the pristine and Pd-UF membranes were ineffective in mitigating the effect of fouling on permeability loss. However, the permeability of the Pd-UF-PMS system exhibited a moderate decline, stabilizing at 76%, which was 8%–12% higher than the other three filtration modes. Moreover, after backwashing, the Pd-UF-PMS system showed the highest cleaning efficacy, being 62% (Fig. 5.2b), outperforming the Pd-UF membrane without PMS (44%), the pristine membrane with PMS (26%), and the pristine membrane without PMS (13%). This can be attributed to the strong oxidation of SA by RS, which makes the oxidized SA fragments easier to be flushed away. The Pd-UF membrane without PMS also exhibited a relatively high backwash efficacy of 44%. Previous studies have reported that the zeta potential of Pd at pH 7 is approximately -35 mV, much lower than -15 mV of the pristine Al_2O_3 membranes (Chen et al., 2022; Sathishkumar et al., 2009). This suggests that the Pd-UF membranes are more negatively charged than the pristine membranes, which weakens the interaction between the foulants and the membrane surface, thereby facilitating their removal during backwashing. With the Pd-UF membrane, PMS was completely and rapidly consumed by the Pd-UF membrane during two-cycle filtration (Fig. 5.2c and S5.3a). This indicates that the Pd-UF membrane effectively activated and consumed PMS. In contrast, only partial PMS consumption was observed with the pristine

membrane, which can be attributed to PMS self-decomposition or the limited catalytic activity of the Al_2O_3-made pristine membrane (Li et al., 2024).

Fig. 5.2d shows that 18% and 12% BT were degraded by the pristine membrane with PMS in the first and second filtration, respectively, whereas almost complete degradation (93%-99%) of BT was achieved by the Pd-UF-PMS system in two-cycle filtration. Due to fouling, flux exhibited a moderate decline in the constant pressure filtration (Fig. S4). However, Fig. S3b shows that fouling had a limited impact on BT degradation by the Pd-UF-PMS system during the 45-min filtration.

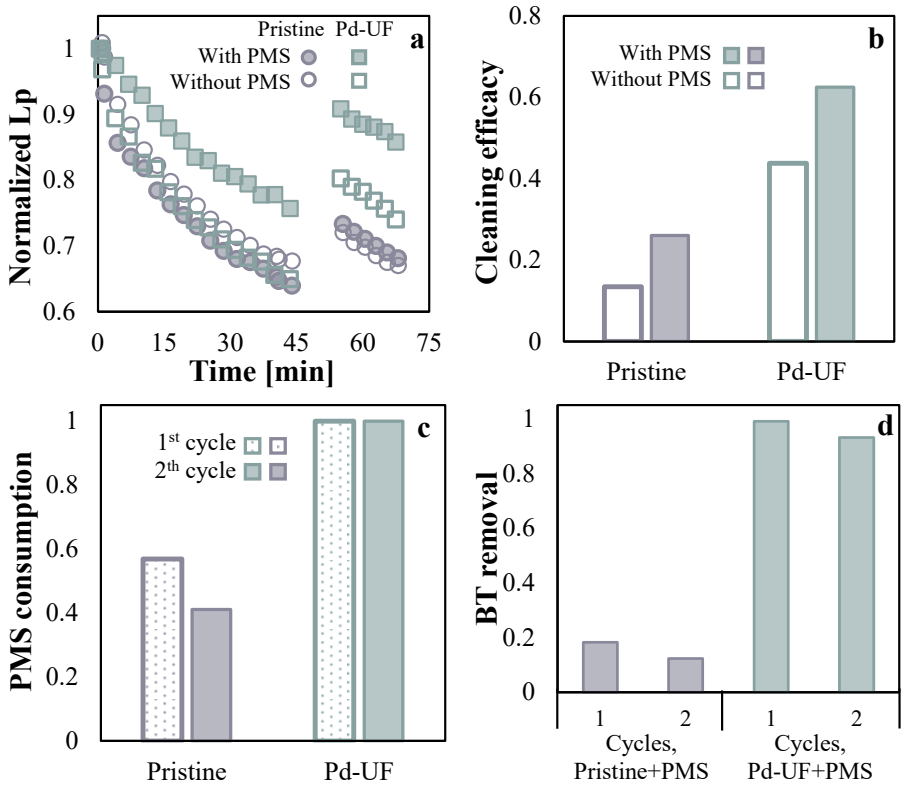

Figure 5.2. Normalized permeability in the filtration by the pristine membrane and the Pd-UF membrane with and without PMS (a), cleaning efficacies (b), PMS concentrations (c), and BT degradation by the pristine membrane and the Pd-UF membrane with 40 μM PMS. The performance was evaluated under constant pressure filtration, starting with an initial flux of 100 L/(m^2·h). The concentrations of alginate, BT, and PMS were 10 mg/L, 5 μg/L, and 40 μM, respectively.

5.3.2. Effect of PMS concentration

Higher PMS concentrations typically enhance both fouling mitigation and OMP degradation. However, it remains unclear how fouling, which is influenced by the PMS concentration, impacts the degradation efficiency of OMPs (Asif et al., 2021; Zhou et al., 2023). Therefore, we examined the impact of PMS concentration (40, 100, and 400 μM) on fouling mitigation and the subsequent effect on the degradation of model OMP, BT.

Normalized permeability (Fig. 5.3a) showed that after 45-min filtration, the Pd-UF membrane maintained 68%, 74%, and 95% of its initial flux for 40, 100, and 400 μM PMS, respectively, indicating enhanced fouling mitigation at higher PMS concentrations. In comparison, the permeability of the pristine membrane dropped to 64%. After 45-min filtration, the pristine membrane without PMS showed the highest R_t (2.6×10^{12} 1/m), followed by the Pd-UF membrane with 40 μM PMS (2.5×10^{12} 1/m), 100 μM PMS (2.2×10^{12} 1/m), and 400 μM PMS (1.7×10^{12} 1/m), respectively, as shown in Fig. 5.3b. The higher permeability drop and resistance in the pristine membrane align with the study by Lin et al. (2021), which is attributed to the compressed SA cake fouling. In the Pd-UF-PMS system, its lower permeability drop can be ascribed to the generation of RS through PMS activation, which facilitates the degradation of SA fouling (Zhao et al., 2020).

To analyze the fouling mechanism, the cake model for constant-flux filtration was applied to the TMP/TMP_0 versus time curve (Fig.5. 3c). The highest cake filtration constant (K_c) of 8.0 1/m was found in the filtration by the pristine membrane without PMS. However, the constant of K_c showed a decrease with PMS for the Pd-UF membranes. Similarly, the correlation coefficient values (R^2) for cake fouling also decreased with the increase of PMS concentration, suggesting the cake fouling was mitigated at higher PMS level. In contrast, R^2 for pore blocking was maintained at a high level, even at 400 μM PMS (Fig. S5.5), indicating that pore blocking was still significant under these conditions. These results perhaps suggest a shift in the dominant fouling mechanism from cake layer formation to pore blocking, likely due to the generation of smaller SA fragments at higher PMS concentrations.

The consumption of PMS, as presented in Fig. 5.3d, shows that 97%, and 94% of PMS were decomposed at 40 μM, and 100 μM, respectively. However, in 400 μM PMS case, both the overall PMS consumption and PMS consumption rate decreased, likely due to the limited active sites. This suggests that while

the Pd-UF membrane effectively activated PMS, optimizing PMS dosage is important for improving its utilization, minimizing treatment costs, and reducing the residual PMS in the effluent.

To understand the effect of fouling on BT degradation, BT degradation by PMS alone and BT removal by the pristine membrane without PMS were compared to the degradation of BT in the Pd-UF-PMS system. PMS alone had a moderate effect on BT degradation, as shown in Fig. 5.3e. In addition, a low BT removal of 6.5% was found for the pristine membrane without PMS (Fig. 5.3f). These findings demonstrate that direct PMS oxidation or separation by the pristine membrane has a limited effect on BT removal.

As reported by Wang et al. (2022), the presence of NOM could inhibit the degradation of OMPs due to competition for reaction sites and reduced catalytic areas. However, this limitation was not observed in the Pd-UF-PMS system. Although PMS concentration had a considerable effect on fouling (Fig. 5.3a), its impact on BT degradation was minor (Fig. 5.3f), even at the lowest PMS concentration under fouling condition. Compared to PMS alone and the pristine membrane without PMS, the Pd-UF-PMS system achieved near-complete BT degradation, with efficacies of 100%, 100%, and 98% at 40, 100, and 400 μM PMS, respectively (Fig. 5.3f).

Zhao et al. (2020) have reported that the presence of PMS during filtration by a catalytic ceramic membrane could alter the fouling mechanism, which is consistent with our results. As shown in Fig. 5.3c, the fouling mechanism shifted from cake layer formation to pore blocking with increasing PMS concentration. Katsoufidou et al. (2007) have also reported that broken, and thus smaller, SA fragments can clog the membrane pores, leading to more pore blocking, which, in turn, causes a prominent permeability decline. Since PMS influences fouling, the mechanism of BT degradation may also vary depending on the fouling mechanisms affected by PMS concentration. At low PMS concentrations, fouling mainly forms a cake layer on the membrane surface (Fig. 5.3c and Fig. S5.5), preventing foulants from infiltrating into the pores. This, in turn, will reduce the competing reaction, thus promoting the OMPs' degradation. At high PMS concentration, more broken SA with a smaller size can infiltrate the pores. However, the high PMS concentration enhanced the generation of RS, which compensated for any fouling-induced limitations and thereby maintained high BT degradation efficacy.

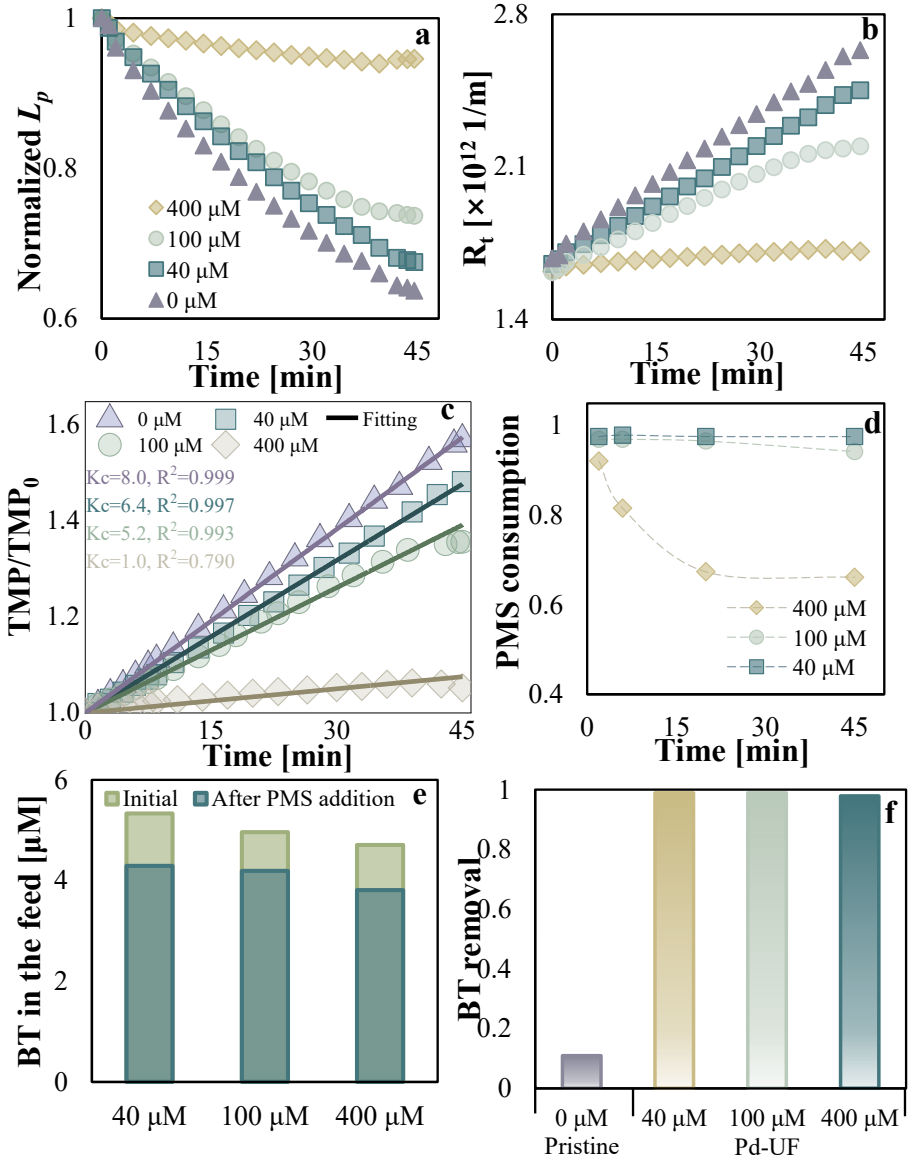

Figure 5.3. The performance of the pristine membrane without PMS and of the Pd-UF membrane with PMS, examined at the flux of 100 L/(m^2·h): (a) normalized permeability, (b) total resistance, (c) normalized TMP and cake fouling mechanism fitting, (d) PMS consumption, (e) BT concentration in the feed before and after dosing PMS, and (f) BT degradation after membrane filtration.

5.3.3. Effect of foulant type

Membrane fouling by BSA, HA, and SA—representing protein, humic substances, and polysaccharides, respectively—was studied. These compounds are major fractions of NOM that are commonly found in natural and industrial wastewater systems (Wang et al., 2023).

Fig. 5.4a shows that BSA fouling resulted in the most rapid permeability decline, with permeability dropping to 51%, followed by SA (68%), and HA (95%). The Pd-UF-PMS system at 100 L/(m^2·h) experienced the highest resistance (R_t) with BSA fouling (3.2 × 10^{12} 1/m), followed by SA (2.5 × 10^{12} 1/m) and HA (1.6 × 10^{12} 1/m). A similar trend has been reported for Fe-activated PMS in treating these NOM fractions during nanofiltration (Bai et al., 2021). Additionally, Angelis and Cortalezzi (2016) have reported that BSA resulted in the lowest mineralization efficiency (below 60%) by Fenton-like reactions, compared to approximately 80% for HA and SA. This suggests that BSA is harder to be degraded by AOPs than HA and SA. Therefore, BSA led to more severe fouling. Fig. S5.6 shows that intermediate pore blocking governed HA filtration, while both pore blocking (intermediate and standard) and cake fouling were predominant in the filtration of BSA and SA. Although the size of these three foulants followed the order HA>BSA>SA (Bai et al., 2021), it seems that HA was more easily degraded by the Pd-UF-PMS system, thus producing smaller byproducts that led to the intermediate pore clogging. In contrast, the pronounced pore blocking and cake fouling observed with BSA and SA can be attributed to their partial fragments and the subsequent formation of larger aggregates through aggregation. (Yang et al., 2023).

Coexisting substances can typically react with RS at high kinetics, which could influence OMPs' degradation to varying degrees, due to the competitive reactions (Hwang et al., 2020; Wang et al., 2022). However, despite the presence of different types of foulants (HA, BSA, and SA), a nearly complete degradation of BT was observed in all fouling cases (Fig. 5.4c). This indicates that competitive reactions associated with these foulants hardly had an impact on BT degradation in Pd-UF-PMS system. This can be attributed to the size exclusion, which prevents parts of the fouling from infiltrating into the pores and contaminating the catalyst in the pores. In addition, the nanoconfinement effect can facilitate the generation of sufficient RS within the pores (Zhang et al., 2021), effectively compensating for any potential competitive reactions caused by the foulants, even under severe internal pore blocking. As reported by Chang et al. (2025), nanoconfined catalytic macrostructures can enrich

PMS, OMPs, and RS, thus promoting their mass transfer for the enhanced degradation efficacy. Furthermore, the high PMS consumption (see Fig. 5.4d) also shows that different foulants and fouling mechanisms had limited effects on PMS activation.

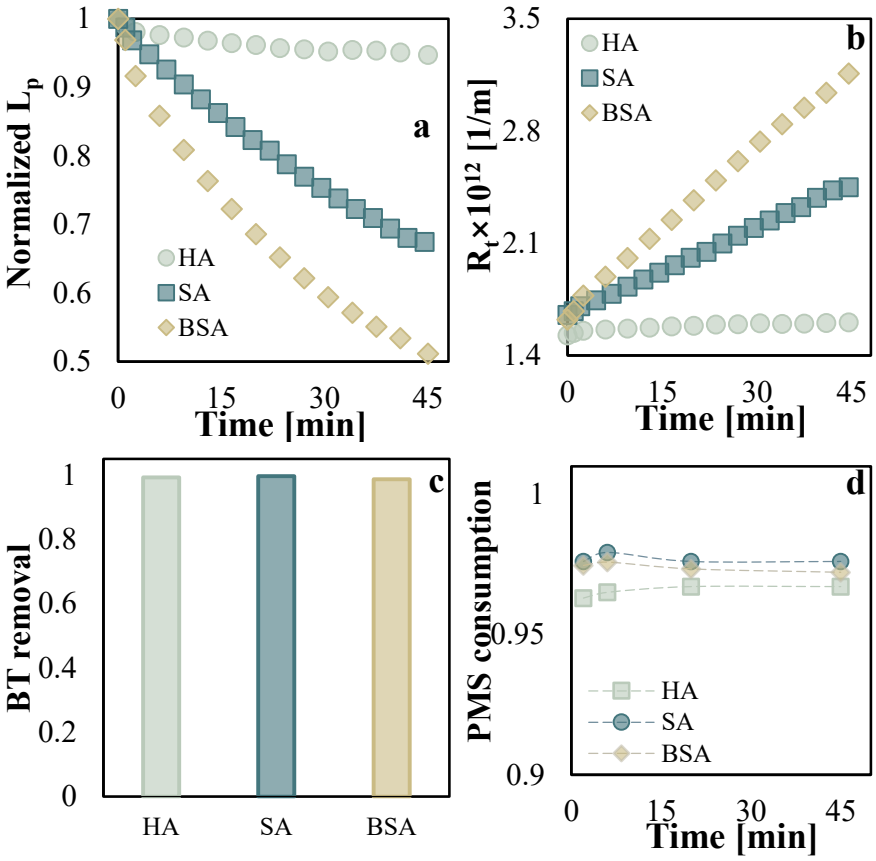

Figure 5.4. The normalized permeability (a), total membrane resistance (b), BT degradation (d), and PMS consumption (c), under the 10 ppm HA, SA, and BSA fouling conditions in constant flux filtration with 40 μM PMS at 100 L/(m^2·h) by the Pd-UF membrane.

5.3.4. Effect of flux

Flux could play a critical role in fouling and can also influence the degradation efficacy of OMPs (Chen et al., 2022; Lotfi et al., 2022). To study these effects, fouling and BT degradation were examined under varying constant flux conditions, as shown in Fig. 5.5.

Normalized permeability at 30 L/(m^2·h) exhibited a gradual and mild decline, dropping to 92% by the end of filtration. However, under higher flux conditions, a more rapid and higher permeability drop was observed, as shown in Fig. 5.5a. Similarly, the R_t values (Fig. 5.5b), at 30 L/(m^2·h) (7.7×10^{11} 1/m) were 2.7 and 4.8 times lower than the values at 100 L/(m^2·h) (2.1×10^{12} 1/m) and 150 L/(m^2·h) (3.7×10^{12} 1/m), respectively. The higher permeability decline and resistance at the higher flux are, as expected, caused by the higher accumulation of SA on the surface. Moreover, the reduced retention time (Fig. S7) of RS at higher flux will also limit fouling degradation during filtration, thereby hindering the detachment of SA from the membrane surface. The influence of retention time is further supported by the observed shift in fouling mechanisms. At lower flux, where retention time is longer, the dominant mechanism appears to shift from cake formation to pore blocking (Fig. S5.8). This shift is likely due to enhanced SA degradation, resulting in smaller fragments that contribute more to pore blockage than to cake layer formation.

Fig. 5.5c shows that BT was completely degraded below the flux of 100 L/(m^2·h) in both fouling and non-fouling cases, while the degradation efficacy decreased to approximately 92% at 150 L/(m^2·h) for both conditions. This suggests that, although different fouling mechanisms (severe pore blocking or cake fouling) occur at varying flux levels (Fig. S5.8), SA fouling has a negligible impact on BT degradation. A high PMS consumption was also observed in all cases, reaching approximately 97% in fouling conditions, and 89%-96% under non-fouling conditions, as shown in Fig. 5.5d. The high effectiveness of the Pd-UF membrane at high fluxes is most likely attributable to the synergistic effect between membrane separation and nanoconfinement (Zhang et al., 2021). However, the kinetics regression analysis (Fig. S5.9) suggests that the optimal operating flux was 100 L/(m^2·h), as the kinetics of BT oxidation and PMS consumption would reach a plateau at flux levels below 100 L/(m^2·h).

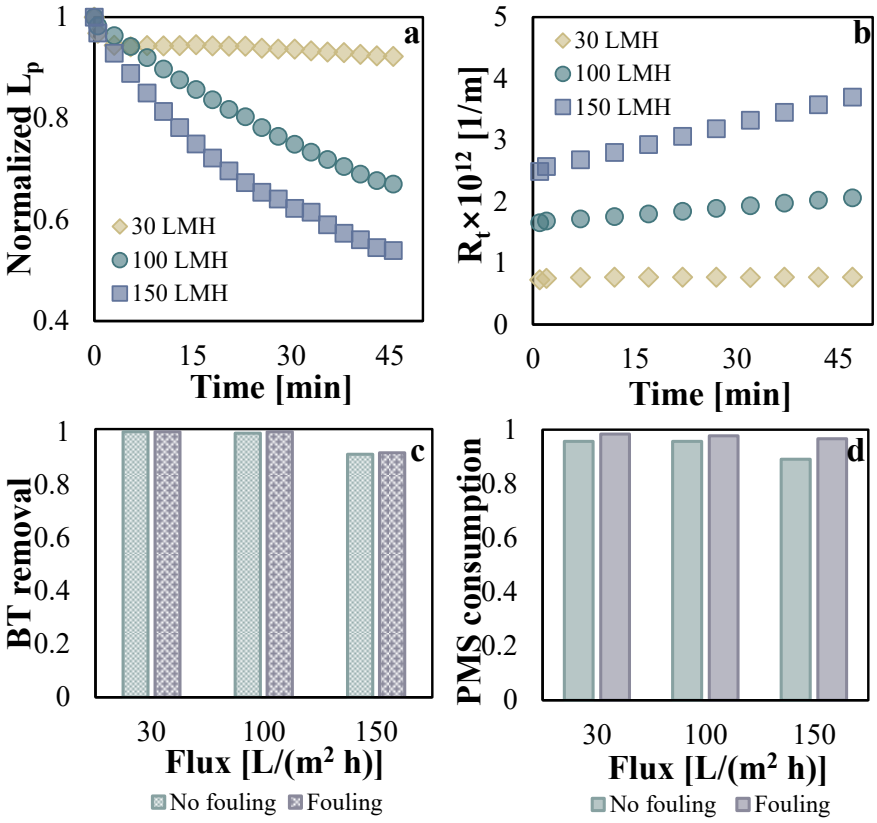

Figure 5.5. Fouling curves (a), R_t (b), BT degradation (c), and PMS consumption (d) under different constant fluxes. The degradation efficacy of BT and consumption of PMS under no fouling conditions were also studied for comparison.

5

5.3.5. Effect of Ca

In the treatment of SA-enriched feed water using membranes, SA fouling structures can form either stretchy egg-box gel layers at a low Ca concentration or rigid cross-linked clusters at a higher Ca concentration, as reported by Zhang et al. (2017). These structural differences, in turn, could influence both the fouling and the oxidation process. Hence, Ca-ion concentrations of 1 mM and 1.9 mM were used to study their effect on fouling and OMPs' degradation by the Pd-UF membrane with 40 µM PMS (at 100 L/(m^2·h)), as shown in Fig. 5.6.

Compared to the high permeability drop of 33% observed in the Pd-UF membrane with 1 mM Ca and PMS, mild permeability declines below 10%

were found in the Pd-UF membrane with 1.9 mM Ca and PMS. The high permeability decline observed at 1 mM Ca is likely attributed to the formation of smaller SA–Ca colloids capable of penetrating membrane pores, the compressibility of the egg-box structure, and its susceptibility to oxidative degradation into smaller fragments(Katsoufidou et al., 2008; Lin et al., 2023). Conversely, high Ca concentrations promoted the formation of rigid SA clusters through strong SA-Ca interactions (Zhang et al., 2017). These rigid clusters were more resistant to degradation by AOPs and were more difficult to compress. As a result, larger SA-Ca structures remained in the case of 1.9 mM Ca, reducing the possibility of pore blocking, and thereby mitigating the permeability decline. Although the Pd-UF-PMS system experienced a high permeability loss in the 1 mM Ca case, it achieved complete BT degradation (Fig. 5.6b). However, the removal efficacy of BT was reduced to 81% in the case of 1.9 mM Ca. This is presumably because the higher Ca concentration (1.9 mM) increases the zeta potential of the SA-Ca fouling layer (You et al., 2020), and consequently enhances the adsorption of negatively charged PMS onto the fouling surface. As a result, less PMS can be available for activation at the catalytic areas, thus inhibiting RS generation, and resulting in lower BT degradation efficacy. Further study is needed to explore how Ca concentrations influence alginate structures and how these structural differences, in turn, affect the degradation of OMP.

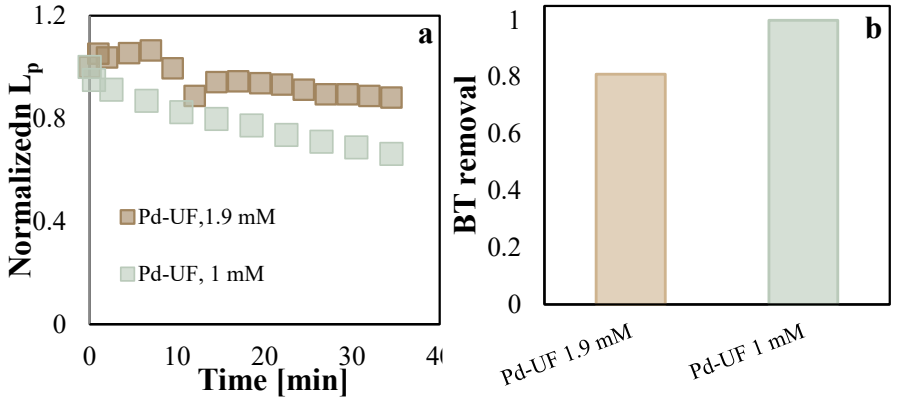

Figure 5.6. The effect of Ca (1 and 1.9 mM) on the removal of fouling (a) and BT (b) by the Pd-UF membrane with 40 μM PMS at 100 L/(m^2·h).

5.3.6. Fouling and multiple OMPs' degradation over multicycles

From Fig. 5.3a, it can be concluded that dosing of 40 μM PMS had a limited effect on fouling mitigation during a single-cycle Pd-UF membrane filtration at the flux of 100 L/(m^2·h), compared to the pristine membrane without PMS dosing. To further study fouling and permeability recovery, multi-cycle fouling and cleaning cycles were conducted under constant flux. A SA solution containing multiple OMPs (BT, DIC, and SOT) and 1 mM Ca was employed for filtration by the Pd-UF membrane with 40 μM PMS and by the pristine membrane without PMS. After each filtration cycle with a constant flux of 100 L/(m^2·h), the membrane was backwashed with demineralized water at 1 bar for 1 min, and the fouling and cleaning processes were repeated for four cycles, as illustrated in Fig. 5.7.

Before the first two cycles, the normalized permeability of the Pd-UF-PMS system (Fig. 5.7a) was similar to that of the pristine membrane without PMS. However, in the third and fourth cycles, the permeability of the Pd-UF membrane recovered to 70% and 61% of its initial value, respectively, after backwashing. In contrast, the pristine membrane without PMS experienced a continuous decline in permeability, dropping to 45% after the fourth cycle. These findings align with the results of R_{ir}, as shown in Fig. 5.7b, where R_{ir} values of the pristine membrane were higher than those of the Pd-UF membrane in all cycles. In addition, the irreversible fouling index ($UMFI_i$) of the Pd-UF-PMS system was 0.003 m^2/L, lower than 0.005 m^2/L for the pristine membrane without PMS, as shown in Fig. S5.10. These results indicate that RS generated from the Pd-UF-PMS system can effectively remove SA fouling, thereby enhancing backwash efficacy for fouling detachment. In contrast, in the absence of AOPs, SA fouling formed a dense, compressed cake layer, which is more difficult to remove, thus leading to ineffective hydraulic backwash, as found in the pristine membrane without PMS.

PMS consumption by the Pd-UF membrane (Fig. 5.7c) showed a moderate decline after the first filtration/backwash cycle but subsequently stabilized at approximately 75% over the following cycles. Probably, after the first fouling cycle, SA deposition partially covered the catalytic sites, and the backwash was insufficient to fully restore them. As a result, the reduced availability of active sites led to a decrease in PMS activation for the degradation of fouling. However, the inhibited PMS activation had a limited effect on the OMPs' degradation by the Pd-UF-PMS system (Fig. 5.7d). Only BT degradation efficacy decreased from 100% in the first cycle to 79% in the last cycle, while

DIC and SOT were completely degraded throughout all cycles. In contrast, the pristine membrane without PMS experienced a gradual decline in OMPs' rejection over multicycles (Fig. 5.7d). In addition, a much lower rejection of all OMPs (0%-11%) was observed in the pristine membrane without PMS. Moreover, PMS alone had minimal effect on OMP degradation, as the concentrations of BT, DIC, and SOT in the feed showed little change before and after PMS addition (Fig. S5.11).

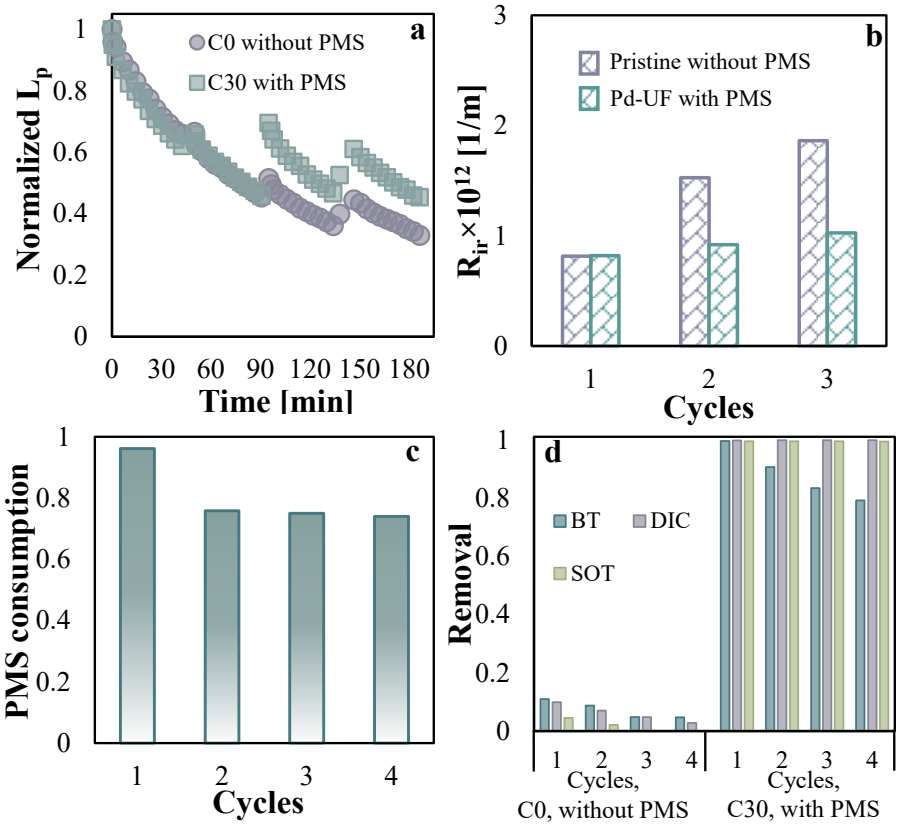

Figure 5.7. Membrane performance in four-cycle operations: normalized permeability (a), irreversible fouling resistance (b), PMS consumption (c), and degradation of BT, DIC, and SOT (d), by the pristine membrane without PMS and the Pd-UF membrane with 40 μM PMS under 100 L/(m^2·h) filtration, followed by a 1-min backwash with demineralized water at 1 bar.

5.3.7. Dominant RS for the degradation of multiple OMPs

The dominant RS in AOPs is typically identified through scavenging experiments, where specific scavengers of TBA, EtOH, FFA, and LAA are individually introduced into the feed solution to selectively scavenge the corresponding RS. A previous study has reported that the dominant RS are dependent on the type of OMPs (Wu et al., 2017). However, the effect of fouling on RS is unclear. Hence, the influence of fouling on RS contribution to the degradation of multiple OMPs was studied. Control experiments were conducted by exploring OMPs' degradation by the Pd-UF-PMS system in the absence of SA and scavengers.

The control experiments (Fig. 5.8a-5.8d) showed that all OMPs (BT, DIC, and SOT) were completely degraded by the Pd-UF-PMS system. However, the presence of scavengers exhibited varying degrees of inhibition on the degradation of the various OMPs. In the absence of SA fouling, BT degradation was governed by both •OH and $^1O_2$, DIC by $O_2•^-$, and SOT by both $^1O_2$ and $O_2•^-$, respectively. This observation is consistent with a previous study showing that different RS contribute differently to the degradation of various OMPs (Rao et al., 2023). Furthermore, scavenging results under fouling conditions revealed that the degradation of BT was dominated by •OH, DIC by $O_2•^-$, and SOT by both $^1O_2$ and $O_2•^-$, respectively. Except for BT, the dominant RS for BT, DIC, and SOT remained the same under both fouling and non-fouling conditions. However, the presence of SA altered the role of RS in OMPs' degradation. This was observed in all cases where the relative contributions of RS to the degradation of OMPs were changed in the presence of SA fouling. For example, the degradation of SOT was increased from 27% in the absence of SA to 91% in the presence of SA, suggesting that $SO_2•^-$ had a higher impact on SOT degradation under SA fouling. This finding reveals that fouling can influence the contribution of RS, and probably further alter the oxidation pathway.

Our work thus highlights the prominent effect of fouling on RS. However, the underlying mechanisms remain complex. A study has shown that scavenging experiments alone may be insufficient to fully elucidate RS behaviour, as the reaction between OMPs, fouling, scavengers, and PMS can collectively influence the pathways of PMS activation, RS formation, and OMPs' degradation (Gao et al., 2022; Wu et al., 2017). In particular, NOM has been reported to inhibit RS activity through the scavenging or reduction processes (Zhang et al., 2025). Moreover, the impact of •OH and $SO_2•^-$ on the

degradation of all OMPs cannot be ignored, as these RS can be bound to membrane surfaces, limiting their accessibility to scavengers in the bulk (Feng et al., 2017; Gao et al., 2022; Zhang et al., 2017). These factors complicate RS mechanisms under fouling and indicate the need for further studies to clarify their roles in OMPs' degradation.

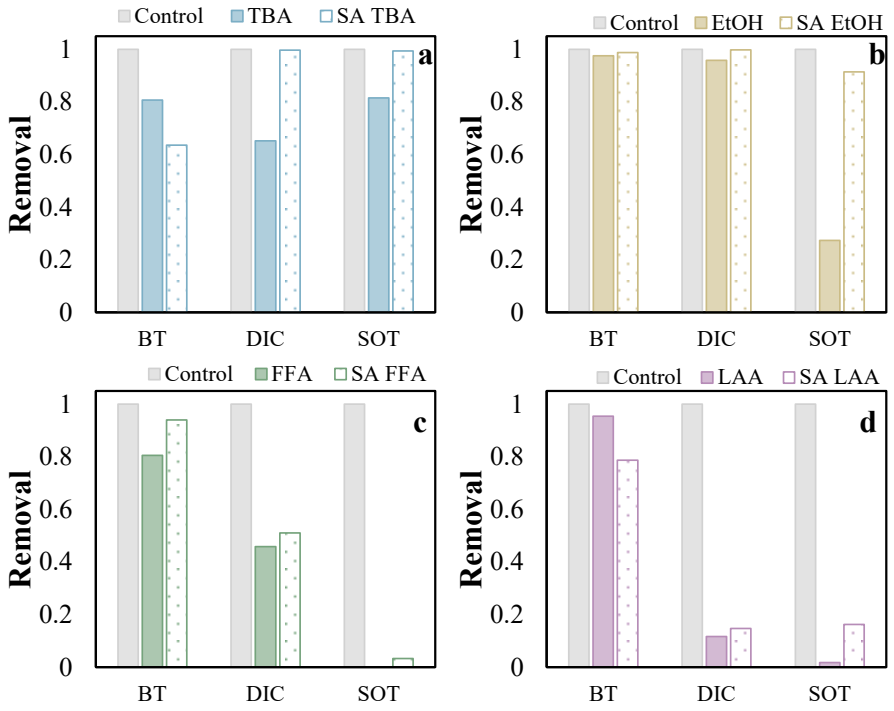

Figure 5.8. Evaluation of the dominated RS in the Pd-UF membrane with 40 μM PMS, performed at the flux of 100 L/(m^2·h). 1000 μM scavengers of TBA, EtOH, FAA, and LAA were separately introduced into the OMPs-PMS solution or the OMPs-PMS-SA solution. OMPs' degradation by the Pd-UF membrane with PMS under no fouling conditions and in the absence of scavengers served as the control experiment.

5.4. Conclusion

This study explored the simultaneous fouling mitigation and OMPs' degradation by catalytic Pd-UF membranes coupled with a low dosage of PMS. The goal was to reveal the effect of fouling on the degradation of OMPs. The findings showed that the Pd-UF-PMS system can effectively mitigate fouling, particularly over multiple cycles. Despite the presence of fouling, the Pd-UF-

PMS system achieved nearly complete BT degradation across a range of PMS concentrations, fluxes, and foulant types. This indicates that fouling had a minimal effect on the BT degradation, likely contributing to the synergistic effect of size exclusion and nanoconfinement. The presence of Ca at relatively high concentrations exhibited a moderate inhibitory impact on the degradation of BT. Moreover, the Pd-UF-PMS system achieved nearly complete degradation of multiple OMPs and high cleaning efficacy over multiple cycles, outperforming the pristine membrane. Although severe fouling, such as cake layer formation and internal pore blockage, was influenced by feedwater chemistry and filtration conditions, the Pd-UF-PMS system consistently exhibited robust performance in degrading OMPs. Nevertheless, these chemical and operational parameters were found to subsequently affect the oxidation mechanisms due to changes in competing reactions, PMS availability, and foulant structures. Scavenging experiments suggested that the dominant reactive species were similar under fouling and non-fouling conditions. However, fouling influenced the relative contribution of the different RS to OMP degradation, highlighting the complex role of fouling in the oxidation pathways. Overall, the potential negative effects of fouling on OMP degradation in the Pd-UF-PMS system were mainly counterbalanced by two key mechanisms: (1) size exclusion of the fouling molecules, which prevented the contamination of catalytic sites and thus ensured the sufficient generation of RS, and (2) nanoconfinement, which enhanced the enrichment and mass transfer of PMS, RS and OMPs within the pores. These advantages make the Pd-UF-PMS system a promising approach for advanced water treatment applications, even under harsh and complex feedwater conditions.

References

Angelis, L.D., Cortalezzi, M.M.F.D., 2016. Improved membrane flux recovery by Fenton-type reactions. J. Membr. Sci. 500, 255–264. https://doi.org/10.1016/j.memsci.2015.11.042

Asif, M.B., Ji, B., Maqbool, T., Zhang, Z., 2021. Algogenic organic matter fouling alleviation in membrane distillation by peroxymonosulfate (PMS): role of PMS concentration and activation temperature. Desalination 516, 115225. https://doi.org/10.1016/j.desal.2021.115225

Awfa, D., Ateia, M., Fujii, M., Yoshimura, C., 2020. Photocatalytic degradation of organic micropollutants: Inhibition mechanisms by different fractions of natural organic matter. Water Res. 174, 115643. https://doi.org/10.1016/j.watres.2020.115643

Bai, L., Liu, Z., Wang, H., Li, G., Liang, H., 2021. Fe(II)-activated peroxymonosulfate coupled with nanofiltration removes natural organic matter and sulfamethoxazole in natural surface water: Performance and mechanisms. Sep. Purif. Technol. 274, 119088. https://doi.org/10.1016/j.seppur.2021.119088

Chang, J., Yu, B., Peng, X., Zhang, P., Xu, X., 2025. Nanoconfined catalytic macrostructures for advanced water remediation: from basic understanding to future application strategies. Water Res. 272, 122960. https://doi.org/10.1016/j.watres.2024.122960

Chen, M., Heijman, S.G.J., Luiten-Olieman, M.W.J., Rietveld, L.C., 2022. Oil-in-water emulsion separation: fouling of alumina membranes with and without a silicon carbide deposition in constant flux filtration mode. Water Res. 216, 118267. https://doi.org/10.1016/j.watres.2022.118267

Dong, H., Xu, Q., Lian, L., Li, Y., Wang, S., Li, C., Guan, X., 2021. Degradation of organic contaminants in the Fe(II)/peroxymonosulfate process under acidic conditions: the overlooked rapid oxidation stage. Environ. Sci. Technol. 55, 15390–15399. https://doi.org/10.1021/acs.est.1c04563

Feng, Y., Lee, P.-H., Wu, D., Shih, K., 2017. Surface-bound sulfate radical-dominated degradation of 1,4-dioxane by alumina-supported palladium (Pd/Al2O3) catalyzed peroxymonosulfate. Water Res. 120, 12–21. https://doi.org/10.1016/j.watres.2017.04.070

Fu, M., Heijman, B., van der Hoek, J.P., 2022. Removal of organic micropollutants from wastewater effluent: selective adsorption by a fixed-bed granular zeolite filter followed by in-situ ozone-based regeneration. Sep. Purif. Technol. 303, 122303. https://doi.org/10.1016/j.seppur.2022.122303

Fu, M., Wang, J., Heijman, B., van der Hoek, J.P., 2021. Removal of organic micropollutants by well-tailored granular zeolites and subsequent ozone-based regeneration. J. Water Process Eng. 44, 102403. https://doi.org/10.1016/j.jwpe.2021.102403

Gao, L., Guo, Y., Zhan, J., Yu, G., Wang, Y., 2022. Assessment of the validity of the quenching method for evaluating the role of reactive species in pollutant abatement during the persulfate-based process. Water Res. 221, 118730. https://doi.org/10.1016/j.watres.2022.118730

Garcia-Ivars, J., Durá-María, J., Moscardó-Carreño, C., Carbonell-Alcaina, C., Alcaina-Miranda, M.-I., Iborra-Clar, M.-I., 2017. Rejection of trace pharmaceutically active compounds present in municipal wastewaters using ceramic fine ultrafiltration membranes: Effect of feed solution pH and fouling phenomena. Sep. Purif. Technol. 175, 58–71. https://doi.org/10.1016/j.seppur.2016.11.027

Hwang, T.-M., Nam, S.-H., Lee, J., Koo, J.-W., Kim, E., Kwon, M., 2020. Hydroxyl radical scavenging factor measurement using a fluorescence excitation-emission matrix and parallel factor analysis in ultraviolet advanced oxidation processes. Chemosphere 259, 127396. https://doi.org/10.1016/j.chemosphere.2020.127396

Katsoufidou, K., Yiantsios, S.G., Karabelas, A.J., 2008. An experimental study of UF membrane fouling by humic acid and sodium alginate solutions: the effect of backwashing on flux recovery. Desalination 220, 214–227. https://doi.org/10.1016/j.desal.2007.02.038

Katsoufidou, K., Yiantsios, S.G., Karabelas, A.J., 2007. Experimental study of ultrafiltration membrane fouling by sodium alginate and flux recovery by backwashing. J. Membr. Sci. 300, 137–146. https://doi.org/10.1016/j.memsci.2007.05.017

Kirschner, A.Y., Cheng, Y.-H., Paul, D.R., Field, R.W., Freeman, B.D., 2019. Fouling mechanisms in constant flux crossflow ultrafiltration. J. Membr. Sci. 574, 65–75. https://doi.org/10.1016/j.memsci.2018.12.001

Kloepfer, A., Gnirss, R., Jekel, M., Reemtsma, T., 2004. Occurrence of benzothiazoles in municipal wastewater and their fate in biological treatment. Water Sci. Technol. 50, 203–208. https://doi.org/10.2166/wst.2004.0329

Kowalska, K., Felis, E., Sochacki, A., Bajkacz, S., 2019. Removal and transformation pathways of benzothiazole and benzotriazole in membrane bioreactors treating synthetic municipal wastewater. Chemosphere 227, 162–171. https://doi.org/10.1016/j.chemosphere.2019.04.037

Kramer, F.C., Shang, R., Heijman, S.G.J., Scherrenberg, S.M., van Lier, J.B., Rietveld, L.C., 2015. Direct water reclamation from sewage using ceramic tight ultra- and nanofiltration. Sep. Purif. Technol. 147, 329–336. https://doi.org/10.1016/j.seppur.2015.04.008

Li, X., Zhang, H., Liu, J., Lu, J., Zhang, W., Hua, M., Lv, L., Pan, B., 2024. Revealing the overlooked catalytic ability of γ-Al2O3: efficient activation of peroxymonosulfate for enhanced water treatment. Environ. Sci. Technol. 58, 22466–22476. https://doi.org/10.1021/acs.est.4c08834

Liang, C., Huang, C.-F., Mohanty, N., Kurakalva, R.M., 2008. A rapid spectrophotometric determination of persulfate anion in ISCO. Chemosphere 73, 1540–1543. https://doi.org/10.1016/j.chemosphere.2008.08.043

Lin, B., Heijman, S.G.J., Rietveld, L.C., 2024. Catalytic pre-coat on ceramic nanofiltration membranes for segregation and Fenton cleaning of high-resistance colloids in direct surface water treatment. J. Membr. Sci. 694, 122401. https://doi.org/10.1016/j.memsci.2023.122401

Lin, B., Heijman, S.G.J., Shang, R., Rietveld, L.C., 2021. Integration of oxalic acid chelation and Fenton process for synergistic relaxation-oxidation of persistent

gel-like fouling of ceramic nanofiltration membranes. J. Membr. Sci. 636, 119553. https://doi.org/10.1016/j.memsci.2021.119553

Lin, B., Rietveld, L.C., Yao, L., Heijman, S.G.J., 2023. Adsorption and cake layer fouling in relation to Fenton cleaning of ceramic nanofiltration membranes. J. Membr. Sci. 122097. https://doi.org/10.1016/j.memsci.2023.122097

Long, Y., Yu, G., Dong, L., Xu, Y., Lin, H., Deng, Y., You, X., Yang, L., Liao, B.-Q., 2021. Synergistic fouling behaviors and mechanisms of calcium ions and polyaluminum chloride associated with alginate solution in coagulation-ultrafiltration (UF) process. Water Res. 189, 116665. https://doi.org/10.1016/j.watres.2020.116665

Lotfi, S., Fischer, K., Schulze, A., Schäfer, A.I., 2022. Photocatalytic degradation of steroid hormone micropollutants by TiO2-coated polyethersulfone membranes in a continuous flow-through process. Nat. Nanotechnol. 17, 417–423. https://doi.org/10.1038/s41565-022-01074-8

Luo, D., Lin, H., Li, X., Wang, Y., Ye, L., Mai, Y., Wu, P., Ni, Z., Lin, Q., Qiu, R., 2024. The dual role of natural organic matter in the degradation of organic pollutants by persulfate-based advanced oxidation processes: a mini-review. Toxics 12, 770. https://doi.org/10.3390/toxics12110770

Meng, C., Ding, B., Zhang, S., Cui, L., Ostrikov, K.K., Huang, Z., Yang, B., Kim, J.-H., Zhang, Z., 2022. Angstrom-confined catalytic water purification within Co-TiOx laminar membrane nanochannels. Nat. Commun. 13, 4010. https://doi.org/10.1038/s41467-022-31807-1

Nandi, A., Chatterjee, I.B., 1987. Scavenging of superoxide radical by ascorbic acid. J. Biosci. 11, 435–441. https://doi.org/10.1007/BF02704692

Rao, Y., Zhou, C., Wu, P., Fan, J., Zhang, Y., Yang, H., Pu, S., 2023. Molecular structure-dependent contribution of reactive species to organic pollutant degradation using nanosheet Bi2Fe4O9 activated peroxymonosulfate. J. Hazard. Mater. 452, 131240. https://doi.org/10.1016/j.jhazmat.2023.131240

Sathishkumar, M., Sneha, K., Kwak, I.S., Mao, J., Tripathy, S.J., Yun, Y.-S., 2009. Phyto-crystallization of palladium through reduction process using Cinnamom zeylanicum bark extract. J. Hazard. Mater. 171, 400–404. https://doi.org/10.1016/j.jhazmat.2009.06.014

Wang, Q., Xu, Z., Cao, Y., Chen, Y., Du, X., Yang, Y., Wang, Z., 2022. Two-dimensional ultrathin perforated Co3O4 nanosheets enhanced PMS-activated selective oxidation of organic micropollutants in environmental remediation. Chem. Eng. J. 427, 131953. https://doi.org/10.1016/j.cej.2021.131953

Wang, Y., Zheng, X., Li, D., Tian, J., Wu, H., Zhang, Y., 2023. Comparison of membrane fouling induced by protein, polysaccharide and humic acid under sodium and calcium ionic conditions. Desalination 548, 116236. https://doi.org/10.1016/j.desal.2022.116236

Wu, Z., Guo, K., Fang, J., Yang, Xueqin, Xiao, H., Hou, S., Kong, X., Shang, C., Yang, Xin, Meng, F., Chen, L., 2017. Factors affecting the roles of reactive species in the degradation of micropollutants by the UV/chlorine process. Water Res. 126, 351–360. https://doi.org/10.1016/j.watres.2017.09.028

Xin, Y., Bligh, M.W., Kinsela, A.S., Waite, T.D., 2016. Effect of iron on membrane fouling by alginate in the absence and presence of calcium. J. Membr. Sci. 497, 289–299. https://doi.org/10.1016/j.memsci.2015.09.023

Yang, J., Bai, L., Zhao, J., Liu, Y., Wang, H., Li, G., Liang, H., 2023. New insights into interfacial interaction and nanoconfinement effect in synergistic oxidation-filtration via CoFe2O4-ceramic membrane activated peroxymonosulfate. Chem. Eng. J. 461, 141846. https://doi.org/10.1016/j.cej.2023.141846

Yangali-Quintanilla, V., Sadmani, A., McConville, M., Kennedy, M., Amy, G., 2009. Rejection of pharmaceutically active compounds and endocrine disrupting compounds by clean and fouled nanofiltration membranes. Water Res. 43, 2349–2362. https://doi.org/10.1016/j.watres.2009.02.027

You, X., Teng, J., Chen, Y., Long, Y., Yu, G., Shen, L., Lin, H., 2020. New insights into membrane fouling by alginate: impacts of ionic strength in presence of calcium ions. Chemosphere 246, 125801. https://doi.org/10.1016/j.chemosphere.2019.125801

Zhang, J., Zhou, Y., Fang, Y., Li, Y., Guan, Z., Huang, Y., Xia, D., 2024. Chalcopyrite functionalized ceramic membrane for micropollutants removal and membrane fouling control via peroxymonosulfate activation: the synergy of nanoconfinement effect and interface interaction. J. Colloid Interface Sci. 658, 714–727. https://doi.org/10.1016/j.jcis.2023.12.116

Zhang, M., Lin, H., Shen, L., Liao, B.-Q., Wu, X., Li, R., 2017. Effect of calcium ions on fouling properties of alginate solution and its mechanisms. J. Membr. Sci. 525, 320–329. https://doi.org/10.1016/j.memsci.2016.12.006

Zhang, S., Hedtke, T., Zhu, Q., Sun, M., Weon, S., Zhao, Y., Stavitski, E., Elimelech, M., Kim, J.-H., 2021. Membrane-confined iron oxychloride nanocatalysts for highly efficient heterogeneous fenton water treatment. Environ. Sci. Technol. 55, 9266–9275. https://doi.org/10.1021/acs.est.1c01391

Zhang, S., Quan, X., Zheng, J.-F., Wang, D., 2017. Probing the interphase “HO zone” originated by carbon nanotube during catalytic ozonation. Water Res. 122, 86–95. https://doi.org/10.1016/j.watres.2017.05.063

Zhang, T., Yang, P., Ji, Y., Lu, J., 2025. The role of natural organic matter in the degradation of phenolic pollutants by sulfate radical oxidation: radical scavenging vs reduction. Environ. Sci. Technol. 59, 3325–3335. https://doi.org/10.1021/acs.est.4c12579

Zhang, W., Zhang, S., Meng, C., Zhang, Z., 2023. Nanoconfined catalytic membranes assembled by cobalt-functionalized graphitic carbon nitride nanosheets for rapid degradation of pollutants. Appl. Catal. B Environ. 322, 122098. https://doi.org/10.1016/j.apcatb.2022.122098

Zhao, Y., Lu, D., Xu, C., Zhong, J., Chen, M., Xu, S., Cao, Y., Zhao, Q., Yang, M., Ma, J., 2020. Synergistic oxidation - filtration process analysis of catalytic CuFe2O4 - tailored ceramic membrane filtration via peroxymonosulfate activation for humic acid treatment. Water Res. 171, 115387. https://doi.org/10.1016/j.watres.2019.115387

Zhou, Q., Song, C., Wang, P., Zhao, Z., Li, Y., Zhan, S., 2023. Generating dual-active species by triple-atom sites through peroxymonosulfate activation for treating micropollutants in complex water. Proc. Natl. Acad. Sci. 120, e2300085120. https://doi.org/10.1073/pnas.2300085120

Zhu, L., 2015. Rejection of Organic Micropollutants by Clean and Fouled Nanofiltration Membranes. J. Chem. 2015, 934318. https://doi.org/10.1155/2015/934318

Supporting Information

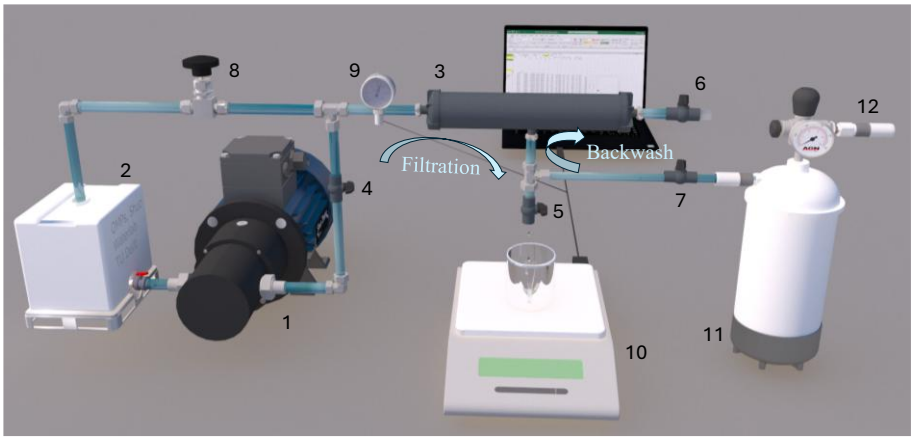

Figure S5.1. Constant pressure setup.

The constant pressure setup (Fig. S5.1) was constructed using a gear pump (No. 1, AxFlow, the Netherlands) to feed the solution from the bulk reservoir (No. 2) through the membrane (No. 3) to the permeate side. During this process, valves No. 4 and 5 were opened, while valves No. 6 and 7 remained closed. A backflow system was incorporated because the lowest operating power of the gear pump could not provide the expected flux. To regulate the transmembrane pressure, a needle valve (No. 8) was connected to the backflow tubing system. Pressure and flux data were recorded using a pressure sensor (No. 9, GS4200-USB, ESI, UK) and a digital balance (No. 10, KERN EWJ 600, Germany), both of which were connected to a computer for real-time monitoring. For backwash, the valves No. 6 and 7 were opened, while valves No. 5 and 6 were closed. The backwash vessel (No. 11), filled with demineralized water and connected to a compressed air system (No. 12), was used to perform the backwash at a controlled pressure.

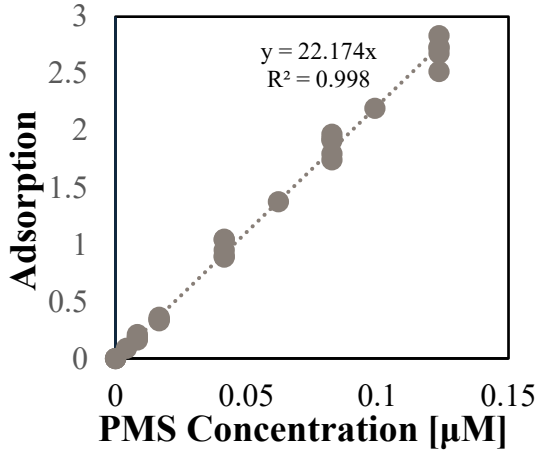

Figure S5.2. Calibration curve for the determination of PMS concentration based on the UV-Vis spectrophotometry at 352 nm.

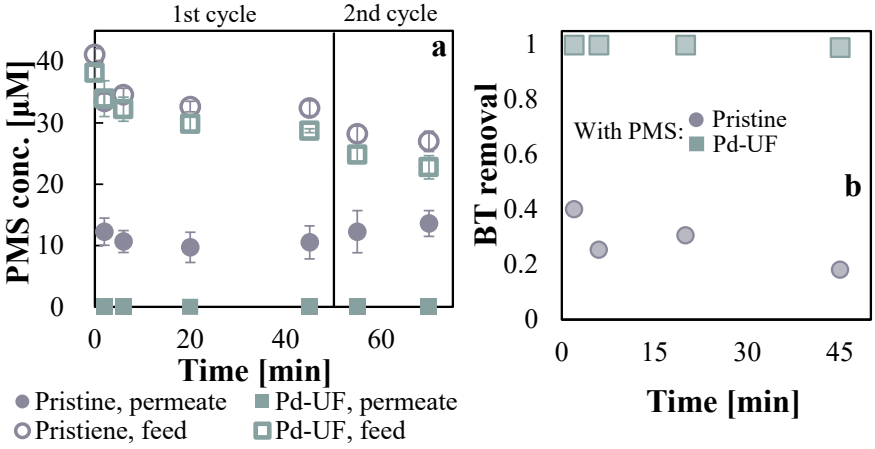

Figure S5.3. (a) PMS concentration in the feed and permeate side. (b) OMPs removal over filtration time by the pristine and Pd-UF membranes with PMS under constant pressure filtration.

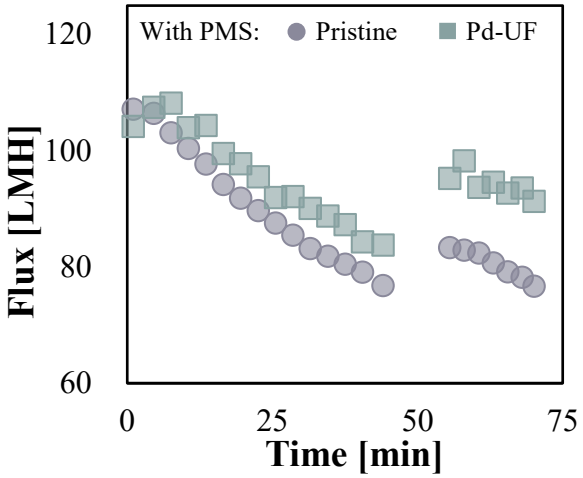

Figure S5.4. Flux change with time by the pristine and Pd-UF membranes with PMS under constant pressure filtration.

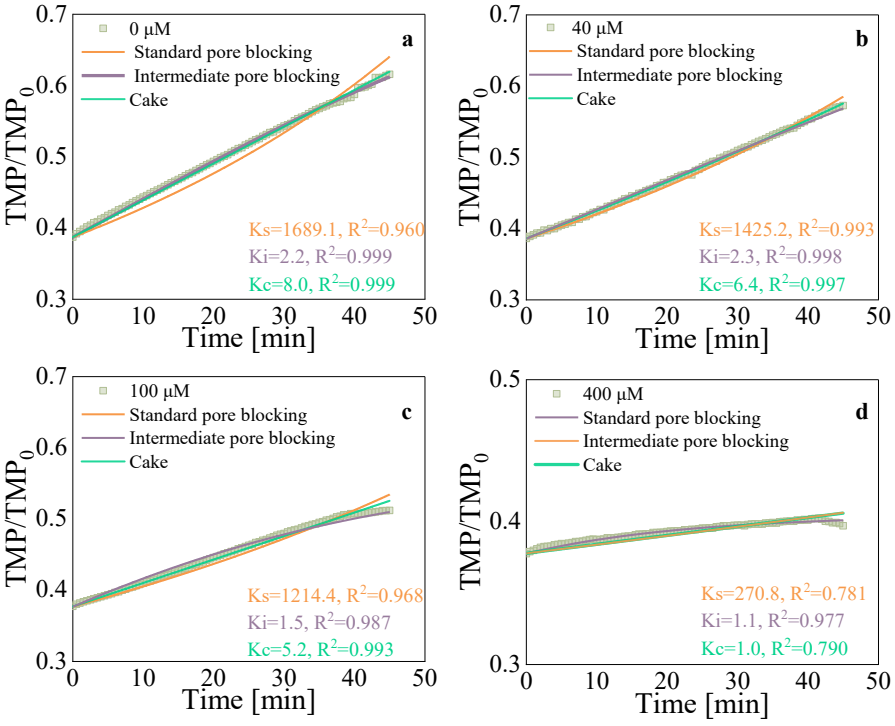

Figure S5.5. Determination of fouling mechanisms (cake filtration, standard pore blocking, and intermediate pore blocking) based on TMP data in the case of 0-400 μ PMS.

The fouling mechanisms. Standard and intermediate pore blocking were evaluated by the model developed for constant flux filtration (Kirschner et al., 2019).

$$TMP = \frac{TMP_0}{(1 - K_S\, a_0\, J\, t)} \quad \text{S5.1}$$

$$TMP = \frac{TMP_0}{(\frac{1}{K_i} + \left(1 - \frac{1}{K_i}\right) \exp(-K_i\, B\, t))} \quad \text{S5.2}$$

Where TMP (bar) is the transmembrane pressure measured during the filtration, TMP_0 is the initial transmembrane pressure, K_s (in 1/m^3) is constant for standard pore blocking, a_0 (in m^2) is the clean membrane surface area, J (in m/s) is flux, t (in min) is the filtration time, K_i is constant for intermediate pore blocking, and B (in 1/s) is the particle resuspension rate.

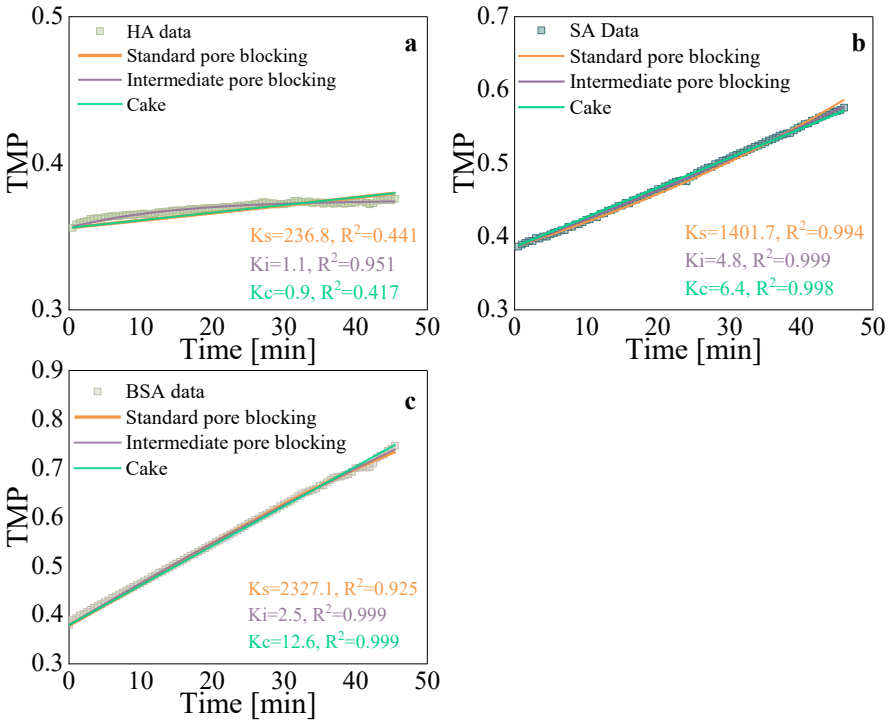

Figure S5.6. Determination of fouling mechanisms (cake filtration, standard pore blocking, and intermediate pore blocking) based on TMP data of HA, SA, and BSA.

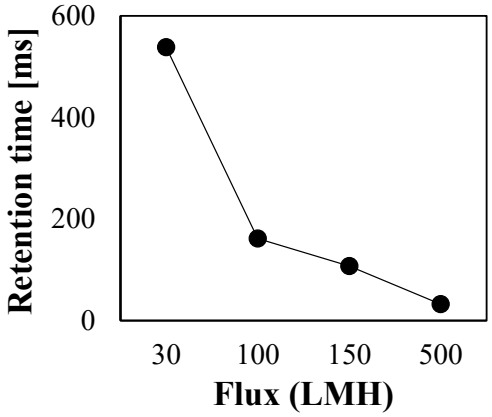

Figure S5.7. The relationship between retention time and flux.

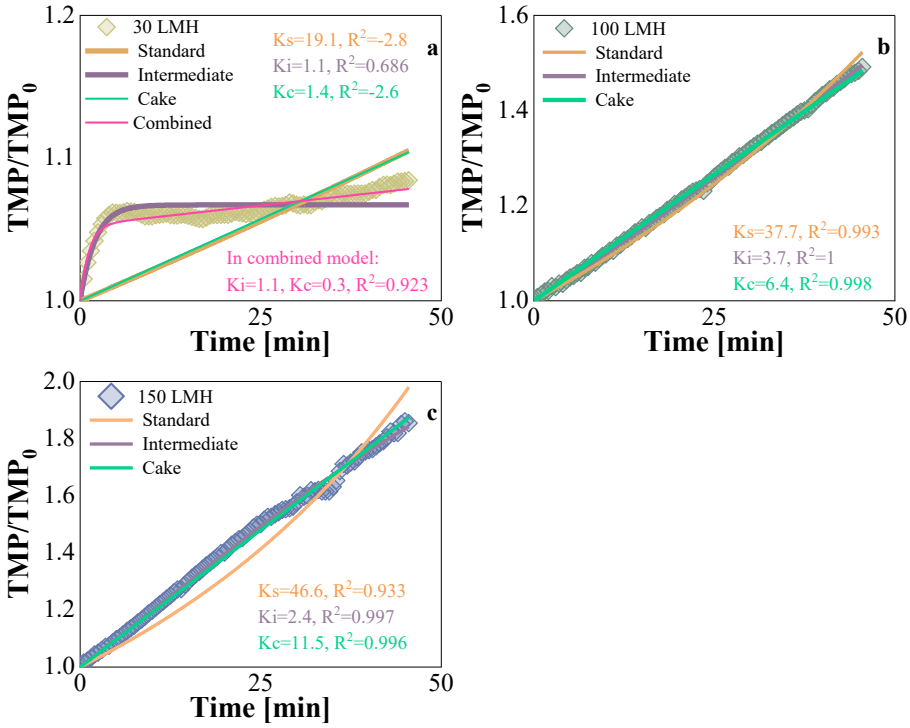

Figure S5.8. Determination of fouling mechanisms (cake filtration, standard pore blocking, and intermediate pore blocking, combined model for intermediate and cake fouling) based on TMP data under different fluxes.

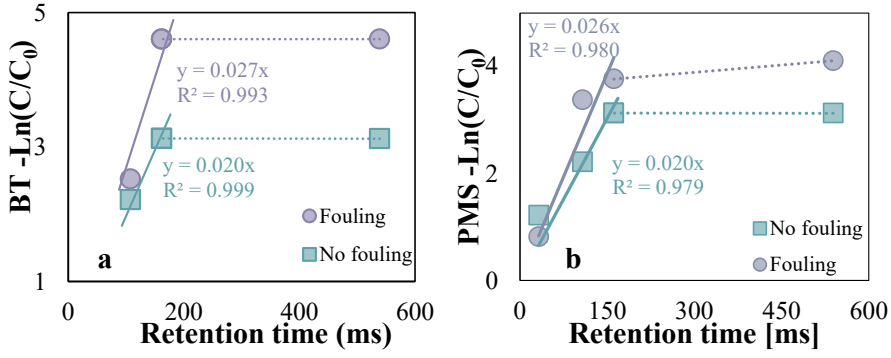

Figure S5.9. Kinetics of (a) BT degradation and (b)PMS consumption.

Calculation of kinetic constant and removal efficacy. The kinetic rate constant (K, in 1/ms) was determined using Eq. S5.3, where C (μg/L) represents the

OMP concentration in the permeate after oxidation, C_0 (μg/L) is the initial concentration, and t (ms) is the retention time calculated from Eq. S5.4.

$$-ln\frac{C}{C_0} = K\,t \qquad \text{S5.3}$$

Retention time calculation:

$$t = \phi\,\frac{J}{h} \qquad \text{S5.4}$$

where t is the residence time (ms), ϕ is the porosity of the membrane (33%, obtained from analysis of SEM by ImagJ), J is the flux (m/s), and h is the thickness of the selective layer (1.36×10^{-5} m). ϕ and h were determined by ImageJ (not shown here) through the top-view and cross-section SEM images, respectively.

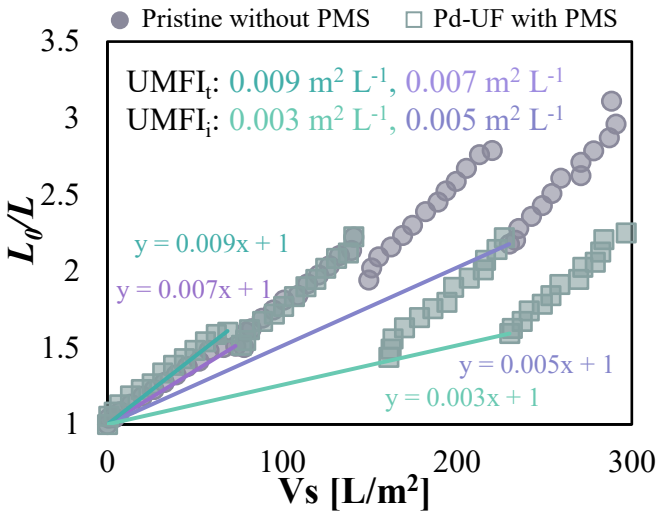

Figure S5.10. Total fouling index ($UMFI_t$) and chemically irreversible fouling index ($UMFI_i$) in the multi-cycle running.

The unified membrane fouling index (UMFI). $UMFI$, independent of the traditional fouling models (e.g., pore blocking and cake filtration), was used to evaluate the fouling potential of the feed water (Huang et al., 2009; Nguyen et

al., 2011; Shang et al., 2015). Defined as the slope of the linear equation in Eq. S6, UMFI (m²/L) relates the normalized specific permeate flux ($J_s' = J/J_0$) to the unit permeate volume (V_s in L/m²). The total fouling index ($UMFI_t$) is derived from each fouling curve, while the chemically irreversible fouling index ($UMFI_c$) is obtained using a two-point method based on $1/J_s'$ values from the first and last cycle.

$$\frac{1}{J_s'} = 1 + (UMFI) \times V_s \qquad \text{S5.5}$$

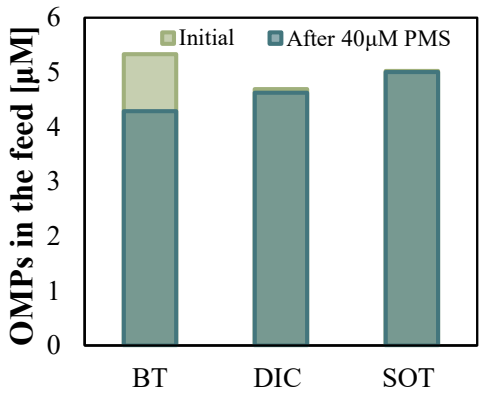

Figure S5.11. Concentrations of BT, DIC, and SOT in the feed, measured before and after PMS addition.

Reference

Huang, H., Young, T., Jacangelo, J.G., 2009. Novel approach for the analysis of bench-scale, low pressure membrane fouling in water treatment. J. Membr. Sci. 334, 1–8. https://doi.org/10.1016/j.memsci.2009.01.049

Kirschner, A.Y., Cheng, Y.-H., Paul, D.R., Field, R.W., Freeman, B.D., 2019. Fouling mechanisms in constant flux crossflow ultrafiltration. J. Membr. Sci. 574, 65–75. https://doi.org/10.1016/j.memsci.2018.12.001

Nguyen, A.H., Tobiason, J.E., Howe, K.J., 2011. Fouling indices for low pressure hollow fiber membrane performance assessment. Water Res. 45, 2627–2637. https://doi.org/10.1016/j.watres.2011.02.020

Shang, R., Vuong, F., Hu, J., Li, S., Kemperman, A.J.B., Nijmeijer, K., Cornelissen, E.R., Heijman, S.G.J., Rietveld, L.C., 2015. Hydraulically irreversible fouling on ceramic MF/UF membranes: comparison of fouling indices, foulant composition and irreversible pore narrowing. Sep. Purif. Technol. 147, 303–310. https://doi.org/10.1016/j.seppur.2015.04.039

五律

雁自向南迁，人停马不前。

衔芦一片落，立苇满江残。

雨打屋檐鸟，潮摧海上帆。

西阳无冷暖，如是大风寒。

2021.10.04

Chapter 6

Conclusions and outlook

6.1. Conclusions

The contribution of fouling and CP caused by nano-sized contaminants to permeability decline was found to be considerable, highlighting the need for efficient fouling mitigation strategies in ceramic membrane filtration. Therefore, catalytic ceramic ultrafiltration (UF) membranes were developed and demonstrated a strong potential for both fouling control and OMPs' degradation. These membranes were modified with $CuFe_2O_4$ via filtration coating and with palladium (Pd) via atomic layer deposition (ALD) and maintained high water permeability after modification. The $CuFe_2O_4$-coated membranes, coupled with Fenton-like backwash, were effective in the degradation of alginate fouling, formed on the membrane surface and within pores. Moreover, membranes with a low Pd loading were fabricated via ALD and integrated with advanced oxidation process (AOP) during filtration through the dosage of peroxymonosulfate (PMS). These Pd-modified membranes exhibited an enhanced cleaning performance and effective degradation of organic micropollutants (OMPs), even under varying and challenging fouling conditions. Overall, the findings demonstrate that catalytic ceramic membranes, when coupled with AOP in backwash or filtration, offer a promising strategy for enhanced membrane performance.

Specific conclusions in response to the research questions proposed in Chapter 1 are presented below.

- ***Research question 1:*** *What is the contribution of CP and fouling to permeability decline?*

The role of CP and fouling in permeability decline was studied by comparing the pure water flux measured before and after filtration of nano-sized colloids/particles. A permeability loss of 43%-95% was attributed to the high CP caused by the colloids. The modified CP model also revealed that a higher CP can result from the lower diffusion of colloids that have a larger size. Although crossflow has been widely reported to mitigate CP, the colloidal CP remained at a high level, e.g., 250 for silica at *Re* of 7317, still resulting in a high permeability loss.

- ***Research question 2:*** *How does Fenton-like cleaning influence backwash?*

$CuFe_2O_4$ was grown on the ceramic UF membrane surface and within pores, showing a minor (5%) permeability loss compared to the pristine membrane. The membranes were then combined with Fenton–like backwash, achieved by adding H_2O_2 to the backwash solution, with the aim of enhancing fouling

removal. Compared to backwash with demineralized water, which achieved only 1–14% cleaning efficacy, even under increased pressure and duration, Fenton-like backwash reached up to approximately 70% efficacy over multiple cycles at a low backwash pressure (0.3 bar). It was found that the low backwash pressure, rather than the prolonged duration, dominated the efficacy of Fenton-like backwash. This can be attributed to the increased residence time of the oxidizing agent in the membrane pores, promoting radical formation. However, the presence of increased concentrations of Ca in the alginate solution reduced efficacy, probably due to the formed rigid alginate-Ca clusters, which limited H_2O_2 transport towards the catalytic surface, hindering radical formation and fouling breakdown.

- ***Research question 3:*** *Can ceramic membranes with low-loading catalysts achieve effective degradation of OMPs?*

Ceramic UF membranes, modified with a low Pd loading via ALD, exhibited a permeability loss of 1%-22%, depending on the number of ALD cycles. The Pd-modified membranes, by activating PMS, achieved nearly 100% removal of the four studied OMPs at the flux of 30 L/(m^2·h), and maintained a high removal efficacy (76–96%) even at a high flux of 200 L/(m^2·h). The high degradation kinetics were primarily attributed to the Pd loaded within membrane pores, which enhanced the kinetics by 567-1389 times, compared to the Pd deposited on the membrane surface. The pore environment provided abundant Pd sites and improved mass transfer of both reactive species (RS) and OMPs. In contrast, Pd deposited only on the membrane surface showed a limited efficacy, probably due to the restricted transport of RS. Furthermore, a high OMPs degradation was maintained across a range of PMS concentrations (20–80 μM), water matrix ions (1 mM Cl^-, SO_4^{2-}, HCO_3^-, or ClO^-), and even in river water. Optimal degradation occurred at neutral pH (pH=7), while extreme pH conditions (2.5 and 11) inhibited PMS activation. The contribution of RS to OMPs' degradation was found to depend on the type of OMPs. High salinity (i.e., brine water) reduced OMPs removal, probably due to competition and RS scavenging. The overall results confirm that a low loading of Pd catalyst on ceramic membrane structures is effective for OMPs degradation.

- ***Research question 4:*** *What role does fouling play in the degradation of OMPs by catalytic ceramic membranes?*

It was found that fouling played a complex but minimal role in the degradation of OMPs when using a catalytic Pd-modified UF membrane coupled with PMS. Fouling, influenced by PMS concentration, foulant type, Ca presence, and flux,

can vary in severity (permeability decline) and mechanism (pore blocking and cake formation). However, these variations had little impact on PMS activation and OMPs' degradation. Nearly complete degradation of OMPs was achieved under a wide range of fouling conditions, attributed to: (i) size exclusion, which prevents foulants from deactivating catalytic sites within the membrane pores, and (ii) nanoconfinement, which promotes the enrichment and mass transfer of RS and OMPs in the pore environment. Dominant RS almost remained consistent under fouling and non-fouling conditions, but fouling altered their relative contributions to OMP decomposition by affecting competing reactions, PMS availability, and foulant structure, thereby influencing the oxidation pathway. Unlike pristine membranes, the coupled system also achieved a high backwash efficacy and a nearly complete OMP degradation over multiple cycles.

6.2. Outlook

6.2.1. Application of catalytic membranes

Stability of catalytic membrane.

As demonstrated in this thesis, catalytic membranes can be coupled with AOP during both backwash and filtration processes to enhance membrane cleaning and the removal of OMPs. However, metal leaching, particularly in newly prepared membranes, must be carefully considered. Metal leaching from catalytic ceramic membranes presents a potential risk of secondary pollution, especially in the application for drinking water production. As discussed in Chapter 2, the leaching will be gradually stopped over time, and the aged $CuFe_2O_4$ membrane maintained a high performance after 96 h leaching. This suggests, a post-treatment step (e.g., treating the membranes in H_2O_2 to remove the unstable catalysts) may help to mitigate leaching without compromising the catalytic performance. In contrast, the Pd-modified ceramic membranes, fabricated by ALD, exhibited higher stability. As shown in Fig. 6.1, during prolonged leaching experiments with PMS and NaClO, respectively,15-80 µg/L Al was leached, much higher than the 2-5 µg/L Pd, as found in both PMS and NaClO cases.

However, ceramic membranes are typically expected to operate over several years. Therefore, long-term stability tests, including repeated cleaning cycles, variable feedwater conditions, and sustained harsh chemical exposure, are essential to fully evaluate the lifespan and durability of the proposed catalytic membranes. Addressing this will be crucial for translating laboratory-scale

innovations into reliable, full-scale water treatment solutions. Moreover, the toxicity of potentially leached metals should be evaluated, especially when catalytic membranes are intended for drinking water production.

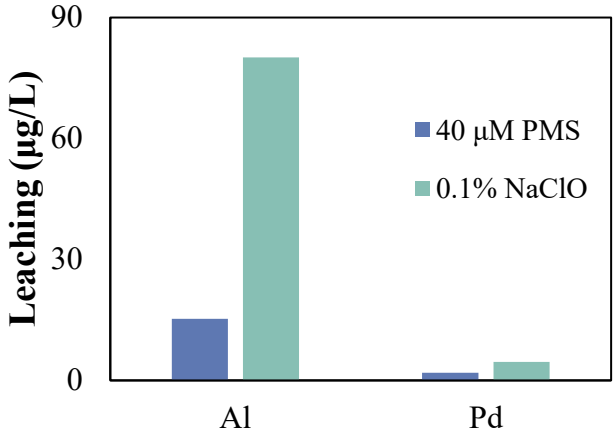

Figure 6.1. Al and Pd leaching from Pd-coated ceramic membranes

Comparison of integrating AOP into backwash or filtration.

Coupling AOP with membrane filtration, by dosing oxidizing agents such as PMS directly into the feed, allows for continuous degradation of OMPs and foulants during filtration. However, a major limitation is the relatively high dosage of chemicals required in the feed stream, which can lead to increased operational costs and raised concerns about the oxidation by-products in the permeate side.

In this thesis, AOP was also integrated into the filtration process by a Pd-deposited membrane. The performance was evaluated using a relatively low dosage of PMS (40–100 µM). While promising results were achieved under these conditions, further research is required to assess whether such low concentrations are effective and practical in real-world applications. Additionally, a detailed cost analysis is needed to evaluate whether this approach is economically competitive with traditional methods for controlling fouling and removing OMPs.

Effect of pore sizes of catalytic membranes on OMPs' degradation

The membrane pore size is a critical factor in separation performance, particularly for the rejection of low-molecular-weight OMPs. In this thesis, it was found that in the filtration by catalytic membranes, the synergistic effect

of size exclusion and catalytic oxidation contributed to fouling mitigation and OMPs' degradation. The membrane pores effectively rejected most foulants, preventing catalyst deactivation, while the catalyst located within the pores enhanced the mass transfer of RS and OMPs due to the so-called nanoconfinement effect.

In the presented study, ceramic UF membranes with an average pore size of 20 nm, as the catalytic support for OMPs' degradation, were employed. Although near-complete OMPs' degradation was achieved even at a high flux, further studies are required to evaluate the impact of pore sizes on overall performance, including smaller (e.g., 1 nm and sub-nano) and larger pores (e.g., 40 and 100 nm). In particular, membranes with larger pore sizes are expected to maintain a high OMPs' degradation efficacy while allowing for a higher water permeability. This enhancement could improve treatment efficacy, reduce energy consumption, and lower operational costs in practical applications. Future work should thus systematically explore the trade-off between pore size, permeability, and catalytic effectiveness to optimize membrane design.

Deeper understanding of mechanisms

This work has revealed that integrating ceramic membranes with AOPs during backwash and filtration can effectively mitigate the fouling and enhance the degradation of OMPs.

For $CuFe_2O_4$ membranes, we propose that the structure of alginate-Ca changed with varying Ca concentrations and strongly affected the performance of Fenton-like backwash. Our proposed mechanism was based on a previous study of Zhang et al. (2017) and our measured cleaning efficacies. However, more studies are required to directly characterize the fouling structures before and after Fenton-like backwash to establish a clear relationship between the alginate–Ca structures and the cleaning performance.

For the Pd-UF-PMS system, the roles of OH and $SO_4^{\bullet -}$ have been found to be probably underestimated due to the limitations of the scavenging experiments. This indicates the need for further studies to clarify their actual contributions to the degradation of multiple OMPs. Advanced analytical techniques will also be required to quantify the specific roles of •OH, $SO_4^{\bullet -}$, $^1O_2$, and $O_2^{\bullet -}$. Besides, we have found that fouling had a limited effect on OMPs' degradation, although fouling could affect the degradation pathway by changing the PMS activation. However, a deeper study is necessary to reveal the specific effect of fouling (types and structures) on PMS activation, competition reactions, and

the contribution of different RS, especially when treating more complex water containing various ions, particles, and NOM.

6.2.2. Development of ceramic membranes with small pore size

Currently, commercial ceramic nanofiltration membranes with MWCO ranging from 200 to 450 Da (corresponding to pore sizes of approximately 0.7–0.9 nm) are available on the market. However, their widespread application remains limited due to broad pore size distributions, high production costs, and relatively low permeability. As the demand for advanced water treatment, resource recovery, and reuse continues to grow, the development of ceramic membranes with narrower pore size distributions and even smaller, well-defined pores is becoming increasingly important. These next-generation membranes offer promising opportunities for the removal of OMPs, precise ion separations, and the recovery of critical resources—particularly those essential to green energy technologies, such as lithium and rare earth elements. Advances in material science and nanotechnology are opening new pathways to realize this goal.

Although ALD has been widely used to tailor the pore size of ceramic membranes, it often results in reduced permeability due to the low porosity and dense nature of the deposited layers. An alternative is molecular layer deposition (MLD), a promising technique capable of fabricating ultrathin separative layers with tunable pore narrowing while maintaining high membrane porosity (Sondhi et al., 2025). Unlike ALD, MLD uses organic precursors for the coating. These organics can be removed through subsequent calcination, potentially facilitating the restoration of porosity.

In addition to MLD, two-dimensional (2D) materials, such as graphene oxide, MXenes, and molybdenum disulfide (MoS_2), present exciting opportunities for narrowing the pore size of ceramic membranes (Gong et al., 2021; Huang et al., 2013). These 2D layers can act as ultra-thin separation barriers or functional coatings, enabling precise molecular sieving and fouling mitigation while maintaining a high permeability. However, challenges remain in terms of the long-term stability, adhesion, and scalability of such 2D materials.

6.2.3 Low loading of catalysts: beyond catalytic membranes

In this thesis, it has been demonstrated that catalytic membranes with a low catalyst loading, particularly those fabricated via ALD, can achieve an effective catalytic performance, with a relatively high stability. The strategic use of minimal catalyst amounts not only reduces fabrication costs and lowers the risk of metal leaching, but also enhances catalyst utilization efficiency.

The development of single-atom catalysts, where individual catalyst atoms are dispersed and stabilized on support surfaces, has demonstrated high catalytic activity and selectivity (Wu and Kim, 2022). This progress further reinforces the potential of low-catalyst-loading approaches for effective and sustainable catalytic applications. However, their industrial application remains limited due to challenges in large-scale synthesis, stability, and integration. In contrast, the low-loading catalyst strategy proposed in this thesis offers a more practical and scalable solution for real-world applications.

Future research, however, should aim to improve low-loading catalyst designs for different catalytic processes, explore other deposition methods beyond ALD such as spraying and electrodeposition (Ganesan and Narayanasamy, 2019), and test their performance under real-world conditions. In addition, applying this strategy beyond membrane systems could broaden its scope of application.

Reference

Sondhi, H., Chen, M., Nijboer, M.P., Nijmeijer, A., Roozeboom, F., Bechelany, M., Kovalgin, A., Luiten-Olieman, M., 2025. Ceramic nanofiltration membranes: creating nanopores by calcination of atmospheric-pressure molecular layer deposition grown titanicone layers. Membranes 15, 86. https://doi.org/10.3390/membranes15030086

Gong, D., Yin, Y., Chen, H., Guo, B., Wu, P., Wang, Y., Yang, Y., Li, Z., He, Y., Zeng, G., 2021. Interfacial ions sieving for ultrafast and complete desalination through 2D nanochannel defined graphene composite membranes. ACS Nano 15, 9871–9881. https://doi.org/10.1021/acsnano.1c00987

Huang, H., Mao, Y., Ying, Y., Liu, Y., Sun, L., Peng, X., 2013. Salt concentration, pH and pressure controlled separation of small molecules through lamellar graphene oxide membranes. Chem. Commun. 49, 5963–5965. https://doi.org/10.1039/C3CC41953C

Wu, X., Kim, J.-H., 2022. Outlook on single atom catalysts for persulfate-based advanced oxidation. ACS EST Eng. 2, 1776–1796. https://doi.org/10.1021/acsestengg.2c00187

Ganesan, A., Narayanasamy, M., 2019. Ultra-low loading of platinum in proton exchange membrane-based fuel cells: a brief review. Mater Renew Sustain Energy 8, 18. https://doi.org/10.1007/s40243-019-0156-x

Zhang, M., Lin, H., Shen, L., Liao, B.-Q., Wu, X., Li, R., 2017. Effect of calcium ions on fouling properties of alginate solution and its mechanisms. J. Membr. Sci. 525, 320–329. https://doi.org/10.1016/j.memsci.2016.12.006

Summary

Membranes are widely recognized as promising technologies for addressing the growing demand for freshwater driven by rapid population growth and industrialization. Ceramic membranes, in particular, offer advantages such as high mechanical strength, chemical resistance, and long lifespan compared to polymeric membranes. However, permeability loss during filtration is one of the challenges. The specific contributions of concentration polarization (CP) and fouling to this decline remain insufficiently understood. Fouling is a major obstacle in ceramic membrane operation, and the removal of organic micropollutants (OMPs)—increasingly detected in different water bodies—poses an additional challenge due to the relatively large pore sizes of ceramic membranes, mostly in the range of microfiltration and ultrafiltration (UF). To address these challenges, various modification strategies have been developed to improve membrane performance in water treatment. One promising approach is to modify ceramic membranes with catalysts, enabling them to perform both separation and catalytic functions. However, currently, developed catalytic ceramic membranes often suffer from severe flux decline after deposition, especially when coated with a dense or thick coating. In addition, catalytic membranes coupled with advanced oxidation processes (AOPs) have typically been achieved by large dosages of oxidizing agents during filtration. The excessive loading of catalysts and the overdosage of chemicals not only increase operational costs but also limit the practical application of catalytic ceramic membranes.

This thesis aims to enhance the performance of ceramic membranes for water treatment, focusing on the challenges of both fouling and OMPs' removal. First, a method was proposed to determine the main reason for flux decline, suggesting that both CP and fouling had impacts on flux decline. Then, catalytic ceramic ultrafiltration membranes, modified with $CuFe_2O_4$ and palladium, were employed to be coupled with H_2O_2 and peroxymonosulfate (PMS) based AOPs, respectively. The catalytic ceramic membranes not only exhibited a high flux after coating but were also effective in fouling removal and OMPs degradation.

High flux loss in membrane filtration can result from both CP and fouling, and a high CP level may further exacerbate fouling. However, the traditional CP model is unable to qualify their individual contributions. To better understand

flux decline, a practical strategy was developed to distinguish the effects of CP and fouling by measuring pure water flux before and after the filtration of nano-sized colloids by ceramic nanofiltration (NF) membrane. The results indicated that colloidal CP could account for 43% to 95% of the total flux decline, with the remainder attributed to fouling. The CP values, calculated by a modified model, showed that the colloidal CP was in the range of 7-460, which is considerably higher than the CP (typically 1-2) caused by ions in spiral-wound reverse osmosis or NF. The highest CP level, i.e., 460, was observed for larger silica colloids, likely due to their slower diffusion. Although an increased crossflow was found to mitigate CP, high CP levels, i.e., values of around 250, were still observed.

To address membrane fouling, $CuFe_2O_4$-coated ceramic UF membranes were fabricated. The catalytic membranes with a minor flux loss after coating were then combined with Fenton-like backwash to enhance fouling removal. A low cleaning efficacy (1%–14%) was found in conventional hydraulic backwash. In contrast, due to the strong radicals induced by H_2O_2-based AOPs, the cleaning efficacy for removing alginate fouling from the catalytic membranes was improved to approximately 70% over multiple cycles. The backwash pressure or flux, rather than duration, was found to govern the AOP-enhanced cleaning performance. This is attributed to the increased residence time of H_2O_2 at low backwash pressure or flux. The presence of calcium (Ca) can form the rigid alginate-Ca clusters, not only negatively influencing the flux but also limiting the transport of radicals to the internal structure to break down the fouling. Besides, the fragments of alginate can reattach to the membrane surface by binding with excess Ca, thus reducing Fenton-like backwash efficacy. During seven-cycle filtration of concentrated alginate feedwater, the catalytic membranes restored 83%-94% flux after Fenton-like backwash. The leaching of catalysts gradually ceased over time, with negligible leaching in NaClO or NaOH.

Building upon this success, the catalytic ceramic membranes were further explored with a low loading of catalyst. Therefore, atomic layer deposition (ALD) was used to achieve a precise and low loading of Pd, ensuring minimal impact on membrane flux. The catalytic membranes modified with 30 ALD cycles were coupled with PMS for in-situ AOP degradation of OMPs during filtration. The coupled system achieved nearly 100% OMP removal at flux below 100 L/(m^2·h) and maintained a high degradation efficacy (76% to 96%) even at a higher flux of 200 L/(m^2·h). The OMPs' degradation was enhanced by Pd deposited within the membrane pores, improving degradation kinetics

by up to three orders of magnitude due to nanoconfinement effects, compared to the effect of Pd deposited on the membrane surface. The contribution of different reactive species (RS) to OMPs degradation was found to depend on the compound. Although ions and natural organic matter had minimal impact, harsh feedwater conditions, such as high salinity of brine water and pH at 2.5 or 11, reduced the degradation of certain OMPs, likely due to inhibited PMS activation.

Although the AOPs-enhanced removal of fouling and OMPs has been widely studied, little is known about the effect of fouling on OMPs' degradation. Therefore, Pd-deposited ceramic ultrafiltration membranes with PMS were used to treat feedwater containing alginate and OMPs. The results showed that the Pd-coated membranes effectively mitigated fouling and achieved a high degradation efficacy of OMPs, even under severe cake fouling or pore blocking. Fouling was found to influence permeability and changed fouling mechanisms (cake fouling and pore blocking) depending on the PMS concentration, flux, foulant type, and Ca concentration, but its effect on OMP degradation was minimal. This is attributed to the synergy between membrane separation of foulants and nanoconfinement, which prevents the deactivation of catalytic sites and enriches RS and OMPs within the membrane pores. Although the governed RS for OMPs degradation almost remained consistent under fouling and non-fouling conditions, fouling altered their relative contributions to OMP degradation. However, different fouling is likely to alter the dominant oxidation pathway during OMP degradation.

Acknowledgement

This doctoral journey has been one of the most challenging and transformative experiences of my life. I would like to take this opportunity to express my sincere gratitude to the many individuals and institutions who have supported me along the way.

First and foremost, I would like to extend my deepest appreciation to my supervisor, Dr. ir. Sebastiaan G. J. Heijman, for his unwavering support, valuable guidance, and constructive feedback throughout my PhD journey. His engineering mindset, sharp problem-solving skills, and down-to-earth attitude have deeply influenced the way I approach research. One moment that left a lasting impression on me was when he came to the university during his summer holiday to work with me in the lab and help resolve a critical issue. His dedication and generosity continue to inspire me.

I am also deeply grateful to Prof. dr. ir. Luuk C. Rietveld for his valuable insights, critical suggestions, and academic leadership. I am especially grateful for the many insightful suggestions he provided during the writing of my papers. His detailed comments, critical questions, and high standards pushed me to refine my arguments, clarify my thoughts, and improve the overall quality of my work. I have learned a great deal from his academic rigor and his approach to scientific writing, which will benefit me for years to come.

I would like to thank Prof. Ruud van Ommen and Dr. Ming Li for their support in material development. I am also grateful to Dr. Paul Venema and Mr. Cai Yang for their help with osmotic pressure measurements and valuable discussions. Thanks as well to my students for their contributions throughout the project.

I would like to thank the committee members, Prof. M.D. Kennedy, Prof. E.R. Cornelissen, Prof. B. Liu, Dr. M.B. Tanis, and Prof. T. Wintgens, for their time in reviewing my dissertation and for their presence at the defence ceremony.

I would also like to thank my colleagues at the Department of Water Management for their friendship, encouragement, and many stimulating discussions. Special thanks to our secretaries for administrative support and to the lab technicians for their assistance with sample measurements and laboratory operations. I am especially grateful to Dr. Nadia van Pelt for her detailed suggestions and kind help in polishing the writing of each paper—from which I learned a great deal.

To all my friends who have stood by me during these years—both near and far—thank you for the laughter, conversations, and encouragement that helped me through the ups and downs.

Above all, I owe my deepest gratitude to my family—my parents, elder sister, younger brother, brother-in-law, and my beloved little nephew—for their unconditional love, sacrifices, and unwavering faith in me. This achievement would not have been possible without their silent strength behind me every step of the way. During moments of doubt and difficulty, a simple phone call with them gave me the strength to move forward again. My path has not always been smooth, and I am deeply thankful for their understanding, patience, and constant support throughout all the hardships. Their quiet presence has been my greatest comfort, and their belief in me has been my strongest motivation. I would like to express my heartfelt gratitude to my sister and brother for taking care of our parents in my absence. I am grateful to my sister and brother for looking after our parents, enabling me to pursue this long doctoral journey far from home.

I am also especially thankful to my girlfriend, soon to be my wife, for being by my side throughout this journey. Her understanding, steady support, and patience during countless late nights and early mornings supported me through the most challenging moments of my PhD. May we, in the days to come, have the steadiness of the Dazhou Mountains to lean on each other; the vastness of Lianyungang Sea to embrace each other; and the shimmering Dutch stars and moon to illuminate each other's lives.

Finally, I would like to thank someone who has never been formally acknowledged—myself.

This long journey has not been without its trials. There were moments of disruption and doubt. First came the decision to completely change the topic direction after three years of effort. Then the pandemic struck, bringing unexpected lab closures and prolonged isolation. Later, just as momentum was returning, the laboratory I relied on was shut down for one year. There were frustrations, delays, and countless quiet struggles—but never once did I truly consider giving up.

This book is the result of not only experiments and data, but of years spent reviewing literature, digging into data, rewriting storylines, and shaping every paragraph with care. It may still be imperfect—but it carries everything I had to give.

I remember one winter, during a trip home, I found an old letter I wrote to my parents as a child. In it, I had scrawled, "I want to become a PhD." I had no idea what that truly meant at the time. But perhaps even then, a small seed of stubbornness had taken root.

Years ago, in a moment of frustration, I once told my mother, that I felt like a donkey—not as fast or graceful as a horse. She said, “But a donkey is just fine. In the old days, donkeys don’t go to war.”

Perhaps she was right. To be a donkey is to move with quiet determination—not made for battle, but made to endure. To carry weight. To keep going. Not everyone gets to be the warrior horse, but perhaps some of donkeys, after all, end up like Afanti’s, or Jiménez’s—wise, patient, and enduring.

Many people, in their acknowledgements, reflect on how fast time flies. For me, it is especially true. But while others may say their PhD took three or four years, I spent seven—seven years working on one thing: completing this book. And like the cover of this book suggests:

Where others might mend the sky, a donkey chose to carve it open, hoping to draw water from the stars.

So, thank you—to myself.

For walking when it was easier to stop.

For carrying the weight when no one saw.

For believing that one day, the sky could be opened—so that a small boat, caught in wind and wave, might finally sail into calm waters filled with starlight.

Shuo Zhang

2025.07.11

Leiden

About the author

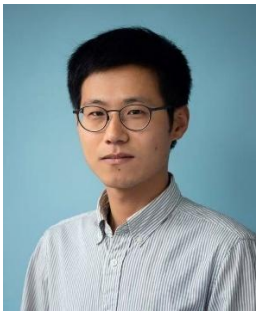

Shuo ZHANG was born on 15 March 1991 in Lianyungang, China—a small but beautiful seaside city.

He received his Bachelor's degree in Applied Chemistry from North China University of Science and Technology in 2015.

He then obtained his Master's degree in Chemical Engineering from Technion – Israel Institute of Technology in 2018, where his research focused on the characterization of anion exchange ionomers for fuel cell applications.

Since October 2018, he has been pursuing his PhD degree at Delft University of Technology (TU Delft), the Netherlands. His doctoral research focuses on ceramic membranes for water treatment, with particular emphasis on membrane modification, fouling mitigation, micropollutant removal, advanced oxidation processes, and low catalyst deposition techniques.

Shuo Zhang has a strong interest in membrane technology, catalyst development, and water engineering. He is committed to pursuing a career that contributes to sustainable and advanced water treatment technologies.

He can be reached at jszhangshuo@sina.com

List of publications

- Wang, X. X., **Zhang, S**., Van Hecke, K., Cui, G. H., & Liu, Y. G. (2015). Synthesis, structures and luminescence properties of two mixed nickel (II) coordination polymers bearing a rigid bis-triazole linker. Transition Metal Chemistry, 40, 565-571.

- Cui, G. H., **Zhang, S**., Zhu H. M. (2015) Adsorptive Removal of Congo red Azo Dye by Cobaltic Metal-Organic Frameworks based on Flexible Bis (benzimidazole). Journal of Environmental Management College of China, 25(3): 51-54.

- Liu, G., Zhang, G., **Zhang, S**., Xu, Y., Yang, X., & Zhang, X. (2020). Degradation and mechanism of microcystin-LR by PbCrO4 nanorods driven by visible light. Chemosphere, 239, 124739.

- **Zhang, S**., Liang, Y. X., Yang, C., Venema, P., Rietveld, L. C., & Heijman, S. G. J (2024). Colloidal concentration polarizations of PEG and silica in ceramic NF filtration. Desalination, 583, 117722.

- Jia, T., Peng, Z. X., Yu, J., Piaggio, A. L., **Zhang, S**., & Kreuk M. K (2024). Detecting the interaction between microparticles and biomass in biological wastewater treatment process with Deep Learning method. Science of the Total Environment, 951, 175813.

- **Zhang, S**., Wang, K. Y., Rietveld, L. C., & Heijman, S. G. J (2025). Fouling removal in ceramic ultrafiltration membrane via catalyst modification with Fenton-like backwash. Journal of membrane science, 734, 124411.

- **Zhang, S**., Li, M., He, T., van Ommen, J. R., Rietveld, L. C., & Heijman, S. G. J. Ceramic ultrafiltration membrane with low palladium loading via atomic later deposition for enhanced micropollutant degradation. (To be submitted)

- **Zhang, S**., Li, M., Ji, Y. N., van Ommen, J. R., Rietveld, L. C., & Heijman, S. G. J. Effect of fouling on the degradation of micropollutants by catalytic ceramic membranes activating peroxymonosulfate. (To be submitted)

- **Zhang, S**., Li, M., Ji, Y. N., van Ommen, J. R., Rietveld, L. C., & Heijman, S. G. J. Effect of pore sizes of membrane on fouling mitigation and micropollutant removal via the activated peroxymonosulfate. (In preparation)

八声甘州

看飘飘暮雪了无踪，是问有谁偷？且江关寂寂，烟长雾远，似我衣绸。拟把高山流水，散落在兰洲。哪必吹梅曲，踏马回眸。

记取经年行迹，过村郊林野，夜宿荒丘。算人间时序，去也不曾休。愿从今、云河清浅，载星辉、共与梦同舟。波光里、又生桥柳，潋影悠悠。

2023.03.10